Development and Evaluation of a Comprehensive Tropospheric Chemistry Model for Regional and Global Applications

Rahul A. Zaveri

Dissertation submitted to the Faculty of the
Virginia Polytechnic Institute and State University
in partial fulfillment of the requirements for the degree of

Doctor of Philosophy
in
Chemical Engineering

Approved
Leonard K. Peters, Chair
William L. Conger
Wayne L. Neu
John C. Little
Rick D. Saylor

June 27, 1997
Blacksburg, Virginia

Keywords: Air quality model, monoterpenes, dimethylsulfide, aerosol chemistry, aqueous chemistry

Development and Evaluation of a Comprehensive Tropospheric Chemistry Model for Regional and Global Applications

Rahul A. Zaveri

Abstract

Accurate simulations of the global radiative impact of anthropogenic emissions must employ a tropospheric chemistry model that predicts realistic distributions of aerosols of all types. The need for a such a comprehensive yet computationally efficient tropospheric chemistry model is addressed in this research via systematic development of the various sub-models/mechanisms representing the gas-, aerosol-, and cloud-phase chemistries.

The gas-phase model encompasses three tropospheric chemical regimes — background and urban, continental rural, and remote marine. The background and urban gas-phase mechanism is based on the paradigm of the Carbon Bond approach, modified for global-scale applications. The rural gas-phase chemistry includes highly condensed isoprene and α-pinene reactions. The isoprene photooxidation scheme is adapted for the present model from an available mechanism in the literature, while an α-pinene photooxidation mechanism, capable of predicting secondary organic aerosol formation, is developed for the first time from the available kinetic and product formation data. The remote marine gas-phase chemistry includes a highly condensed dimethylsulfide (DMS) photooxidation mechanism, based on a comprehensive scheme available in the literature. The proposed DMS mechanism can successfully explain the observed latitudinal variation in the ratios of methanesulfonic acid to non-sea-salt sulfate concentrations.

A highly efficient dynamic aerosol growth model is developed for condensing inorganic gases. Algorithms are presented for calculating equilibrium surface concentrations over dry and wet multicomponent aerosols containing sulfate, nitrate, chloride, ammonium, and sodium. This alternative model is capable of predictions as accurate for completely dissolved aerosols, and more accurate for completely dry aerosols than some of the similar models available in the literature.

For cloud processes, gas to liquid mass-transfer limitations to aqueous-phase reactions within cloud droplets are examined for all absorbing species by using the two-film model coupled with a comprehensive gas and aqueous-phase reaction mechanisms. Results indicate appreciable limitations only for the OH, HO_2, and NO_3 radicals. Subsequently, an accurate highly condensed aqueous-phase mechanism is derived for global-scale applications.

This work was supported by the U.S. EPA Aerosol Program under contract CR822079-01-0 and by the NASA Aerosol Program under Grant NAGW 3367.

To the loving memory of my grandfather.

Acknowledgements

I wish to express my deepest gratitude for Professor Len K. Peters. I am most thankful for his support and guidance throughout the past four years I have worked with him on my graduate studies. I also greatly appreciate his patience and help in putting this dissertation together in time.

I am grateful to my doctoral advisory committee for their time and interest in my work.

Sincere thanks are extended to Richard C. Easter, Rick D. Saylor, Yang Zhang, Steve J. Ghan, Elaine G. Chapman, and Carl M. Berkowitz for many educative discussions and ideas, without which this dissertation would not have been possible.

I am especially thankful to my colleagues Pius C. S. Lee and Jason M. Gillian for their friendship and help throughout this study.

I am deeply indebted to Dr. Ron Kriz for going out of his way to provide excellent computational and laboratory facilities for this work. I am also thankful to the system administrator, Tim Tomlin and secretaries Gail Williams, Diane Patty, Diane Cannaday, Chris Moore, and Carol Stables for taking care of the logistics, and making my student-life a lot easier.

I would also like to thank S. Hatakeyama for sharing his unpublished data on α-pinene photooxidation; S. L. Clegg for providing his $(NH_4)_2SO_4$-H_2SO_4 activity coefficient code; I. N. Tang and A. S. Wexler for helpful comments on multicomponent inorganic aerosol equilibria, and sending preprints of their recent papers; and M. J. Rood for helpful comments on the metastability of ambient aerosols.

This research would not have been possible without the generous support from the U.S. Environmental Protection Agency under contract CR822079-01-0, and the National Aeronautics and Space Administration under grant NAGW 3367. I am grateful to Dr. Joeseph Sickles of EPA, and Dr. Kenneth Bergman of NASA for the same.

I would like to thank my parents and my sister for their unlimited love, support, encouragement, and patience during the years I have been away from them; thanks are also due to the beloved Udani family for the same. And finally, I am most thankful to Jillu for absolutely everything.

Contents

Acknowledgements **v**

List of Tables **xi**

List of Figures **xvii**

1 Introduction **1**

1.1 Background and Motivation 1

1.2 Requirements of a Global Tropospheric Chemistry Model 3

1.3 Organization of Chapters 6

2 Urban and Background Gas-Phase Chemistry **7**

2.1 Inorganic Chemistry 7

2.2 Hydrocarbon Chemistry 9

2.2.1 Lumped Molecule Approach 11

2.2.2 Lumped Structure Approach 17

2.2.3 Global-Scale Carbon Bond Mechanism: CBM-Z 23

2.3 Mechanism Intercomparison 26

2.3.1 Model Inputs 26

2.3.2 Results and Discussion 30

2.4 Concluding Remarks 43

3 Rural Gas-Phase Chemistry: Isoprene **44**

3.1 Literature Review 44

3.2 Isoprene Mechanisms 47

3.3 Mechanism Intercomparison 49

3.3.1 Model Inputs 49

3.3.2 Results and Discussion 53

3.4 Concluding Remarks 66

4 Monoterpene Photooxidation Chemistry: α-Pinene **67**
4.1 Description of the Published Data Sets . . . 71
4.2 Modeling and Parameter Estimation for α-Pinene . . . 76
4.2.1 Reaction with OH in the Absence of NO_x . . . 76
4.2.2 Reaction with Ozone in the Absence of NO_x . . . 84
4.2.3 Reactions with OH and Ozone in the Presence of NO_x . . . 92
4.3 Summary and Remarks . . . 96
4.4 Mechanism Evaluation Under Atmospheric Conditions . . . 98
4.4.1 Box-Model Formulation and Inputs . . . 98
4.4.2 Simulation Results and Mechanism Analysis . . . 103
4.5 Condensed Mechanism . . . 117
4.6 Concluding Remarks . . . 119

5 Marine Gas-Phase Chemistry: DMS **120**
5.1 Literature Review . . . 124
5.1.1 Initial DMS-OH Reaction . . . 127
5.1.2 Decomposition of the CH_3SO_2 Radical . . . 129
5.1.3 Decomposition of the CH_3SO_3 Radical . . . 130
5.2 Condensed Mechanism . . . 131
5.3 Model Evaluation Under Atmospheric Conditions . . . 135
5.3.1 Model Inputs . . . 135
5.3.2 Results and Discussion . . . 135
5.4 Concluding Remarks . . . 143

6 Aerosol-Phase Chemistry **144**
6.1 Aerosol Ions and Electrolytes . . . 145
6.2 Phase-states and Deliquescence . . . 150
6.2.1 Illustration of the ZSR Model . . . 154
6.2.2 Temperature Effects . . . 154
6.3 Aerosol Size Distributions . . . 158
6.4 Dynamic Condensation Equations . . . 164
6.4.1 Mass-Transfer Coefficient . . . 164
6.5 Equilibrium Surface Concentrations for Dry Aerosol . . . 166

6.5.1 Fine-Mode Aerosol . . . 168
6.5.2 Sea-Salt Aerosol . . . 170
6.6 Equilibrium Surface Concentrations for Liquid Aerosol . . . 172
6.6.1 Water Content and Kelvin Effect . . . 172
6.6.2 Multicomponent Ionic Equilibria . . . 173
6.6.3 Activity Coefficient . . . 175
6.7 Test Simulations . . . 178
6.8 Concluding Remarks . . . 192

7 Cloud-Phase Chemistry 193
7.1 Mass Transfer with Chemical Reaction . . . 194
7.1.1 Theory . . . 194
7.1.2 Two-Film Model . . . 196
7.1.3 Dynamic Coupled Phase Equations . . . 198
7.2 Comprehensive Mechanism . . . 199
7.3 Condensed Mechanism . . . 209
7.4 Concluding Remarks . . . 218

8 Summary 219
8.1 Gas-Phase . . . 219
8.2 Condensed-Phases . . . 221
8.3 Future Work . . . 223

Bibliography 224

A Empirical Data 245

Vita 250

List of Tables

2.1 List of Inorganic Species Present in the Gas-Phase Mechanism. 8
2.2 List of Inorganic Photolytic Reactions in the Gas Phase. 9
2.3 List of Inorganic Reactions in the Gas Phase (based on Gery *et al.* (1989) and Stockwell *et al.* (1990)). 10
2.4 Troe Reactions and Rate Constants[a] (from Stockwell *et al.*, 1990). 11
2.5 List of Organic Species in RADM2. 13
2.6 Organic Chemistry in the RADM2 Mechanism (Stockwell *et al.*, 1990). . . . 14
2.7 List of Organic Species in CBM-IV. 19
2.8 The Published Carbon Bond Mechanism IV (Gery *et al.*, 1989): CBM-IV (P). 20
2.9 List of Additional Organic Species in CBM-Z over CBM-IV (P). 24
2.10 Additional Organic Reactions in CBM-Z over CBM-IV (P). 24
2.11 Comparison Between the Differing CBM-IV (P) and CBM-Z Reactions. . . . 25
2.12 Mechanism Nomenclature. 25
2.13 Urban Nonmethane Organic Carbon (NMOC) Composition (from Stockwell *et al.* (1990)). 28
2.14 Nonmethane Organic Carbon Apportionment into the Organic Surrogates for Each Mechanism. 29
2.15 Hypothetical NO_x, SO_2, and NMOC Emissions Scenarios. 29

3.1 List Organic Species in RADM-C for Isoprene Chemistry. 47
3.2 RADM-C Isoprene Mechanism from Zimmermann and Poppe (1996.) 48
3.3 Isoprene Chemistry Mechanism in the Published CBM-IV (Gery *et al.*, 1989). 49
3.4 Equivalent RADM2 and CBM-Z Species Relevant to the Isoprene Chemistry. 50
3.5 Equivalent CBM-Z Isoprene Chemistry Based on the RADM-C Mechanism. . 51
3.6 Mechanism Nomenclature. 52
3.7 Hypothetical Emission Scenarios for Isoprene Chemistry Intercomparison. . . 52

4.1 Monoterpenes Identified in Foliar Emissions[a]. 69
4.2 Selected Experimental Data Sets of α-Pinene Oxidation. 74

4.3 Experimental Conditions and Inital Concentrations for the Selected α-Pinene Oxidation Data Sets. 75
4.4 Estimated Photolytic Rate Constants (min^{-1}) for H1991 Data Sets. 80
4.5 Proposed α-Pinene Photooxidation Mechanism 97
4.6 Emission Flux Parameters for α-Pinene, and Isoprene for Fluxes over Deciduous and Coniferous Forests during July (based on Lamb *et al.*, 1993). . . . 101
4.7 Hypothetical Emissions Scenarios and Aloft-Air Concentrations. 101
4.8 List Organic Species in Condensed α-pinene Mechanism. 118
4.9 Condensed α-Pinene Photooxidation Mechanism 118

5.1 List Organic Species in Condensed DMS Mechanism. 132
5.2 Gas-Phase Condensed DMS Photooxidation Mechanism 134
5.3 Hypothetical Emissions Scenarios. 137
5.4 Predicted Average Gas-Phase DMS/SO_2 Concentration Ratios. 141
5.5 Predicted Average MSA/NSSS Molar Concentration Ratios. 142

6.1 Thermodynamic Parameters for Typical Aerosol Electrolytes[a]. 148
6.2 Assumed Possible Electrolytes in Coarse-Mode Sea-Salt Aerosol. 149
6.3 Assumed Possible Electrolytes in Fine-Mode Sulfate Aerosol. 149
6.4 Chemical and Physical Description of the Different Aerosol Modes. 162
6.5 Equilibrium Reactions Involved with Aerosols. 167
6.6 Irreversible Reactions Involved with Dry Aerosols. 167
6.7 Hypothetical Test Cases 178

7.1 Comprehensive Aqueous-Phase Mechanism (Based on Pandis and Seinfeld, 1989). 201
7.2 Gas-Liquid Interfacial Dissolution Equilibria (from Pandis and Seinfeld, 1989). 205
7.3 Aqueous-Phase Dissociation Equilibria (from Pandis and Seinfeld, 1989). . . 206
7.4 Hypothetical Test Scenarios. 207
7.5 Comparison of Mass-Transfer and Reaction Rate Constants for OH[a]. 208
7.6 Comparison of Mass-Transfer and Reaction Rate Constants for NO_3[a]. 208
7.7 Comparison of Mass-Transfer and Reaction Rate Constants for HO_2[a]. 208
7.8 Condensed Aqueous-Phase Mechanism 211

8.1 Summary of Various Chemistry Models/Mechanisms. 223

A.1 List of coefficients used in Equation (A.2). 245
A.2 Deliquescence points of pure salts at 298.15 K and their temperature dependency parameters in Equation (6.16). 246
A.3 Polynomial coefficients for binary activity coefficients fitted for ionic strengths up to 100 mol kg^{-1}. 247
A.4 Diffusivities and mass accommodation coefficients. 248
A.5 Diffusion volumes of organic molecules (Fuller *et al.*, 1966). 249

List of Figures

1.1 Schematic representation of the greenhouse and whitehouse effects. 5

2.1 Prescribed diurnal temperature variation. 30
2.2 Concentration evolution using the RADM2, CBM-Z, CBM-IV (R), and CBM-IV (P) mechanisms for scenario S4: (a) O_3; (b) H_2O_2. 33
2.3 Concentration evolution using the RADM2, CBM-Z, CBM-IV (R), and CBM-IV (P) mechanisms for scenario S4: (a) NO_3; (b) NO2. 34
2.4 Concentration evolution using the RADM2, CBM-Z, CBM-IV (R), and CBM-IV (P) mechanisms for scenario S4: (a) OH; (b) HO_2. 35
2.5 Simulated concentrations after 3 model days using the RADM2, CBM-Z, CBM-IV (R), and CBM-IV (P) mechanisms: (a) O_3; (b) H_2O_2. 36
2.6 Simulated concentrations after 3 model days using the RADM2, CBM-Z, CBM-IV (R), and CBM-IV (P) mechanisms: (a) H_2SO_4; (b) HNO_3. 37
2.7 Percentage concentration deviations from CBM-Z, CBM-IV (R), and CBM-IV (P) with respect to RADM2 predictions after 3 model days: (a) O_3; (b) H_2O_2. 38
2.8 Percentage concentration deviations from CBM-Z, CBM-IV (R), and CBM-IV (P) with respect to RADM2 predictions after 3 model days: (a) H_2SO_4; (b) HNO_3. 39
2.9 Simulated concentrations after 3 model days using the RADM2 and CBM-Z mechanisms: (a) HCOOH; (b) CH_3COOH. No organic acids are produced in the CBM-IV. 40
2.10 CPU time required by the RADM2, CBM-Z, and CBM-IV (P) mechanisms to simulate 3 model days. The CBM-IV (R) CPU timings are similar to those of CBM-IV (P). 41
2.11 Comparison of mechanism size between CBM-IV (P), CBM-Z, and RADM2. 42

3.1 July Isoprene emission flux based on the global inventory of Guenther *et al.* (1995). 45

3.2 Isoprene concentration evolution using the RADM-C, CBM-Z (old), and CBM-Z (new) mechanisms for: (a) scenario I2; (b) scenario I4. 55
3.3 Concentration evolution using the RADM-C, CBM-Z (old), and CBM-Z (new) mechanisms for scenario I2: (a) O_3; (b) H_2O_2. 56
3.4 Concentration evolution using the RADM-C, CBM-Z (old), and CBM-Z (new) mechanisms for scenario I2: (a) NO_3; (b) NO2. 57
3.5 Concentration evolution using the RADM-C, CBM-Z (old), and CBM-Z (new) mechanisms for scenario I2: (a) OH; (b) HO_2. 58
3.6 Concentration evolution using the RADM-C, CBM-Z (old), and CBM-Z (new) mechanisms for scenario I4: (a) O_3; (b) H_2O_2. 59
3.7 Concentration evolution using the RADM-C, CBM-Z (old), and CBM-Z (new) mechanisms for scenario I4: (a) NO_3; (b) NO2. 60
3.8 Concentration evolution using the RADM-C, CBM-Z (old), and CBM-Z (new) mechanisms for scenario I4: (a) OH; (b) HO_2. 61
3.9 Percentage concentration deviations from the CBM-Z (old), and CBM-Z (new) with respect to RADM2 predictions after 3 model days: (a) O_3; (b) H_2O_2. . 62
3.10 Percentage concentration deviations from the CBM-Z (old), and CBM-Z (new) with respect to RADM2 predictions after 3 model days: (a) H_2SO_4; (b) HNO_3. 63
3.11 Percentage concentration deviations from the CBM-Z (old), and CBM-Z (new) with respect to RADM2 predictions after 3 model days: (a) HCOOH; (b) CH_3COOH. 64
3.12 CPU time required by the RADM-C, CBM-Z (new), and CBM-Z (old) mechanisms to simulate 3 model days. 65

4.1 July Monoterpene emission flux based on the global inventory of Guenther *et al.* (1995). 68
4.2 Relative terpene content in volatile emission from Scots pine (Isidorov *et al.*, 1985). 70
4.3 Proposed α-pinene + OH reaction mechanism. 77
4.4 Proposed α-pinene ozonolysis mechanism. 78
4.5 (a) Chamber radiation flux for H1991 data sets (Hatakeyama, 1997), (b) Product of the absorption cross-section and photolysis quantum yield spectra for relevant species. 81

4.6 Plots of pinonaldehyde concentration against α-pinene conversion with k4 as a parameter for the experimental conditions of H1991a5. 83
4.7 Plots of pinonaldehyde concentration against α-pinene conversion with k2 as a parameter for the experimental conditions of H1991a5. 84
4.8 Plot of simulated vs observed pinonaldehyde yields for the best estimates of k2, k4, and y. 85
4.9 Simulated (lines) and experimental (symbols) profiles of α-pinene, aerosol carbon, and ozone for the data set H1991b. 86
4.10 Simulated (lines) and experimental (symbols) profiles of α-pinene, O_3 and their reaction products for the data set H1989a. 89
4.11 Simulated and experimental yields of aerosol carbon over a wide range of initial α-pinene concentration. Data set H1989c. 90
4.12 Simulated (symbols), and observed (solid line) overall yields of H_2O_2 over a wide range of initial α-pinene, and O_3 concentrations under the experimental conditions of the data set S1991a. 91
4.13 Hypothesized α-pinene-NO_3 reaction mechanism. 94
4.14 Dependence of pinonaldehyde production on the rate constant k5. Solid and broken lines are simulated profiles, filled circles are experimental values from the data set H1991c1. 95
4.15 Simulated (lines), and experimental (symbols) time evolution of the major gaseous species in the reaction of α-pinene and OH in the presence of NO_x (data set H1991c2). 96
4.16 Schematic illustration of the box-model. 99
4.17 Prescribed diurnal variations of mixed-layer height, and temperature. 100
4.18 Parameterized (lines) and observed (symbols) emission fluxes of isoprene, and α-pinene for (a) coniferous forest, and (b) deciduous forest (from Lamb *et al.*, 1993). 102
4.19 Diurnal concentration profiles for scenarios C2, D2 and without biogenic HCs: (a) α-pinene; (b) isoprene. 107
4.20 Diurnal concentration profiles for scenarios C2, D2 and without biogenic HCs: (a) O_3; (b) H_2O_2. 108

4.21 Diurnal concentration profiles for scenarios C2, D2 and without biogenic HCs: (a) OH; (b) NO_3. 109
4.22 Diurnal concentration profiles for scenarios C2, D2 and without biogenic HCs: (a) NO_3; (b) NO_2. 110
4.23 Diurnal relative depletion profiles of (a) α-pinene, and (b) isoprene due to reactions with O_3, OH and NO_3 for scenario C2. 111
4.24 Diurnal relative depletion profiles of (a) α-pinene, and (b) isoprene due to reactions with O_3, OH and NO_3 for scenario D2. 112
4.25 Daily average relative depletions of (a) α-pinene, and (b) isoprene due to reactions with O_3, OH, and NO_3. 113
4.26 Diurnal instantaneous yields of (a) SOA, and (b) SONA with respect to APIN conversion for scenarios C1, C2, and C3. 114
4.27 Diurnal instantaneous yields of (a) SOA, and (b) SONA with respect to APIN conversion for scenarios D1, D2, and D3. 115
4.28 Daily average SOA, SONA, and total aerosol carbon yields for all scenarios. 116

5.1 July DMS emission flux based on the global inventory of Spiro *et al.* (1992). 121
5.2 January DMS emission flux based on the global inventory of Spiro *et al.* (1992). 122
5.3 Anthropogenic SO_2 emission flux based on the global inventory of Spiro *et al.* (1992). 123
5.4 Comprehensive DMS photooxidation scheme proposed by Yin *et al.* (1990a). 125
5.5 (a) Rate constants of the two initial DMS-OH reaction pathways, and (b) their branching ratios (after Hynes *et al.*, 1986). 126
5.6 Observed MSA/NSSS ratios: (a) Latitudinal variation in summer; (b) Seasonal variation at Cape Grim (refer text for references). 128
5.7 Condensed DMS photooxidation scheme (this work). 133
5.8 Production and loss of DMS-derived sulfur compounds in cloud-free marine boundary layer. 136
5.9 Diurnal concentration profiles for scenarios M1, M2 and M3 at 300 K: (a) DMS; (b) SO_2. Filled circles are field measurements from Yvon and Saltzman (1996). 138
5.10 Diurnal concentration profiles for scenarios M1, M2 and M3 at 300 K: (a) DMSO; (b) $DMSO_2$. 139

5.11 Diurnal concentration profiles for scenarios M1, M2 and M3 at 280 K: (a) DMSO; (b) $DMSO_2$. 140

6.1 Variation of saturation water activity as a function of relative amounts of $(NH_4)_2SO_4$ and NH_4NO_3 in a mixed-salt system (based on the saturation data of Seidell and Linke (1965)). The filled circles indicate three eutonic points and the corresponding water activities are the mutual DRHs. 151
6.2 Growth cycle of various single-salt aerorol particles. The ratio w/w_o represents the ratio of the wet aerosol mass to the dry mass. 152
6.3 Mass fraction of solute (mfs) vs. water activity for NH_4^+ - SO_4^{2-} system with X_T ranging from 0.2 to 1. 155
6.4 Mass fraction of solute (mfs) vs. water activity for NH_4^+ - SO_4^{2-} system with $X_T = 1.4$. 156
6.5 Mass fraction of solute (mfs) vs. water activity for NH_4^+ - SO_4^{2-} system with $X_T = 1.8$. 157
6.6 Variation of the deliquescence relative humidities with temperature based on the parameters given in Table A.2 for (a) ammonium salts, and (b) sodium salts. 159
6.7 Variation of the freezing point of an electrolyte solution as a function of the solution water activity at 298.15 K. 160
6.8 Normalized log-normal number, surface, and volume concentration distributions of different modes based on the number geometric mean diameters and geometric standard deviations listed in Table 6.4. 163
6.9 Concentration evolution profiles for case A1: (a) gas-phase species; (b) corresponding aerosol-phase generic species. 179
6.10 (a) Aerosol growth curves for case A1; (b) evolution of individual electrolytes in the aerosol phase. 180
6.11 Concentration evolution profiles for case A2: (a) gas-phase species; (b) corresponding aerosol-phase generic species. 181
6.12 (a) Aerosol growth curves for case A2; (b) evolution of individual electrolytes in the aerosol phase. 182
6.13 Concentration evolution profiles for case A3: (a) gas-phase species; (b) corresponding aerosol-phase generic species. 183

6.14 (a) Aerosol growth curves for case A3; (b) evolution of individual electrolytes in the aerosol phase. 184
6.15 Concentration evolution profiles for case A4: (a) gas-phase species; (b) corresponding aerosol-phase generic species. 185
6.16 (a) Aerosol growth curves for case A4; (b) evolution of individual electrolytes in the aerosol phase. 186
6.17 Concentration evolution profiles for case A5: (a) gas-phase species; (b) corresponding aerosol-phase generic species. 187
6.18 (a) Aerosol growth curves for case A5; (b) evolution of individual electrolytes in the aerosol phase. 188
6.19 Concentration evolution profiles for case A6: (a) gas-phase species; (b) corresponding aerosol-phase generic species. 189
6.20 (a) Aerosol growth curves for case A6; (b) evolution of individual electrolytes in the aerosol phase. 190

7.1 Variation of enhancement factor as a function of diffuso-reactive parameter . 198
7.2 Comprehensive aqueous-phase S(IV) to S(VI) conversion pathways 210
7.3 Condensed aqueous-phase S(IV) to S(VI) conversion pathways 211
7.4 Total sulfate evolution from: (a) full aqueous-phase mechanism of Pandis and Seinfeld; (b) condensed mechanism derived in this work. 213
7.5 Total nitrate evolution from: (a) full aqueous-phase mechanism of Pandis and Seinfeld; (b) condensed mechanism derived in this work. 214
7.6 Total formic acid evolution from: (a) full aqueous-phase mechanism of Pandis and Seinfeld; (b) condensed mechanism derived in this work. 215
7.7 Aqueous-phase O_3 evolution from: (a) full aqueous-phase mechanism of Pandis and Seinfeld; (b) condensed mechanism derived in this work. 216
7.8 Aqueous-phase H_2O_2 evolution from: (a) full aqueous-phase mechanism of Pandis and Seinfeld; (b) condensed mechanism derived in this work. 217

Chapter 1

Introduction

1.1 Background and Motivation

One of the most pressing problems facing the nations of the world during the 1990s and into the 21st century is the effect of human activities on the atmospheric environment. One such climatic threat, popularly known as "global warming", has recently been the topic of debates on numerous news media, as well as the focus of large national and international research programs. The naturally occurring atmospheric greenhouse gases such as water vapor and carbon dioxide (CO_2) play a crucial role in regulating the temperature of the atmosphere by transmitting the incoming shortwave solar radiation, and absorbing the long-wave radiation (infrared) emitted by the Earth's surface. This is known as the "greenhouse effect", by analogy to the supposed operating principle of greenhouses. In the absence of the natural greenhouse effect, the average surface temperature would be -19°C (-2.2°F) instead of the present value of 15°C (59°F).

For the past 200 years, the atmospheric carbon dioxide concentration has been climbing rapidly due to fossil-fuel burning and massive deforestation. The atmospheric CO_2 level has increased by about 25% since 1850 (Schneider, 1989). Theoretically, higher average atmospheric concentrations of CO_2 must eventually result in a warmer global climate. An average global warming by just 3°C compressed into a mere century could have unprecedented consequences on the planet's ecosystems. Current best estimates, based on complex atmosphere-ocean models, suggest that the climate should have warmed by almost 1°C since 1900; however, the observed average global temperature record indicates a rise of only about 0.5°C (Hasselmann, 1997). Moreover, despite the sharp rise in the average global temperatures during the last decade, no significant increase has been observed in the northern high latitudes (Charlson and Wigley, 1994).

Along with CO_2 emissions, fossil fuel combustion (especially coal) also releases sulfur dioxide (SO_2), which is oxidized in the atmosphere to sulfuric acid (H_2SO_4). Sulfuric acid vapor is known to form hygroscopic particles (also called sulfate aerosol) in the atmosphere,

which can efficiently form clouds under favorable conditions. These sub-micron size atmospheric particles and cloud droplets tend to reflect and scatter the incoming shortwave solar radiation back to the space, causing a cooling effect on the climate. By analogy to the greenhouse effect, this phenomenon is termed the "whitehouse effect" (Schwartz, 1996).

Evidence is mounting that such anthropogenic aerosols may be influencing the climate in a manner that partially compensates for warming due to the increasing greenhouse gases. Measurements of atmospheric sulfate indicate much higher concentrations in the vicinity of industrialized regions, and generally higher concentrations in the Northern Hemisphere than in the less industrialized Southern Hemisphere (Schwartz, 1988a). The higher sulfate aerosol concentrations enhance the scattering of sunlight to space, both through the direct scattering of sunlight by the aerosols themselves (direct effect) and through the influence of sulfate aerosols on the number concentrations of cloud droplets and hence the reflectivity of clouds (indirect effect). Preliminary estimates of the radiative impact of anthropogenic sulfur emissions indicate a perturbation of roughly -1 W m^{-2} in the global planetary radiation balance (Charlson *et al.*, 1991, 1992; Schlesinger *et al.*, 1992). Such a radiative cooling is comparable in magnitude to the radiative heating due to the increase in anthropogenic greenhouse gases to date (Shine *et al.*, 1990). This may explain why the climate has not warmed as much as predicted by climate models forced by realistic increases in greenhouse gas concentrations.

However, estimates of the radiative impact of anthropogenic sulfate to date have been based on relatively crude models of the tropospheric chemistry (Erickson *et al.*, 1991; Luecken *et al.*, 1991; Langner and Rodhe, 1991). The relationship between sulfate concentration and aerosol number concentration is extremely complex (Charlson *et al.*, 1990), with the fraction of sulfuric acid vapor that nucleates to form new sulfate aerosols being highly dependent on the concentration and size of pre-existing aerosols (Langner *et al.*, 1992). The pre-existing aerosols not only include those resulting from anthropogenic sulfate, but all other atmospheric aerosols of natural or anthropogenic origin such as wind-blown dust particles; organic aerosols formed from naturally emitted hydrocarbons; sea-salt aerosols from sea spray; and sulfate aerosol resulting from naturally emitted sulfur compounds. Primary emissions of smoke or soot particles resulting from biomass burning also play an important role in the tropospheric aerosol budget.

An accurate simulation of the global radiative impact of anthropogenic sulfate must

employ a tropospheric chemistry model that predicts realistic distributions of aerosol of all types, coupled with a general circulation model that accounts for the important aerosol feedbacks with clouds. This dissertation was motivated by the need for such a chemistry model suitable for large-scale simulations. The following section identifies and describes some of the important requirements of a global tropospheric chemistry model.

1.2 Requirements of a Global Tropospheric Chemistry Model

Figure 1.1 illustrates the basic components of the complex global tropospheric chemistry leading to aerosol formation. The most important emissions are identified as:

1. Anthropogenic pollutants such as NO_x, SO_2, and reactive hydrocarbons.
2. Biogenic hydrocarbons such as isoprene and monoterpenes from continental vegetation.
3. Biogenic sulfur compounds such as dimethylsulfide (DMS) and hydrogen sulfide from oceanic environments.
4. Primary aerosol particles such as soot, dust, and sea-salt aerosol.

Once emitted, these compounds undergo transport due to convection and turbulent diffusion, and transformations due to chemical reactions.

A global tropospheric chemistry simulation, therefore, involves spatially and temporally varying emissions of various species into a three-dimensionally discretized global atmosphere. Although the emissions of primary gases and particles are usually prescribed or parameterized during a simulation, the subsequent chemistry leading to aerosol formation must be treated in a dynamic fashion. As a result, complex chemistry integrations along with inter-phase mass transfer calculations must be performed at every time step, over thousands of grid points (typically ranging from over 40,000 to 200,000), for more than one hundred different chemical species distributed in three different phases — gas, aerosol, and cloud. The dynamic transport-chemistry equations are written as

Gas-phase:

$$\frac{\partial \mathrm{C_i}}{\partial \mathrm{t}} + \nabla \cdot (\vec{\mathrm{v}}\mathrm{C_i}) = \nabla \cdot (\hat{\mathrm{K}} \cdot \nabla \mathrm{C_i}) + \mathrm{S_i} + \mathrm{G_i} + \mathrm{R_i} \tag{1.1}$$

Other phases (cloud, aerosol):

$$\frac{\partial \mathrm{V_p C_{i,p}}}{\partial \mathrm{t}} + \nabla \cdot [(\vec{\mathrm{v}} - \vec{\mathrm{v}}_{\mathrm{s,p}})\mathrm{V_p C_i}] = \nabla \cdot (\mathrm{C_{i,p}} \hat{\mathrm{K}}_\mathrm{p} \cdot \nabla \mathrm{V_p}) + \mathrm{S_{i,p}} + \mathrm{G_{i,p}} + \mathrm{R_{i,p}} \tag{1.2}$$

where
C_i is the concentration of species i,
p is the phase index,
$C_{i,p}$ is the concentration of species i in phase p,
$\vec{v}$ is the time-averaged wind field,
$\vec{v}_{s,p}$ is the settling velocity of phase p,
V_p is the volume of phase p per unit volume of air,
$\hat{K}$ is the turbulent eddy diffusivity tensor for the gas-phase,
$\hat{K}_p$ is the eddy diffusivity tensor for phase p (depends on the characteristic size of the phase),
S_i and $S_{i,p}$ are the emission rates of species i in the gas-phase and phase p, respectively,
G_i and $G_{i,p}$ are the rates of interphase mass transfer of species i
R_i and $R_{i,p}$ are the rates of chemical reactions of species i.

This dissertation deals with the analysis and representation of the inter-phase mass transfer and chemical reaction terms in the above equations (1.1) and (1.2). Because of the highly non-linear nature of the chemistry, coupled with widely different reaction time scales of different species, the resulting set of ordinary differential equations is stiff. The chemistry calculations are, therefore, computationally very expensive, and typically constitute about 90% of the total CPU time. Thus, the two most important requirements of the chemistry model are that it must be compact and very efficient, and at the same time, must be detailed enough to accurately represent the complex chemistries of the important compounds in the different phases mentioned above.

A number of global-scale tropospheric chemistry models have been developed in the past (Peters *et al.*, 1995). Some of the recent tropospheric sulfur cycle models include those of Erickson *et al.* (1991), Langner and Rodhe (1991), Pham *et al.* (1995), Chin *et al.* (1996), and Feichter *et al.* (1996). These models have been particularly useful in estimating various types of sulfur budgets in the global troposphere. The chemical mechanisms implemented in such models are usually kept very simple, so that low simulation turn-around times can be achieved. However, for the very same reason, such models cannot be effectively applied for estimating climate forcing studies, which involve complex feedbacks between chemistry and meteorology. To this end, state-of-the-art gas-, aerosol-, and cloud-phase chemistry mechanisms are developed for use in large-scale tropospheric chemistry models. Box-models of each mechanism are constructed and individually tested for accuracy and efficiency. Each

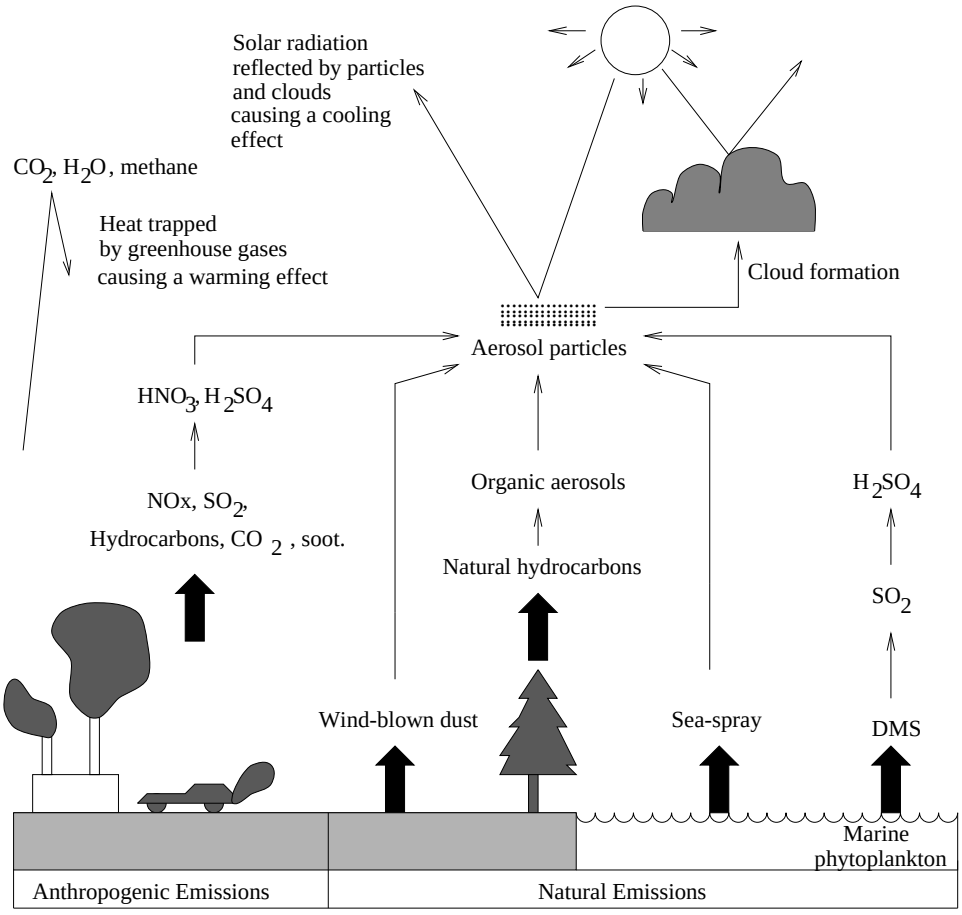

Figure 1.1: Schematic representation of the greenhouse and whitehouse effects.

mechanism/model is presented in a separate chapter as described below.

1.3 Organization of Chapters

The first mechanism presented in chapter 2 forms the core of the entire tropospheric chemistry model. It represents the basic gas-phase inorganic and hydrocarbon chemistry of the troposphere, including the urban gas-phase hydrocarbon chemistry. All subsequent mechanisms/models are coupled to this mechanism.

The next two chapters focus on the gas-phase chemistry of the important continental biogenic hydrocarbons. Chapter 3 describes the adaptation of an available gas-phase isoprene mechanism for the present model. The monoterpene chemistry is derived for the first time from the available kinetic and product formation data, and is presented in Chapter 4.

Chapter 5 presents the gas-phase chemical mechanism of dimethylsulfide, which is the most important naturally occurring sulfur-containing compound in the marine troposphere. The available comprehensive mechanism in the literature is critically examined in the light various field and laboratory experiments, and subsequently condensed into a compact version for global-scale applications.

Chapter 6 introduces a newly developed dynamic multicomponent aerosol growth model for condensing/evaporating inorganic gases. Various thermodynamic and kinetic aspects of the model are discussed and exploited for optimizing the growth calculations.

Finally, in Chapter 7 the cloud-phase chemistry of the important soluble species is presented. The potential for mass-transfer limitations to the aqueous-phase reactions of absorbing species is examined by using the two-film model coupled with a comprehensive aqueous-phase reaction mechanism. Subsequently, a highly condensed mechanism is derived for global-scale applications.

The major results and conclusions of each mechanism/model are summarized in Chapter 8.

Chapter 2

Urban and Background Gas-Phase Chemistry

The gas-phase chemical mechanism is the core component of a multi-phase atmospheric chemistry modeling system. Chemistry in the condensed phases such as cloud droplets and aerosol particles are directly or indirectly affected by the reactions taking place in the gaseous phase. The accuracy of the modeling system as a whole, therefore, relies heavily on its gas-phase mechanism. To simplify the development and analysis of a comprehensive gas-phase mechanism, a modular approach is adopted in which several different sets of reactions are developed and coupled together in a step-wise manner. This chapter describes the selection and development of the inorganic and hydrocarbon chemistries suitable for regional and global applications.

2.1 Inorganic Chemistry

Inorganic chemistry consists of reactions of ubiquitous trace gases such as nitrogen oxides (NO_x), ozone, and other oxidants. These reactions play an important role in the photochemical cycling of tropospheric ozone, and are particularly important in a polluted urban atmosphere, because of the relatively higher NO_x concentration levels occurring as a result of automobile emissions. In remote regions, natural processes such as lightning and soil emissions significantly contribute to the ambient NO_x levels, thereby affecting the tropospheric ozone budgets.

During the past two to three decades, several gas-phase chemical mechanisms have been developed for urban- and regional-scale air pollution models. These mechanisms have continually undergone modifications and improvements resulting from many years of smog chamber and kinetic studies. Thus, the modern gas-phase chemical mechanisms have reached a fairly advanced state of development and understanding. Not surprisingly, the inorganic reactions are more or less the same in most of the mechanisms available in the recent literature (Lurmann *et al.*, 1987; Gery *et al.*, 1989; Stockwell *et al.*, 1990), with some differences in the rate constant expressions. The inorganic species of interest for tropospheric chemistry are listed in Table 2.1. Abundant species such as oxygen and nitrogen molecules are treated as

Table 2.1: List of Inorganic Species Present in the Gas-Phase Mechanism.

No.	Species	Representation
1.	Nitric oxide	NO
2.	Nitrogen dioxide	NO_2
3.	Nitrogen trioxide (nitrate radical)	NO_3
4.	Nitrogen pentoxide	N_2O_5
5.	Nitrous acid	HNO_2
6.	Nitric acid	HNO_3
7.	Pernitric acid	HNO_4
8.	Ozone	O_3
9.	Excited-state oxygen atom	$O(^1D)$
10.	Ground-state oxygen atom	$O(^3P)$
11.	Hydroxyl radical	OH
12.	Hydroperoxy radical	HO_2
13.	Hydrogen peroxide	H_2O_2
14.	Sulfur dioxide	SO_2
15.	Sulfuric acid	H_2SO_4
16.	Hydrochloric acid	HCl
17.	Ammonia	NH_3
18.	Carbon monoxide	CO
19.	Carbon dioxide	CO_2
20.	Water vapor	H_2O

stable compounds, and are assumed as 21% and 79% of the total molecular air concentration, respectively. The inorganic reactions based on the mechanisms of Gery *et al.* (1989) and Stockwell *et al.* (1990) are selected for the present model, and compiled in Tables 2.2 and 2.3; the majority of the rate constants are taken from the latter, more recent reference. Rate constants of the Troe reactions listed in Table 2.4 are calculated as

$$k = \left[\frac{k_o^T[M]}{1 + [M]k_o^T/k_\infty^T}\right]^{0.6[1+(\log([M]k_o^T k_\infty^T))^2]^{-1}} \tag{2.1}$$

where $k_o^T = k_o^{300}(T/300)^{-n}$; and $k_\infty^T = k_\infty^{300}(T/300)^{-m}$

Table 2.2: List of Inorganic Photolytic Reactions in the Gas Phase.

No.	Reaction	Rate Constant k [s^{-1}]
1.	$NO_2 + h\nu \xrightarrow{O_2} NO + O(^3P)$	Radiation dependent
2.	$NO_3 + h\nu \longrightarrow .89NO_2 + .89O(^3P) + .11NO$	Radiation dependent
3.	$HNO_2 + h\nu \longrightarrow OH + NO$	Radiation dependent
4.	$HNO_3 + h\nu \longrightarrow OH + NO_2$	Radiation dependent
5.	$HNO_4 + h\nu \longrightarrow HO_2 + NO_2$	Radiation dependent
6.	$O_3 + h\nu \longrightarrow O(^3P)$	Radiation dependent
7.	$O_3 + h\nu \longrightarrow O(^1D)$	Radiation dependent
8.	$H_2O_2 + h\nu \longrightarrow 2OH$	Radiation dependent

2.2 Hydrocarbon Chemistry

Unlike the standard inorganic chemistry, the treatment of gas-phase hydrocarbon chemistry often differs considerably among most mechanisms. The detailed explicit mechanisms try to treat all emitted chemical species and their reactions individually, and therefore, tend to be very bulky (Leone and Seinfeld, 1985; Kerr and Calvert, 1985; Carter *et al.*, 1986). Such elaborate mechanisms are computationally extremely expensive, and cannot be used for regional and global applications. Due to the stringent computational time and memory constraints, several simplified mechanisms have been developed that attempt to maintain a balance between chemical detail and mechanism length (Dodge, 1977; Whitten *et al.*, 1980; Atkinson *et al.*, 1982; McRae *et al.*, 1982; Lurmann *et al.*, 1987; Stockwell, 1986; Gery *et al.*, 1989; Stockwell *et al.*, 1990).

These mechanisms are derived using the same body of kinetic data from which the explicit mechanisms are developed; however, they differ in the simplification techniques, popularly known as "lumping techniques." In general, three different lumping techniques have been used in the past to simplify the complex organic chemistry of the polluted troposphere: (1) surrogate species (Dodge, 1977); (2) lumped molecule (Atkinson *et al.*, 1982a; McRae *et al.*, 1982; Lurmann *et al.*, 1987; Stockwell, 1986, 1990); and (3) lumped structure (Whitten *et al.*, 1980; Gery *et al.*, 1989). Of these three techniques, the latter two have been the most popular because of their higher efficiency and accuracy compared to the surrogate species technique. The popular lumped molecule and lumped structure mechanisms are considered here to represent the urban organic chemistry in the global mechanism.

Table 2.3: List of Inorganic Reactions in the Gas Phase (based on Gery *et al.* (1989) and Stockwell *et al.* (1990)).

No.	Reaction			Rate Constant k [molecule − cm^3 − s]
9.	$O(^1D)$	$\xrightarrow{M}$	$O(^3P)$	$1.9 \times 10^8 \exp(390/T)$
10.	$O(^1D) + H_2O$	$\longrightarrow$	2OH	2.2×10^{-10}
11.	$O(^3P)$	$\xrightarrow{O_2,M}$	O_3	$[M] \times 6 \times 10^{-34} \times (T/300)^{-2.3}$
12.	$O(^3P) + NO_2$	$\longrightarrow$	NO	$6.5 \times 10^{-12} \exp(-120/T)$
13.	$O(^3P) + NO_2$	$\xrightarrow{M}$	NO_3	$1.6 \times 10^{-13} \exp(687/T)$
14.	$O(^3P) + NO$	$\xrightarrow{M}$	NO_2	$2.2 \times 10^{-13} \exp(602/T)$
15.	$O_3 + NO$	$\longrightarrow$	NO_2	$2.0 \times 10^{-12} \exp(-1400/T)$
16.	$O_3 + NO_2$	$\longrightarrow$	NO_3	$1.4 \times 10^{-13} \exp(-2500/T)$
17.	$O_3 + OH$	$\longrightarrow$	HO_2	$1.6 \times 10^{-12} \exp(-940/T)$
18.	$O_3 + HO_2$	$\longrightarrow$	OH	$1.1 \times 10^{-14} \exp(-500/T)$
19.	$OH + NO$	$\xrightarrow{M}$	HNO_2	see Table 2.4
20.	$OH + NO_2$	$\xrightarrow{M}$	HNO_3	see Table 2.4
21.	$OH + HNO_2$	$\longrightarrow$	NO_2	6.6×10^{-12}
22.	$OH + HNO_3$	$\xrightarrow{M}$	NO_3	$k_o + k_a/(1 + k_a/k_b)$, see (1)
23.	$OH + HNO_4$	$\longrightarrow$	NO_2	$1.3 \times 10^{-12} \exp(380/T)$
24.	$OH + HO_2$	$\longrightarrow$		$4.6 \times 10^{-11} \exp(230/T)$
25.	$OH + H_2O_2$	$\longrightarrow$	HO_2	$3.3 \times 10^{-12} \exp(-200/T)$
26.	$HO_2 + HO_2$	$\xrightarrow{M}$	H_2O_2	$k_c + k_p$, see (2)
27.	$HO_2 + HO_2 + H_2O$	$\xrightarrow{M}$	H_2O_2	$(k_c + k_p)k_w$, see (2)
28.	$HO_2 + NO$	$\longrightarrow$	$OH + NO_2$	$3.7 \times 10^{-12} \exp(240/T)$
29.	$HO_2 + NO_2$	$\xrightarrow{M}$	HNO_4	see Table 2.4
30.	HNO_4	$\xrightarrow{M}$	$HO_2 + NO_2$	$k_{30} \times 4.76 \times 10^{26} \exp(-10900/T)$
31.	$NO_3 + NO$	$\longrightarrow$	$2NO_2$	$1.7 \times 10^{-11} \exp(150/T)$
32.	$NO_3 + NO_2$	$\longrightarrow$	$NO + NO_2$	$2.5 \times 10^{-14} \exp(-1230/T)$
33.	$NO_3 + NO_2$	$\xrightarrow{M}$	N_2O_5	see Table 2.4
34.	$NO_3 + HO_2$	$\longrightarrow$	HNO_3	2.5×10^{-12}
35.	$N_2O_5 + H_2O$	$\longrightarrow$	$2HNO_3$	2.0×10^{-21}
36.	N_2O_5	$\xrightarrow{M}$	$NO_3 + NO_2$	$k_{33} \times 9.09 \times 10^{26} \exp(-11200/T)$
37.	$NO + NO + O_2$	$\xrightarrow{O_2}$	$2NO_2$	$3.3 \times 10^{-39} \exp(530/T)$
38.	$NO + NO_2 + H_2O$	$\longrightarrow$	$2HNO_2$	4.4×10^{-40}
39.	$HNO_2 + HNO_2$	$\longrightarrow$	$NO + NO_2$	1.0×10^{-20}
40.	$CO + OH$	$\xrightarrow{O_2}$	HO_2	$1.5 \times 10^{-13} \times (1 + 2.44 \times 10^{-20}[M])$
41.	$SO_2 + OH$	$\longrightarrow$	$H_2SO_4 + HO_2$	see Table 2.4

(1) $k_o = 7.2 \times 10^{-15} \exp(785/T)$, $k_a = 4.1 \times 10^{-16} \exp(1440/T)$, $k_b = 1.9 \times 10^{-33} \exp(725/T)[M]$.
(2) $k_c = 2.3 \times 10^{-13} \exp(600/T)$, $k_p = [M]1.7 \times 10^{-33} \exp(1000/T)$, $k_w = 1.4 \times 10^{-21} \exp(2200/T)$ (from Stockwell, 1995).

Table 2.4: Troe Reactions and Rate Constants[a] (from Stockwell *et al.*, 1990).

No.	Reaction	k_o^{300}	n	k_∞^{300}	m
19.	$OH + NO \xrightarrow{M} HNO_2$	7.0×10^{-31}	2.6	1.5×10^{-11}	0.5
20.	$OH + NO_2 \xrightarrow{M} HNO_3$	2.6×10^{-30}	3.2	2.4×10^{-11}	1.3
29.	$HO_2 + NO_2 \xrightarrow{M} HNO_4$	1.8×10^{-31}	3.2	4.7×10^{-12}	1.4
33.	$NO_3 + NO_2 \xrightarrow{M} N_2O_5$	2.2×10^{-30}	4.3	1.5×10^{-12}	0.5
41.	$SO_2 + OH \longrightarrow H_2SO_4 + HO_2$	3.0×10^{-31}	3.3	1.5×10^{-12}	0.0

Calculate k ($cm^3 molecule^{-1} s^{-1}$) by Equation 2.1.

2.2.1 Lumped Molecule Approach

In the lumped molecule technique, a large number of organic compounds are grouped together into a concise set of volatile organic compound (VOC) categories based on similarity in oxidation reactivity and emission magnitudes (Middleton *et al.*, 1990). Within each category of VOC (e.g., alkanes, alkenes, aromatics, etc.), there are several lumped molecule species that span the required reactivity range. The emitted organic compounds are lumped into these surrogate species of similar reactivity and molecular weight. The lumped molecule mechanism developed by Stockwell *et al.* (1990) for the second generation Regional Acid Deposition Model (RADM2) is one of the most widely used in the current literature.

The RADM2 mechanism is an upgrade of its predecessor RADM1 (Stockwell, 1986), and has a more detailed treatment of the important VOC categories. More specifically, the RADM2 mechanism contains: (1) three classes of higher alkanes; (2) two higher alkene classes distinguishing between internal and terminal alkenes; (3) separate classes for aldehydes, ketones, and dicarbonyl species; (4) two aromatic classes with a more detailed treatment of the subsequent chemistry; and (5) a more detailed treatment of peroxy radical-peroxy radical reactions. Furthermore, because of their relatively long-lifetimes, methane, ethane, and ethene reactions are treated explicitly. Although the 1990 version of the RADM2 mechanism also contains isoprene as an explicit species, it is not considered here. There have been recent updates to the isoprene chemistry, and are discussed at length in the next chapter. Table 2.5 shows the 41 organic species used in the RADM2 mechanism; the organic mechanism is compiled in Table 2.6. The inorganic reactions and rate constants used are the ones listed in Table 2.3.

As its name suggests, the RADM2 chemical mechanism was designed for regional-scale air quality modeling, and therefore, should be equally applicable in representing anthropogenic organic chemistry at the global scale.

Table 2.5: List of Organic Species in RADM2.

No.	Species	Representation
1.	Methane	CH_4
2.	Ethane	C_2H_6
3.	Alkanes with $k_{OH} \sim (2.7 \times 10^{-13}$ - $3.4 \times 10^{-12})$	HC3
4.	Alkanes with $k_{OH} \sim (3.4 \times 10^{-12}$ - $6.8 \times 10^{-12})$	HC5
5.	Alkanes with $k_{OH} > 6.8 \times 10^{-12}$	HC8
6.	Ethene	OL2
7.	Terminal alkenes	OLT
8.	Internal alkenes	OLI
9.	Toluene	TOL
10.	Cresol and other hydroxy substituted aromatics	CSL
11.	Xylene and more reactive aromatics	XYL
12.	Formaldehyde	HCHO
13.	Acetaldehyde and higher aldehydes	ALD
14.	Ketones	KET
15.	Glyoxal	GLY
16.	Methylglyoxal	MGLY
17.	Unsaturated Dicarbonyl	DCB
18.	Peroxyacetyl nitrate and higher PANs	PAN
19.	$H(CO)CH = CHO_3NO_2$	TPAN
20.	Organic nitrate	ONIT
21.	Methyl hydrogen peroxide	OP1
22.	Higher organic peroxides	OP2
23.	Peroxyacetic acid	PAA
24.	Formic acid	ORA1
25.	Acetic acid and higher acids	ORA2
26.	Methylperoxy radical	CH_3O_2
27.	Ethylperoxy radical	ETHP
28.	Peroxy radical formed from HC3	HC3P
29.	Peroxy radical formed from HC5	HC5P
30.	Peroxy radical formed from HC8	HC8P
31.	Peroxy radical formed from OL2	OL2P
32.	Peroxy radical formed from OLT	OLTP
33.	Peroxy radical formed from OLI	OLIP
34.	Peroxy radical formed from TOL	TOLP
35.	Peroxy radical formed from XYL	XYLP
36.	Peroxy radical formed from KET	KETP
37.	Acetylperoxy radical	ACO_3
38.	$H(CO)CH = CHCO_3$	TCO_3
39.	NO_3-alkene adduct	OLN
40.	NO to NO_2 operator	XO_2
41.	NO_2 to nitrate operator	XNO_2

Table 2.6: Organic Chemistry in the RADM2 Mechanism (Stockwell *et al.*, 1990).

No.	Reaction			Rate Constant k [molecule − cm^3 − s]
1.	CH_4 + OH	⟶	CH_3O_2	$T^2\ 6.95 \times 10^{-18} \exp(-1280/T)$
2.	CH_3O_2 + NO	⟶	HCHO + HO_2 + NO_2	$4.2 \times 10^{-12} \exp(180/T)$
3.	CH_3O_2 + HO_2	⟶	OP1	$7.7 \times 10^{-14} \exp(1300/T)$
4.	CH_3O_2 + CH_3O_2	⟶	1.5HCHO + HO_2 + .5CH_3OH	$1.9 \times 10^{-13} \exp(220/T)$
5.	OP1 + OH	⟶	.5CH_3O_2 + .5HCHO + .5OH	1.0×10^{-11}
6.	C_2H_6 + OH	⟶	ETHP	$T^2\ 1.37 \times 10^{-17} \exp(-444/T)$
7.	ETHP + NO	⟶	ALD + HO_2 + NO_2	$4.2 \times 10^{-12} \exp(180/T)$
8.	ETHP + HO_2	⟶	H_2O	$7.7 \times 10^{-14} \exp(1300/T)$
9.	ETHP + CH_3O_2	⟶	.75HCHO + HO_2 + .75ALD	$1.4 \times 10^{-13} \exp(220/T)$
10.	HCHO + OH	⟶	HO_2 + CO	1.0×10^{-11}
11.	HCHO + $O(^3P)$	⟶	OH + HO_2 + CO	$3.0 \times 10^{-11} \exp(-1550/T)$
12.	HCHO + NO_3	⟶	HNO_3 + HO_2 + CO	6.3×10^{-16}
13.	HC3 + OH	⟶	.83HC3P + .17HO_2 + .075ALD + 025KET + .009HCHO	$1.59 \times 10^{-11} \exp(-540/T)$
14.	HC5 + OH	⟶	HC5P + .25XO_2	$1.73 \times 10^{-11} \exp(-380/T)$
15.	HC8 + OH	⟶	HC8P + .75XO_2	$3.64 \times 10^{-11} \exp(-380/T)$
16.	OL2 + OH	⟶	OL2P	$2.15 \times 10^{-12} \exp(411/T)$
17.	OLT + OH	⟶	OLTP	$5.32 \times 10^{-12} \exp(504/T)$
18.	OLI + OH	⟶	OLIP	$1.07 \times 10^{-11} \exp(549/T)$
19.	TOL + OH	⟶	.75TOLP + .25CSL + .25HO_2	$2.1 \times 10^{-12} \exp(322/T)$
20.	XYL + OH	⟶	.83XYLP + .17CSL + .17HO_2	$1.89 \times 10^{-11} \exp(116/T)$
21.	CSL + OH	⟶	.1HO_2 + .9XO_2 + .9TCO_3 - .9OH	4.0×10^{-11}
22.	ALD + OH	⟶	ACO_3	$6.87 \times 10^{-12} \exp(256/T)$
23.	KET + OH	⟶	KETP	$1.20 \times 10^{-11} \exp(-745/T)$
24.	GLY + OH	⟶	HO_2 + 2CO	1.15×10^{-11}
25.	MGLY + OH	⟶	ACO_3 + CO	1.70×10^{-11}
26.	DCB + OH	⟶	TCO_3	2.80×10^{-11}
27.	OP2 + OH	⟶	.5HC3P + .5ALD + .5 OH	1.00×10^{-11}
28.	PAA + OH	⟶	ACO_3	1.00×10^{-11}
29.	PAN + OH	⟶	HCHO +NO_3+ XO_2	$6.85 \times 10^{-18} \exp(-444/T)$
30.	ONIT + OH	⟶	HC3P + NO_2	$1.55 \times 10^{-11} \exp(-540/T)$
31.	ACO_3 + NO_2	⟶	PAN	$2.80 \times 10^{-12} \exp(181/T)$
32.	PAN	⟶	ACO_3 + NO_2	$1.95 \times 10^{+16} \exp(-13543/T)$
33.	TCO_3 + NO_2	⟶	TPAN	4.70×10^{-12}
34.	TPAN	⟶	TCO_3 + NO_2	$1.95 \times 10^{+16} \exp(-13543/T)$
35.	HC3P + NO	⟶	.75ALD + .25KET + .09HCHO + .036ONIT + .964NO_2 + .964HO_2	$4.20 \times 10^{-12} \exp(180/T)$
36.	HC5P + NO	⟶	.38ALD + .69KET + .08ONIT + .92NO_2 + .92HO_2	$4.20 \times 10^{-12} \exp(180/T)$

(continued on next page)

Table 2.6: (*continued*)

37.	HC8P + NO	$\longrightarrow$	.35ALD + 1.06KET + .04HCHO + .24ONIT + .76NO_2 + .76HO_2	$4.20 \times 10^{-12} \exp(180/T)$
38.	OL2P + NO	$\longrightarrow$	1.6HCHO + HO_2 + NO_2 + .2 ALD	$4.20 \times 10^{-12} \exp(180/T)$
39.	OLTP + NO	$\longrightarrow$	ALD +HCHO + HO_2 + NO_2	$4.20 \times 10^{-12} \exp(180/T)$
40.	OLIP + NO	$\longrightarrow$	HO_2 + 1.45ALD + .28HCHO + .1KET + NO_2	$4.20 \times 10^{-12} \exp(180/T)$
41.	ACO_3 + NO	$\longrightarrow$	CH_3O_2 + NO_2	$4.20 \times 10^{-12} \exp(180/T)$
42.	TCO_3 + NO	$\longrightarrow$	NO_2 + .92HO_2 + .89GLY + .11MGLY + .05ACO_3 + .95CO + 2XO_2	$4.20 \times 10^{-12} \exp(180/T)$
43.	TOLP + NO	$\longrightarrow$	NO_2 + HO_2 + .17MGLY + .16GLY + .7DCB	$4.20 \times 10^{-12} \exp(180/T)$
44.	XYLP + NO	$\longrightarrow$	NO_2 + HO_2 + .45MGLY + .806DCB	$4.20 \times 10^{-12} \exp(180/T)$
45.	KETP + NO	$\longrightarrow$	MGLY + NO_2 + HO_2	$4.20 \times 10^{-12} \exp(180/T)$
46.	OLN + NO	$\longrightarrow$	HCHO + ALD + 2NO_2	$4.20 \times 10^{-12} \exp(180/T)$
47.	ALD + NO_3	$\longrightarrow$	ACO_3 + HNO_3	$1.40 \times 10^{-12} \exp(180/T)$
48.	GLY + NO_3	$\longrightarrow$	HNO_3 + HO_2 + 2CO	$6.00 \times 10^{-13} \exp(-2058/T)$
49.	MGLY + NO_3	$\longrightarrow$	HNO_3 + ACO_3 + CO	$1.40 \times 10^{-12} \exp(-1900/T)$
50.	DCB + NO_3	$\longrightarrow$	HNO_3 + TCO_3	$1.40 \times 10^{-12} \exp(-1900/T)$
51.	CSL + NO_3	$\longrightarrow$	HNO_3 + XNO_2 + .5CSL	2.20×10^{-11}
52.	OL2 + NO_3	$\longrightarrow$	OLN	$2.00 \times 10^{-12} \exp(-2923/T)$
53.	OLT + NO_3	$\longrightarrow$	OLN	$1.00 \times 10^{-11} \exp(-1895/T)$
54.	OLI + NO_3	$\longrightarrow$	OLN	$3.23 \times 10^{-11} \exp(-975/T)$
55.	OL2 + O_3	$\longrightarrow$	HCHO +.42CO + .4ORA1 + .12HO_2	$1.20 \times 10^{-14} \exp(-2633/T)$
56.	OLT + O_3	$\longrightarrow$	.53HCHO +.5ALD + .33CO + .2ORA1 + .2ORA2 + .23HO_2 + .22CH_3O_2 + .1OH + .06CH_4	$1.32 \times 10^{-14} \exp(-2105/T)$
57.	OLI + O_3	$\longrightarrow$	.18HCHO + .72ALD + .1KET + .23CO + .06ORA1 + .29ORA2 + .09CH_4+ .26HO_2 + .14OH + .31CH_3O_2	$7.29 \times 10^{-15} \exp(-1136/T)$
58.	HC3P + HO_2	$\longrightarrow$	OP2	$7.70 \times 10^{-14} \exp(1300/T)$
59.	HC5P + HO_2	$\longrightarrow$	OP2	$7.70 \times 10^{-14} \exp(1300/T)$
60.	HC8P + HO_2	$\longrightarrow$	OP2	$7.70 \times 10^{-14} \exp(1300/T)$
61.	OL2P + HO_2	$\longrightarrow$	OP2	$7.70 \times 10^{-14} \exp(1300/T)$
62.	OLTP + HO_2	$\longrightarrow$	OP2	$7.70 \times 10^{-14} \exp(1300/T)$
63.	OLIP + HO_2	$\longrightarrow$	OP2	$7.70 \times 10^{-14} \exp(1300/T)$
64.	KETP + HO_2	$\longrightarrow$	OP2	$7.70 \times 10^{-14} \exp(1300/T)$
65.	ACO_3 + HO_2	$\longrightarrow$	OP2	$7.70 \times 10^{-14} \exp(1300/T)$
66.	TOLP + HO_2	$\longrightarrow$	OP2	$7.70 \times 10^{-14} \exp(1300/T)$
67.	XYLP + HO_2	$\longrightarrow$	OP2	$7.70 \times 10^{-14} \exp(1300/T)$

(continued on next page)

Table 2.6: (*continued*)

68.	$TCO_3 + HO_2$	$\longrightarrow$	OP2	$7.70 \times 10^{-14} \exp(1300/T)$
69.	$OLN + HO_2$	$\longrightarrow$	ONIT	$7.70 \times 10^{-14} \exp(1300/T)$
70.	$HC3P + CH_3O_2$	$\longrightarrow$	$.84HCHO + HO_2 + .77ALD + .26KET$	$4.20 \times 10^{-14} \exp(220/T)$
71.	$HC5P + CH_3O_2$	$\longrightarrow$	$.77HCHO + HO_2 + .41ALD + .75KET$	$3.40 \times 10^{-14} \exp(220/T)$
72.	$HC8P + CH_3O_2$	$\longrightarrow$	$.8HCHO + HO_2 + .46ALD + 1.39KET$	$2.90 \times 10^{-14} \exp(220/T)$
73.	$OL2P + CH_3O_2$	$\longrightarrow$	$1.55HCHO + HO_2 + .35ALD$	$1.40 \times 10^{-13} \exp(220/T)$
74.	$OLTP + CH_3O_2$	$\longrightarrow$	$1.25HCHO + HO_2 + .75ALD$	$1.40 \times 10^{-13} \exp(220/T)$
75.	$OLIP + CH_3O_2$	$\longrightarrow$	$.89HCHO + HO_2 + .725ALD .55KET$	$1.70 \times 10^{-14} \exp(220/T)$
76.	$KETP + CH_3O_2$	$\longrightarrow$	$.75HCHO + HO_2 + .75MGLY$	$1.70 \times 10^{-14} \exp(220/T)$
77.	$ACO_3 + CH_3O_2$	$\longrightarrow$	$HCHO + .5HO_2 + .5CH_3O_2 + .5ORA2$	$9.60 \times 10^{-13} \exp(220/T)$
78.	$TOLP + CH_3O_2$	$\longrightarrow$	$HCHO + 2HO_2 + .17MGLY + .16GLY + .7DCB$	$1.70 \times 10^{-14} \exp(220/T)$
79.	$XYLP + CH_3O_2$	$\longrightarrow$	$HCHO + 2HO_2 + .45MGLY + .806DCB$	$1.70 \times 10^{-14} \exp(220/T)$
80.	$TCO_3 + CH_3O_2$	$\longrightarrow$	$.5HCHO + .5ORA2 + .46HO_2 + .445GLY + .055MGLY + .025ACO_3 + .475CO + XO_2$	$9.60 \times 10^{-13} \exp(220/T)$
81.	$OLN + CH_3O_2$	$\longrightarrow$	$1.75HCHO + .5HO_2 + ALD + NO_2$	$1.70 \times 10^{-14} \exp(220/T)$
82.	$ACO_3 + ETHP$	$\longrightarrow$	$ALD + .5HO_2 + .5CH_3O_2 + .5ORA2$	$3.40 \times 10^{-13} \exp(220/T)$
83.	$ACO_3 + HC3P$	$\longrightarrow$	$.77ALD + .26KET + .5HO_2 + .5CH_3O_2 + .5ORA2$	$1.00 \times 10^{-13} \exp(220/T)$
84.	$ACO_3 + HC5P$	$\longrightarrow$	$.41ALD + .75KET + .5HO_2 + .5CH_3O_2 + .5ORA2$	$8.40 \times 10^{-14} \exp(220/T)$
85.	$ACO_3 + HC8P$	$\longrightarrow$	$.46ALD + 1.39KET + .5HO_2 + .5CH_3O_2 + .5ORA2$	$7.20 \times 10^{-14} \exp(220/T)$
86.	$ACO_3 + OL2P$	$\longrightarrow$	$.8HCHO + .6ALD + .5HO_2 + .5CH_3O_2 + .5ORA2$	$3.40 \times 10^{-13} \exp(220/T)$
87.	$ACO_3 + OLTP$	$\longrightarrow$	$ALD + .5HCHO + .5HO_2 + .5CH_3O_2 + .5ORA2$	$3.40 \times 10^{-13} \exp(220/T)$
88.	$ACO_3 + OLIP$	$\longrightarrow$	$.725ALD + .55KET + .14HCHO + .5HO_2 + .5CH_3O_2 + .5ORA2$	$4.20 \times 10^{-14} \exp(220/T)$
89.	$ACO_3 + KETP$	$\longrightarrow$	$MGLY + .5HO_2 + .5CH_3O_2 + .5ORA2$	$4.20 \times 10^{-14} \exp(220/T)$
90.	$ACO_3 + ACO_3$	$\longrightarrow$	$2CH_3O_2$	$1.19 \times 10^{-12} \exp(220/T)$
91.	$ACO_3 + TOLP$	$\longrightarrow$	$CH_3O_2 + .17MGLY + .16GLY + .7DCB + HO_2$	$4.20 \times 10^{-14} \exp(220/T)$

(continued on next page)

Table 2.6: (*continued*)

92.	ACO_3 + XYLP	$\longrightarrow$	CH_3O_2 + .45MGLY + .806DCB + HO_2	$4.20 \times 10^{-14} \exp(220/T)$
93.	ACO_3 + TCO_3	$\longrightarrow$	CH_3O_2 + .92HO_2 + .89GLY + .11GMLY + .05ACO_3 + .95CO + 2XO_2	$1.90 \times 10^{-12} \exp(220/T)$
94.	ACO_3 + OLN	$\longrightarrow$	HCHO + ALD + .5ORA2 + NO_2 + .5CH_3O_2	$4.20 \times 10^{-14} \exp(220/T)$
95.	OLN + OLN	$\longrightarrow$	2HCHO + 2ALD + 2NO_2	$3.60 \times 10^{-16} \exp(220/T)$
96.	XO_2 + HO_2	$\longrightarrow$	OP2	$7.70 \times 10^{-14} \exp(220/T)$
97.	XO_2 + CH_3O_2	$\longrightarrow$	HCHO + HO_2	$1.70 \times 10^{-14} \exp(220/T)$
98.	XO_2 + ACO_3	$\longrightarrow$	CH_3O_2	$4.20 \times 10^{-14} \exp(220/T)$
99.	XO_2 + XO_2	$\longrightarrow$		$3.60 \times 10^{-16} \exp(220/T)$
100.	XO_2 + NO	$\longrightarrow$	NO_2	$4.20 \times 10^{-12} \exp(220/T)$
101.	XNO_2 + NO_2	$\longrightarrow$	ONIT	$4.20 \times 10^{-12} \exp(220/T)$
102.	XNO_2 + HO_2	$\longrightarrow$	OP2	$7.70 \times 10^{-14} \exp(220/T)$
103.	XNO_2 + CH_3O_2	$\longrightarrow$	HCHO + HO_2	$1.70 \times 10^{-14} \exp(220/T)$
104.	XNO_2 + ACO_3	$\longrightarrow$	CH_3O_2	$4.20 \times 10^{-14} \exp(220/T)$
105.	XNO_2 + XNO_2	$\longrightarrow$		$3.60 \times 10^{-16} \exp(220/T)$
106.	HCHO + $h\nu$	$\longrightarrow$	2HO_2 + CO	Radiation depemdent
107.	HCHO + $h\nu$	$\longrightarrow$	CO	Radiation depemdent
108.	ALD + $h\nu$	$\longrightarrow$	CH_3O_2 + HO_2 + CO	Radiation dependent
109.	OP1 + $h\nu$	$\longrightarrow$	HCHO + HO_2 + OH	Radiation dependent
110.	OP2 + $h\nu$	$\longrightarrow$	ALD + HO_2 + OH	Radiation dependent
111.	PAA + $h\nu$	$\longrightarrow$	CH_3O_2 + CO_2 + OH	Radiation dependent
112.	KET + $h\nu$	$\longrightarrow$	ACO_3 + ETHP	Radiation dependent
113.	GLY + $h\nu$	$\longrightarrow$	.13HCHO + 1.87CO	Radiation dependent
114.	GLY + $h\nu$	$\longrightarrow$	.45HCHO + 1.55CO + .8HO_2	Radiation dependent
115.	MGLY + $h\nu$	$\longrightarrow$	ACO_3 + HO_2 + CO	Radiation dependent
116.	DCB + $h\nu$	$\longrightarrow$	.98HO_2 + TCO_3 + .02ACO_3	Radiation dependent
117.	ONIT + $h\nu$	$\longrightarrow$	.2ALD + .8KET +HO_2 + NO_2	Radiation dependent

2.2.2 Lumped Structure Approach

As opposed to the molecular reactivity lumping, this approach involves lumping organics according to the types of bonds present in their molecular structures. Thus, the chemistry is categorized according to the reactions of similar carbon bonds. The major advantage of the structural-lumping approach is that relatively fewer categories are needed to represent bond groups as compared to the molecular-lumping technique. The Carbon Bond Mechanism IV (CBM-IV) developed by Gery *et al.* (1989) is the most recent condensed lumped-structure mechanism derived from an extended Carbon Bond Mechanism (CBM-EX), and contains significant improvements to the earlier CBM-III (Killus and Whitten, 1982).

Basically, three carbon bond surrogates and two molecular surrogates are used in CBM-IV

to describe the organic chemistry of an urban atmosphere. The carbon bond surrogates represent the three types of carbon bonds commonly found as parts of larger organic molecules. They include: the one-carbon atom surrogate PAR to represent the single bonded carbon atoms in alkanes and most of the alkyl groups found in other organics; the two-carbon atom surrogate OLE to represent the terminal alkenes (1-alkenes); and a third surrogate, ALD2, also containing two carbon atoms, to represent the -CHO group and the adjacent carbon atom in acetaldehyde and higher aldehydes. ALD2 is also used to represent internal alkenes (2-alkenes) since these oxidize very rapidly in ambient atmosphere to produce two acetaldehyde or higher aldehyde molecules. The two molecular surrogates TOL and XYL represent the aromatic hydrocarbon chemistry in a manner quite similar to that in RADM2. The seven-carbon surrogate TOL is used to categorize monoalkylbenzene structures, and its chemistry is parameterized using the reactions of toluene. XYL is an eight-carbon surrogate used to represent dialkylbenzenes and trialkylbenzenes, and its chemistry is modeled after m-xylene. Additionally, reactions of ethene and formaldehyde are treated explicitly because of their unique chemistries. Although methane is implicitly written in the published version of CBM-IV, it is treated as an explicit species here to be consistent with the treatment in RADM2. Also, the published CBM-IV does not contain sulfur dioxide and sulfuric acid, which are added here for the same reason. A complete list of the 18 organic species in CBM-IV is given in Table 2.7. The published CBM-IV reactions and the rate constants are listed in Table 2.8. The inorganic reactions are repeated since their rate constant expressions are slightly different than those used for RADM2.

On comparing the CBM-IV and RADM2 mechanisms, it is clearly evident that the CBM-IV is much smaller in size with respect to the number of organic species and reactions, and is, therefore, much more efficient to solve. On the other hand, it is also less detailed in the resolution of hydrocarbons such as alkenes, carbonyls, and especially lesser reactive alkanes which are thought to be important at the global scale. It is also obvious that RADM2 has more comprehensive interactions of various intermediates and radicals that are either ignored or not retained in CBM-IV. Due to these limitations, the CBM-IV is suitable for urban-scale to meso-scale applications only.

In the preliminary simulations, considerable differences were observed between the predictions from the published CBM-IV and RADM2 mechanisms. These differences could arise mainly due to two reasons: (1) differences in the inorganic reactions and rate constants, and

Table 2.7: List of Organic Species in CBM-IV.

No.	Species	Representation
1.	Methane	CH_4
2.	Formaldehyde	HCHO
3.	Higher aldehyde	ALD2
4.	Peroxyacyl radical	C_2O_3
5.	Peroxyacyl nitrate	PAN
6.	Paraffin bond (C—C)	PAR
7.	Secondary organic oxy radical	ROR
8.	Ethene	ETH
9.	Olefinic carbon bond C=C	OLE
10.	Toluene	TOL
11.	Xylene	XYL
12.	Cresol and higher M.W. phenols	CRES
13.	Toluene-hydroxyl radical adduct	TO_2
14.	Methylphenoxy radical	CRO
15.	High M.W. aromatic oxidation fragment	OPEN
16.	Methylglyoxal	MGLY
17.	NO to NO_2 operator	XO_2
18.	NO to nitrate operator	XO_2N

(2) differences in the organic chemistry treatments. The relative contributions of these two types of mechanism differences to the differences in predictions are not known. To eliminate the first difference, another version of CBM-IV was coded with revised inorganic chemistry, identical to that used for the RADM2 mechanism, i.e., as in Table 2.3. Furthermore, to reduce the second set of differences, the published organic chemistry of CBM-IV was partially modified as described in the following subsection. The predictions from these four mechanisms are compared in Section 2.3.

Table 2.8: The Published Carbon Bond Mechanism IV (Gery *et al.*, 1989): CBM-IV (P).

No.	Reaction			Rate Constant k [molecule − cm^3 − s]
	Inorganic Chemistry			
1.	$NO_2 + h\nu$	$\xrightarrow{O_2}$	NO+ $O(^3P)$	radiation dependent
2.	$O(^3P)$	$\xrightarrow{O_2,M}$	O_3	$1.4 \times 10^3 \exp(1175/T)$
3.	O_3+ NO	$\longrightarrow$	NO_2	$1.8 \times 10^{-12} \exp(-1370/T)$
4.	$O(^3P) + NO_2$	$\longrightarrow$	NO	9.3×10^{-12}
5.	$O(^3P) + NO_2$	$\xrightarrow{M}$	NO_3	$1.6 \times 10^{-13} \exp(687/T)$
6.	$O(^3P)$ + NO	$\xrightarrow{M}$	NO_2	$2.2 \times 10^{-13} \exp(602/T)$
7.	$O_3 + NO_2$	$\longrightarrow$	NO_3	$1.2 \times 10^{-13} \exp(-2450/T)$
8.	$O_3 + h\nu$	$\longrightarrow$	$O(^3P)$	radiation dependent
9.	$O_3 + h\nu$	$\longrightarrow$	$O(^1D)$	radiation dependent
10.	$O(^1D)$	$\xrightarrow{M}$	$O(^3P)$	$1.9 \times 10^8 \exp(390/T)$
11.	$O(^1D) + H_2O$	$\longrightarrow$	2OH	2.2×10^{-10}
12.	O_3 + OH	$\longrightarrow$	HO_2	$1.6 \times 10^{-12} \exp(-940/T)$
13.	$O_3 + HO_2$	$\longrightarrow$	OH	$1.4 \times 10^{-14} \exp(-580/T)$
14.	$NO_3 + h\nu$	$\longrightarrow$	$.89NO_2$ + $.89O(^3P)$ + .11NO	radiation dependent
15.	NO_3 + NO	$\longrightarrow$	$2NO_2$	$1.3 \times 10^{-11} \exp(250/T)$
16.	$NO_3 + NO_2$	$\longrightarrow$	NO+ NO_2	$2.5 \times 10^{-14} \exp(-1230/T)$
17.	$NO_3 + NO_2$	$\xrightarrow{M}$	N_2O_5	$5.3 \times 10^{-13} \exp(256/T)$
18.	$N_2O_5 + H_2O$	$\longrightarrow$	$2HNO_3$	1.3×10^{-21}
19.	N_2O_5	$\xrightarrow{M}$	NO_3+ NO_2	$3.5 \times 10^{14} \exp(-10897/T)$
20.	NO + NO	$\xrightarrow{O_2}$	$2NO_2$	$1.8 \times 10^{-20} \exp(530/T)$
21.	NO + $NO_2 + H_2O$	$\longrightarrow$	$2HNO_3$	4.4×10^{-40}
22.	OH+ NO	$\xrightarrow{M}$	HNO_2	$4.5 \times 10^{-13} \exp(806/T)$
23.	$HNO_2 + h\nu$	$\longrightarrow$	OH+ NO	radiation dependent
24.	OH + HNO_2	$\longrightarrow$	NO_2	6.6×10^{-12}
25.	$HNO_2 + HNO_2$	$\longrightarrow$	NO + NO_2	1.0×10^{-20}
26.	OH + NO_2	$\xrightarrow{M}$	HNO_3	$1.0 \times 10^{-12} \exp(713/T)$
27.	OH + HNO_3	$\xrightarrow{M}$	NO_3	$5.1 \times 10^{-15} \exp(1000/T)$
28.	HO_2 + NO	$\longrightarrow$	OH + NO_2	$3.7 \times 10^{-12} \exp(240/T)$
29.	$HO_2 + NO_2$	$\xrightarrow{M}$	HNO_4	$1.2 \times 10^{-13} \exp(749/T)$
30.	HNO_4	$\xrightarrow{M}$	$HO_2 + NO_2$	$4.8 \times 10^{13} \exp(-10121/T)$
31.	OH + HNO_4	$\longrightarrow$	NO_2	$1.3 \times 10^{-12} \exp(380/T)$
32.	$HO_2 + HO_2$	$\xrightarrow{M}$	H_2O_2	$5.9 \times 10^{-14} \exp(1150/T)$
33.	$HO_2 + HO_2 + H_2O$	$\xrightarrow{M}$	H_2O_2	$2.2 \times 10^{-38} \exp(5800/T)$
34.	$H_2O_2 + h\nu$	$\longrightarrow$	2OH	radiation dependent

(continued on next page)

Table 2.8: (*continued*)

35.	$OH + H_2O_2$	$\longrightarrow$	HO_2	$3.1 \times 10^{-12} \exp(-187/T)$
36.	$CO + OH$	$\xrightarrow{O_2}$	HO_2	2.2×10^{-13}
37.	$SO_2 + OH$	$\longrightarrow$	$H_2SO_4 + HO_2$	Troe expression
	Organic Chemistry			
38.	$HCHO + OH$	$\xrightarrow{O_2}$	$HO_2 + CO$	1.0×10^{-11}
39.	$HCHO + h\nu$	$\xrightarrow{O_2}$	$2HO_2 + CO$	radiation dependent
40.	$HCHO + h\nu$	$\longrightarrow$	CO	radiation dependent
41.	$HCHO + O(^3P)$	$\longrightarrow$	$OH + HO_2 + CO$	$3.0 \times 10^{-11} \exp(-1550/T)$
42.	$HCHO + NO_3$	$\xrightarrow{O_2}$	$HNO_3 + HO_2 + CO$	6.3×10^{-16}
43.	$ALD2 + O(^3P)$	$\xrightarrow{O_2}$	$C_2O_3 + OH$	$1.2 \times 10^{-11} \exp(-986/T)$
44.	$ALD2 + OH$	$\longrightarrow$	C_2O_3	$7.0 \times 10^{-12} \exp(250/T)$
45.	$ALD2 + NO_3$	$\xrightarrow{O_2}$	$C_2O_3 + HNO_3$	2.5×10^{-15}
46.	$ALD2 + h\nu$	$\xrightarrow{2O_2}$	$HCHO + XO_2 + 2HO_2 + CO$	radiation dependent
47.	$C_2O_3 + NO$	$\xrightarrow{O_2}$	$HCHO + XO_2 + HO_2 + NO_2$	$3.5 \times 10^{-11} \exp(-180/T)^a$
48.	$C_2O_3 + NO_2$	$\longrightarrow$	PAN	$2.6 \times 10^{-12} \exp(-380/T)^a$
49.	PAN	$\longrightarrow$	$C_2O_3 + NO_2$	$2.0 \times 10^{16} \exp(-180/T)^a$
50.	$2C_2O_3$	$\longrightarrow$	$2HCHO + 2XO_2 + 2HO_2$	2.0×10^{-12}
51.	$C_2O_3 + HO_2$	$\longrightarrow$	$.79HCHO + .79XO_2 + .79HO_2 + .79OH$	6.5×10^{-12}
52.	$CH_4 + OH$	$\xrightarrow{O_2}$	$HCHO + XO_2 + HO_2$	$T^2 6.95 \times 10^{-18} \exp(-1280/T)$
53.	$PAR + OH$	$\longrightarrow$	$.87XO_2 + .13XO_2N + .11HO_2 + .11ALD_2 + .76ROR - .11PAR$	8.1×10^{-13}
54.	ROR	$\longrightarrow$	$1.1ALD_2 + .96XO_2 + .94HO_2 + .04XO_2N + .02ROR - 2.1PAR$	$1.0 \times 10^{15} \exp(-8000/T)$
55.	ROR	$\longrightarrow$	HO_2	1.6×10^3
56.	$ROR + NO_2$	$\longrightarrow$		1.5×10^{-11}
57.	$OLE + O(^3P)$	$\longrightarrow$	$.63ALD2 + .38HO_2 + .3CO + .22PAR + .28XO_2 + .2OH + .2HCHO + .02XO_2N$	$1.2 \times 10^{-11} \exp(-324/T)$
58.	$OLE + OH$	$\longrightarrow$	$HCHO + ALD2 + XO_2 + HO_2 - PAR$	$5.2 \times 10^{-12} \exp(504/T)$
59.	$OLE + O_3$	$\longrightarrow$	$.5ALD2 + .74HCHO + .33CO + .44HO_2 + .1OH$	$1.4 \times 10^{-14} \exp(-2105/T)$

(continued on next page)

Table 2.8: (*continued*)

			.22XO_2 - PAR	
60.	OLE + NO_3	$\longrightarrow$	.91XO_2 + HCHO + NO_2 + ALD2 + .09XO_2N - PAR	7.7×10^{-15}
61.	ETH + $O(^3P)$	$\longrightarrow$	HCHO + .7XO_2 + CO + 1.7HO_2 + .3OH	$1.0 \times 10^{-11} \exp(-792)$
62.	ETH + OH	$\longrightarrow$	XO_2 + 1.56HCHO + HO_2 + .22ALD2	$2.0 \times 10^{-12} \exp(411/T)$
63.	ETH + O_3	$\longrightarrow$	HCHO + .42CO + .12HO_2	$1.3 \times 10^{-14} \exp(-2633)$
64.	TOL + OH	$\longrightarrow$	.08XO_2 + .36CRES + .44HO_2 + .56TO_2	$2.1 \times 10^{-12} \exp(322/T)$
65.	XYL + OH	$\longrightarrow$	.7HO_2 + .5XO_2 + .2CRES + .8MGLY + 1.1PAR + .3TO_2	$1.7 \times 10^{-11} \exp(116/T)$
66.	TO_2 + NO	$\longrightarrow$	.9NO_2 + .9OPEN + .9HO_2	8.1×10^{-12}
67.	TO_2	$\longrightarrow$	CRES + HO_2	4.2
68.	CRES + OH	$\longrightarrow$	.4CRO + .6XO_2 + .6HO_2 + .3OPEN	4.1×10^{-11}
69.	CRES + NO_3	$\longrightarrow$	CRO + HNO_3	2.2×10^{-11}
70.	CRO + NO_2	$\longrightarrow$		1.4×10^{-11}
71.	OPEN + OH	$\longrightarrow$	XO_2 + C_2O_3 + 2CO + 2HO_2 + HCHO	3.0×10^{-11}
72.	OPEN + $h\nu$	$\longrightarrow$	C_2O_3 + CO + HO_2	radiation dependent
73.	OPEN + O_3	$\longrightarrow$	.03ALD2 + .62C_2O_3 + .7HCHO + .03XO_2 + + .08OH + .76HO_2 + .2MGLY+ .69CO	$5.4 \times 10^{-17} \exp(-500/T)$
74.	MGLY + OH	$\longrightarrow$	XO_2 + C_2O_3	1.7×10^{-11}
75.	MGLY + $h\nu$	$\longrightarrow$	C_2O_3 + CO + HO_2	radiation dependent
76.	XO_2 + NO	$\longrightarrow$	NO_2	8.1×10^{-12}
77.	XO_2 + XO_2	$\longrightarrow$		$1.7 \times 10^{-14} \exp(1300/T)$
78.	XO_2N + NO	$\longrightarrow$		6.8×10^{-13}
79.	XO_2 + HO_2	$\longrightarrow$		$7.7 \times 10^{-14} \exp(1300/T)^b$

[a] Rate constants revised as per the recommendations in Simonaitis *et al.* (1997).

[b] Reaction added as per the recommendation in Simonaitis *et al.* (1997).

2.2.3 Global-Scale Carbon Bond Mechanism: CBM-Z

As indicated earlier, the organic chemistry in the published CBM-IV (CBM-IV (P)) is highly condensed and compact, thereby making it suitable for use in large three-dimensional air quality computer models. However, because of longer time scales associated with regional- and global-scale models, one must treat the chemistry of lesser reactive compounds such as methane and ethane, and their reaction intermediates, methylperoxy and ethylperoxy radicals, in an explicit manner. The CBM-IV (P) is somewhat "over-condensed" in this regard. Also, there is no surrogate representation of ketone groups. To this end, the CBM-IV (P) was expanded and modified to include 8 additional species and 14 reactions as described in Tables 2.9 and 2.10, respectively. The additional reactions include some of the important peroxy radical-peroxy radical interactions as well as peroxy radical-NO_x reactions. These reactions are based on the equivalent reactions given in RADM2. The acetone reactions are taken from the detailed CBM-EX given in Gery *et al.* (1989).

Some of the existing reactions in the CBM-IV (P) also needed modifications to treat CH_3O_2 radical explicitly. These modifications were based on the detailed chemistry of CBM-EX in which CH_3O_2 is treated as an explicit species. In the CBM-IV (P), CH_3O_2 is eliminated and replaced by XO_2 + HO_2 + HCHO. The universal surrogate XO_2 is used to convert NO to NO_2 using an average rate constant. This means that CH_3O_2 formed in a given reaction instantaneously reacts with NO to give CH_3O, which in turn reacts with O_2 to yield HO_2 + HCHO. Although the latter is a good assumption, the former is not always true, particularly under low NO_x conditions typical of rural and remote atmospheric environments. Secondly, the formations of formic and acetic acids, which were neglected in the CBM-IV (P), are now included in the CBM-Z.

Table 2.11 lists the relevant reactions as given in the CBM-IV (P) and their modified versions in the proposed CBM-Z. All other organic reactions and their rate constants in the CBM-Z and CBM-IV (P) are identical. The inorganic chemistry is identical to that used for RADM2 (Tables 2.2 and 2.3).

It is useful to compare the performance of the CBM-Z model against that of RADM2, CBM-IV (P), and CBM-IV (R). This is the topic of the next section.

Table 2.9: List of Additional Organic Species in CBM-Z over CBM-IV (P).

No.	Species	Representation
1.	Ethane	C_2H_6
2.	Methylperoxy radical	CH_3O_2
3.	Ethylperoxy radical	ETHP
4.	Formic acid	HCOOH
5.	Acetic acid	CH_3COOH
6.	Methyl hydrogen peroxide	CH_3OOH
7.	Acetone	AONE
8.	Acetylmethylperoxy radical	ANO2

Table 2.10: Additional Organic Reactions in CBM-Z over CBM-IV (P).

No.	Reaction			Rate Constant k [molecule $-$ cm^3 $-$ s]
1.	$CH_3O_2 + NO$	$\longrightarrow$	$HCHO + HO_2 + NO_2$	$4.2 \times 10^{-12} \exp(180/T)$
2.	$CH_3O_2 + HO_2$	$\longrightarrow$	CH_3OOH	$7.7 \times 10^{-14} \exp(1300/T)$
3.	$CH_3O_2 + CH_3O_2$	$\longrightarrow$	$1.5HCHO + HO_2 +$	$1.9 \times 10^{-13} \exp(220/T)$
4.	$CH_3OOH + h\nu$	$\xrightarrow{O_2}$	$HCHO + HO_2 + OH$	radiation dependent
5.	$CH_3OOH + OH$	$\longrightarrow$	$.5CH_3O_2 + .5HCHO + .5OH$	1.0×10^{-11}
6.	$C_2H_6 + OH$	$\longrightarrow$	ETHP	$T^2 1.37 \times 10^{-17} \exp(-444/T)$
7.	ETHP + NO	$\longrightarrow$	$ALD_2 + HO_2 + NO_2$	$4.2 \times 10^{-12} \exp(180/T)$
8.	ETHP + HO_2	$\longrightarrow$		$7.7 \times 10^{-14} \exp(1300/T)$
9.	ETHP + CH_3O_2	$\longrightarrow$	$.75HCHO + HO_2 + .75ALD_2$	$1.4 \times 10^{-13} \exp(220/T)$
10.	$C_2O_3 + CH_3O_2$	$\longrightarrow$	$HCHO + .5HO_2 +$ $.5CH_3O_2 + CH_3COOH$	$9.6 \times 10^{-13} \exp(220/T)$
11.	C_2O_3 + ETHP	$\longrightarrow$	$ALD_2 + .5HO_2 +$ $.5CH_3O_2 + .5CH_3COOH$	$3.4 \times 10^{-13} \exp(220/T)$
12.	AONE + $h\nu$	$\xrightarrow{2O_2}$	$C_2O_3 + CH_3O_2$	radiation dependent
13.	AONE + OH	$\longrightarrow$	ANO_2	$3.9 \times 10^{-13} \exp(1175/T)$
14.	ANO_2 + NO	$\longrightarrow$	$C_2O_3 + HCHO + NO_2$	8.1×10^{-12}

Table 2.11: Comparison Between the Differing CBM-IV (P) and CBM-Z Reactions.

No.[a]	Reactants		Products	
			CBM-IV (Gery *et al.*, 1989)	CBM-Z (This work)
46.	ALD2 + $h\nu$	$\xrightarrow{2O_2}$	HCHO + XO_2 + CO + $2HO_2$	CH_3O_2 + HO_2 + CO
47.	C_2O_3 + NO	$\xrightarrow{O_2}$	HCHO + XO_2 + NO_2 + HO_2	CH_3O_2 + NO_2
50.	$2C_2O_3$	$\longrightarrow$	$2HCHO + 2XO_2 + 2HO_2$	$2CH_3O_2$
51.	C_2O_3 + HO_2	$\longrightarrow$	$.79HCHO + .79XO_2 + .79OH + .79HO_2$	$.79CH_3O_2$ + .79OH
52.	CH_4+ OH	$\xrightarrow{O_2}$	HCHO + XO_2 + HO_2	CH_3O_2
58.	OLE + OH	$\longrightarrow$	HCHO + ALD2 + XO_2+ HO_2 - PAR	CH_3O_2 + ALD2 - PAR
59.	OLE + O_3	$\longrightarrow$	$.5ALD2 + .74HCHO + .33CO + .44HO_2 + .22XO_2 + .1OH$ - PAR	$.5ALD2 + .524HCHO + .228HO_2 + .216CH_3O_2 + .33CO + .1OH$ $.2HCOOH + .2CH_3COOH$
61.	ETH + $O(^3P)$	$\longrightarrow$	$HCHO + .7XO_2 + CO + .3OH + 1.7HO_2$	$.7CH_3O_2 + .3HCHO + .3OH + HO_2 + CO$
63.	ETH + O_3	$\longrightarrow$	$HCHO + .42CO + .12HO_2$	$HCHO + .42CO + .12HO_2 + .4HCOOH$

[a] Reaction numbers correspond with those in Table 2.8.

Table 2.12: Mechanism Nomenclature.

Nomenclature	Inorganic Chemistry	Organic Chemistry
RADM2	Table 2.2 and 2.3	Table2.6
CBM-IV (P)	Table 2.8	Table2.8
CBM-IV (R)	Table 2.2 and 2.3	Table2.8
CBM-Z	Table 2.2 and 2.3	Described in Subsection 2.2.3

2.3 Mechanism Intercomparison

Both CBM-IV and RADM2 have been evaluated against several smog-chamber data at relatively high initial reactant concentrations (ppm levels). However, since no smog-chamber experiments have been performed with low (ppb level) initial concentrations typically found in the atmosphere, the performance of any given mechanism under atmospheric conditions has yet to be validated. However, since RADM2 has more detailed radical-radical interactions and more explicit representation of the hydrocarbon chemistry than in CBM-IV, we will use the RADM2 mechanism as the reference mechanism for evaluating the performance of CBM-IV under atmospheric conditions.

Predictions of ozone and other important oxidants from the CBM-IV, RADM2, and the mechanism of Lurmann *et al.* (1987) have been compared quite extensively by Dodge (1989). Approximately 400 variable-volume box-model simulations were made over a range of initial conditions for a number of scenarios representative of urban and rural environments. All urban simulations were performed from 0800 to 2000 local daylight time using a diurnally varying temperature and radiation profile corresponding to mid-July conditions for Philadelphia, PA, or Tulsa, OK, latitudes. The simulations were initiated with a mixing height of 300 m, which was allowed to increase to 1300 m or 2100 m during the day. As the mixing height increased, VOC, O_3, and CO were entrained into the box from aloft where fixed concentrations were specified at all times. Also, O_3, H_2O_2, NO_2, HNO_3, and PAN were allowed to dry deposit at the surface with diurnally varying dry deposition velocities. The mechanisms were found to yield nearly identical predictions for ozone, PAN, and nitric acid under most scenarios, except in simulations with high NO_x levels, high aromatic hydrocarbons, and low afternoon temperatures. Also, predictions of H_2O_2 were in good agreement except at high VOC/NO_x ratios, where differences up to a factor of 3 were found.

2.3.1 Model Inputs

A similar exercise is carried out in this work for comparing predictions from the four mechanisms listed in Table 2.12. However, a constant-volume box-model was used here (i.e., with a constant mixing height) to eliminate the effects of entrainment on predictions of certain species. In box-models, entrainment of a species always tends to give a resultant concentration closer to its specified aloft-air concentration, and thus mitigates the actual

differences arising from differences in the mechanisms. For similar reasons, dry deposition of gases was also neglected.

The effects of initial concentrations on the predictions were eliminated by initializing the simulations with zero NO_x and non-methane hydrocarbon (NMHC) concentrations. The only initially non-zero species were O_3, CO, and CH_4 specified at 30, 100 and 1600 ppb respectively. NO_x and NMHCs were emitted into the box at a prescribed flux which varied diurnally as parameterized below

$$E_i = E_{1,i} \times \cos(\theta_z) + E_{2,i} \qquad \forall \cos(\theta_z) \geq 0 \tag{2.2}$$

$$E_i = E_{2,i} \qquad \forall \cos(\theta_z) < 0 \tag{2.3}$$

where E_i is the emission flux for the i^{th} species, and θ_z is the theoretical solar zenith angle at any given latitude, longitude, and local time. Equations 2.2 and 2.3 represent the daytime and nighttime fluxes, respectively. In actual practice, the flux parameters E_1 and E_2 were specified for NO_x and SO_2 only, while the emissions of the NMHCs were calculated using a prescribed [NMOC]/[NO_x] molar ratio (NMOC stands for non-methane organic carbon). Of the total NO_x emitted, 90% was assumed in the form of NO, with the remainder as NO_2.

The urban NMOC composition was adopted from Stockwell *et al.* (1990) and is shown in Table 2.13. Using the partitioning rules recommended by the developers of the CBM-IV and RADM2, the emitted species were apportioned into the surrogate species for each mechanism as shown in Table 2.14. A total of 6 hypothetical scenarios with increasing degree of pollution were used to examine performance of the mechanisms. The emission flux parameters for these scenarios are listed in Table 2.15. Scenario S1 represents a relatively clean rural atmosphere, while S6 corresponds to a relatively dirty urban boundary layer.

Each simulation was performed for 3 model days beginning at 00 hours, July 1. A constant mixing-height of 1000 m was used for the entire run, while a diurnal variation of temperature representative of continental northern hemisphere July conditions was prescribed as shown in Figure 2.1. The temperature and emission fluxes were updated every hour. A constant water vapor concentration of 3.8×10^{17} molecule cm^{-3}, corresponding to 50% relative humidity at 298 K, was also prescribed. The system of non-linear ordinary differential equations describing the dynamic chemistry was solved using LSODES, a GEAR-type solver (Hindmarsh, 1983). Only the last 2 day's results were used for analysis and comparison.

Table 2.13: Urban Nonmethane Organic Carbon (NMOC) Composition (from Stockwell *et al.* (1990)).

Organic category/ compound	Fraction of group (%)	Fraction of NMOC (%)
Alkanes		**55.0**
Ethane	10	5.5
Propane	15	8.3
n-Butane	15	8.3
n-Pentane	15	8.3
n-Hexane	15	8.3
n-Heptane	15	8.3
n-Octane	15	8.3
Alkenes		**20.0**
Ethene	35	7.0
Propene	40	8.0
t-2-Butene	25	5.0
Aromatics		**20.0**
Benzene	20	4.0
Toluene	40	8.0
m-Xylene	25	5.0
Mesitylene	15	3.0
Aldehydes		**5.0**
Formaldehyde	50	2.5
Aldehyde	50	2.5

Table 2.14: Nonmethane Organic Carbon Apportionment into the Organic Surrogates for Each Mechanism.

CBM-IV		CBM-Z		RADM2	
Species i	mol i per 100 mol C	Species i	mol i per 100 mol C	Species i	mol i per 100 mol C
PAR	59.42	C_2H_6	2.75	C_2H_6	2.75
		PAR	53.92	HC3	2.75
				HC5	5.09
				HC8	2.21
ETH	3.50	ETH	3.50	OL2	3.50
OLE	4.00	OLE	4.00	OLT	4.00
				OLI	1.25
TOL	1.81	TOL	1.81	TOL	1.81
XYL	0.96	XYL	0.96	XYL	0.96
HCHO	2.50	HCHO	2.50	HCHO	2.50
ALD2	3.54	ALD2	3.54	ALD2	1.04

Table 2.15: Hypothetical NO_x, SO_2, and NMOC Emissions Scenarios.

Scenario	NO_x and SO_2 E_1 (μmol m^{-2} h^{-1})	NO_x and SO_2 E_2 (μmol m^{-2} h^{-1})	[NMOC]/[NO_x] (mol/mol)
S1	0.8	0.2	10
S2	1.6	0.4	20
S3	4.0	1.0	30
S4	8.0	2.0	10
S5	16.0	4.0	20
S6	32.0	8.0	30

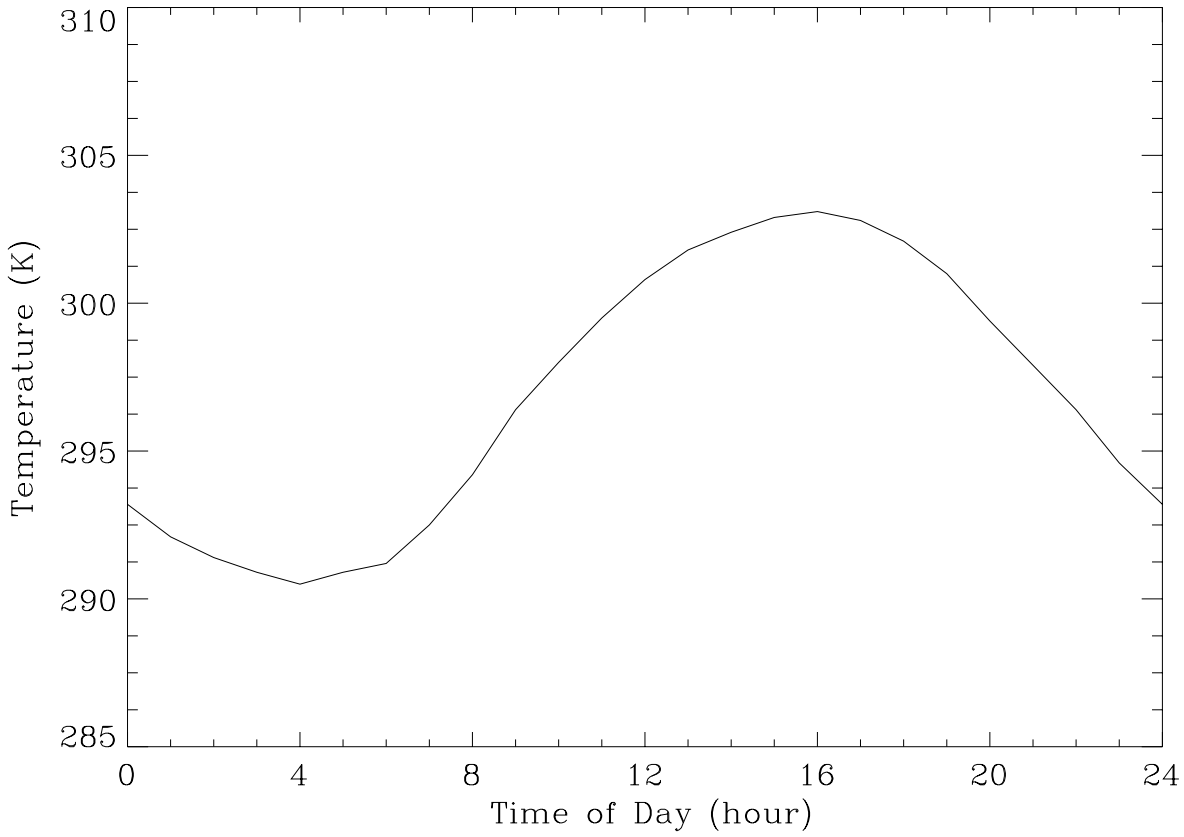

Figure 2.1: Prescribed diurnal temperature variation.

2.3.2 Results and Discussion

Performance of an atmospheric chemistry mechanism strongly depends on its ability to predict accurately the major oxidants. Typically, these include O_3, H_2O_2, NO_3, NO_2, OH, and HO_2. Predictions of the species of final interest such as H_2SO_4, HNO_3, and organic acids, directly or indirectly depend on the reactions of their precursors with the above oxidants.

Scenario S4 is selected to illustrate diurnal evolutions of the oxidants. Figures 2.2 through 2.4 show the concentrations of O_3, H_2O_2, NO_3, NO_2, OH, and HO_2 predicted by the RADM2, CBM-Z, CBM-IV (R), and CBM-IV (P) mechanisms. It is important to recall that the organic chemistries in both CBM-IV (R) and CBM-IV (P) are identical, while only the inorganic reactions and rate constants are slightly different. Interestingly, predictions of O_3 and H_2O_2 from the CBM-IV (R) and CBM-IV (P) deviate in opposite directions with respect to RADM2. However, the predictions from the CBM-Z agree with RADM2 very well. This

clearly indicates the importance of explicit treatment of methyl and ethyl peroxy radicals, as described in Subsection 2.2.3.

The predictions of NO_3 radical from all four mechanisms are in reasonably good agreement; however, the NO_2 concentration profile from the RADM2 mechanism tends to deviate from the other three, particularly after sunset. This discrepancy is probably due to the significantly different activation energies recommended by the RADM2 and CBM-IV developers for the formation and thermal decomposition of PAN. Since the recommendations in the CBM-IV are more recent, they will be adopted in the final mechanism (Simonaitis *et al.*, 1997). The daytime predictions of OH and HO_2 from all four mechanisms agree quite well; however, the nighttime concentrations are considerably different. The nighttime levels of both OH and HO_2 from the CBM-IV (P) exceed those from RADM2 by more than an order of magnitude. The CBM-IV (R) predictions are closer to RADM2 due to identical inorganic chemistry, while those from CBM-Z are the closest due to the improved organic chemistry.

Another set of plots (Figures 2.5 and 2.6) display the final concentrations of O_3, H_2O_2, H_2SO_4, and HNO_3 (i.e., at the end of three days) from the four mechanisms, for all six scenarios. Corresponding to these plots, Figures 2.7 and 2.8 show the percentage concentration deviations from CBM-Z, CBM-IV (R), and CBM-IV (P) with respect to the RADM2 predictions. It is interesting to note that the ozone predictions from the CBM-IV (R) deviates more than the CBM-IV (P), even though the inorganic chemistry in CBM-IV (R) is same as that in RADM2. The exact cause of this behavior is difficult to locate; however, this does seem to suggest that some of the inorganic reaction rate constants in the CBM-IV (P) mechanism may have been tuned to reproduce the experimental ozone data. This line of reasoning is supported by the lower O_3 concentration deviations from CBM-Z, indicating that O_3 predictions improved due to improvement in the organic chemistry treatment.

The improvement in the H_2O_2 predictions in the CBM-Z mechanism is the most remarkable. The CBM-IV (P) consistently overpredicts H_2O_2 by about 70%, while the CBM-IV (R) deviations range from about -45% to +60%. The CBM-Z predictions only deviate from 6 to 12% only. Overpredictions of H_2O_2 by the CBM-IV (P) are most likely caused by the overpredictions of the HO_2 radical, which in turn are due to the implicit CH_3O_2 representation by $XO_2 + HO_2 + HCHO$. Hydrogen peroxide is an important oxidant in aqueous-phase reactions which take place in cloud droplets. It accounts for the majority of the in-cloud sulfate formation from SO_2 oxidation, and thus, its importance in cloud-water acidification.

Because of the high solubility of H_2O_2 in water, its gas-phase concentrations will have a direct impact on the oxidizing capacity of a cloudy environment, and accurate predictions of H_2O_2 are important to the fidelity of the overall chemistry mechanism.

Gas-phase production of H_2SO_4 is directly proportional to the OH radical concentrations. Thus, deviations in the H_2SO_4 concentrations also reflect the deviations in the OH concentrations. Note that the CBM-IV (P) always overpredicts OH, and hence, H_2SO_4concentrations are higher by 5-20% with respect to the RADM2 mechanism, while CBM-IV (R) and CBM-Z always tend to underpredict within 1-10%. An error of about 10% in OH predictions is quite acceptable considering the complexity of the entire chemical mechanism.

The HNO_3 formation pathways are a bit more complicated than those for H_2SO_4. It can form via inorganic reactions involving various oxides of nitrogen, and also due to reactions of NO_3 with organics such as aldehydes and cresol. The CBM-IV (P) mechanism underpredicts by 10-60%, while CBM-IV (R) and CBM-Z underpredict by only 2-25%. Moreover, CBM-IV (R) predictions consistently deviate slightly more than CBM-Z predictions. These results indicate that the first improvement in HNO_3 predictions by CBM-IV (R) is due to the revised inorganic chemistry, and the second improvement in CBM-Z predictions is due to the modified organic chemistry.

Figure 2.9 compares the predictions of formic and acetic acids from RADM2 and CBM-IV. Clearly, CBM-Z predictions of both organic acids are in excellent agreement with RADM2. These acids may also play important roles in cloud-water acidification and the aqueous-phase chemistry. Thus, the added capability in CBM-Z to predict them should prove useful in regional and global applications.

Finally, the computational times required to simulate three model days using the CBM-IV (P), CBM-Z, and RADM2 mechanisms are compared in Figure 2.10. These timing estimates are for optimized FORTRAN codes executed on a SUN SPARC station 2. The CBM-IV (P) consistently requires only about 40% of the time as does RADM2. And fortunately, the more accurate CBM-Z is only slightly more expensive than the published version. Also summarized in Figure 2.11 are the mechanism sizes with respect to the number of organic species and reactions. The CBM-IV (P) is less than half as large as RADM2 in both respects, while CBM-Z is only marginally more complex. Such memory savings are extremely important for three-dimensional global simulations with finer grid resolutions.

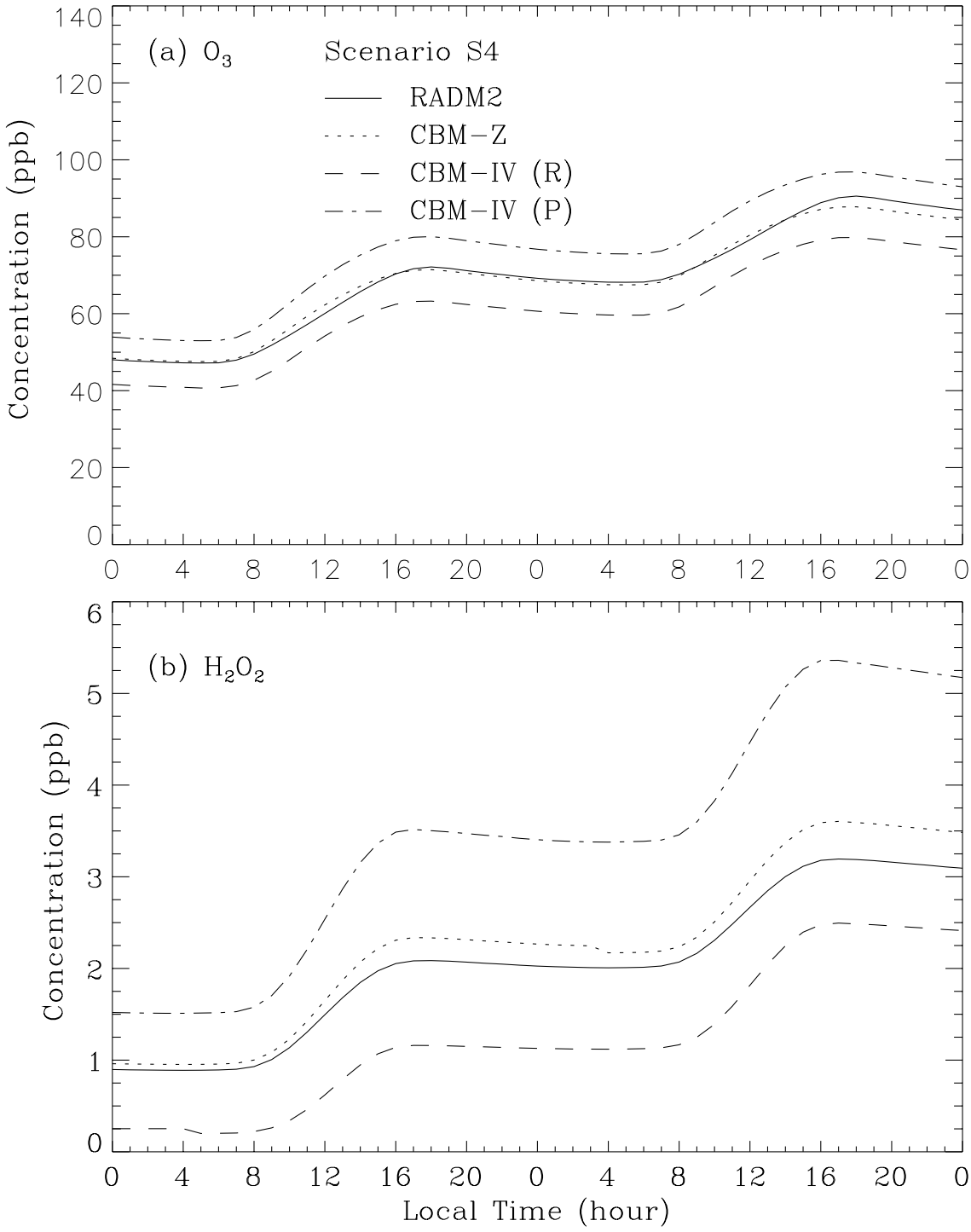

Figure 2.2: Concentration evolution using the RADM2, CBM-Z, CBM-IV (R), and CBM-IV (P) mechanisms for scenario S4: (a) O_3; (b) H_2O_2.

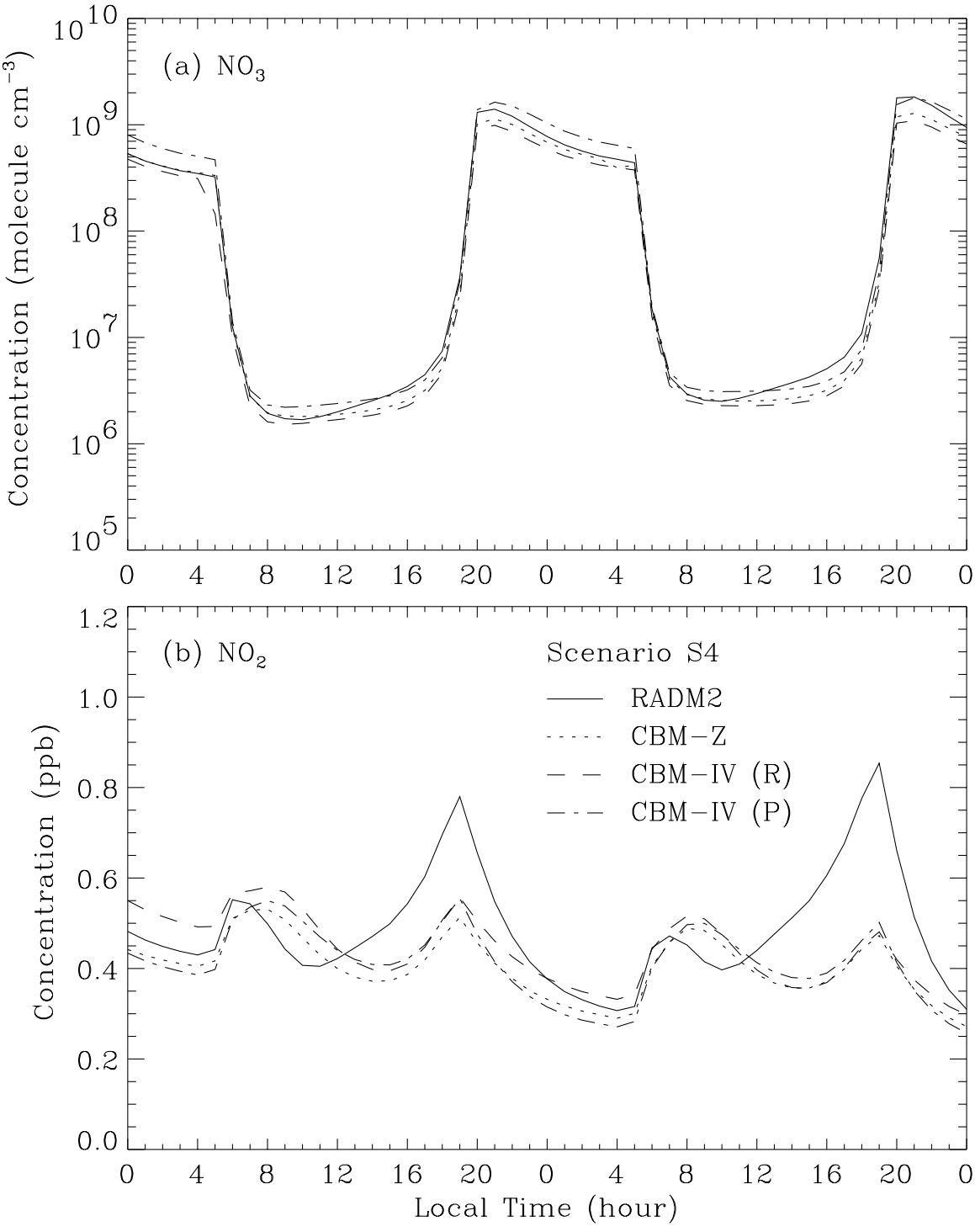

Figure 2.3: Concentration evolution using the RADM2, CBM-Z, CBM-IV (R), and CBM-IV (P) mechanisms for scenario S4: (a) NO_3; (b) NO2.

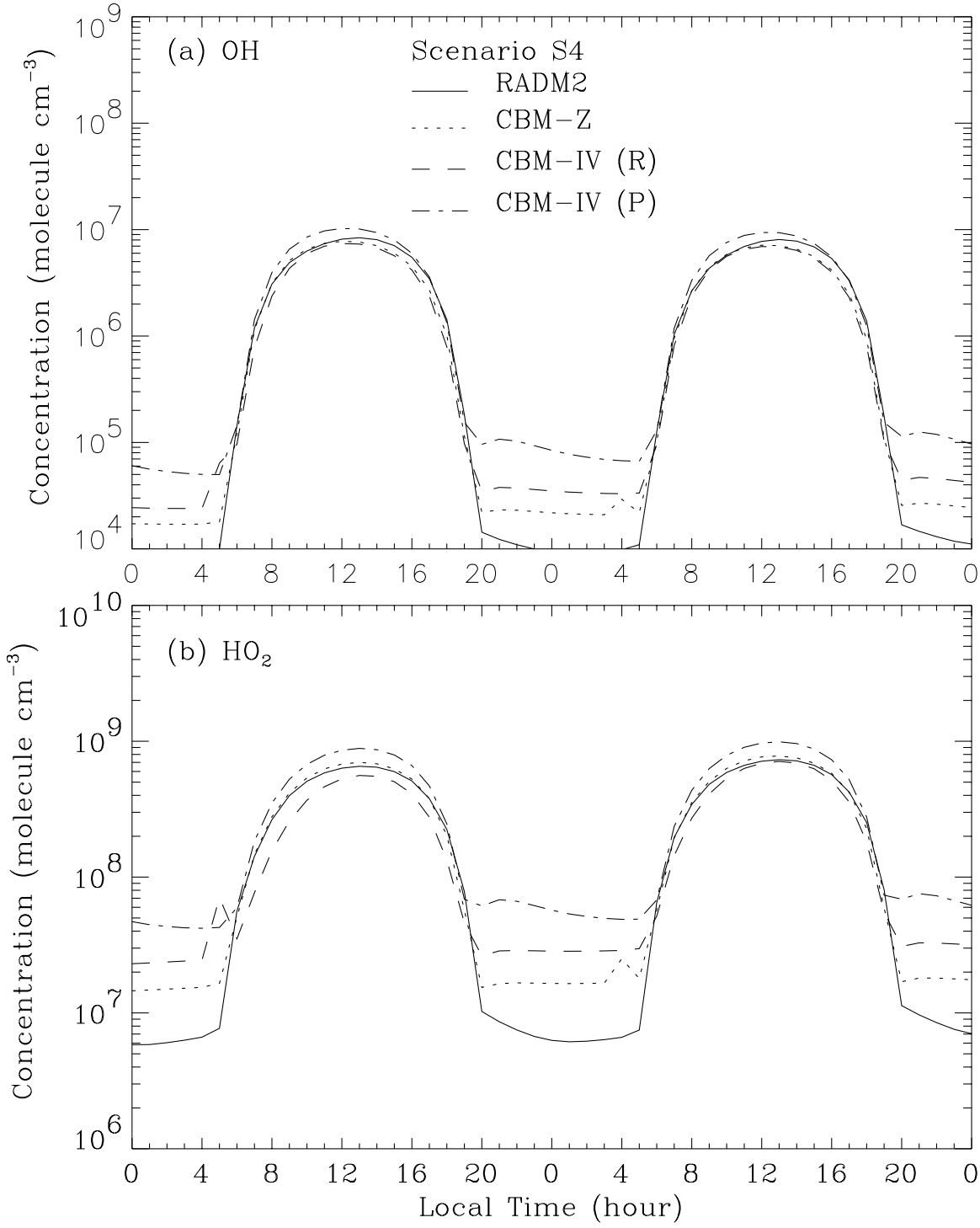

Figure 2.4: Concentration evolution using the RADM2, CBM-Z, CBM-IV (R), and CBM-IV (P) mechanisms for scenario S4: (a) OH; (b) HO_2.

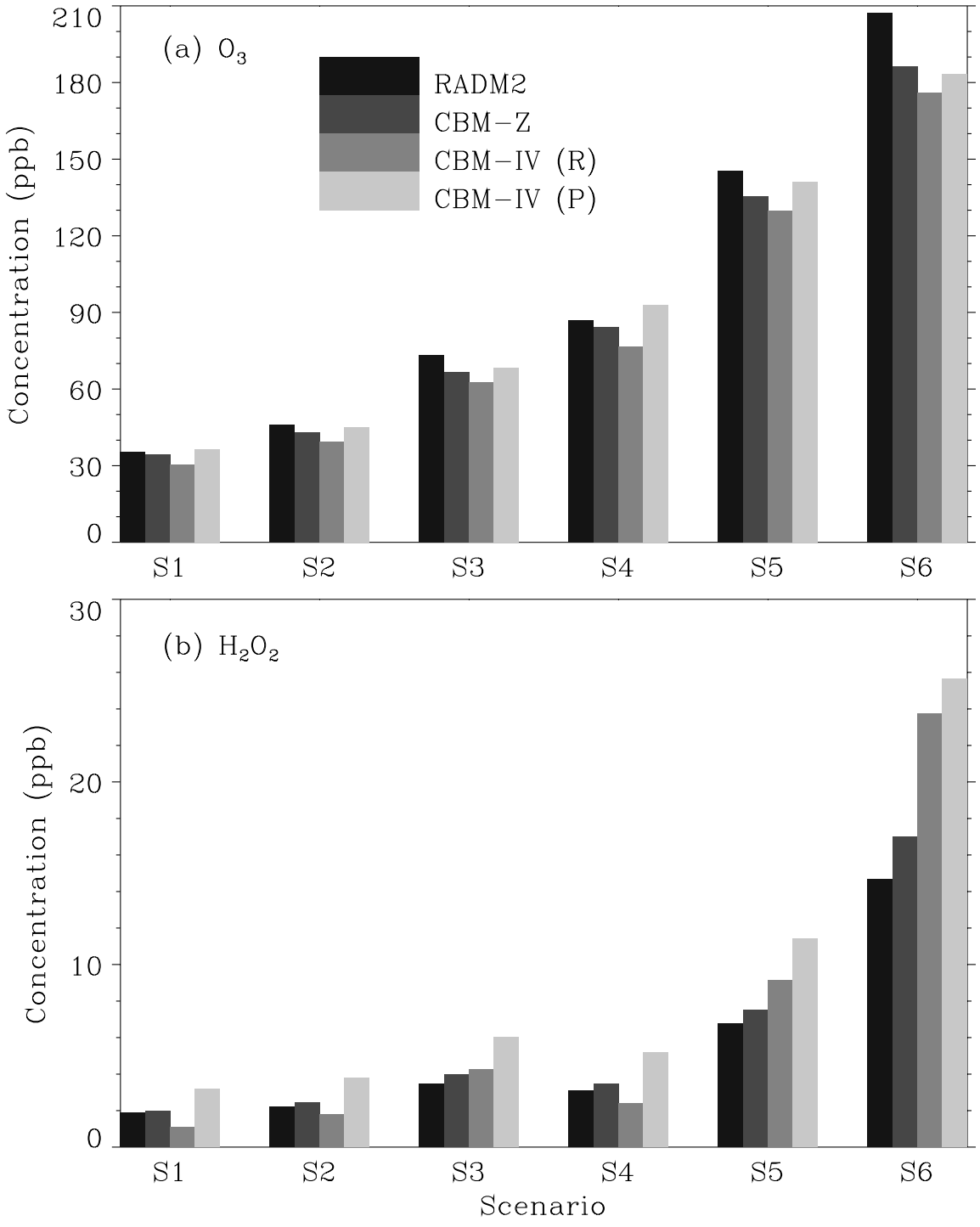

Figure 2.5: Simulated concentrations after 3 model days using the RADM2, CBM-Z, CBM-IV (R), and CBM-IV (P) mechanisms: (a) O_3; (b) H_2O_2.

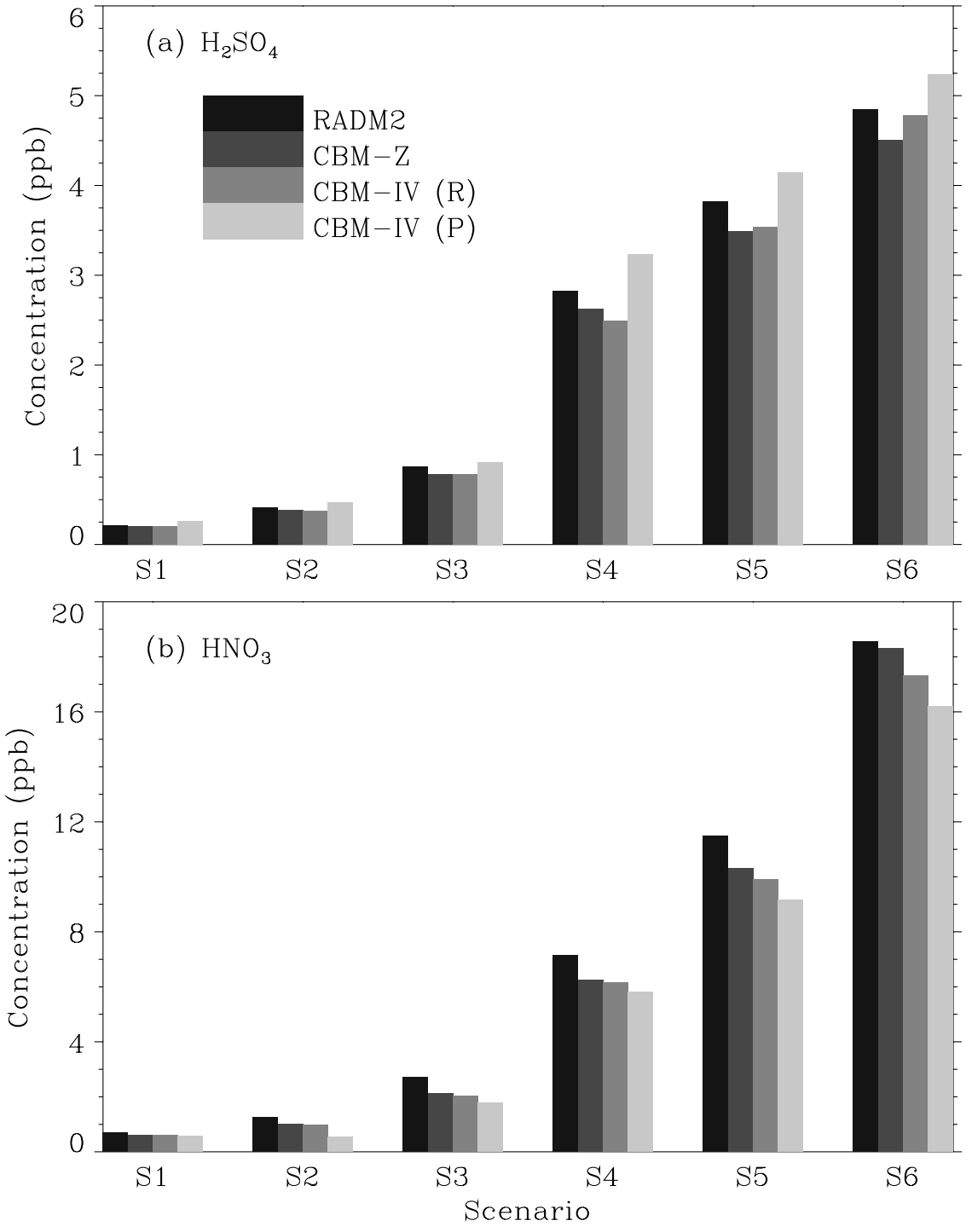

Figure 2.6: Simulated concentrations after 3 model days using the RADM2, CBM-Z, CBM-IV (R), and CBM-IV (P) mechanisms: (a) H_2SO_4; (b) HNO_3.

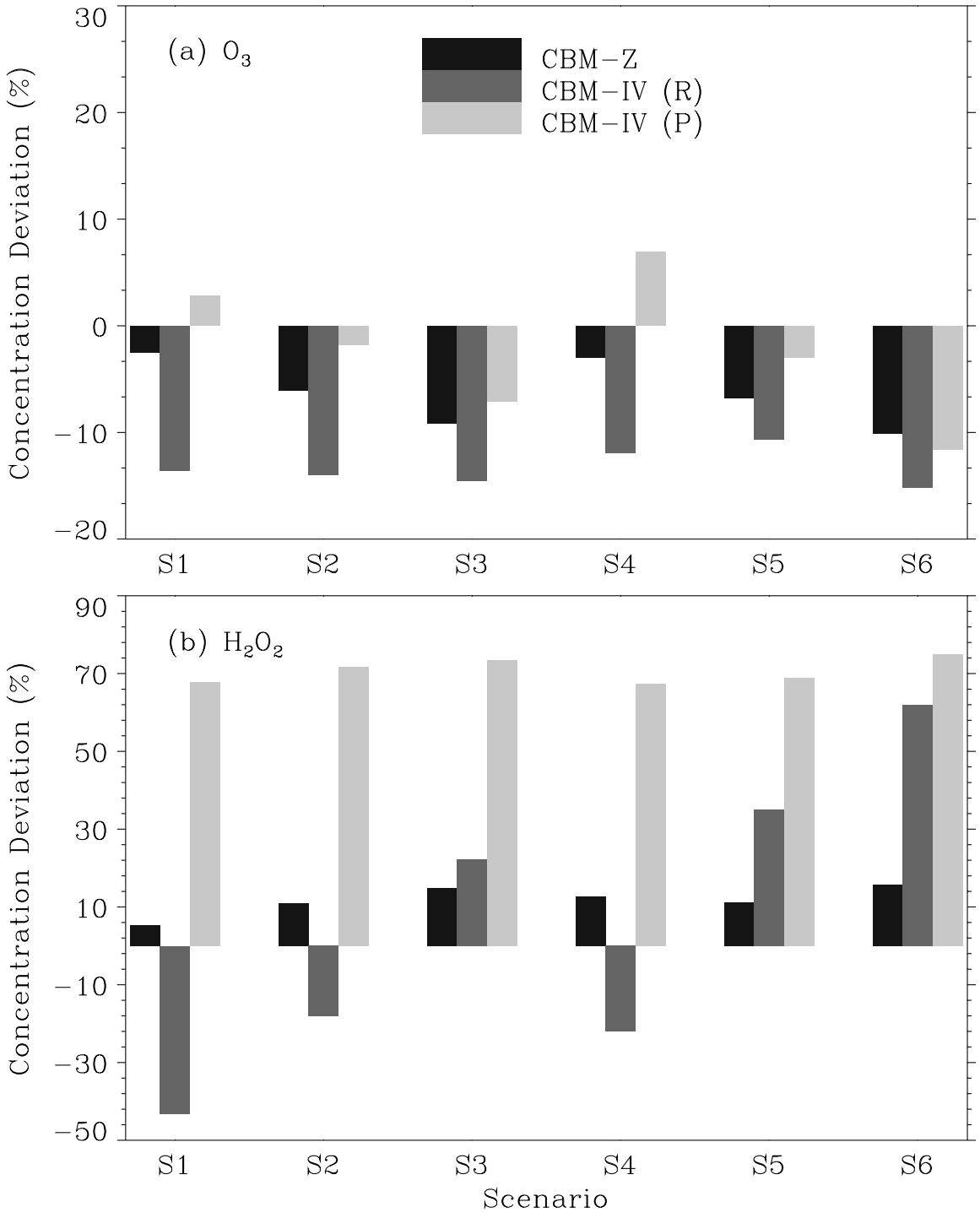

Figure 2.7: Percentage concentration deviations from CBM-Z, CBM-IV (R), and CBM-IV (P) with respect to RADM2 predictions after 3 model days: (a) O_3; (b) H_2O_2.

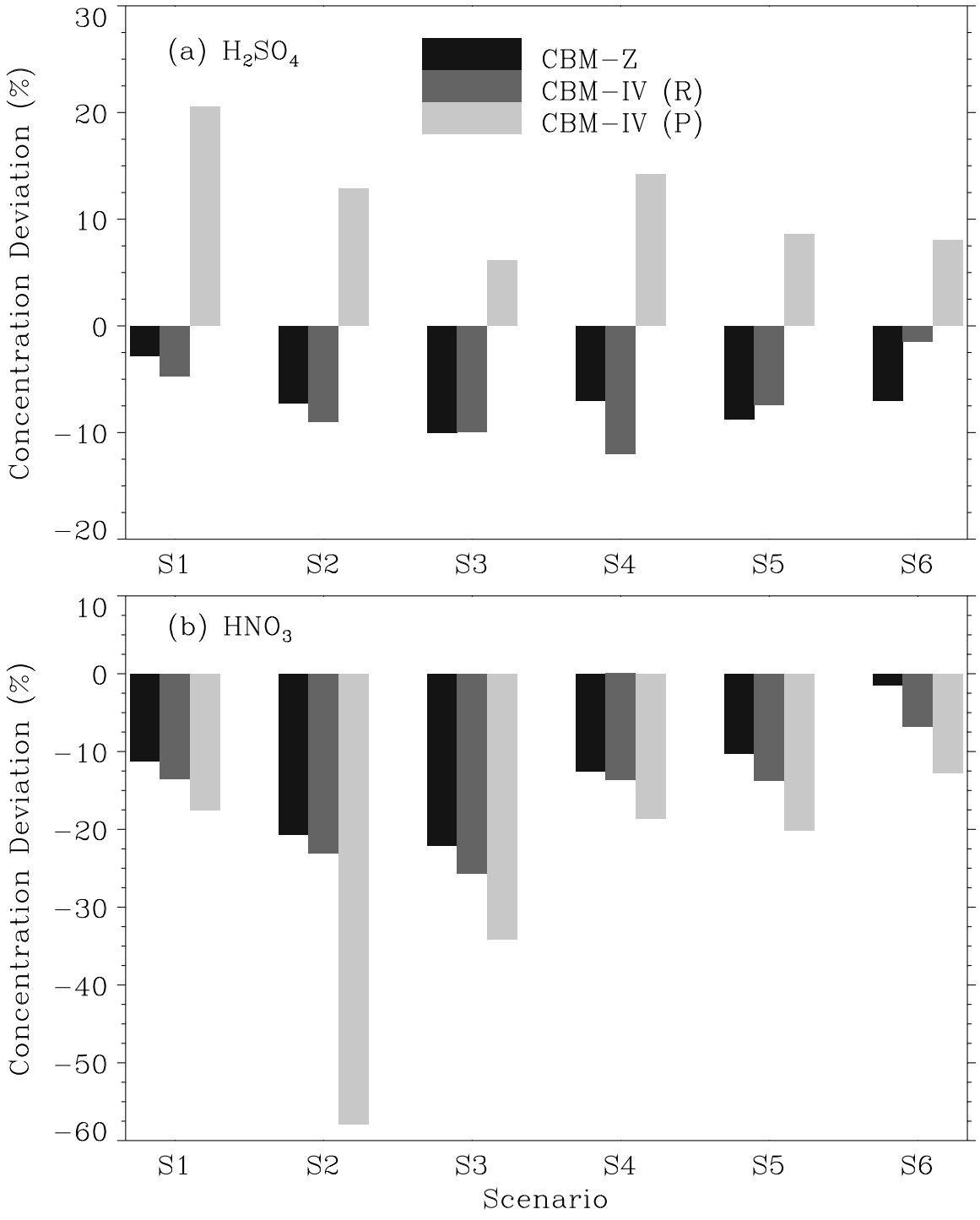

Figure 2.8: Percentage concentration deviations from CBM-Z, CBM-IV (R), and CBM-IV (P) with respect to RADM2 predictions after 3 model days: (a) H_2SO_4; (b) HNO_3.

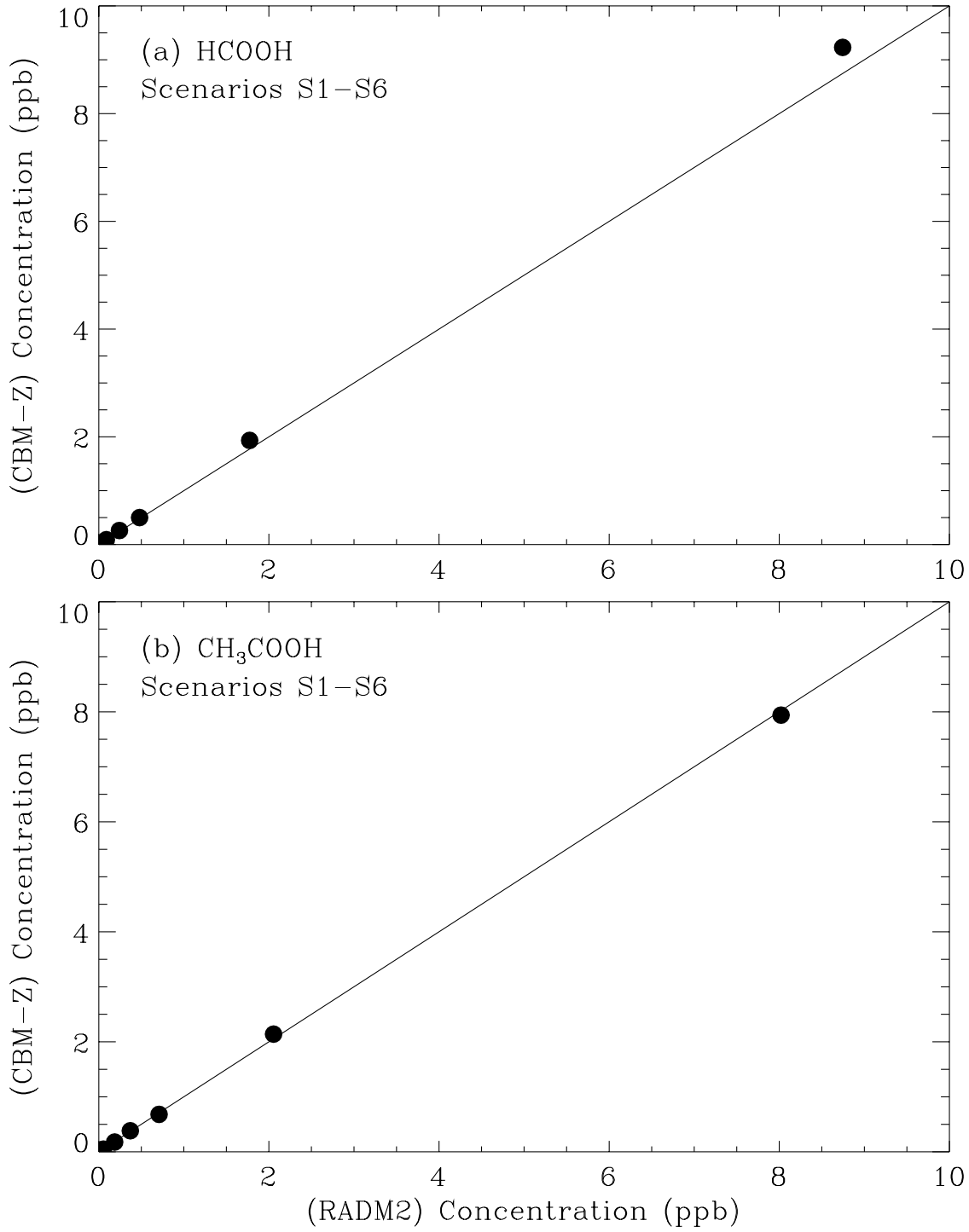

Figure 2.9: Simulated concentrations after 3 model days using the RADM2 and CBM-Z mechanisms: (a) HCOOH; (b) CH_3COOH. No organic acids are produced in the CBM-IV.

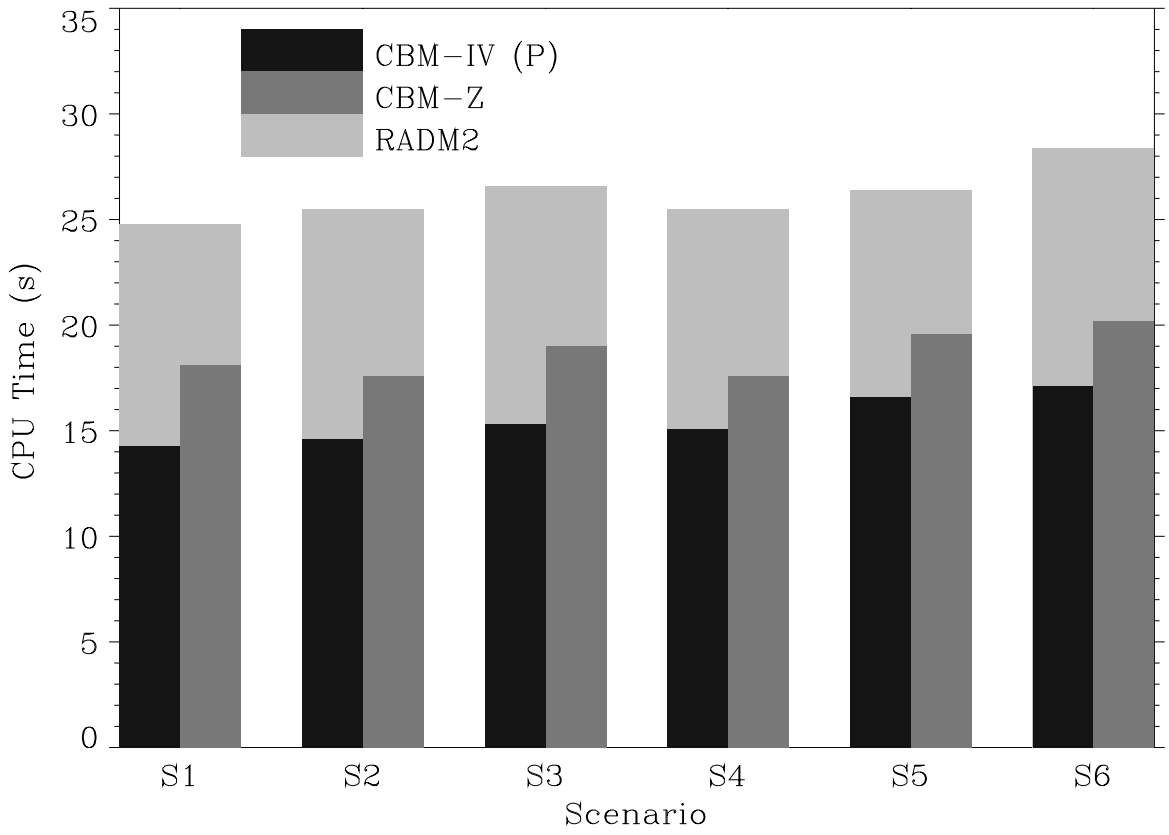

Figure 2.10: CPU time required by the RADM2, CBM-Z, and CBM-IV (P) mechanisms to simulate 3 model days. The CBM-IV (R) CPU timings are similar to those of CBM-IV (P).

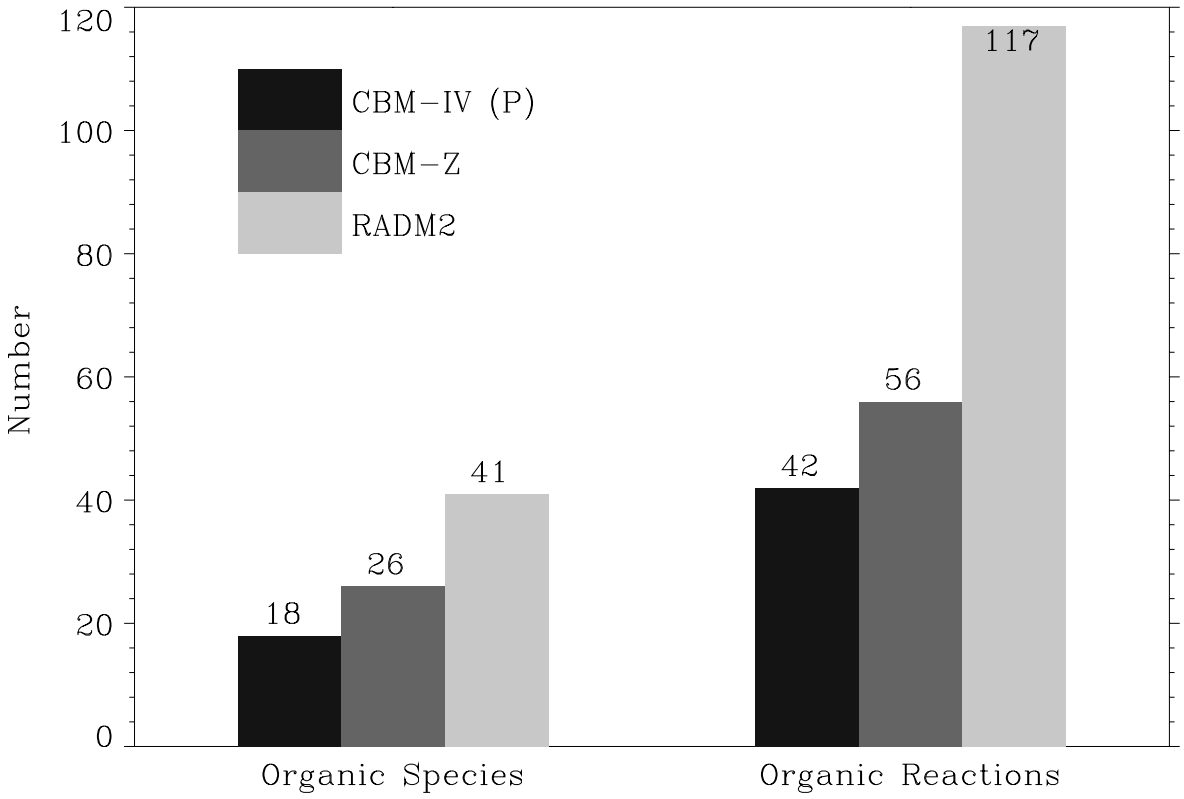

Figure 2.11: Comparison of mechanism size between CBM-IV (P), CBM-Z, and RADM2.

2.4 Concluding Remarks

Assuming that the detailed RADM2 chemical mechanism is more accurate than the highly condensed CBM-IV, the model intercomparison results offer the following conclusions:

- The proposed CBM-Z developed from the published CBM-IV is in very good agreement with the RADM2 mechanism with respect to the predictions of all important oxidants and other species of interest. The published and revised inorganic chemistry versions of CBM-IV are, however, in relatively poor agreement with RADM2 in general, and especially with respect to H_2O_2 predictions.

- The improved predictions of the CBM-Z are due to two reasons: (1) using the same inorganic reactions and rate constants as used in the RADM2 calculations; and (2) employing explicit treatment for the lesser reactive alkanes, methane and ethane, and their intermediates, methyl and ethylperoxy radicals.

- As a recommendation for future model intercomparison studies, it would be more appropriate to use the same inorganic chemistry for all the chemical mechanisms under consideration to isolate the differences in the various approximate treatments of the complex organic chemistry.

- The CBM-Z is still considerably smaller than the detailed RADM2 mechanism with respect to the number of organic species and reactions. As a result, it requires significantly less computational memory and time, which always are critical considerations in three-dimensional regional- and global-scale models.

Chapter 3

Rural Gas-Phase Chemistry: Isoprene

Continental biogenic hydrocarbon emissions mainly consist of isoprene and monoterpenes. These are produced by vegetation and emitted into the atmosphere in significant quantities. The most recent global estimates put isoprene emissions at the top at 503 Tg C yr^{-1}, followed by monoterpenes at 127 Tg C yr^{-1} (Guenther *et al.*, 1995). These natural hydrocarbon burdens clearly overwhelm the anthropogenic non-methane hydrocarbon emissions which are estimated at 75 Tg yr^{-1} (Piccot *et al.*, 1992).

Isoprene and monoterpenes are highly reactive under ambient conditions, and play a major role in the photochemical oxidant cycle in rural areas. Upon oxidation in the atmosphere, these hydrocarbons form a variety of highly reactive radicals and other species which ultimately degrade to form CO and CO_2. These biogenics also exhibit ozone forming potential in the presence of NO_x (Lurmann *et al.*, 1983). Thus, regional- and global-scale tropospheric chemical mechanisms should have adequate representation of these species. This chapter deals with the development of an isoprene reaction mechanism as a supplement for the CBM-Z already presented in the previous chapter, while the monoterpene chemistry is investigated in the next chapter.

3.1 Literature Review

Isoprene (2-methyl 1,3 butadiene) is emitted in significant amounts from deciduous trees such as oaks, aspen, and sycamore and to a lesser extent from coniferous trees such as pine, fir, and larch (Rasmussen, 1972; Jones and Rasmussen, 1975; Isidorov *et al.*, 1985, Fall, 1991; Guenther *et al.*, 1991; Guenther *et al.*, 1993). Its concentrations in a typical deciduous forest can reach 37.5 ppb at the ground level and 4 ppb in the upper surface layer (∼300 m) (Martin *et al.*, 1991; Andronache *et al.*, 1994). Isoprene concentrations in a coniferous forest may be an order of magnitude lower. Figure 3.1 illustrates the global extent and magnitude of isoprene emissions during July (Guenther *et al.*, 1995).

Like other alkenes and dienes, isoprene reacts rapidly with O_3, OH and NO_3 under ambient conditions. Smog chamber experiments to study its atmospheric chemistry have

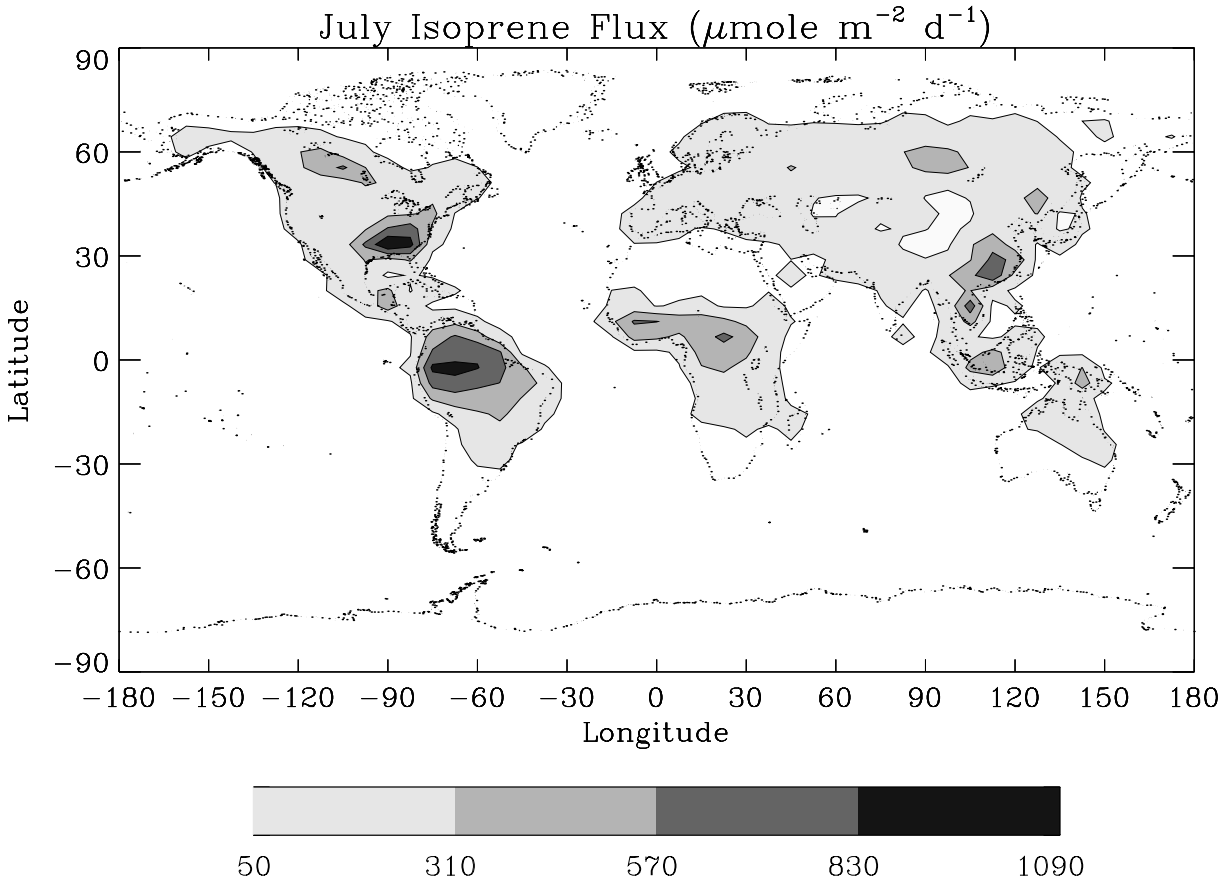

Figure 3.1: July Isoprene emission flux based on the global inventory of Guenther *et al.* (1995).

been carried out since the late 1970s (Arnts and Gay, 1979; Kamens *et al.*, 1982). Lloyd *et al.* (1983) first attempted to develop a chemical mechanism based on the data of Kamens *et al.* (1982), which provided useful concentration-time profiles for the reactants and several products including methyl vinyl ketone (MVK) and methacrolein (MAC). Both the published RADM2 (Stockwell *et al.*, 1990) and CBM-IV (Gery *et al.*, 1989) mechanisms also included isoprene chemistry. Only the initial reaction of isoprene with OH was correctly represented in RADM2, while the reactions of the subsequent products were modeled in a manner similar to the degradation of propene. Specific products like methyl vinyl ketone and methacrolein were not incluced. Not surprisingly, the RADM2 isoprene chemistry failed to reliably predict the concentrations of ozone and other photooxidants observed in smog chamber experiments (Carter and Lurmann, 1989). On the other hand, the CBM-IV isoprene chemistry was condensed from a detailed mechanism which included explicit treatment of MVK and MAC. The condensed version in the CBM-IV, however, does not have these as explicit species, but are represented in terms of carbon bond surrogates such as OLE, ALD2, and PAR.

More recent investigations (Tuazon and Atkinson, 1989, 1990a,b; Paulson *et al.*, 1992a,b; Grosjean *et al.*, 1993; Aschmann and Atkinson, 1994) have identified additional products and their reactions, giving a more complete picture of the complex isoprene chemistry. Based on the recent kinetic data, Zimmermann and Poppe (1996) developed a detailed isoprene chemical mechanism as an extension to the RADM2 mechanism, replacing the old version. A total of 39 species and 153 reactions were introduced in RADM2 to describe the isoprene chemistry in an explicit manner. In the same paper, the authors condensed the detailed mechanism into a more tractable and efficient version, requiring only 6 new species and 16 additional reactions. The condensed mechanism gave approximately the same results as the detailed version. At about the same time, Carter and Atkinson (1996) and Carter (1996) also developed detailed and condensed reaction mechanisms of isoprene photooxidation for use in SAPRC-90 gas-phase mechanism. Since the RADM2 mechanism can be easily adapted into the existing CBM-IV framework, the RADM-C mechanism is considered here as the reference mechanism.

The purpose of this chapter is to update the published CBM-IV isoprene mechanism (denoted by CBM-IV (old)) based on the newly developed RADM-C mechanism of Zimmermann and Poppe (1996), and compare the three under a range of conditions.

Table 3.1: List Organic Species in RADM-C for Isoprene Chemistry.

No.	Species	Representation
1.	Isoprene [$CH_2 = CC(CH_3) = CH_2$]	ISOP
2.	Surrogate of all peroxy radicals from Isoprene	ISOPP
3.	NO_3-Isoprene adduct	ISOPN
4.	Methacrolein [$CH_2C(CH_3)CHO$]	MAC
5.	Methyl vinyl ketone [$CH_3COCH = CH_2$]	MVK
6.	Peroxy radicals from MAC	MACP
7.	Peroxy radicals from MVK	MVKP

3.2 Isoprene Mechanisms

The condensed isoprene mechanism (RADM-C) of Zimmermann and Poppe (1996) retained the two major long-lived products MVK and MAC. Also included are a peroxy radical surrogate (ISOPP), representing the sum of all peroxy radicals produced by the isoprene-OH reaction, peroxy radicals (MVKP and MACP) resulting from the reactions of MAC and MVK with OH, and an isoprene-NO_3 adduct (ISOPN). Explicit treatment of, at least, these species was found necessary for a reasonably accurate simulation of the oxidant cycle. The complete list of species involved in the isoprene mechanism is summarized in Table 3.1, and the list of reactions is given in Table 3.2. These species and reactions supplement the RADM2 mechanism described in Chapter 2, and the entire mechanism is referred to as RADM-C here.

On the other hand, the published CBM-IV isoprene chemistry consists of only four initial reactions with $O(^3P)$, OH, O_3, and NO_3. As indicated before, the products are represented by the existing carbon bond surrogates, thus requiring only one new species, i.e., isoprene itself. Table 3.3 shows the isoprene reactions as published in Gery *et al.* (1989). These reactions are added to the CBM-Z developed in Chapter 2, and the resulting mechanism is referred as CBM-Z (old)

Using the equivalence between the RADM2 and CBM-Z species (Table 3.4), an equivalent CBM-Z isoprene mechanism can be expressed based on the newly developed RADM-C mechanism. The equivalencies between the species of the two mechanisms are based on the definitions of the species and the recommendations given by their developers (Gery *et al.*,

Table 3.2: RADM-C Isoprene Mechanism from Zimmermann and Poppe (1996.)

No.	Reaction			Rate Constant k [molecule-cm^3-s]
1.	ISOP + OH	$\longrightarrow$	ISOPP	$2.55 \times 10^{-11} \exp(409/T)$
2.	ISOP + NO_3	$\longrightarrow$	ISOPN	$3.03 \times 10^{-12} \exp(-446/T)$
3.	ISOP + O_3	$\longrightarrow$	.55MAC + .21MVK + .3O(^{3}P) + .5OH + .89HCHO + .11HO_2 + .18CO + .07OLT + .15ORA2 + .07ORA1 + .09CH_3O_2 + .01GLY	$1.23 \times 10^{-14} \exp(-2013/T)$
4.	MAC + OH	$\longrightarrow$	.5MACP + .8ACO_3 + .5HCHO	$1.86 \times 10^{-11} \exp(175/T)$
5.	MVK + OH	$\longrightarrow$	MVKP	$4.13 \times 10^{-12} \exp(452/T)$
6.	MAC + O_3	$\longrightarrow$	.76MGLY + .23O(^{3}P) + .46OH + .7HCHO + .11ORA1 + .23ORA2	$4.4 \times 10^{-15} \exp(-2500/T)$
7.	MVK + O_3	$\longrightarrow$	.76MGLY + .23O(^{3}P) + .46OH + .7HCHO + .11ORA1 + .24CH_3O_2 + .24CO	$4.4 \times 10^{-15} \exp(-2000/T)$
8.	ISOPP + NO	$\longrightarrow$	.87NO_2 + .87HO_2 + .38MVK .28MAC + .62HCHO + .13ONIT + .013GLY + .05MGLY + .25XO_2 + .08ALD + .04KET + .02ORA2	$4.2 \times 10^{-12} \exp(180/T)$
9.	MACP + NO	$\longrightarrow$	.8KET + .2HCHO + .2MGLY + HO_2 + NO_2	$4.2 \times 10^{-12} \exp(180/T)$
10.	MVKP + NO	$\longrightarrow$	.7ACO_3 + .8ALD + .3HCHO .3HO_2 + .3MGLY + NO_2	$4.2 \times 10^{-12} \exp(180/T)$
11.	ISOPN + NO	$\longrightarrow$	2NO_2 + HCHO + .5MVK + .5MAC	$4.2 \times 10^{-12} \exp(180/T)$
12.	ISOPP + HO_2	$\longrightarrow$	OP2	$7.7 \times 10^{-14} \exp(1300/T)$
13.	MACP + HO_2	$\longrightarrow$	OP2	$7.7 \times 10^{-14} \exp(1300/T)$
14.	MVKP + HO_2	$\longrightarrow$	OP2	$7.7 \times 10^{-14} \exp(1300/T)$
15.	ISOPP + ISOPP	$\longrightarrow$	.34MAC + .42MVK + .3OLT + .06DCB + .1OLI + 1.3HO_2 + .55HCHO + .1MGLY	1.0×10^{-13}
16.	MVK + NO_3	$\longrightarrow$	NO_2 + CH_3O_2 + MGLY	6.0×10^{-14}
17.	MAC + NO_3	$\longrightarrow$	.5HNO_3 + .5NO_2 + .8ACO_3 + .5MGLY	1.0×10^{-14}
18.	MVKP + ISOPP	$\longrightarrow$	.3MAC + .3MVK + .6MGLY + HCHO + 1.2HO_2 + .1DCB + .4OLT + .3OLI	5.0×10^{-14}
19.	MACP + ISOPP	$\longrightarrow$	.3MAC + .3MVK + .6MGLY + HCHO + 1.2HO_2 + .1DCB + .4OLT + .3OLI	5.0×10^{-14}

Table 3.3: Isoprene Chemistry Mechanism in the Published CBM-IV (Gery *et al.*, 1989).

No.	Reaction			Rate Constant[a] k [molecule-cm^3-s]
1.	ISOP+ O(^{3}P)	$\longrightarrow$	.6HO_2 + .8ALD_2 + .5CO + .55OLE+ .5XO_2 + .45ETH+ .9PAR	1.8×10^{-11}
2.	ISOP+ OH	$\longrightarrow$	HCHO+ XO_2 + .67HO_2 + .4MGLY+ .2C_2O_3 + ETH+ .2ALD_2 + .13XO_2N	$2.55 \times 10^{-11} \exp(409/T)$
3.	ISOP+ O_3	$\longrightarrow$	HCHO+ .4ALD_2 + .06CO + .55ETH+ .2MGLY+ .1PAR+ .44HO_2 + .1OH	$1.23 \times 10^{-14} \exp(-2013/T)$
4.	ISOP+ NO_3	$\longrightarrow$	XO_2N	$3.03 \times 10^{-12} \exp(-446/T)$

[a]The rate constants for all the initial reactions, except with O(^{3}P), are adopted from RADM-C (Zimmerman and Poppe, 1996).

1989; Stockwell *et al.*, 1990). Equivalent CBM-Z species could be found for all RADM2 species except GLY, OP2, and ONIT; these are, therefore, simply neglected. The equivalent CBM-Z isoprene mechanism contains the same additional species listed in Table 3.1, and similar reactions as in the RADM-C (Table 3.5). The equivalent CBM-Z isoprene mechanism, referred as to CBM-Z (new), is thus, a good approximation to the RADM-C but not exactly identical.

3.3 Mechanism Intercomparison

The goal of this section is to compare the performance of the three isoprene mechanisms discussed above, namely, the RADM-C, CBM-Z (old), and CBM-Z (new) (see Table 3.6 for nomenclature description). A constant-volume box model was employed to simulate the diurnal photochemistry of isoprene; and since the focus is mainly on mechanism intercomparison, hypothetical isoprene and NO_x emissions were prescribed to represent a wide range of scenarios.

3.3.1 Model Inputs

Isoprene emission fluxes depend on both solar radiation intensity and temperature, and thus, exhibit a daytime maximum and decrease to zero at nighttime (Lamb *et al.*, 1993). Although quite sophisticated emission models are available (Guenther *et al.*, 1993), the

Table 3.4: Equivalent RADM2 and CBM-Z Species Relevant to the Isoprene Chemistry.

No.	Equivalent Species	
	RADM2	CBM-Z
1.	ORA1	HCOOH
2.	ORA2	CH_3COOH
3.	GLY	—
4.	MGLY	MGLY
5.	ALD	ALD2
6.	KET	AONE
7.	ACO_3	C_2O_3
8.	DCB	OPEN
9.	OLT	OLE
10.	OLI	2ALD2
11.	OP2	—
12.	XO_2	XO_2
13.	ONIT	—

diurnal variation of isoprene emission flux may be simply parameterized with the solar zenith angle for the purpose of this exercise (see Equation 2.3). The diurnal NO_x and SO_2 emissions are also parameterized in a similar fashion. Table 3.7 shows the list of emission parameters for six scenarios. The first three scenarios (I1-I3) represent isoprene emissions from typical deciduous forests, while the last three (I4-I6) are for coniferous type forests. Three levels of NO_x pollution, ranging from rural to urban, are selected for each forest type. However, no urban hydrocarbons are emitted in any scenario to maintain the focus on isoprene mechanism comparison.

Each simulation was performed for 3 model days beginning 00 hours, July 1. A constant mixing-height of 1000 m was used for the entire run, while a diurnal variation of temperature representative of continental northern hemisphere July conditions was prescribed as shown in Figure 2.1. The temperature and emission fluxes were updated every hour. A constant water vapor concentration of 3.8×10^{17} molecule cm^{-3}, corresponding to 50% relative humidity at 298 K, was also prescribed. The system of non-linear ordinary differential equations describing the dynamic chemistry were solved using LSODES, a GEAR-type solver (Hindmarsh, 1983). Only the last 2 day's results were used for analysis and comparison.

Table 3.5: Equivalent CBM-Z Isoprene Chemistry Based on the RADM-C Mechanism.

No.	Reaction			Rate Constant k [molecule-cm^3-s]
1.	ISOP + OH	$\longrightarrow$	ISOPP	$2.55 \times 10^{-11} \exp(409/T)$
2.	ISOP + NO_3	$\longrightarrow$	ISOPN	$3.03 \times 10^{-12} \exp(-446/T)$
3.	ISOP + O_3	$\longrightarrow$	.55MAC + .21MVK + .3O(^{3}P) + .5OH + .89HCHO + .11HO_2 + .18CO + .07OLE + .09CH_3O_2 + .07HCOOH + .15CH_3COOH&	$1.23 \times 10^{-14} \exp(-2013/T)$
4.	MAC + OH	$\longrightarrow$	.5MACP + .8C_2O_3 + .5HCHO	$1.86 \times 10^{-11} \exp(175/T)$
5.	MVK + OH	$\longrightarrow$	MVKP	$4.13 \times 10^{-12} \exp(452/T)$
6.	MAC + O_3	$\longrightarrow$	.76MGLY + .23O(^{3}P) + .46OH + .7HCHO + .11HCOOH + .23CH_3COOH	$4.4 \times 10^{-15} \exp(-2500/T)$
7.	MVK + O_3	$\longrightarrow$	.76MGLY + .23O(^{3}P) + .46OH + .7HCHO + .11HCOOH + .24CO + .24CH_3O_2	$4.4 \times 10^{-15} \exp(-2000/T)$
8.	ISOPP + NO	$\longrightarrow$	.87NO_2 + .87HO_2 + .38MVK .28MAC + .62HCHO + .25XO_2 + .05MGLY + .08ALD2 + .04AONE + .02CH_3COOH	$4.2 \times 10^{-12} \exp(180/T)$
9.	MACP + NO	$\longrightarrow$	.8AONE + .2HCHO + .2MGLY + HO_2 + NO_2	$4.2 \times 10^{-12} \exp(180/T)$
10.	MVKP + NO	$\longrightarrow$	.7C_2O_3 + .8ALD2 + .3HCHO .3HO_2 + .3MGLY + NO_2	$4.2 \times 10^{-12} \exp(180/T)$
11.	ISOPN + NO	$\longrightarrow$	2NO_2 + HCHO + .5MVK + .5MAC	$4.2 \times 10^{-12} \exp(180/T)$
12.	ISOPP + HO_2	$\longrightarrow$		$7.7 \times 10^{-14} \exp(1300/T)$
13.	MACP + HO_2	$\longrightarrow$		$7.7 \times 10^{-14} \exp(1300/T)$
14.	MVKP + HO_2	$\longrightarrow$		$7.7 \times 10^{-14} \exp(1300/T)$
15.	ISOPP + ISOPP	$\longrightarrow$	.34MAC + .42MVK + .3OLE + .06OPEN + .2ALD2 + 1.3HO_2 + .55HCHO + .1MGLY	1.0×10^{-13}
16.	MVK + NO_3	$\longrightarrow$	NO_2 + CH_3O_2 + MGLY	6.0×10^{-14}
17.	MAC + NO_3	$\longrightarrow$	.5HNO_3 + .5NO_2 + .8C_2O_3 + .5MGLY	1.0×10^{-14}
18.	MVKP + ISOPP	$\longrightarrow$	.3MAC + .3MVK + .6MGLY + HCHO + 1.2HO_2 + .1OPEN + .4OLE + .6ALD2	5.0×10^{-14}
19.	MACP + ISOPP	$\longrightarrow$	.3MAC + .3MVK + .6MGLY + HCHO + 1.2HO_2 + .1OPEN + .4OLE + .6ALD2	5.0×10^{-14}

Table 3.6: Mechanism Nomenclature.

Nomenclature	Basic Chemistry	Isoprene Chemistry
RADM-C	RADM2 (Chapter 2)	Table 3.2
CBM-Z (old)	CBM-Z (Chapter 2)	Table 3.3
CBM-Z (new)	CBM-Z (Chapter 2)	Table 3.5

Table 3.7: Hypothetical Emission Scenarios for Isoprene Chemistry Intercomparison.

Scenario	Isoprene		NO_x and SO_2	
	E_1	E_2	E_1	E_2
	(μmol m^{-3} h^{-1})		(μmol m^{-3} h^{-1})	
I1	100	0	0.8	0.2
I2	80	0	4.0	1.0
I3	60	0	16.0	4.0
I4	10	0	0.8	0.2
I5	8	0	4.0	1.0
I6	6	0	16.0	4.0

3.3.2 Results and Discussion

Scenarios I2 and I4 are selected as the two base simulations representing suburban deciduous and rural coniferous forest settings, respectively. The diurnal variations of isoprene, O_3, H_2O_2, NO_3, NO_2, OH, and HO_2 predicted by the three mechanisms are presented in Figures 3.2 through 3.8 for the two base scenarios.

Even though isoprene is emitted identically for all three mechanisms, the CBM-Z (old) considerably overpredicts the concentrations as compared to the RADM-C and CBM-Z (new) mechanisms in both the base scenarios. The predictions from the latter two, however, are in excellent agreement, which indicates that the CBM-Z (old) underpredicts the oxidants responsible for isoprene consumption. Indeed, the concentrations of O_3, OH, and NO_3 predicted by the CBM-Z (old) are considerably lower; however, the concentration of H_2O_2 is considerably higher. And as expected, the predictions of these oxidants from the RADM-C and CBM-Z (new) mechanisms are in excellent agreement. Between the two base scenarios, the deviations in the CBM-Z (old) predictions from the RADM-C and CBM-Z (new) are more pronounced in I2 than I4. This is because of much higher isoprene concentrations in the deciduous forest scenario (I2) as compared to the coniferous forest scenario (I4). Interestingly, HO_2 predictions from all three mechanisms are in good agreement with each other for both scenarios during the daytime; however, the CBM-Z (old) predictions are significantly higher than the other two mechanisms during the nighttime hours.

Figures 3.9 and 3.11 show the final (after 3 days) concentration deviations in the CBM-Z (old) and CBM-Z (new) predictions with respect to the RADM-C mechanism for O_3, H_2O_2, H_2SO_4, HNO_3, and organic acids for all 6 scenarios. The CBM-Z (old) severely underpredicts ozone concentrations (as much as -75%) under low NO_x deciduous forest scenarios (I1, and I2), while as much as -30% in the low NO_x coniferous forest scenario (I4). However, negligible differences (less than 5%) are observed in the final ozone concentrations for the last two scenarios (I5 and I6), where the isoprene concentrations are relatively much lower. The maximum deviation from the CBM-Z (new) is only about -13% for scenario I2, and less than 10% for other scenarios. In the case of H_2O_2, the CBM-Z (old) severely overpredicts for the rural deciduous forest scenario (I1) by about 230%, while about 20 to 70% for other scenarios. On the other hand, the CBM-Z (new) underpredicts the final H_2O_2 concentrations by less than 18% for I1 and I2, and less than 10% for the rest of the scenarios. Negligible differences (less than 3%) were observed for the last two scenarios.

The gas-phase H_2SO_4 production is directly proportional to the concentration of the OH radical. The CBM-Z (old) underpredicts the H_2SO_4 concentrations by 65% for scenario I2, and 40% for I4, both having indentical NO_x emissions. Less than 13% deviations are observed for the remaining scenarios, with negligible difference for the last scenario. The CBM-Z (new) H_2SO_4 predictions are within $\pm$5% for all scenarios, again with negligible deviation for the last scenario. CBM-Z (old) also considerably underpredicts HNO_3 concentrations, between -40 to -90% for scenarios I1-I4, and by 20% for I5. Negligible difference ($\sim$5%) is observed for scenario I6. On the other hand, the maximum deviation by CBM-Z (new) is about 30% for scenario I2, with less than 20% for the remaining scenarios. Less than 5% underprediction is observed for the last scenario (I6).

Formic acid, by far, is the most overpredicted by the CBM-Z (old). The deviations range from 40 to 450% for scenarios I2-I6, and -60% for I1. The CBM-Z (new) predictions are within -10% deviation. The higher organic acid concentrations (represented by acetic acid) from the CBM-Z (old) deviate from the RADM-C predictions by +80 to -90%, while the CBM-Z (new) overpredicts only by 5 to 20%.

Figure 3.12 shows the CPU time requirements by the three mechanisms to simulate three model days. The CBM-Z (old) mechanism required only about 50% of the time spent by the RADM-C mechanism, while the CBM-Z (new) required about 66% of the time, only marginally greater than the CBM-Z (old).

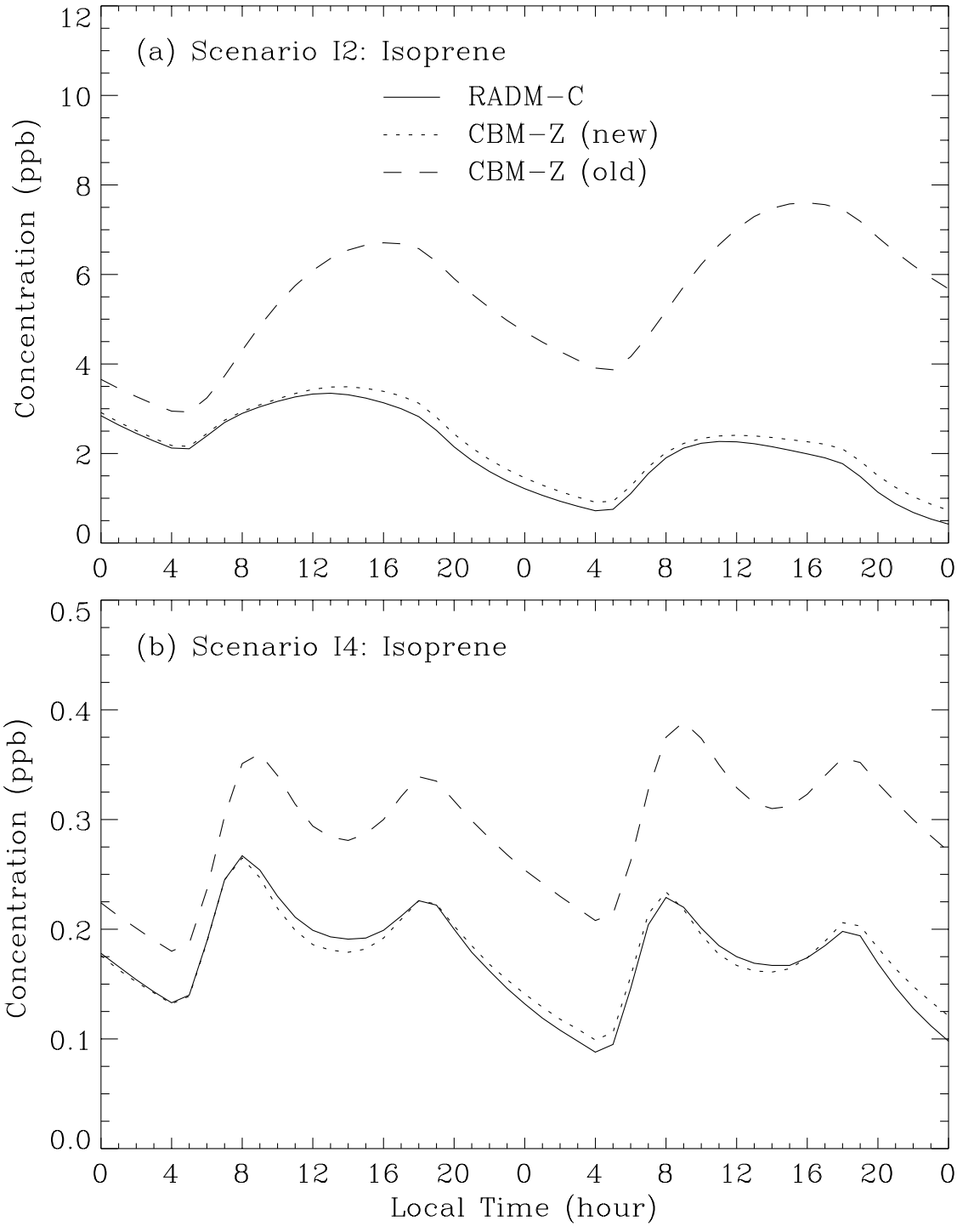

Figure 3.2: Isoprene concentration evolution using the RADM-C, CBM-Z (old), and CBM-Z (new) mechanisms for: (a) scenario I2; (b) scenario I4.

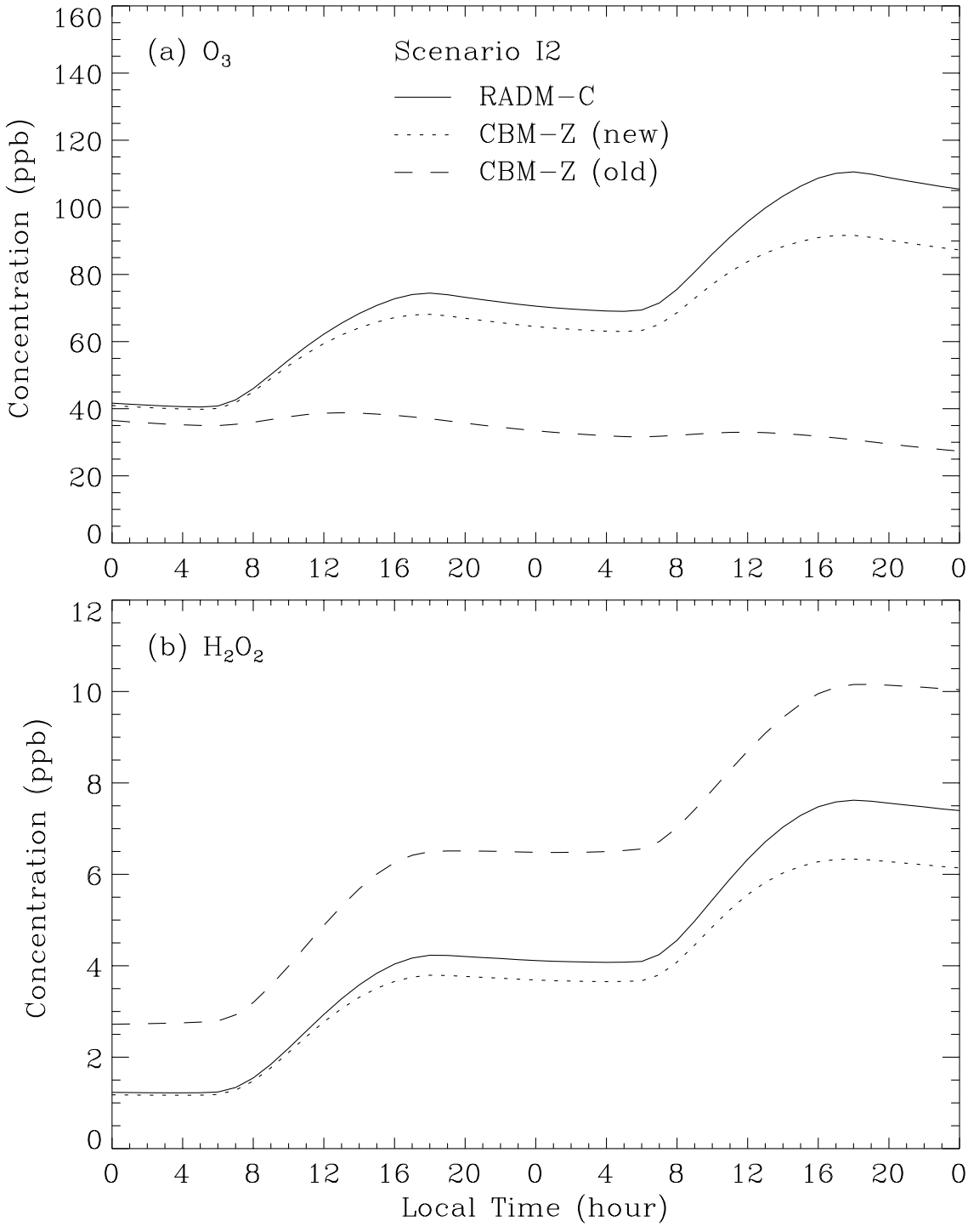

Figure 3.3: Concentration evolution using the RADM-C, CBM-Z (old), and CBM-Z (new) mechanisms for scenario I2: (a) O_3; (b) H_2O_2.

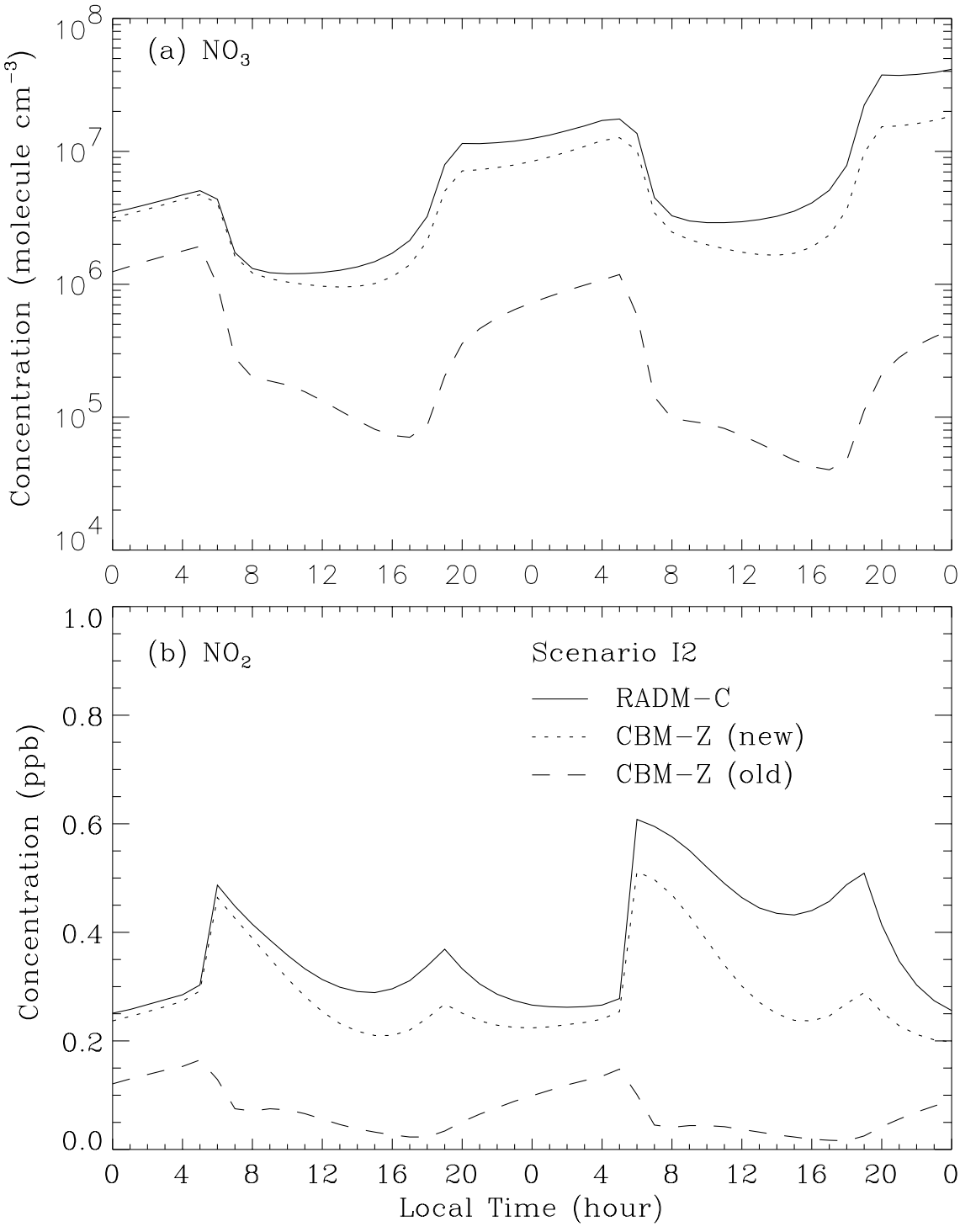

Figure 3.4: Concentration evolution using the RADM-C, CBM-Z (old), and CBM-Z (new) mechanisms for scenario I2: (a) NO_3; (b) NO2.

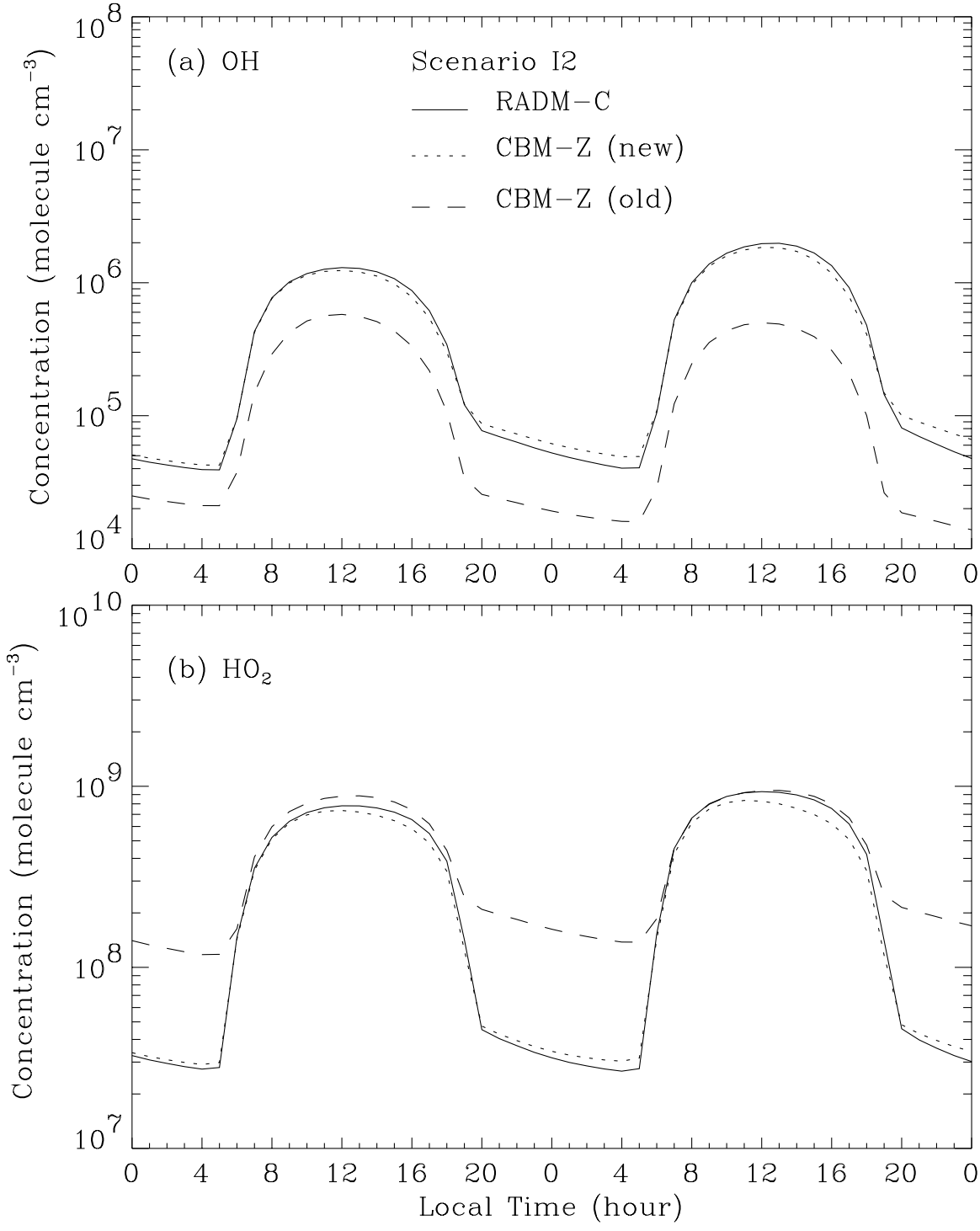

Figure 3.5: Concentration evolution using the RADM-C, CBM-Z (old), and CBM-Z (new) mechanisms for scenario I2: (a) OH; (b) HO_2.

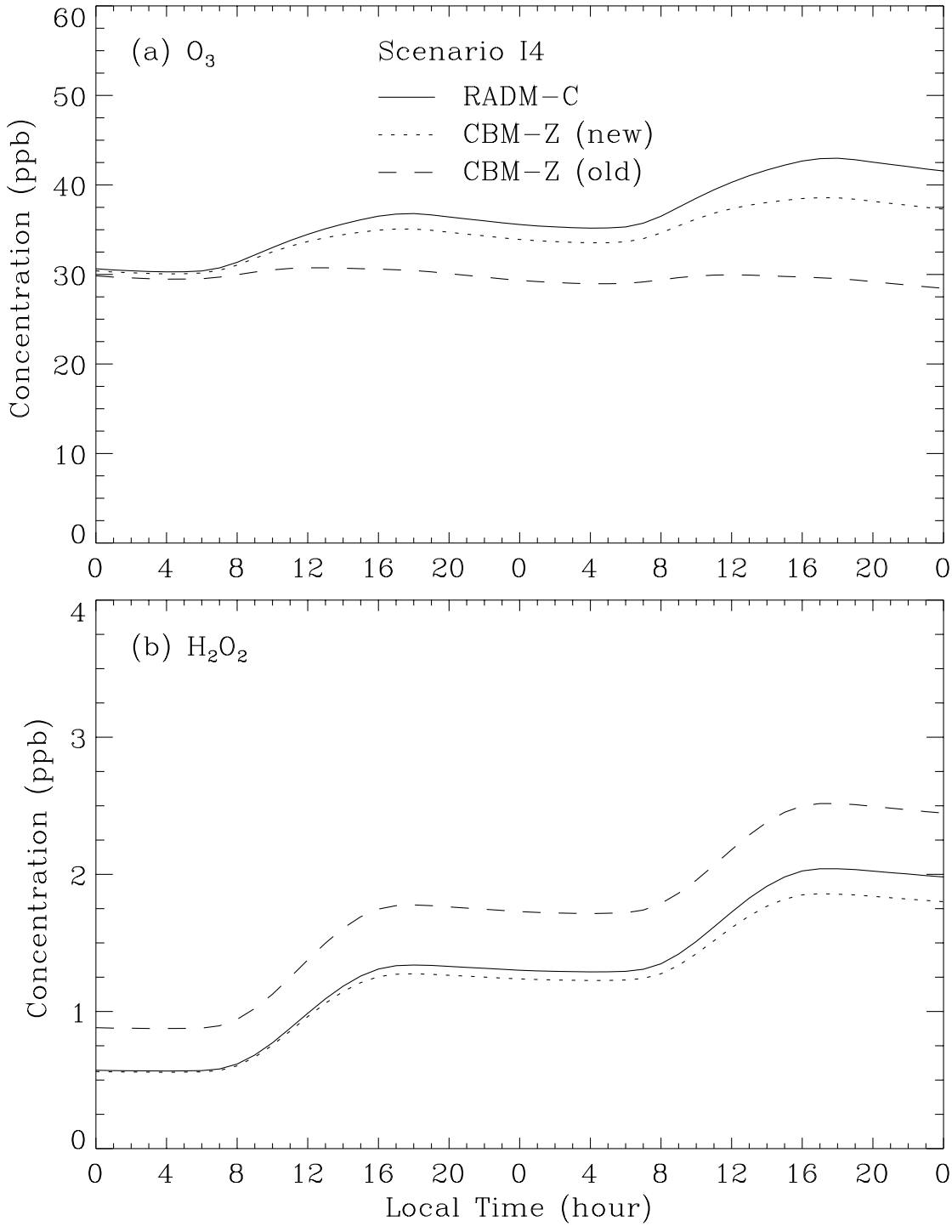

Figure 3.6: Concentration evolution using the RADM-C, CBM-Z (old), and CBM-Z (new) mechanisms for scenario I4: (a) O_3; (b) H_2O_2.

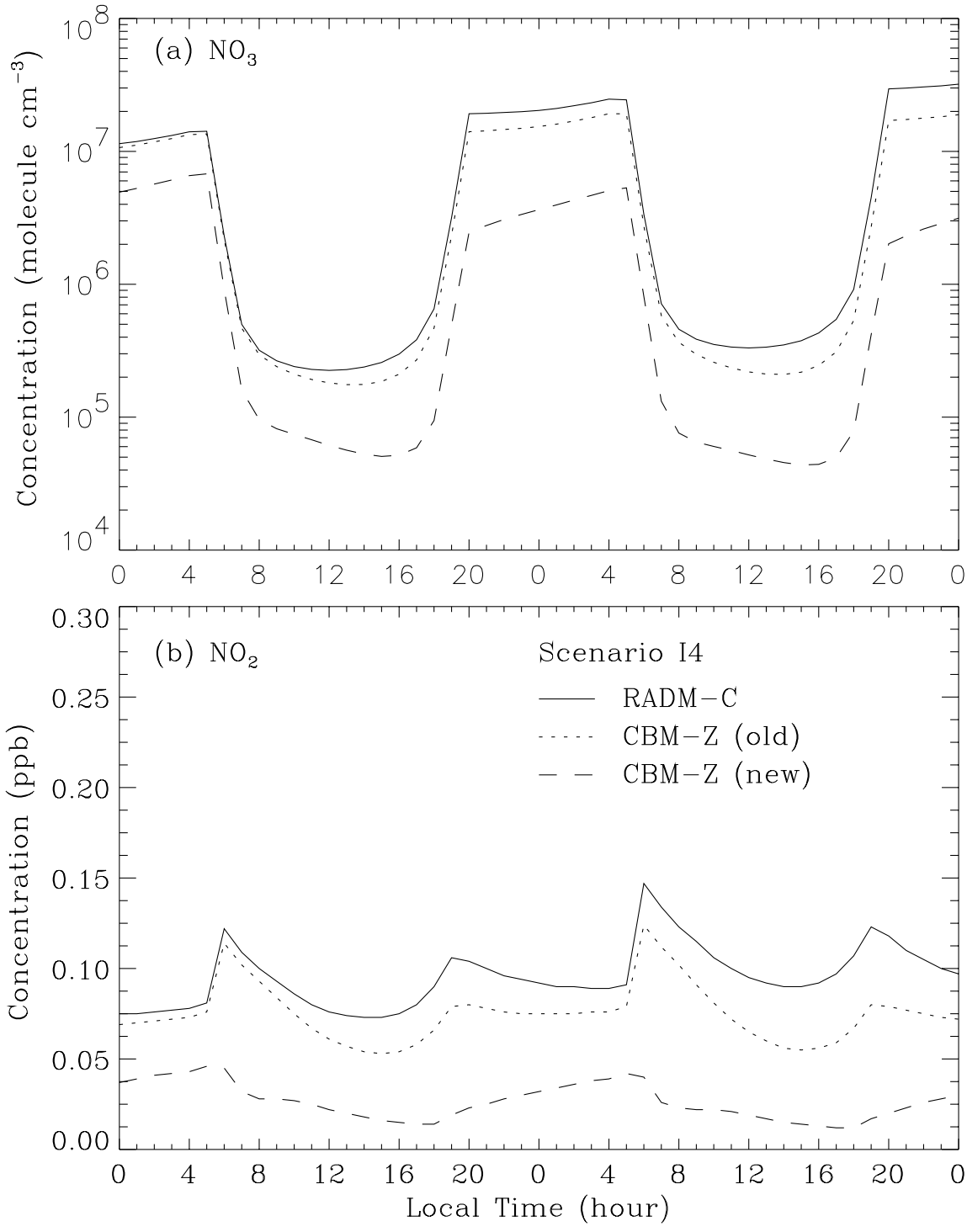

Figure 3.7: Concentration evolution using the RADM-C, CBM-Z (old), and CBM-Z (new) mechanisms for scenario I4: (a) NO_3; (b) NO2.

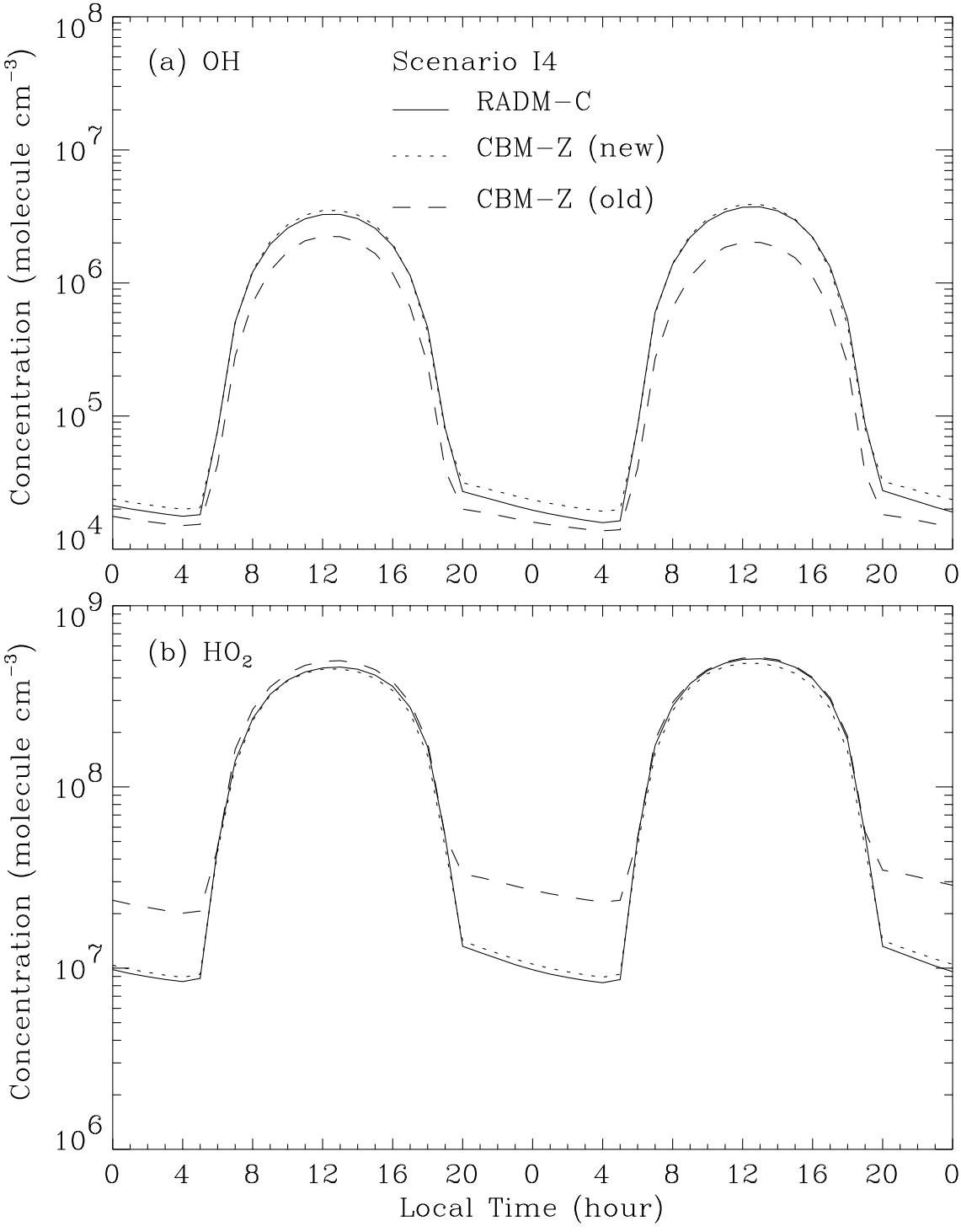

Figure 3.8: Concentration evolution using the RADM-C, CBM-Z (old), and CBM-Z (new) mechanisms for scenario I4: (a) OH; (b) HO_2.

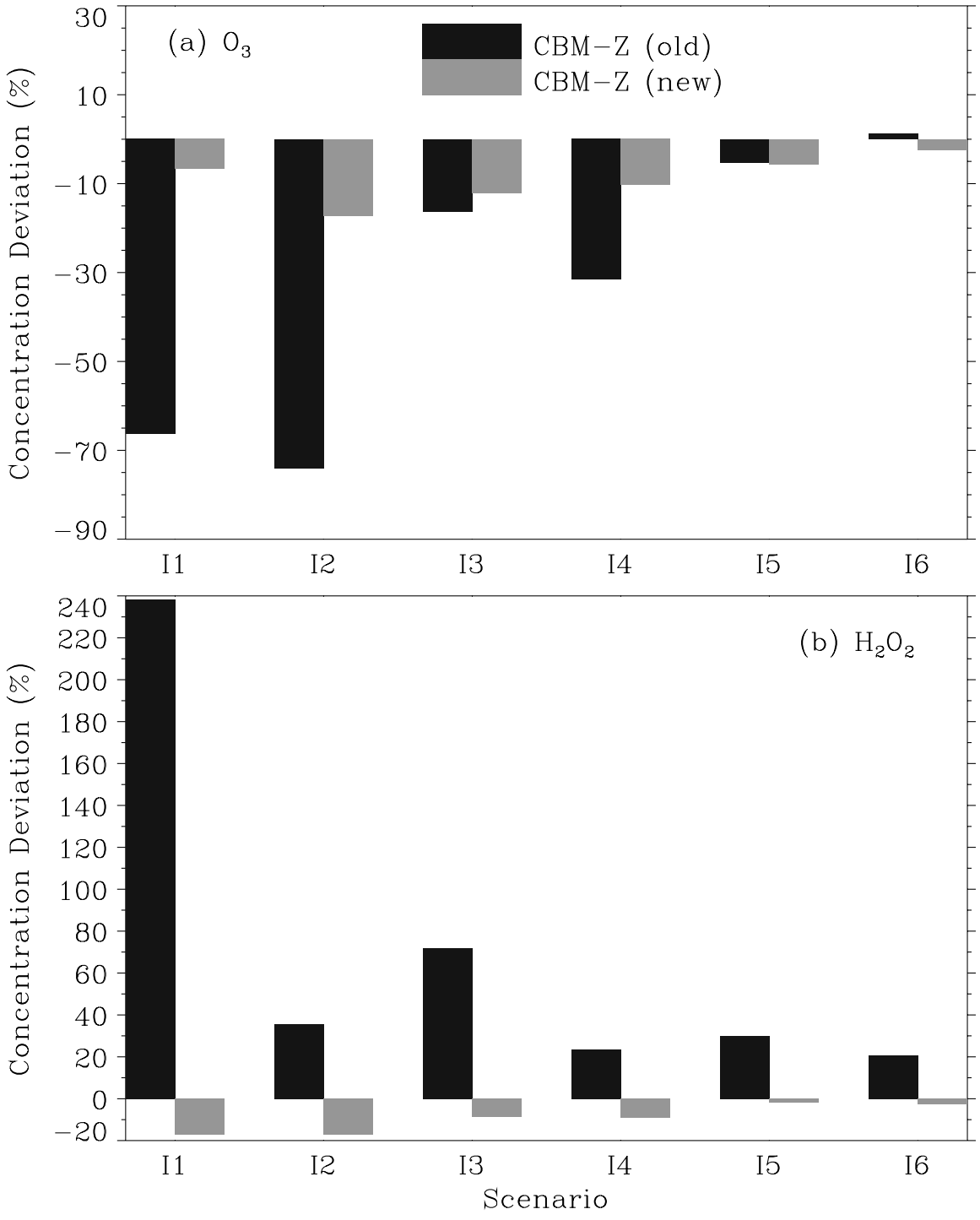

Figure 3.9: Percentage concentration deviations from the CBM-Z (old), and CBM-Z (new) with respect to RADM2 predictions after 3 model days: (a) O_3; (b) H_2O_2.

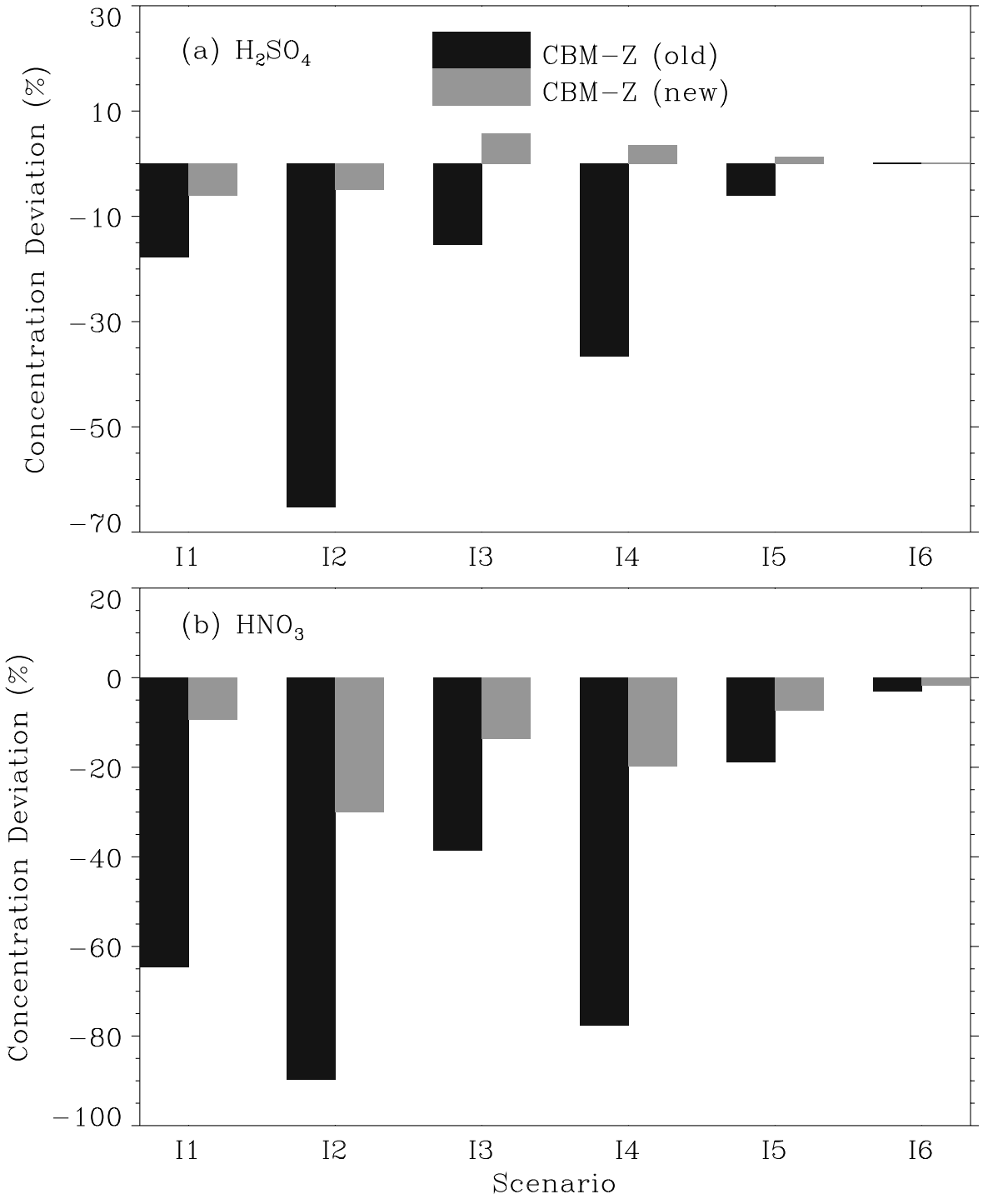

Figure 3.10: Percentage concentration deviations from the CBM-Z (old), and CBM-Z (new) with respect to RADM2 predictions after 3 model days: (a) H_2SO_4; (b) HNO_3.

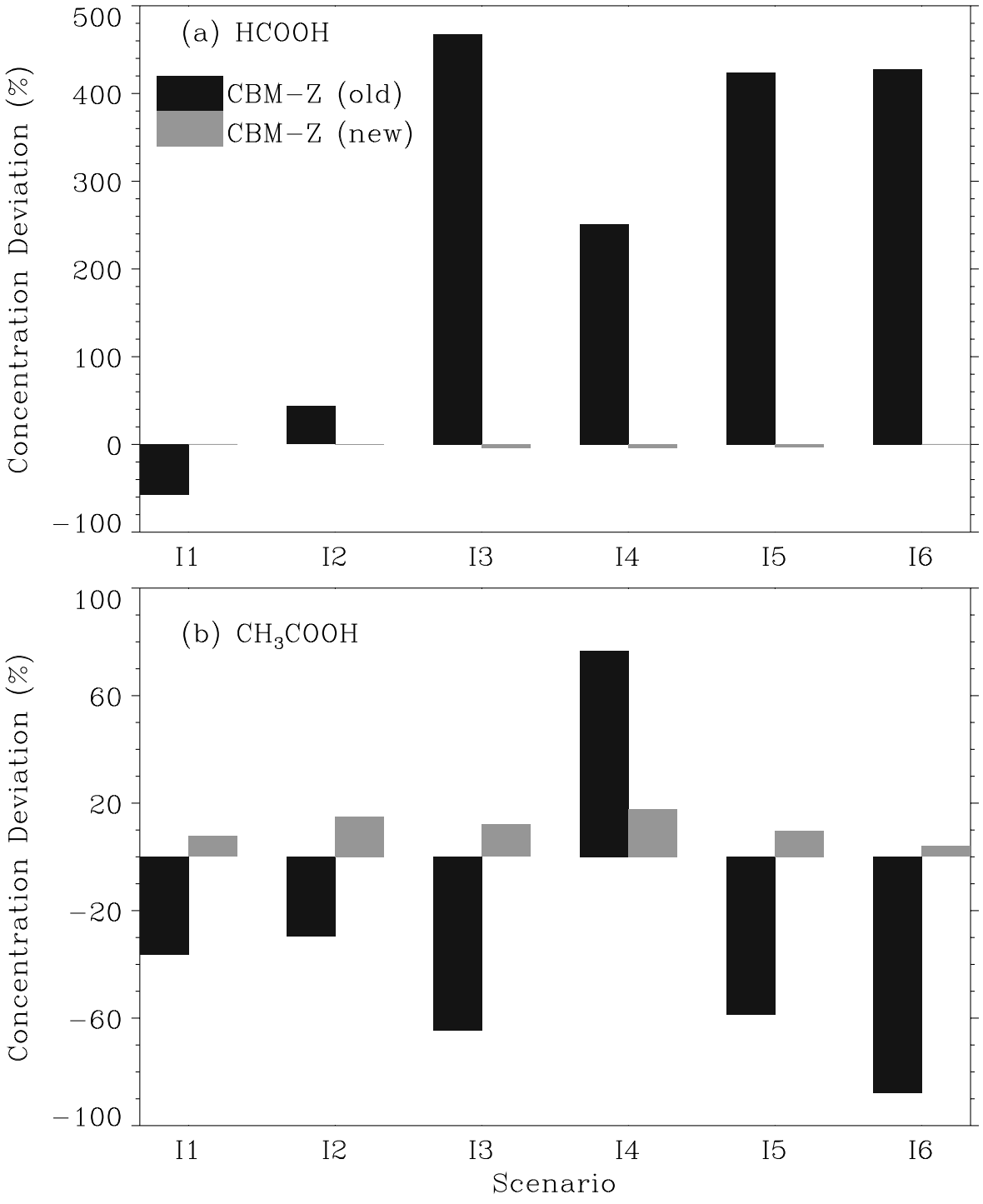

Figure 3.11: Percentage concentration deviations from the CBM-Z (old), and CBM-Z (new) with respect to RADM2 predictions after 3 model days: (a) HCOOH; (b) CH_3COOH.

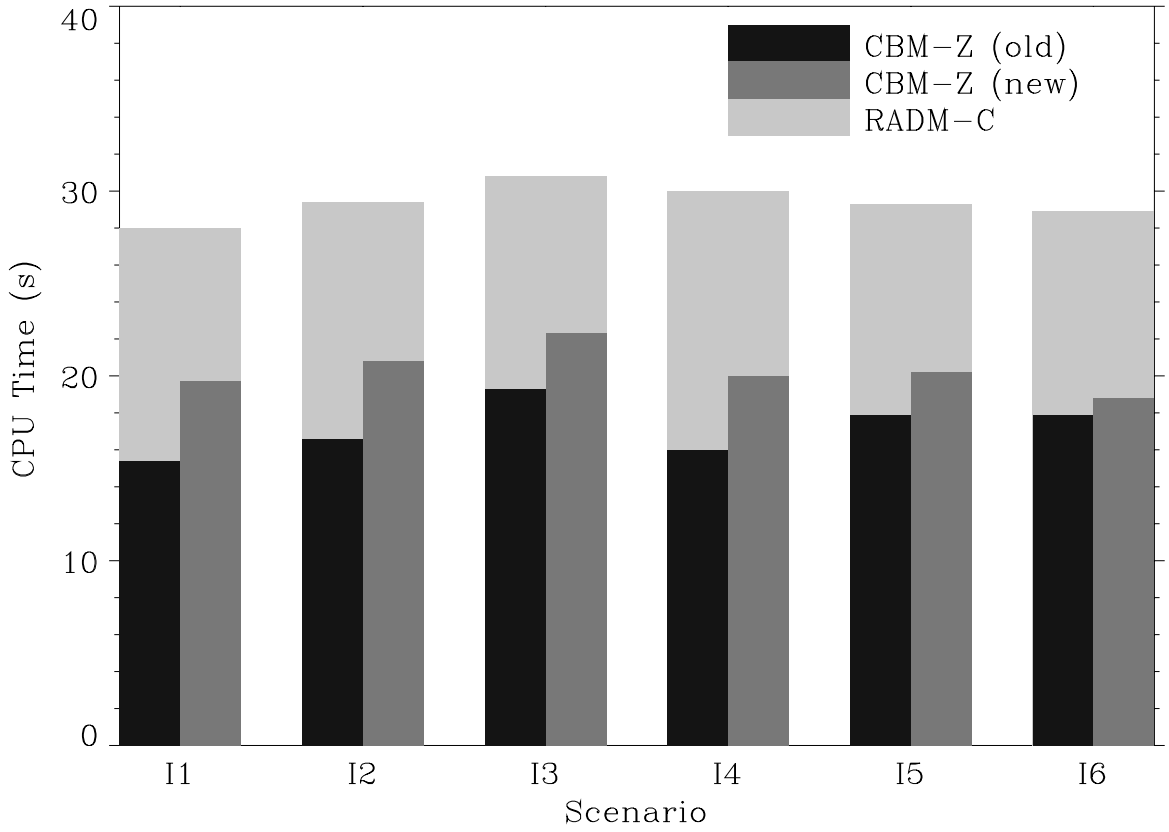

Figure 3.12: CPU time required by the RADM-C, CBM-Z (new), and CBM-Z (old) mechanisms to simulate 3 model days.

3.4 Concluding Remarks

Having compared the predictions of several species from the three mechanisms, it appears that the isoprene chemistry in the CBM-IV (CBM-Z (old)) may be considerably misrepresented, giving large deviations in O_3, H_2O_2, and NO_3 concentrations with respect to the RADM-C predictions. These errors propagate back to isoprene by affecting its depletion, and as a result, the deviations in the concentrations of most species including isoprene, O_3, H_2O_2, and NO_x gradually tend to grow. Negligible deviations in these species are observed only in the scenario with very low isoprene emissions. However, the formation of organic acids, especially HCOOH, appears to be in significant error for all scenarios. Formic acid is known to participate in aqueous-phase free-radical chemistry, and thus, large errors in its gas-phase predictions may be further amplified in the presence of clouds.

The proposed CBM-Z (new) isoprene mechanism is in excellent agreement with its equivalent mechanism RADM-C. The deviations in the concentrations of all important oxidants are marginal, and sometimes even negligible. Moreover, the CPU time requirements are also only marginally higher than for the original isoprene chemistry. Thus, the new CBM-Z isoprene mechanism is adopted for the present model. Additional work must be done to compare the proposed mechanism with the mechanism of Carter and Atkinson (1996).

Chapter 4

Monoterpene Photooxidation Chemistry: α-Pinene

As mentioned earlier, monoterpenes constitute the second largest class of continental biogenic hydrocarbons emitted into the atmosphere. Monoterpene concentrations in ambient forest air have been observed in the range of 0.1-20 ppb (Yokouchi *et al.*, 1983; Isidorov *et al.*, 1985; Riba *et al.*, 1987; Petersson, 1988). Due to their highly reactive nature, the atmospheric chemistry of monoterpenes is expected to play an important role in the global carbon cycle, as well as in the local and regional ground-level photochemical ozone formation. Additionally, monoterpenes are known to yield reaction products that may nucleate to form secondary organic aerosols under ambient conditions. Organic aerosols can scatter solar radiation and cause visibility degradation. Went (1960b) first attributed the "blue haze" over vegetated land masses to aerosols formed from these biogenic hydrocarbons. Furthermore, in forested regions influenced by anthropogenic emissions, product gases such as HNO_3 and H_2SO_4 can condense on these organic aerosols, making them highly hygroscopic. Depending on the relative humidity, these mixed aerosols can absorb considerable amounts of water, and also activate to form cloud droplets. Thus, our interest in monoterpene chemistry at the global-scale is two fold — its effect on the global oxidant cycle, and its contribution to the global aerosol and cloud populations. Figure 4.1 illustrates the global extent and magnitude of total monoterpene emissions during July (Guenther *et al.*, 1995).

A variety of monoterpenes are emitted into the atmosphere. Table 4.1 lists some which have been identified in foliar emissions. Individual tree species may emit more than ten different monoterpenes; however, usually not more than three are dominant. For example, α-pinene, β-pinene, and limonene comprise the majority of the total monoterpenes emitted by Scots pine needles, with α-pinene being more than 40% (Isidorov *et al.*, 1985) (Figure 4.2). Isidorov *et al.* (1985) also found α-pinene as the main component (40-65%) in the coniferous forests of the U.S.S.R. Several other field measurements around the world also indicate that α-pinene may be the most dominant of all monoterpenes emitted in forests, followed by β-pinene (Hov *et al.*, 1983; Roberts *et al.*, 1983; Roberts *et al.*, 1985; Yokouchi *et al.*, 1983; Riba *et al.*, 1987).

The current literature on the reactions and products of individual monoterpenes is still

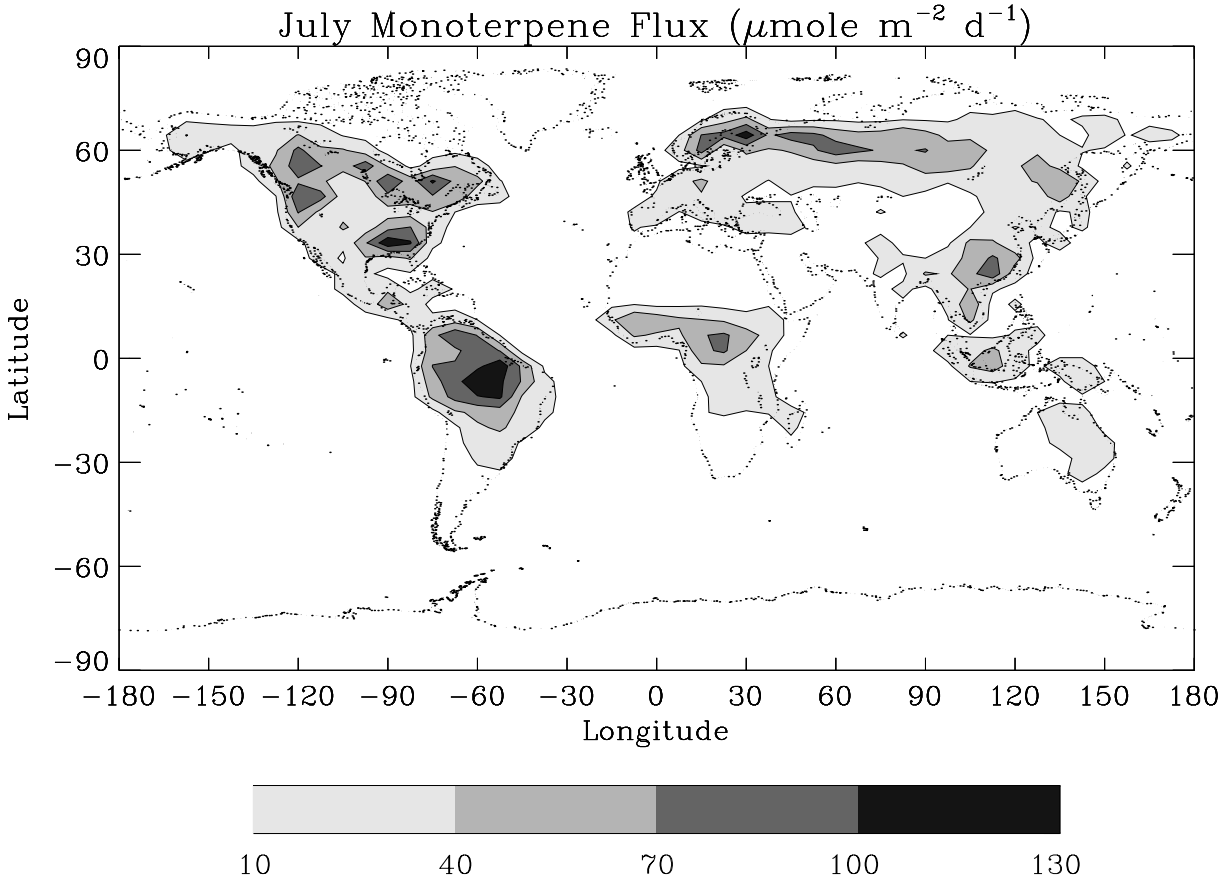

Figure 4.1: July Monoterpene emission flux based on the global inventory of Guenther *et al.* (1995).

Table 4.1: Monoterpenes Identified in Foliar Emissions[a].

Major	Frequent	Occasional
α-Pinene	α-Terpinene	α-Fenchene
β-Pinene	β-Terpinene	β-Fenchene
d-Limonene	γ-Terpinene	δ-Fenchene
β-Phellandrene	α-Thujene	ϵ-Fenchene
Camphene	Tricyclene	Bornylene
Myrcene	Terpinolene	Alloocimene
Δ^3-Carene	*p*-Cymene	Methyl Chavicol
1,8-Cineole	α-Phellandrene	*p*-Cymen-8-ol
Sabinene	trans-Ocimene	Linalool
	cis-Ocimene	Camphor
	2-Carene	2-Methyl-6-methylene-
		1,7-octadiene-3-one
		Pinocarvone
		Verbenone
		Fenchone
		Thujone

[a]Guenther *et al.*, 1994, and references therein.

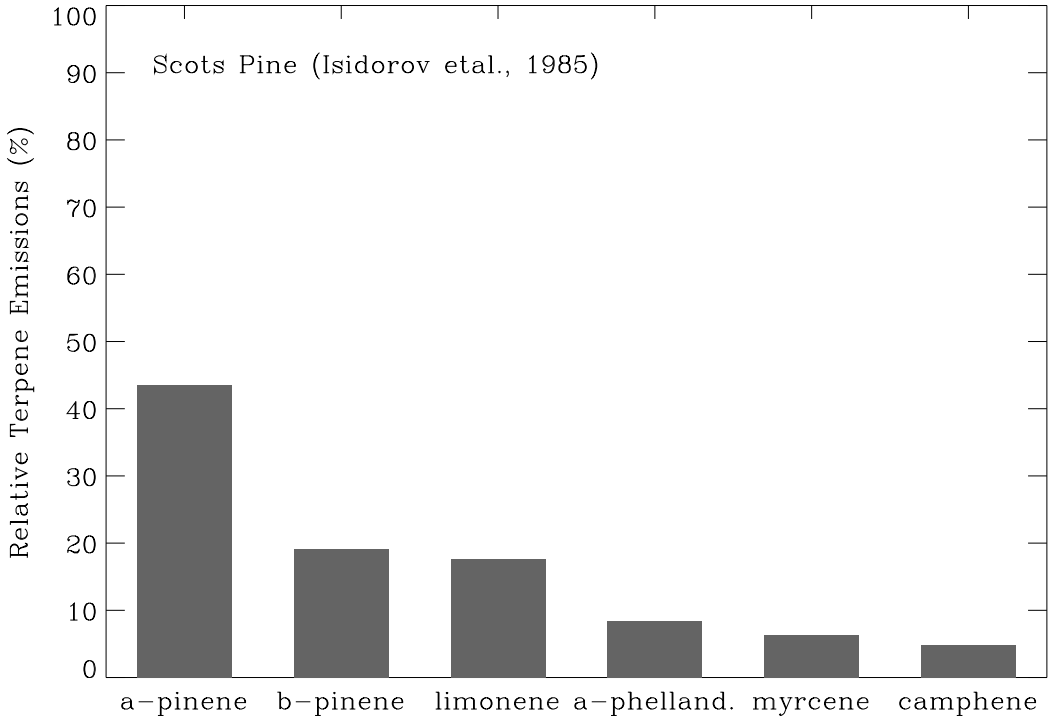

Figure 4.2: Relative terpene content in volatile emission from Scots pine (Isidorov *et al.*, 1985).

relatively sparse, except for α-pinene, and β-pinene. Many laboratories since the late 1970's have investigated ozone and aerosol formation from monoterpene photooxidation, with a greater emphasis on α-pinene and β-pinene (Westberg and Rasmussen, 1972; Arnts *et al.*, 1981; Kaiserman and Corse, 1981; Hull, 1981; Kamens *et al.*, 1981; Yokouchi and Ambe, 1985; Hooker *et al.*, 1985; Hatakeyama *et al.*, 1989, 1991; Pandis *et al.*, 1991; Zhang *et al.*, 1992; Odum *et al.*, 1996). Most studies focusing on aerosol formation reported widely different aerosol yields, probably because of different initial concentrations of reactants, and operating conditions. The precise chemical pathways leading to the formation of the condensable products, including the stoichiometry and rate constants, are still quite uncertain. As an alternative approach, Pandis *et al.* (1992) parameterized the aerosol yields of several organic compounds, including α-pinene and β-pinene, based on their earlier experimental work (Pandis *et al.*, 1991; Shaw *et al.*, 1991). This simple approach, though quite attractive, can neither simulate the effects of monoterpene chemistry on the oxidant cycle, nor can it predict aerosol yields under ambient conditions different than experimental conditions. A

mechanistic approach is, therefore, desirable.

Unfortunately, due to lack of necessary kinetic data, it is not possible to develop a mechanism that treats all the monoterpenes listed in Table 4.1. Even if it were possible, such a mechanism would be too cumbersome for practical applications. Fortunately, however, considerable data exist on α-pinene, and since it is the most dominant monoterpene emitted into the atmosphere, all monoterpenes could be modeled as α-pinene. This chapter deals with the development and evaluation of such a photooxidation mechanism.

4.1 Description of the Published Data Sets

Although the rate constants for the initial reactions of α-pinene are now well known, the present literature still lacks important kinetic information for the subsequent reactions involved in, or competeing with, aerosol formation. Lloyd *et al.* (1983) first attempted to simulate the photochemistry of α-pinene, primarily for ozone formation rather than for aerosol formation. Their mechanism, though quite speculative, yielded some useful insights into the problem. In this work, their mechanism is improved and extended to include the capability of predicting aerosol yields under different conditions. The necessary kinetic constants for the intermediate reactions are estimated by the product modeling approach using published experimental data. The data sets were identified for their suitability for this work based on the experimental conditions, the species analyzed, and the type of the data published. The selected experiments can be arranged in an increasing order of complexity as described below, and also are summarized in Table 4.2. The experimental conditions and initial concentrations for each data set are compiled in Table 4.3.

1. Reaction with OH in the absence of NO_x.
   These experiments were performed by Hatakeyama *et al.* (1991) in an indoor chamber to investigate the reaction products. The OH radicals were generated by photolyzing gaseous H_2O_2 with UV light using a solar simulator.

   - The first data set, denoted by H1991a (see Table 4.2), consists of the initial pinonaldehyde yields as a function of the initial [α-pinene]/[H_2O_2] ratio, for the same temperature, relative humidity, and light intensity. These experiments were performed in a 6 m^3 chamber, and the solar simulator and the end windows were modified to utilize shorter wavelength light (above 220 nm) for effective photolysis

of H_2O_2. Ozone was formed at a rate of about 0.5 ppm h^{-1} due to O_2 photolysis. All runs were stopped within 15 minutes to mininize the secondary reactions of products (Hatakeyama, 1997). The plots of pinonaldehyde concentration (corrected for decay due to OH oxidation) against the amount of α-pinene converted were linear, and the yields were estimated from the slopes of the straight lines.

- The data set (H1991b) consists of time profiles of α-pinene and aerosol carbon for a single experiment carried out in a 4 m^3 chamber. The end windows were made of quartz to allow transmission of UV radiation above 260 nm. Ozone was formed at a rate of about 0.27 ppm h^{-1}. The wall decay rates of O_3 and H_2O_2 were about 11% h^{-1}, while that of particulate carbon mass was about 20% h^{-1} under irradiation.

2. Reaction with O_3 in the absence of NO_x.

   This reaction is expected to be more complicated because of the uncertainty of the fate of the resulting Criegee intermediates. A fraction of these highly energetic biradicals is thought to decompose to yield OH radicals, which in turn, will react with α-pinene itself. Therefore, this reaction is considered after the reaction of α-pinene with OH alone.

   - The data set (H1989a) of Hatakeyama *et al.* (1989) consists of the time profiles of various gaseous species for an experiment carried out in a 6 m^3 chamber in the dark. The gases were analyzed by FTIR spectroscopy. The wall decay rates of O_3 and H_2O_2 were about 11% h^{-1}.
   - The data set (H1989b) consists of similar experiments with inital concentrations of α-pinene and O_3 ranging from 0.96-1.0 ppm and 0.70-1.24 ppm, respectively; however, only the final yields of the gaseous products were published.
   - In the third set of experiments (H1989c) by the same authors, the total aerosol yields were determined in the reaction of O_3 with α-pinene in a 4 m^3 chamber. Several runs were carried out for initial α-pinene concentrations ranging from 0.01 to 0.12 ppm, and a constant O_3 concentration of 0.8 ppm. The aerosol formation was monitored by a condensation nucleus counter (CNC) measuring the number concentration, and an electrical aerosol size analyzer giving the total volume concentration. The wall decay rate of particulate carbon mass was about

10% h^{-1}.

- The data sets (A1992a) of Atkinson *et al.* (1992) and of Hakola *et al.* (1994) consist of the direct OH radical yields for the α-pinene-O_3 reaction under two different relative humidities. The experiments were conducted in a 6.4 m^3 all-Teflon chamber equipped with two parallel banks of black lights for irradiation. The OH radical yields were determined indirectly by scavenging them with excess cyclohexane, and measuring the amounts of cyclohexanone and cyclohexanol formed as a result. Since about 95% of the OH was estimated to be scavenged, the pinonaldehyde yields measured also represent the direct yields for the α-pinene-O_3 reaction.
- The data set (S1991a) of Simonaitis *et al.* (1991) gives the yield of H_2O_2 in the α-pinene-O_3 reaction. The experiments were performed in a 31 m^3 reaction chamber with walls made of FEP Teflon. The yields were measured under two different RH levels. The initial O_3 concentration ranged from 0.06-0.4 ppm, and the initial α-pinene concentration ranged from 0.04-0.9 ppm. A fluorimetric technique was used to monitor H_2O_2 and total organic peroxides.

3. Reaction with OH and O_3 in the presence of NO_x.

   Photooxidation of α-pinene in the presence NO_x generally produces both OH and O_3. This system is expectedly more complex than the two discussed above due to additional reactions involving α-pinene oxidation products and NO_x. Also, NO_3 is known to react with α-pinene.

   - The data set (H1991c) consists of one time profile and one yield profile of the gaseous species for the chamber experiments of Hatakeyama *et al.* (1991). The experimental set-up and measurement techniques were similar to that described for H1991a,b.
   - The data set (H1991d) gives a yield profile of aerosol formation in the presence of NO_x. The other experimental conditions were identical to those in H1991b.

Table 4.2: Selected Experimental Data Sets of α-Pinene Oxidation.

Data Set[a]	Species Measured	Published Data
1. Reaction with OH in the absence of NO_x		
H1991a (7)	Pinonaldehyde	Initial yields
H1991b (1)	α-pinene, and aerosol carbon	Time profiles
2. Reaction with O_3 in the absence of NO_x		
H1989a (1)	α-pinene, O_3, formyls, HCHO, CO, CO_2, and HCOOH	Time profiles
H1989b (4)	O_3, CO, CO_2, HCHO, HCOOH, and formyls	Final yields
H1989c (8)	Aerosol carbon	Final yields
A1992a (2)	OH, and pinonaldehyde	Total yields
S1991a (2)	H_2O_2	Total yields
3. Reaction with OH, and O_3 in the presence of NO_x		
H1991c (2)	α-pinene, NO, NO_2, and pinonaldehyde	Time and Yield profiles
H1991d (1)	Aerosol carbon	Yield profile

[a] A data set is denoted by the first letter of the author's last name, followed by the publication year, and an alphabet to distinguish the set. The following number in parantheses is the number of experiments or final results in the set.
H1989, Hatakeyama *et al.* (1989); H1991, Hatakeyama *et al.* (1991);
A1992, Atkinson *et al.* (1992) and Hakola *et al.* (1994);
S1991, Simonaitis *et al.* (1991).

Table 4.3: Experimental Conditions and Inital Concentrations for the Selected α-Pinene Oxidation Data Sets.

Data Set	j(NO_2) (min^{-1})	T (K)	P (atm)	RH (%)	$[APIN]_0$	$[H_2O_2]_0$	$[O_3]_0$ (ppm)	$[NO]_0$	$[NO_2]_0$
H1991a1	0.069	303	0.97	dry[a]	1.07	101.32	-	-	-
H1991a2	0.069	303	0.97	dry	0.87	27.76	-	-	-
H1991a3	0.069	303	0.97	dry	1.66	19.87	-	-	-
H1991a4	0.069	303	0.97	dry	0.88	10.00	-	-	-
H1991a5	0.069	303	0.97	dry	1.95	13.03	-	-	-
H1991a6	0.069	303	0.97	dry	2.99	13.42	-	-	-
H1991a7	0.069	303	0.97	dry	4.93	6.32	-	-	-
H1991b	0.17	303	1.1	85	1.31	15.0	-	-	-
H1989a	-	303	1.0	dry	1.00	-	1.77	-	-
H1989b1	-	303	1.0	dry	0.98	-	1.24	-	-
H1989b2	-	303	1.0	dry	0.96	-	1.19	-	-
H1989b3	-	303	1.0	dry	0.96	-	1.18	-	-
H1989b4	-	303	1.0	dry	1.00	-	0.70	-	-
H1989c (8)	-	303	1.08	50	.01-.12	-	0.80	-	-
A1992a1[b]	-	296	0.97	∼4	∼1	-	∼0.8	-	-
A1992a2[b]	-	296	0.97	∼40	∼1	-	∼0.8	-	-
S1991a1[c]	-	299	1.0	dry	.04-.9	-	.06-.4	-	-
S1991a2	-	299	1.0	24	.04-.9	-	.06-.4	-	-
H1991c1	0.069	303	0.97	dry	0.95	30.0	-	2.27	-
H1991c2	0.069	303	0.97	dry	0.775	18.0	-	0.825	-
H1991d	0.17	303	1.10	85	1.31	15.0	-	7.50	-

[a] Dry runs were made with purified air, and may have traces of water vapor.

[b] A1992 experiments were made in the presence of excess cyclohexane (∼1000 ppm), and also at lower concentrations (∼1 ppm). Total ozone concentration of 0.8 ppm was made up by four equal additions to the chamber during the experiment.

[c] Pressure is assumed 1 atm; RH $< 1 \times 10^3$ ppm, $[\text{alkene}]_0/[O_3]_0 \sim (0.17 - 6.5)$.

4.2 Modeling and Parameter Estimation for α-Pinene

In the last two decades, several researchers have proposed schemes for α-pinene reaction pathways and aerosol formation. Figure 4.3 shows the proposed reaction pathways following OH radical attack on α-pinene. This mechanism is based on the two schemes given by Hatakeyama *et al.* (1989, 1991). Figure 4.4 illustrates the pathways after reaction with O_3, based on the mechanism hypothesized by Lloyd *et al.* (1983) and Hooker *et al.* (1985). However, as mentioned earlier, the intermediate reactions are poorly understood, and their rate constants have not been explicitly measured.

In the following sub-sections, these mechanisms are systematically exploited to estimate the unknown rate constants and elementary product yields. Once a parameter is determined, it is kept constant for the subsequent simulations unless noted otherwise. As explained in the previous section, it would be intuitive to begin with the α-pinene-OH reaction in the absence of NO_x, and follow with more complex systems.

4.2.1 Reaction with OH in the Absence of NO_x

The following reactions are based on the mechanism depicted in Figure 4.3. Reaction (R1) is actually a two-step process of addition of OH to α-pinene (APIN), followed by addition of O_2 to give a β-hydroxyalkylperoxy radical, denoted by PO_2. The latter addition step, being much faster, is lumped with the former while writing the overall reaction. Reaction (R2) is a multi-step intramolecular reaction forming pinonaldehyde (PALD) proposed by Hatakeyama *et al.* (1989, 1991). Reaction of PO_2 with HO_2 forms a non-volatile organic hydroperoxide (POOH) which is thought to nucleate to give secondary organic aerosol (SOA). Here, all POOH produced is assumed to instantly form SOA, and these two species will be used synonymously henceforth. The self-reaction of PO_2 (R4) forms 'y' alkoxy radicals, and other gaseous products. Large tertiary alkoxy radicals are expected to rapidly decompose (R5) and form carbonyl compounds in the presence of O_2; in the present case, PO should form PALD.

Pinonaldehyde can further oxidize (R6) to PCO_3, an acetylperoxy like radical; or photolyze (R7) to yield another alkylperoxy type radical, QO_2, with one carbon atom less than α-pinene. It is also assumed to photolyze by a Norrish Type II process (R8) (Calvert and Pitts, 1966; Lloyd *et al.*, 1983) to give an acetaldehyde molecule, and a ringed molecule with

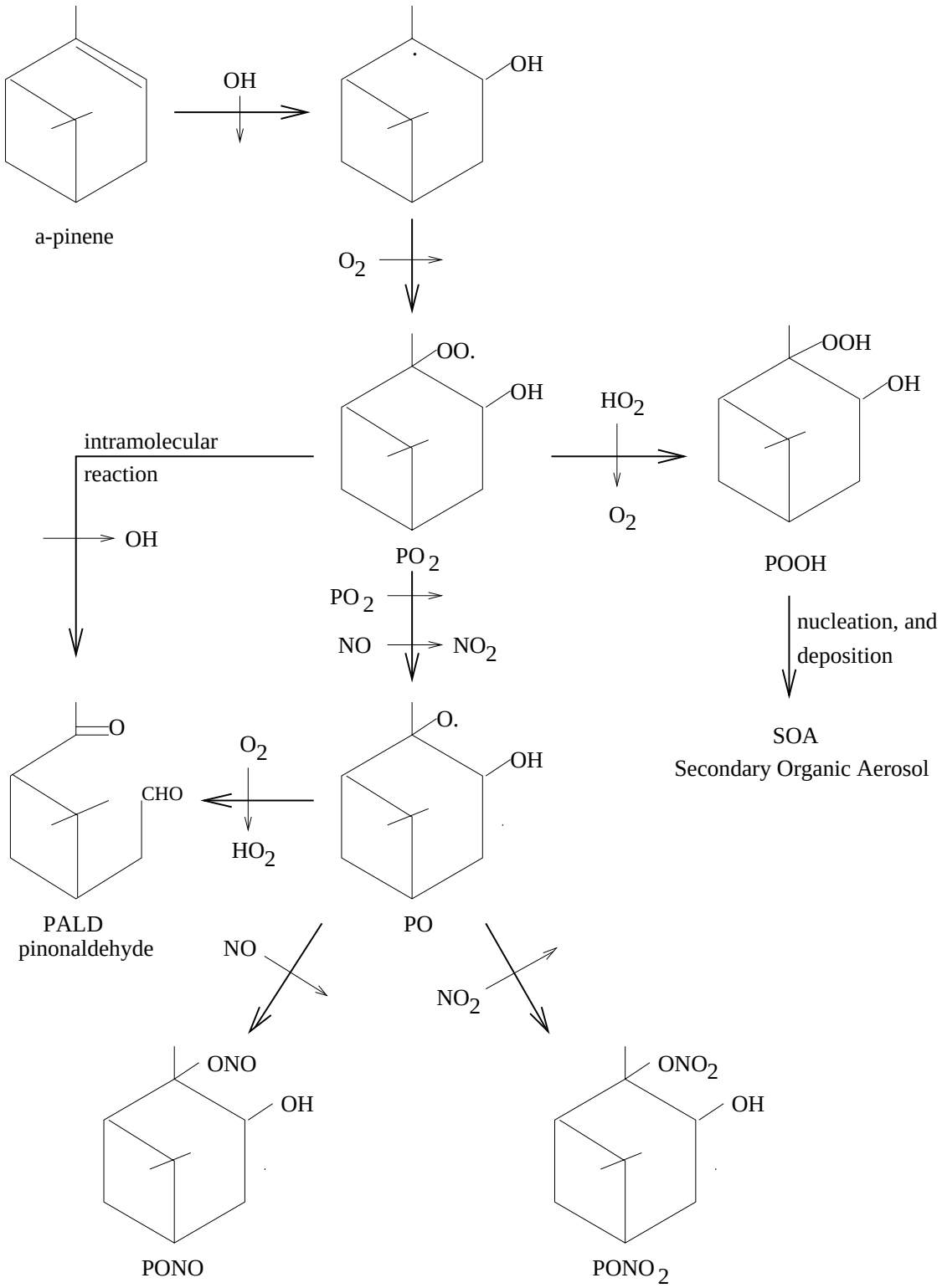

Figure 4.3: Proposed α-pinene + OH reaction mechanism.

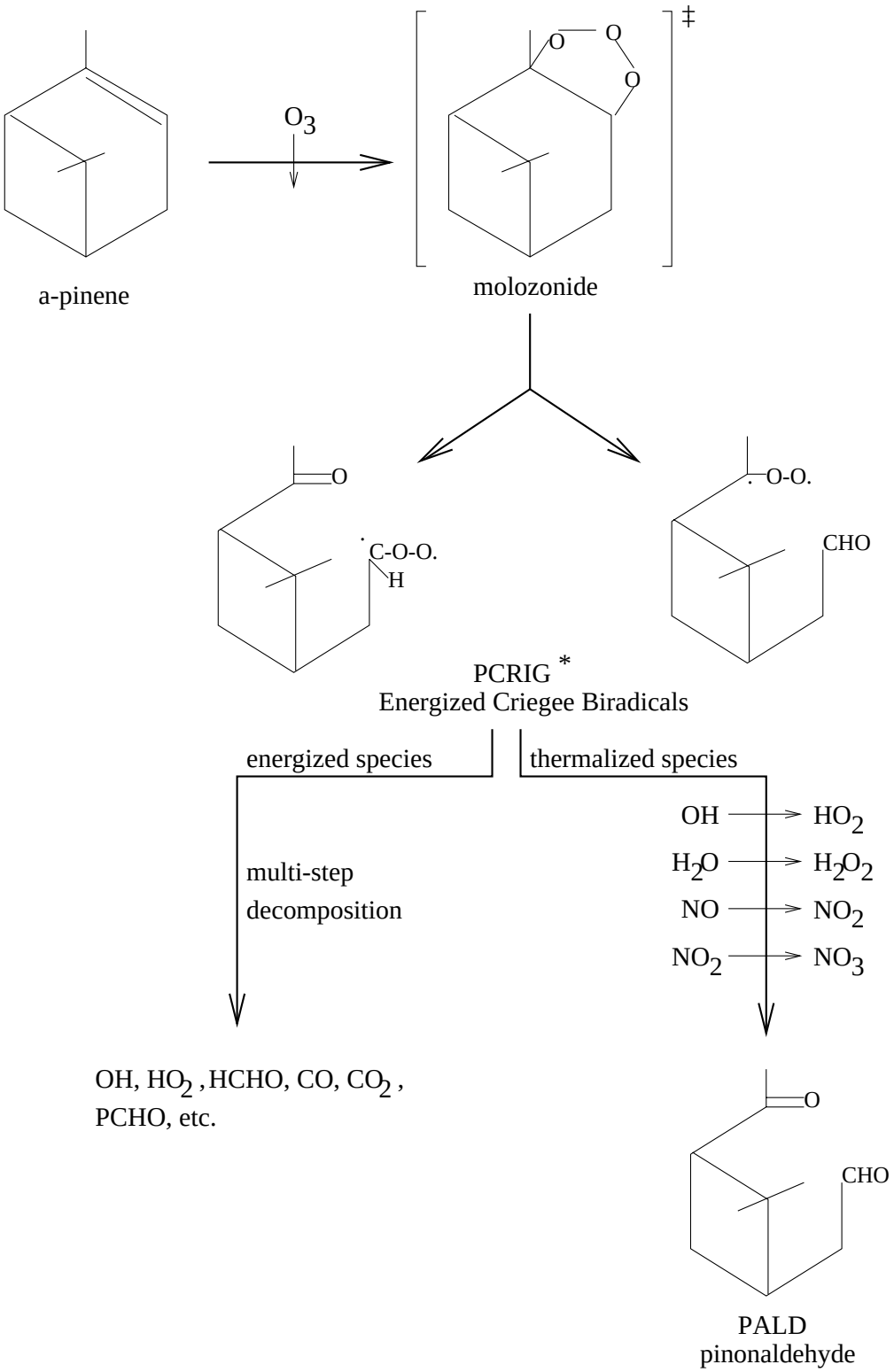

Figure 4.4: Proposed α-pinene ozonolysis mechanism.

a keto and olefinic groups; these products are represented in terms of the surrogate species of the carbon bond mechanism. The rate constants below are expressed in cm^3-molecule-s units.

(R1)	APIN + OH	$\xrightarrow{O_2}$	PO_2	k1 = $8.5 \times 10^{-12} \exp(550/T)$, measured, Atkinson (1994)
(R2)	PO_2	$\longrightarrow$	PALD + OH	k2, unknown
(R3)	$PO_2 + HO_2$	$\longrightarrow$	POOH or SOA	k3 = $7.7 \times 10^{-14} \exp(1300/T)$, recommended, DeMore *et al.* (1988)
(R4)	$PO_2 + PO_2$	$\longrightarrow$	yPO + (1-y)OGP	k4 and y, unknown
(R5)	PO	$\xrightarrow{O_2}$	PALD + HO_2	k5 $\sim 1.0 \times 10^3$, rapid, Finlayson-Pitts and Pitts (1986)
(R6)	PALD + OH	$\longrightarrow$	PCO_3	k6 = $1.1 \times 10^{-11} \exp(250/T)$, Hakola *et al.* (1994)
(R7)	PALD + $h\nu$	$\longrightarrow$	$QO_2 + HO_2$ + CO	10 j(ALD2), Lloyd *et al.* (1983)
(R8)	PALD + $h\nu$	$\longrightarrow$	ALD2 + OLE + 3PAR + AONE	j(ALD2), Lloyd *et al.* (1983)

In the above reactions, k2, k4, and y are the only unknowns, while the other rate constants have been either measured or are assumed based on some similar reactions whose rate constants are known. For example, (R3) is assumed to proceed at a rate similar to a normal alkylperoxy-HO_2 reaction. The rate constant for PALD oxidation with OH was calculated by Hakola *et al.* (1994) using a structure-activity relationship method (Atkinson, 1987), revised for polycyclic systems (Atkinson and Aschmann, 1992). The decomposition rate constant of PO is highly uncertain, but is expected to be on the order of 1000 s^{-1}. In the presence of NO_x, the decomposition step will compete with the reactions with NO and NO_2, and are treated in section 4.2.3; however, any large value (e.g., > 10 s^{-1}) would essentially give the same results in the absence of NO_x.

The normal PALD photolysis is assumed to be ten times faster than that of acetaldehyde (ALD2), while the Norrish Type II reaction is assumed to have a photolysis rate constant equal to j(ALD2). Hatakeyama *et al.* (1991) represented the chamber irradiance in terms of the photolytic rate constant of NO_2 (see Table 4.3); however, other photolytic rate constants must be calculated using the chamber radiation flux spectrum (J_c), and the species absorption cross section (CS) and quantum yield (QY) spectra. Figure 4.5 shows the radiation flux spectrum corresponding to j(NO_2) = 0.069 min^{-1} (Hatakeyama, 1997), and the product spectra of CS and QY for the relevant species (Finlayson-Pitts and Pitts, 1986).

Table 4.4: Estimated Photolytic Rate Constants (min^{-1}) for H1991 Data Sets.

	Photolytic Rate constants (min^{-1})	
	λ(220 - 400 nm)	λ(260 - 400 nm)
j(NO_2)	0.069	0.17
j(H_2O_2)	1.92×10^{-3}	1.26×10^{-3}
j(ALD2)	8.08×10^{-4}	2.04×10^{-3}
j(HCHOa)[1]	8.56×10^{-4}	2.16×10^{-3}
j(HCHOb)[2]	6.48×10^{-4}	1.62×10^{-3}
j(O_3a)[3]	2.45×10^{-2}	4.80×10^{-2}
j(O_3b)[4]	2.14×10^{-1}	4.20×10^{-1}

[1] HCHO + $h\nu \longrightarrow 2HO_2$ + CO
[2] HCHO + $h\nu \longrightarrow$ CO
[3] $O_3 + h\nu \longrightarrow O(^1D)$
[4] $O_3 + h\nu \longrightarrow O(^3P)$

The photolytic rate constants are evaluated by the formula

$$\mathrm{j} = \sum_{\lambda_1}^{\lambda_2} \mathrm{CS}(\lambda) \times \mathrm{QY}(\lambda) \times \mathrm{J_c}(\lambda), \tag{4.1}$$

where J_c, CS, and QY are averages over a chosen interval of wavelength λ, say 10 nm. The summation is over the range $\lambda_1 = 220$ or 260 nm to $\lambda_2 = 400$ nm. The estimated in-chamber photolytic rate constants for other species corresponding to the two values of j(NO_2) used in the experiments are listed in Table 4.4.

Assuming (R1) through (R8) are the most dominant reaction pathways in the absence of O_3 and NO_x, then augmenting them with the CBM-Z developed so far should yield a mechanism capable of simulating the NO_x-free experiments H1991a and H1991b.

The yields of pinonaldehyde in the data set H1991a can be used for estimating the unknown rate constants k2 and k4, and the yield y appearing in Reaction (R4). The kinetics of the self-reaction (R4) have been studied for some simple alkylperoxy radicals, and the rate constants are in the range $\sim(10^{-13}$-$10^{-17})$ cm^3 $molecule^{-1}$ s^{-1}. The rate constant is generally found to decrease as the radical goes from primary to secondary to tertiary, probably due to steric effects. Recently, Kirchner and Stockwell (1996) developed a formula for peroxy radical self-reactions based on: the number of carbon atoms (N, N$\leq$7) in the alkyl peroxy radical; presence of additional oxygen atoms in the electron withdrawing alkyl groups (A = 1 if additional O atoms are present, A = 0 if absent); and the number (α) of alkyl or alkoxy

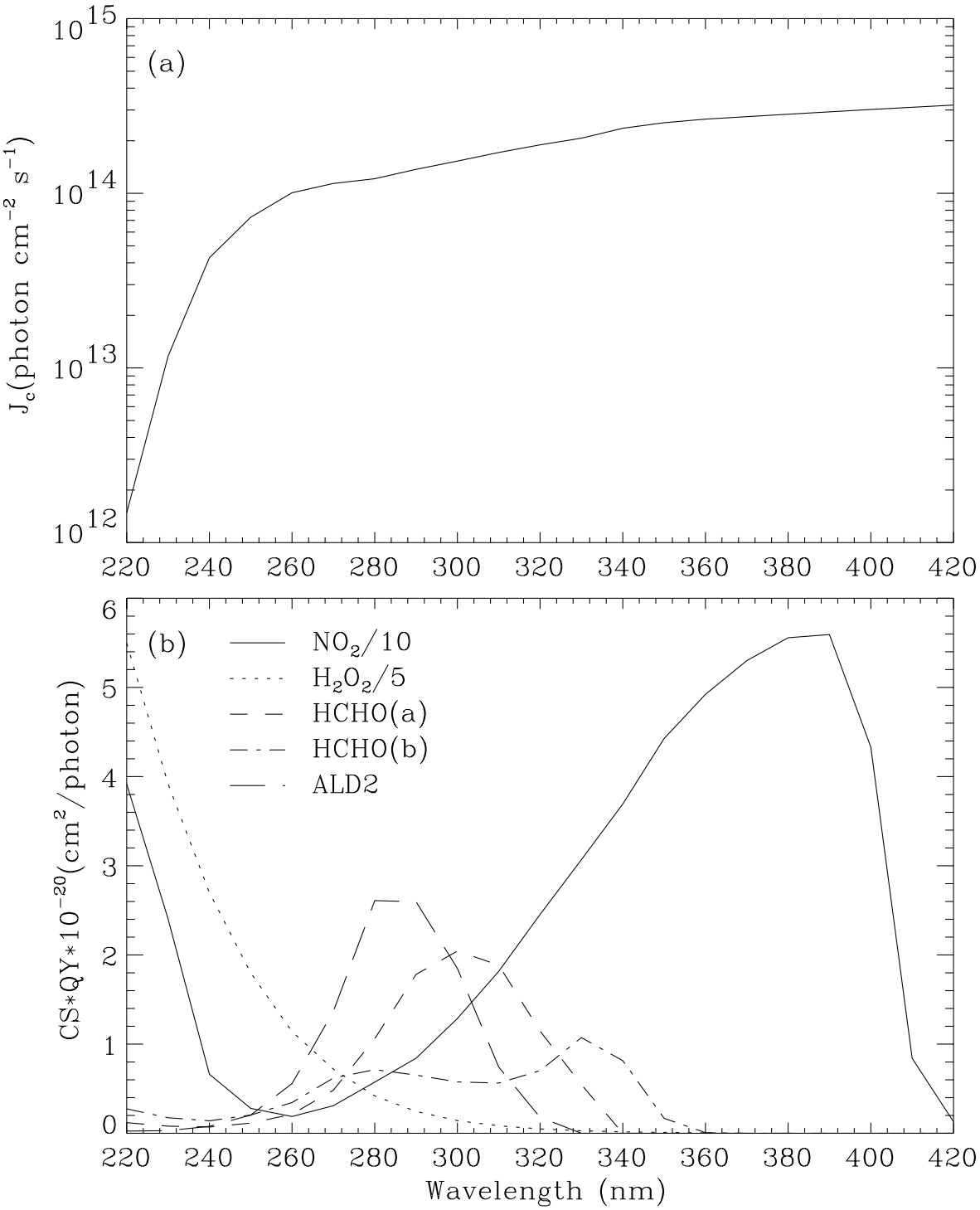

Figure 4.5: (a) Chamber radiation flux for H1991 data sets (Hatakeyama, 1997), (b) Product of the absorption cross-section and photolysis quantum yield spectra for relevant species.

groups connected to the C-O-O group.

$$k \approx 2 \times 10^{-14} \exp\left(3.8A - 5\alpha + \frac{3N}{1 + 0.02N^2}\right) \quad \text{cm}^3 \text{ molecule}^{-1} \text{ s}^{-1} \tag{4.2}$$

Since PO_2 is a tertiary alkylperoxy radical containing an additional oxygen atom in the alkyl group connected to the C-O-O group, $\alpha = 3$ and A = 1. However, even though it has 10 carbon atoms, N = 7 as per the recommendation for the formula. These parameter values give a rate constant of k4 = 1.1×10^{-14} cm^3 molecule^{-1} s^{-1}, which is about three orders of magnitude larger than that for a simple tertiary alkyl peroxy radical such as $(CH_3)_3CO_2$. To confirm the calculated order of magnitude of k4, a series of simulations was made by varying it over the range $\sim (10^{-13} - 10^{-17})$ cm^3 molecule^{-1} s^{-1}, with k2 = 0.0 and y = 2. Figure 4.6 shows the corrected yields of PALD (i.e., without decay due to oxidation or photolysis) plotted against α-pinene conversion.

Clearly, during the first 15 minutes, PALD yield, that is the slope of the curve, changes with conversion for the values of k4 below 10^{-14} cm^3 molecule^{-1} s^{-1}, unlike the observed yield of 17.1% which was found to remain constant throughout the experiment (Hatakeyama, 1997). It, therefore, appears that for the plot to be linear, k4 must be lie between 10^{-14} and 10^{-13} cm^3 molecule^{-1} s^{-1} . This is completely consistent with the value predicted by (4.2), though the value of y must be lower than 2 to reproduce the observed PALD yield of 17.1%.

At this point, it would be imperative to examine the effect of k2 on PALD yield. Four simulations were performed by assuming y = 2.0, and k4 = 1×10^{-17} cm^3 molecule^{-1} s^{-1}, which is the lower limit, and varying k2 over the range $\sim$(0.0005-0.005) s^{-1}. The plots of corrected PALD concentrations against α-pinene conversion are shown in Figure 4.7. Interestingly, all the plots are non-linear even though the simulated yields are in the vicinity of the observed value. This indicates that the proposed intramolecular mechanism is probably not responsible for the observed PALD formation; Reaction (R2) is, thus, eliminated.

Several simulations were performed to estimate the values of k4 and y using all seven H1991a data sets. Though no single combination could exactly reproduce all the observed PALD yields, the values k4 = 4×10^{-14} cm^3 molecule^{-1} s^{-1} , and y = 1.1 gave a reasonably good fit (Figure 4.8). The estimated values have an uncertainty factor of about 1.5. Inability to reproduce all the observations accurately may be attributed to some unaccounted reaction(s), or to possible error in corrected experimental PALD concentrations. Hatakeyama

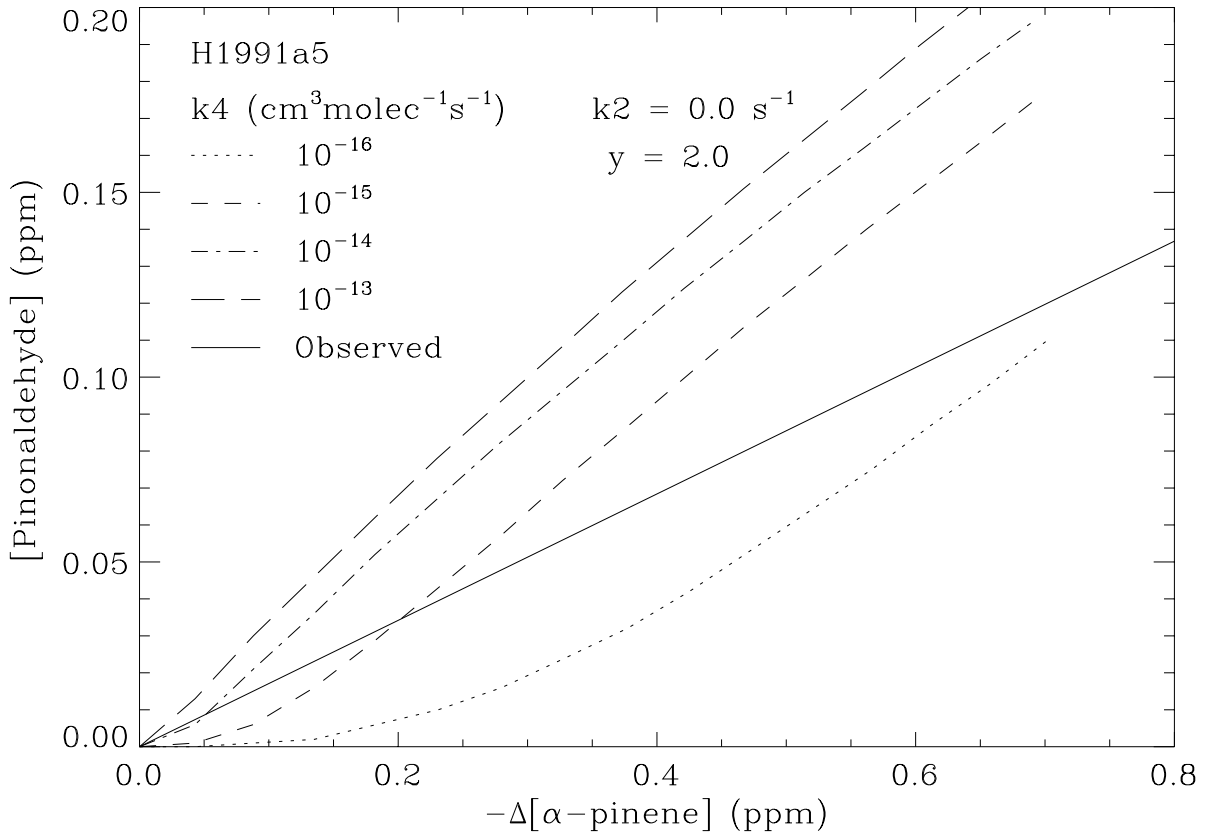

Figure 4.6: Plots of pinonaldehyde concentration against α-pinene conversion with k4 as a parameter for the experimental conditions of H1991a5.

et al. (1991) used k6 = 1.6×10^{-12} cm^3 molecule^{-1} s^{-1} in correcting the observed concentrations, which is about a factor of 1.7 lower than the value recommended by Hakola *et al.* (1994). Also, they did not account for PALD decay due to photolysis. Unfortunately, the raw experimental data are presently not available for direct comparison with the simulated outputs. Nevertheless, the simulation results are quite good.

Having estimated the necessary parameters, we now proceed to reproduce the data set H1991b. Figure 4.9 shows the simulated profiles of α-pinene decay, and O_3 and aerosol carbon evolutions against the experimental observations. The overall agreement is excellent for α-pinene and O_3 and quite adequate for aerosol carbon, and within experimental errors. The maximum concentration of ozone formed due to O_2 photolysis is below 0.045 ppm, and the loss of α-pinene due to reaction with O_3 is estimated to be $\sim$7%. The lower aerosol carbon concentrations observed may be due to a larger wall-loss rate than estimated, and or

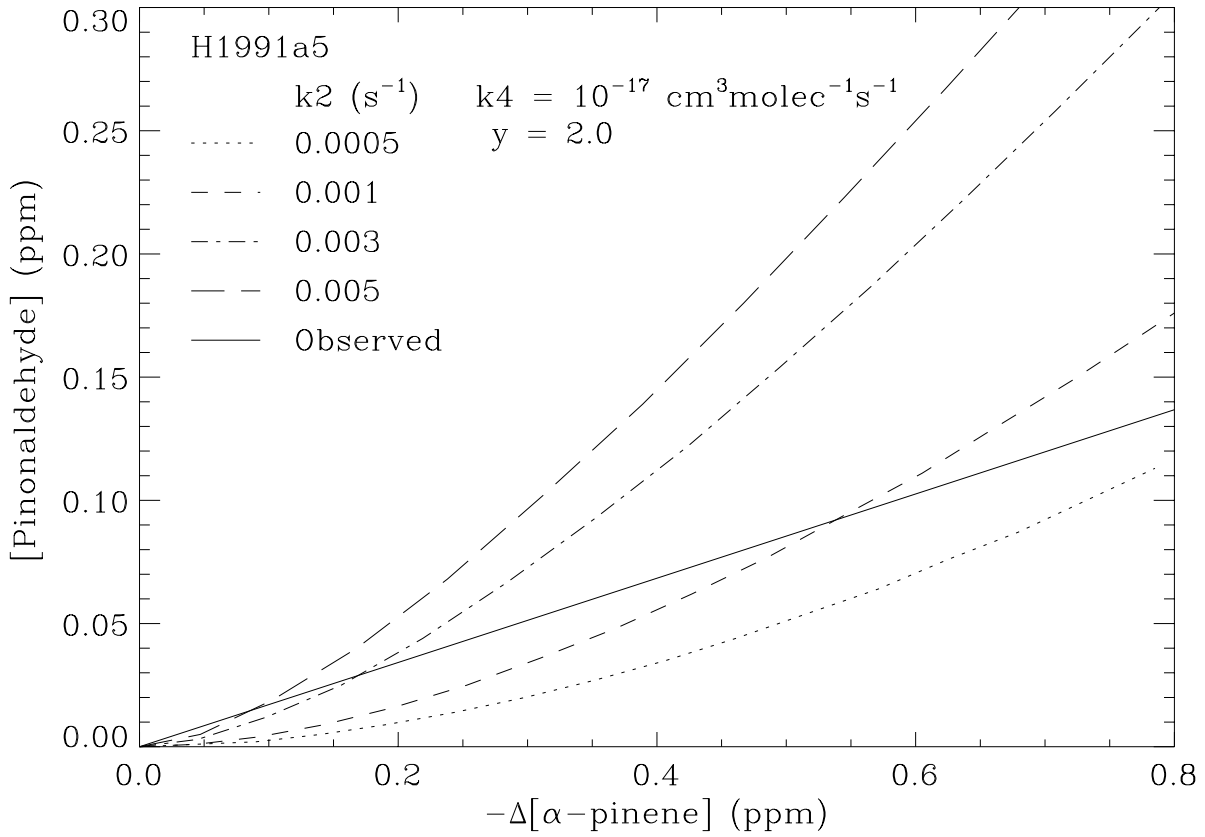

Figure 4.7: Plots of pinonaldehyde concentration against α-pinene conversion with k2 as a parameter for the experimental conditions of H1991a5.

experimental errors associated with the aerosol measurements.

4.2.2 Reaction with Ozone in the Absence of NO_x

As explained earlier, the next logical step is to consider the reaction of α-pinene with O_3. The following reactions are added to the set presented in the previous subsection (also see Figure 4.4). The rate constants are expressed in cm^3-molecule-s units.

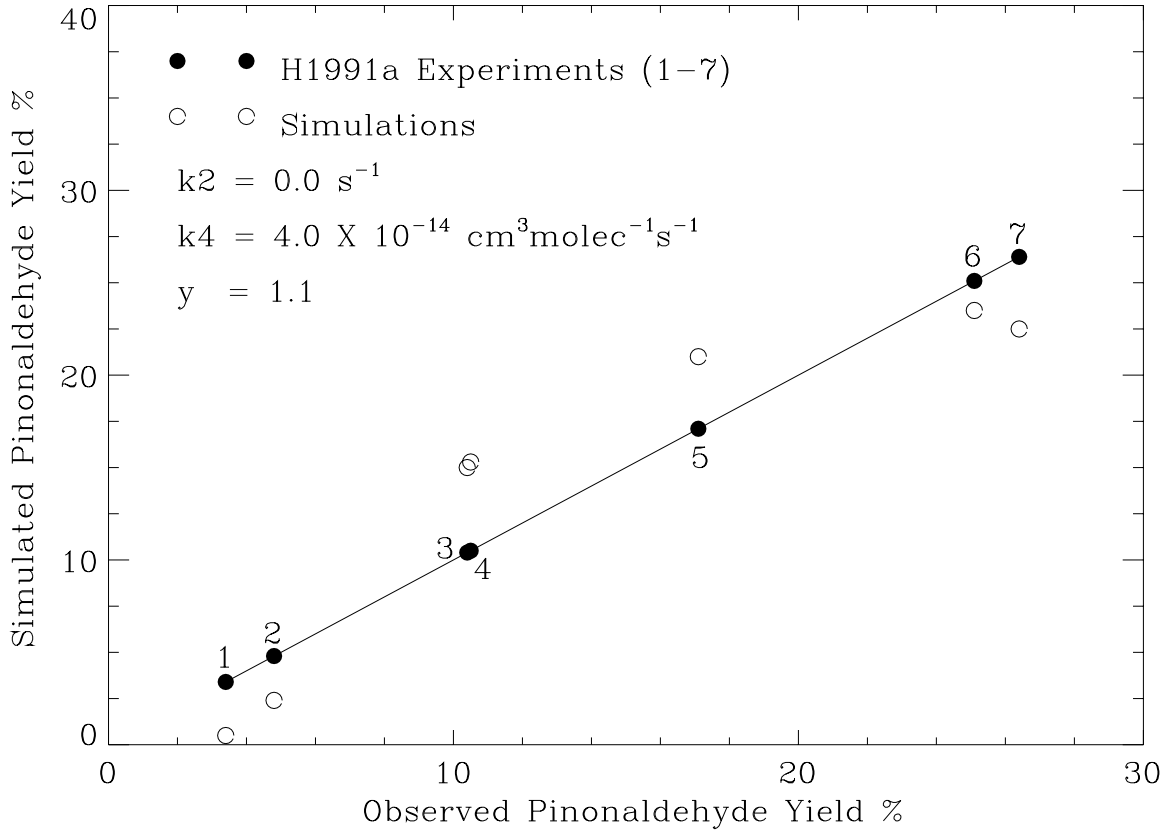

Figure 4.8: Plot of simulated vs observed pinonaldehyde yields for the best estimates of k2, k4, and y.

(R9)	APIN + O_3	$\xrightarrow{M}$	aPCRIG* + (1-a)PCRIG	k9 = $(9.7 - 14.5) \times 10^{-17}$, measured, Atkinson *et al.* (1990), and Grimsrud *et al.* (1975); a = 0.8, see text
(R10)	PCRIG*	$\longrightarrow$	pOH + qHO_2 + rHCHO + sCO + tCO_2 + uPCHO + vOGP	k10 > 1.0, rapid; p, q, r, s, t, u, v, unknown; q ≤ r, see text
(R11)	PCRIG + H_2O	$\longrightarrow$	PALD + H_2O_2	k11 = 1.6×10^{-17}, estimated, Suto *et al.* (1985)
(R12)	PCRIG + OH	$\longrightarrow$	PALD + HO_2	k12, assumed, see text

The initial reaction is addition of O_3 across the double bond forming a molozonide, which quickly decomposes to form energy-rich Criegee biradicals. Since the double bond is asymmetrical, two different biradicals may form; however, since the split is unknown, both

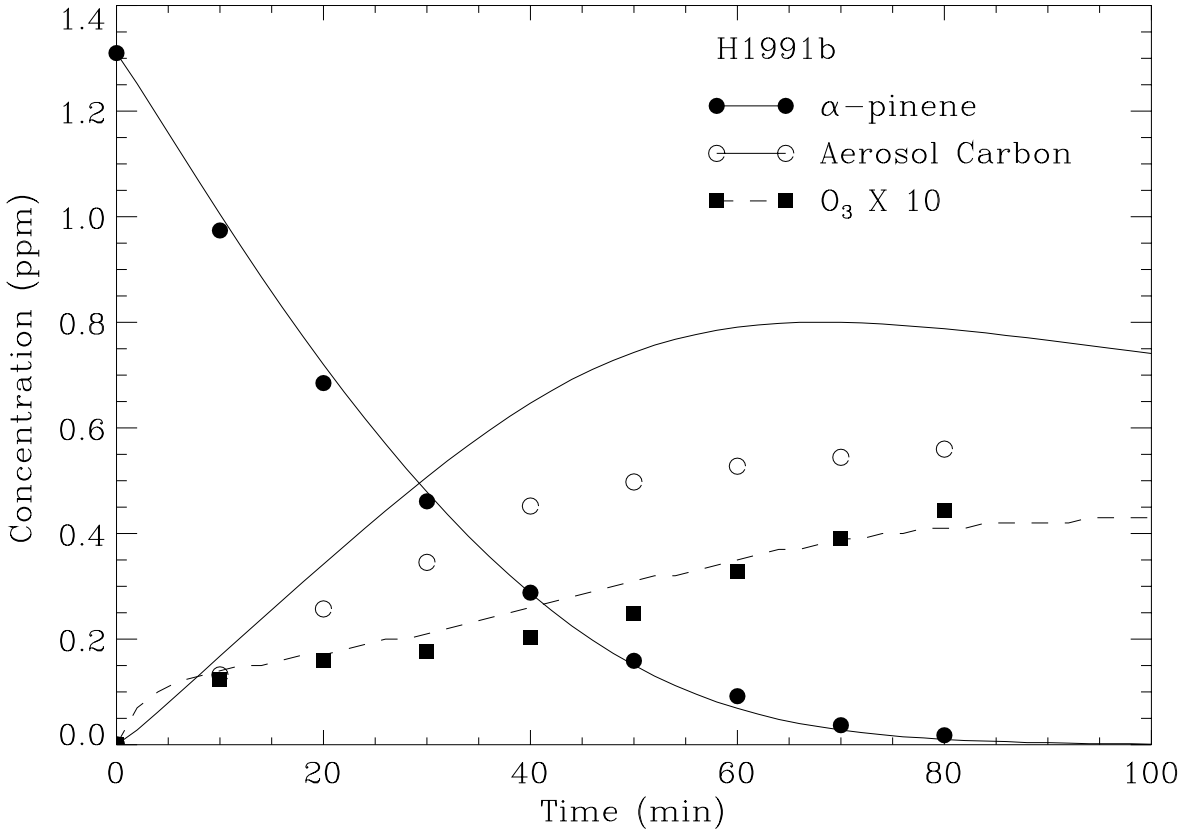

Figure 4.9: Simulated (lines) and experimental (symbols) profiles of α-pinene, aerosol carbon, and ozone for the data set H1991b.

biradicals are denoted here by PCRIG*. These vibrationally excited species may stabilize (or thermalize) to form PCRIG, which can further react with other species such as H_2O and OH in the absence of NO_x. On the other hand, PCRIG* may decompose to give reactive radicals such as OH and HO_2, among other species (Herron *et al.*, 1982; Atkinson and Lloyd, 1984; Atkinson *et al.*, 1992).

Atkinson *et al.* (1992) reported the OH formation yields from the gas-phase reaction of O_3 with α-pinene at 0.82 and 0.85 under two different relative humidities of about 4 and 40% respectively, with the yields having an estimated overall uncertainty of a factor of $\sim$1.5 (data sets A1992a). Other experimental conditions for these sets are given in Table 4.3. The nearly constant OH yield indicates that decomposition and stabilization of the energized biradicals are independent of the water vapor concentration. The rates of these processes are known to depend on the system temperature and total pressure, and since the energized biradicals

are short lived, we can lump these steps along with the initial reaction as written in (R9). The yield, 'a', for PCRIG* may thus be assumed to remain constant at a given temperature and pressure (of air). The direct yield of OH formation from α-pinene-O_3 reaction should be the yield of OH in Reaction (R10), 'p', multiplied by the yield of PCRIG*, 'a'. Thus, a$\times$p must be $\approx$(0.82-0.85) within a factor of 1.5. Furthermore, Hakola *et al.* (1994) reported a direct pinonaldehyde yield of 0.19$\pm$0.04 in the above experiments.

Presently, there exists no experimental evidence in the literature for the reaction of a thermalized Criegee biradical with OH (R12); however, it could be important, especially under low humidities and low NO_x concentrations. The rate constant for such a reaction would probably be on the order of 10^{-11} cm^3 molecule^{-1} s^{-1}. Its effect on the overall chemistry is examined below.

At this point, it would be worthwhile to interpret the observation of Hakola *et al.* (1994) mentioned above. In their experiments, the only source of PALD would be Reaction (R11), since negligible OH was available for other reactions, namely (R1) and R(12), that can lead to PALD formation. And since both Criegee biradicals will give PALD on reacting with H_2O, the effective yield of thermalized Criegee biradicals must be 0.19. Thus, yield 'a' in (R9) should be 0.81.

Other decomposition products in (R10) were observed by Hatakeyama *et al.* (1989), which include HCHO, CO, CO_2, and formyls. Formyls probably consisted of pinonaldehyde and other CHO containing compounds (except HCHO) denoted by PCHO; however, these could not be distinguished by the FTIR spectroscopic technique employed. Also, HCHO is probably rapidly formed from the primary decomposition product CH_3O via

$$CH_3O + O_2 \longrightarrow HCHO + HO_2.$$

Thus, HO_2 yield would be nearly the same or lower than that of HCHO. Time evolution of the gaseous products was reported by the authors for one experiment (data set H1989a), along with the final yields for four other similar runs (data sets H1989b). These data sets are most suitable for determining the unknown parameters in Reaction (R10). Using the above estimated value for yield 'a', three simulations were performed for H1989a with different relative humidities (0.0%, 0.1%, and 1.0%). In all three runs, a value of k9 = 1.2×10^{-16} cm^3 molecule^{-1} s^{-1} was required to reproduce the decay of ozone and α-pinene. This value is slightly higher than the most recent measurement by Atkinson *et al.* (1990) at 296$\pm$2 K,

but within the recommended upper limit when corrected to 303 K using an activation energy of -904 K (Atkinson *et al.*, 1982b). The estimated yield, 'p', of OH radicals is 0.7, which gives a direct yield from α-pinene of a$\times$p = 0.57, and is equal to the lower limit estimated by Atkinson *et al.* (1992). The rate constant k12 was varied from 0.0 to 5.0×10^{-11} cm^3 $molecule^{-1}$ s^{-1}, but neither significant contribution to PALD production nor any appreciable effect on α-pinene decay was observed except in the absolutely dry case of RH = 0.0%, where it was responsible for about 4.7% PALD production. This result suggests that (R12) may not be important under ambient atmospheric conditions, and is eliminated.

A final overall PALD yield of about 17% was obtained for the runs with RH = 0.1% and 1.0%; however, only about 3% was obtained when RH = 0.0%. This clearly shows that Reaction (R11) is responsible for the majority of PALD produced in H1989a and H1989b experiments. Also, according to the model results, PALD is about 38% of the total formyls observed; the balance of 62% must be made up by other higher aldehydes, lumped together as PCHO. In summary, the following yields for Reaction (R10) are recommended: OH, p = 0.7; HO_2, q $\leq$ 0.45; HCHO, r = 0.45; CO, s = 0.15; CO_2, t = 0.55; PCHO, u = 0.615 (assumed as C_{10} molecules). To complete the carbon balance, v = 0.285 for other gaseous products (OGP), also assumed as C_{10} molecules. The subsequent reactions of OGP are ignored.

The simulated and experimental profiles for H1989a are in excellent agreement, and are displayed in Figure 4.10. The subsequent decay of formyls is probably due to deposition of both PALD and PCHO on the chamber wall and aerosol surface; however, the lower limit of the vapor pressure for either species would have to be more than at least 60-100 ppb. The ambient concentrations of α-pinene rarely exceed 20 ppb, and both PALD and PCHO are not likely to accumulate above 20 ppb due to reactions with OH. Thus, accurate determination of their vapor pressures is of little value in the final applications of the model under ambient atmospheric conditions.

Additional simulations were performed for the H1989b data sets, and the average ratio $-\Delta[\alpha\text{-pinene}]/\Delta[O_3]$ during the first 10 minutes was calculated for each simulation. The ratios ranged from 1.43 - 1.52 and an average value of 1.48 was obtained, which agrees with the observed average value of Hatakeyama *et al.* (1989).

In the data set H1989c, Hatakeyama *et al.* observed an average aerosol carbon yield of 18.3 $\pm$ 2.1%. The yield appeared to be independent of the initial α-pinene concentration

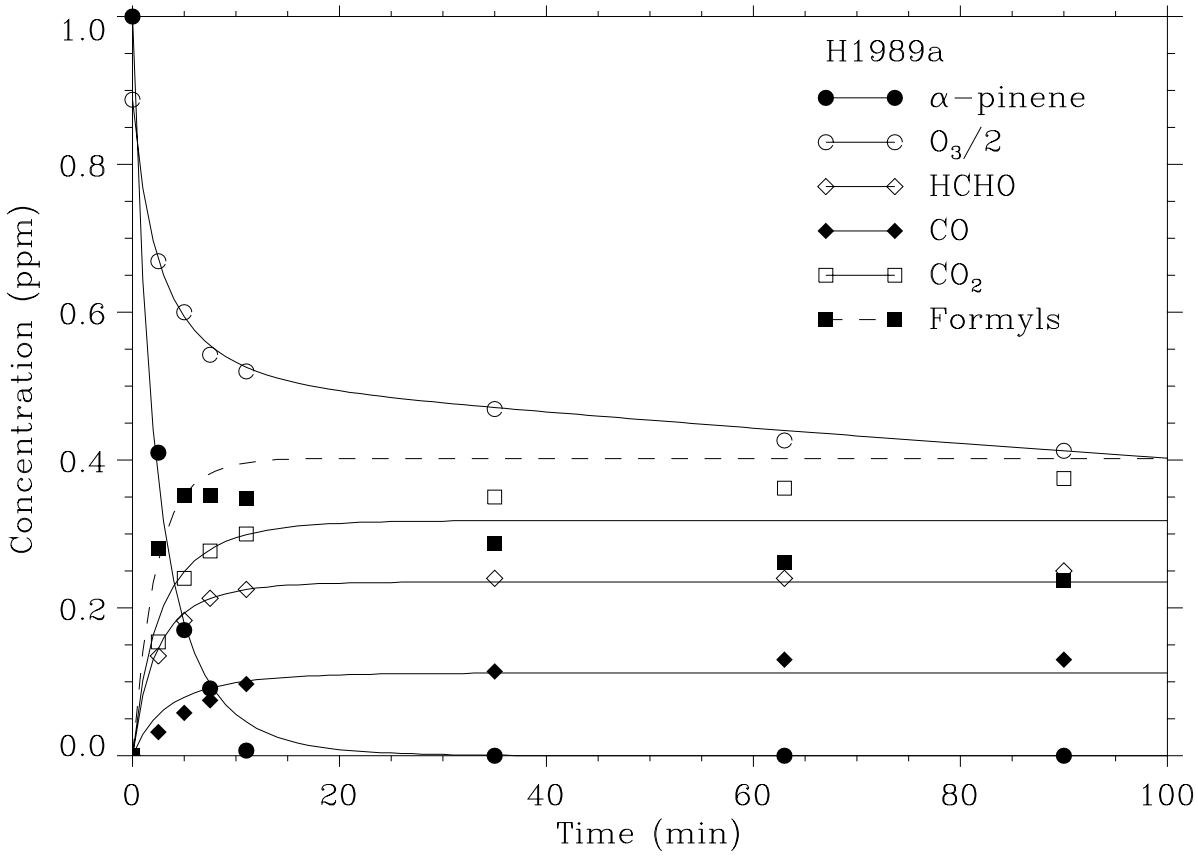

Figure 4.10: Simulated (lines) and experimental (symbols) profiles of α-pinene, O_3 and their reaction products for the data set H1989a.

in the range $\sim$(0.01 - 0.12 ppm), with initial ozone concentrations kept at 0.8 ppm for all runs. Since the initial α-pinene concentrations used were quite low, PALD and PCHO are not expected to deposit on the chamber walls or contribute to aerosol mass. Assuming that the α-pinene-O_3 reaction yields no direct aerosol formation, all of the observed aerosol carbon must come from the previously proposed reaction of PO_2 with HO_2, (R3). Figure 4.11 shows the simulated and observed overall aerosol yields under the experimental conditions of H1989c runs for three different values of the HO_2 yield 'q' in Reaction (R10). The simulated yields are the total yields, i.e., without any loss to the chamber walls, and are in accord with the observed aerosol yields. Since the observed yields were, probably, not corrected for wall losses, a maximum yield of about 20.5% is used to parameterize q, and a value of 0.30 is recommended.

The experiments of Simonaitis *et al.* (1991) offer evidence for H_2O_2 formation during the

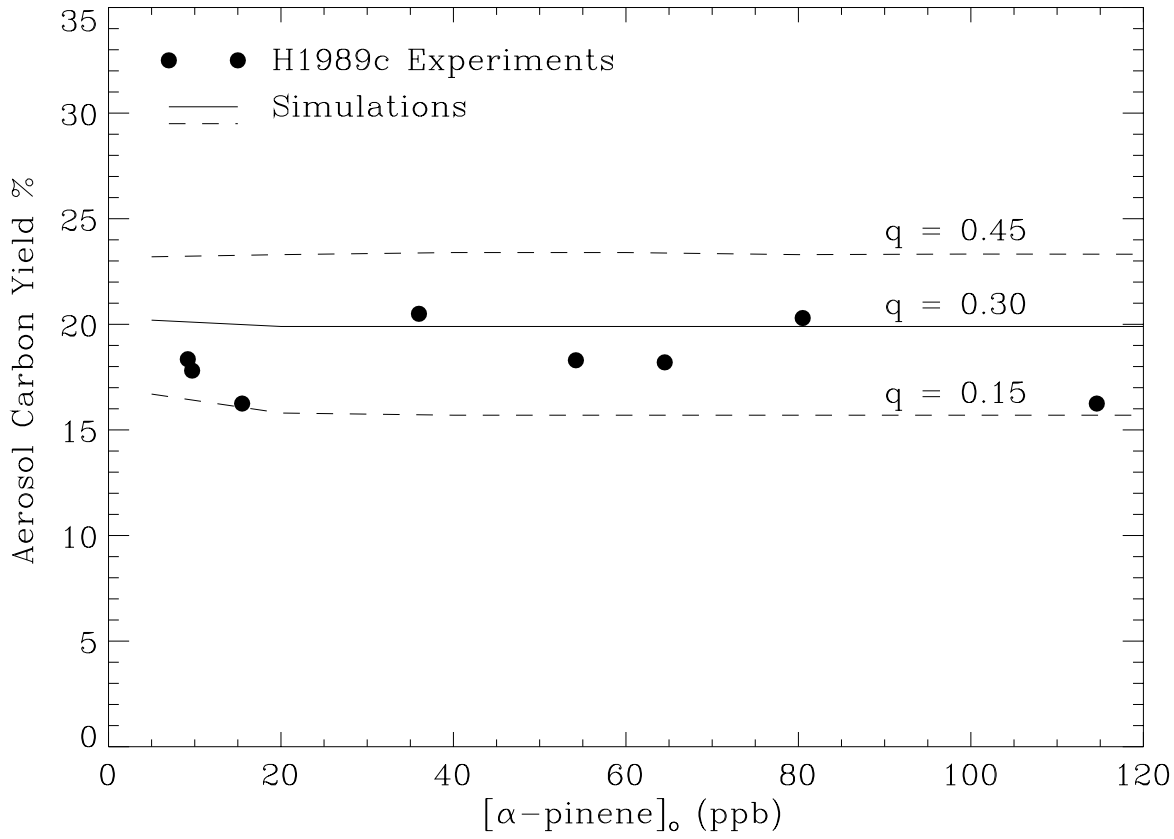

Figure 4.11: Simulated and experimental yields of aerosol carbon over a wide range of initial α-pinene concentration. Data set H1989c.

reaction of α-pinene with O_3 in the dark (data sets S1991a). According to their analyses, an overall yield of 9% H_2O_2 was observed under the high relative humidity runs (RH = 24%), and was independent of the initial α-pinene and O_3 concentrations. In the dry runs (RH $< 2\%$), the overall yield of H_2O_2 decreased by a factor of two, and hence, they attributed almost all of the H_2O_2 production to the reaction of water vapor with thermalized Criegee biradical (R11), with negligible contribution from the HO_2 self-reaction.

$$\begin{aligned} HO_2 + HO_2 &\xrightarrow{M} H_2O_2, \\ HO_2 + HO_2 + H_2O &\xrightarrow{M} H_2O_2 + H_2O. \end{aligned}$$

This implies that the mechanism developed so far, if reasonably accurate, should be capable of predicting the H_2O_2 formation. Several simulations were performed with different

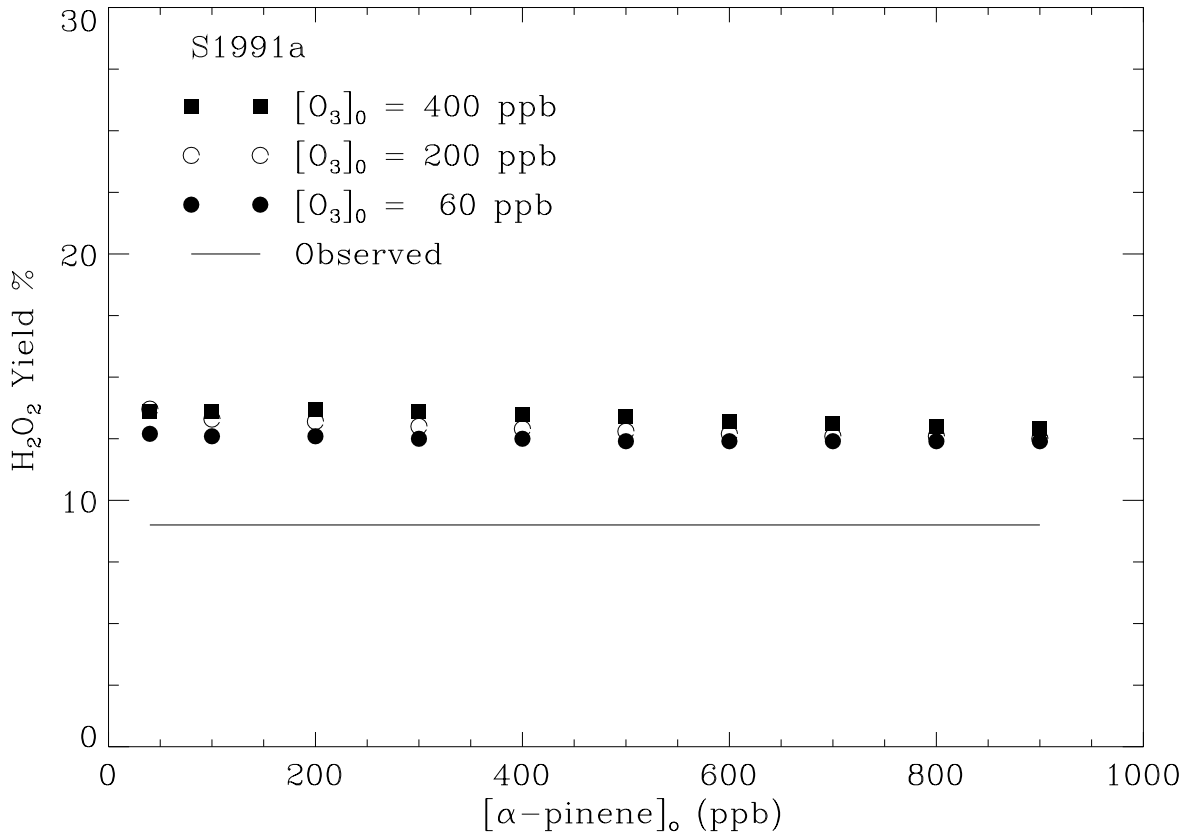

Figure 4.12: Simulated (symbols), and observed (solid line) overall yields of H_2O_2 over a wide range of initial α-pinene, and O_3 concentrations under the experimental conditions of the data set S1991a.

initial α-pinene, and O_3 concentrations as used in the S1991a experiments, and the overall yields of H_2O_2, neglecting wall losses, were computed. Indeed, the simulated yields are in the range of 12-14%, only slightly higher than observed (see Figure 4.12). Also, the yields were lower by a factor of two when RH was about 0.001% (not shown in the figure). In the complete absence of water vapor, the simulated H_2O_2 yields were lower than 1%. Thus, Reaction (R11) can be an important source of H_2O_2 in forest air, especially at higher ground-level ozone concentrations.

4.2.3 Reactions with OH and Ozone in the Presence of NO_x

Finally, the reactions discussed in the previous two subsections are considered here in the presence of NO_x. The NO_x-free mechanism consisting of Reactions (R1) through (R12) is augmented with the reactions listed below. Again, the rate constants are expressed in cm^3-molecule-s units.

(R13)	PO_2 + NO	$\xrightarrow{O_2}$	PO + NO_2	k13 = $4.2 \times 10^{-12} \exp(180/T)$, recommended, DeMore *et al.* (1988)
(R14)	PO + NO	$\longrightarrow$	PONO	k14 $\approx 3 \times 10^{-11}$, Finlayson-Pitts and Pitts (1986)
(R15)	PO + NO_2	$\longrightarrow$	$PONO_2$	k15 $\approx 1.5 \times 10^{-11}$, Finlayson-Pitts and Pitts (1986)
(R16)	PCRIG + NO	$\longrightarrow$	PALD + NO_2	k16 = $2.1 \times 10^{-9}\ T^{-1}$, Lloyd *et al.* (1983)
(R17)	PCRIG + NO_2	$\longrightarrow$	PALD + NO_3	k17 = $2.1 \times 10^{-10}\ T^{-1}$, Lloyd *et al.* (1983)
(R18)	PCO_3 + NO	$\xrightarrow{O_2}$	QO_2 + NO_2 + CO_2	k18 = $3.5 \times 10^{-11} \exp(-180/T)$, Simonaitis *et al.* (1997)
(R19)	PCO_3 + NO_2	$\longrightarrow$	PNIT	k19 = $2.6 \times 10^{-12} \exp(-380/T)$, Simonaitis *et al.* (1997)
(R20)	PNIT	$\longrightarrow$	PCO_3 + NO_2	k20 = $4.0 \times 10^{+16} \exp(-13543/T)$, Simonaitis *et al.* (1997)
(R21)	QO_2 + NO	$\xrightarrow{O_2}$	NO_2 + HO_2 + AONE + ALD2 + 4PAR	k21 = $4.2 \times 10^{-12} \exp(180/T)$, DeMore *et al.* (1988)
(R22)	APIN + NO_3	$\longrightarrow$	$PO_2(ONO_2)$	k22 = 6.1×10^{-12}, Atkinson *et al.* (1985)
(R23)	$PO_2(ONO_2)$ + HO_2	$\longrightarrow$	SONA	k23 = $7.7 \times 10^{-14} \exp(1300/T)$, DeMore *et al.* (1988)
(R24)	$PO_2(ONO_2)$ + NO	$\longrightarrow$	NO_2 + nitrates	k24 = $4.2 \times 10^{-12} \exp(180/T)$, DeMore *et al.* (1988)
(R25)	$PO_2(ONO_2)$ + $PO_2(ONO_2)$	$\longrightarrow$	nitrates	k25 = 1.1×10^{-14}, Kirchner and Stockwell (1996)

As shown in Figure 4.3, the reaction of PO_2 with NO gives an alkoxy radical, which may decompose to give PALD as already discussed, or may futher react with NO_x to form alkyl nitrites and nitrates. The rate constants of alkoxy radical and NO reactions are highly uncertain, but are estimated to be in the vicinity of $\sim 3 \times 10^{-11}$ cm^3 $molecule^{-1}$ s^{-1}. The rate constants of alkoxy radical and NO_2 reactions are also uncertain, and are thought to be $\sim$50% of those for the reaction with NO, i.e., $\sim 1.5 \times 10^{-11}$ cm^3 $molecule^{-1}$ s^{-1}. Assuming these values for our model, the lumped pseudo first-order rate constant of PO at [NO] and [NO_2]

= 1 ppm, would be about 1110 s^{-1}, and is comparable to the decomposition rate constant. The decomposition rate constant (k5) becomes a critical parameter as it determines the production of PALD and HO_2 in the presence of NO_x. Fortunately, k5 can be estimated with the use of the data set H1991c, and is discussed shortly.

Reactions of the stabilized Criegee biradicals with NO and NO_2 have been proposed by Herron *et al.* (1982) and Lloyd *et al.* (1983), and the rate constants for a typical Criegee biradical have been adopted from the latter. Similar to the reaction with H_2O, both biradicals are expected to give PALD upon reaction with NO_x. The Reactions (R18) through (R20) are the typical acetyl peroxy-NO_x type reactions producing an alkyl peroxy radical with one less carbon atom (QO_2), and a PAN like nitrate (PNIT). Due to lack of information on the precise fate of QO_2 in the reaction with NO, its products are represented by CBM-Z species for closure (R21).

Although the initial reaction of α-pinene with NO_3 has been studied, its products and their susbsequent reactions are not well understood. A rate constant of 6.2×10^{-12} cm^3 $molecule^{-1}$ s^{-1} (Atkinson *et al.*, 1985) has significant impact on the nighttime loss of α-pinene. A typical nighttime NO_3 concentration of 10 ppt implies a relatively short α-pinene lifetime of 11 min compared to ~4.6 hours with respect to both ozone and OH during the daytime. Assuming that α-pinene behaves like a typical internal alkene, the NO_3 addition across the double bond should produce a tertiary radical, which in the presence of oxygen could form an alkyl peroxy radical, $PO_2(ONO_2)$ (see Figure 4.13). Subsequent reactions are similar to those occuring in the α-pinene-OH mechanism, leading to a secondary organic nitrate aerosol (SONA) formation, and other species such as dinitrates, nitrites, and 3-nitrooxynopinone. These reactions and products are purely speculative and are based on studies of the reactions of propene in the presence of NO_x by Akimoto and co-workers (Akimoto *et al.*, 1978; Akimoto *et al.*, 1980; Bandow *et al.*, 1980; Shepson *et al.*, 1985). Due to lack of any experimental evidence, the present model is limited to the inclusion of the proposed first generation product $PO_2(ONO_2)$ and its reactions.

The data set H1991c1 gives corrected pinonaldehyde concentration as a function of α-pinene conversion for the reaction with OH in the presence of NO_x. This information can be used to provide an estimate for the rate constant k5. A value of 1600 s^{-1} appears to reproduce the observed pinonaldehyde concentration profile while NO was still present in the system (Figure 4.14). Two other values of k5 are also shown in the plot for comparison. Using the

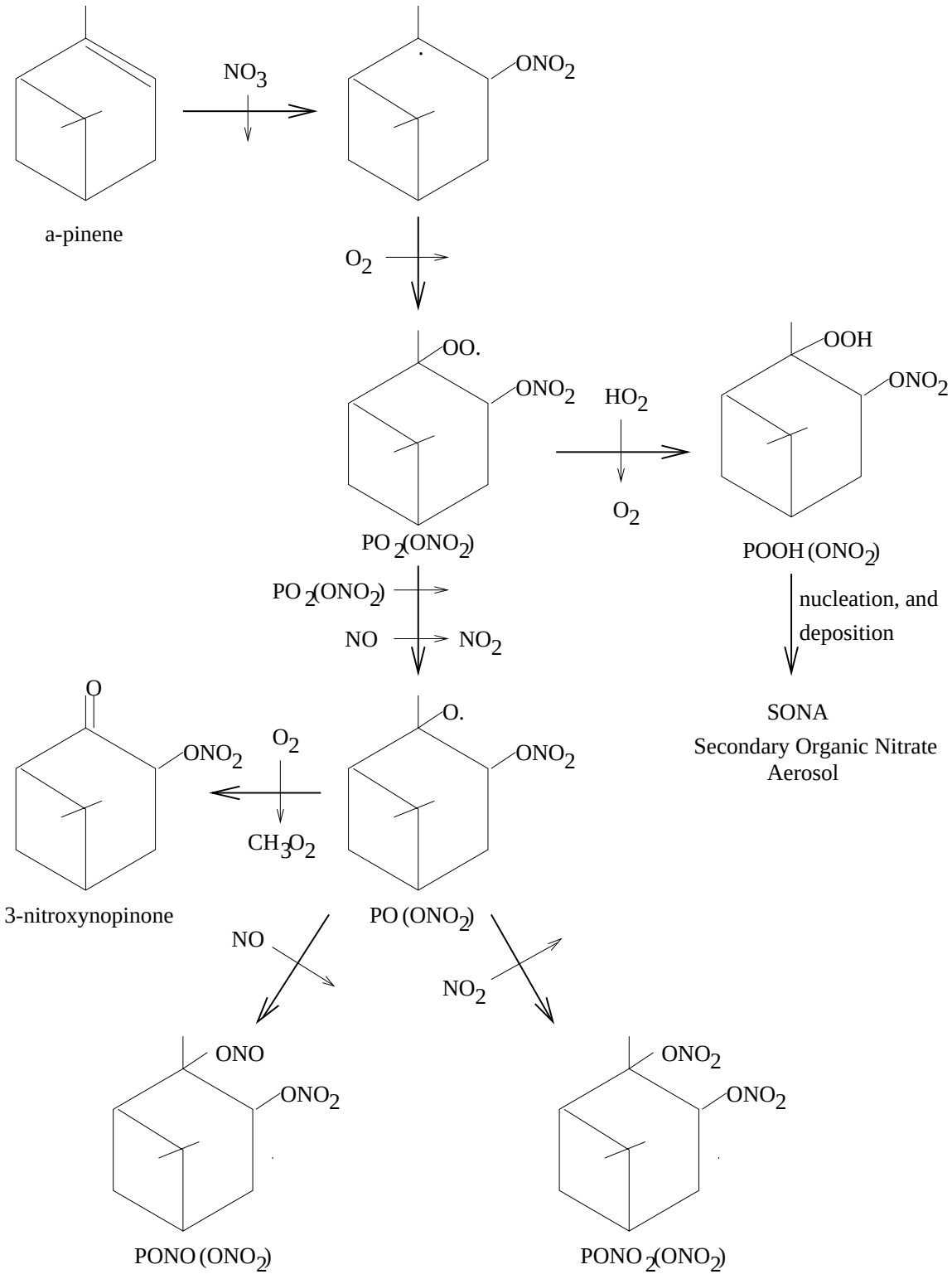

Figure 4.13: Hypothesized α-pinene-NO_3 reaction mechanism.

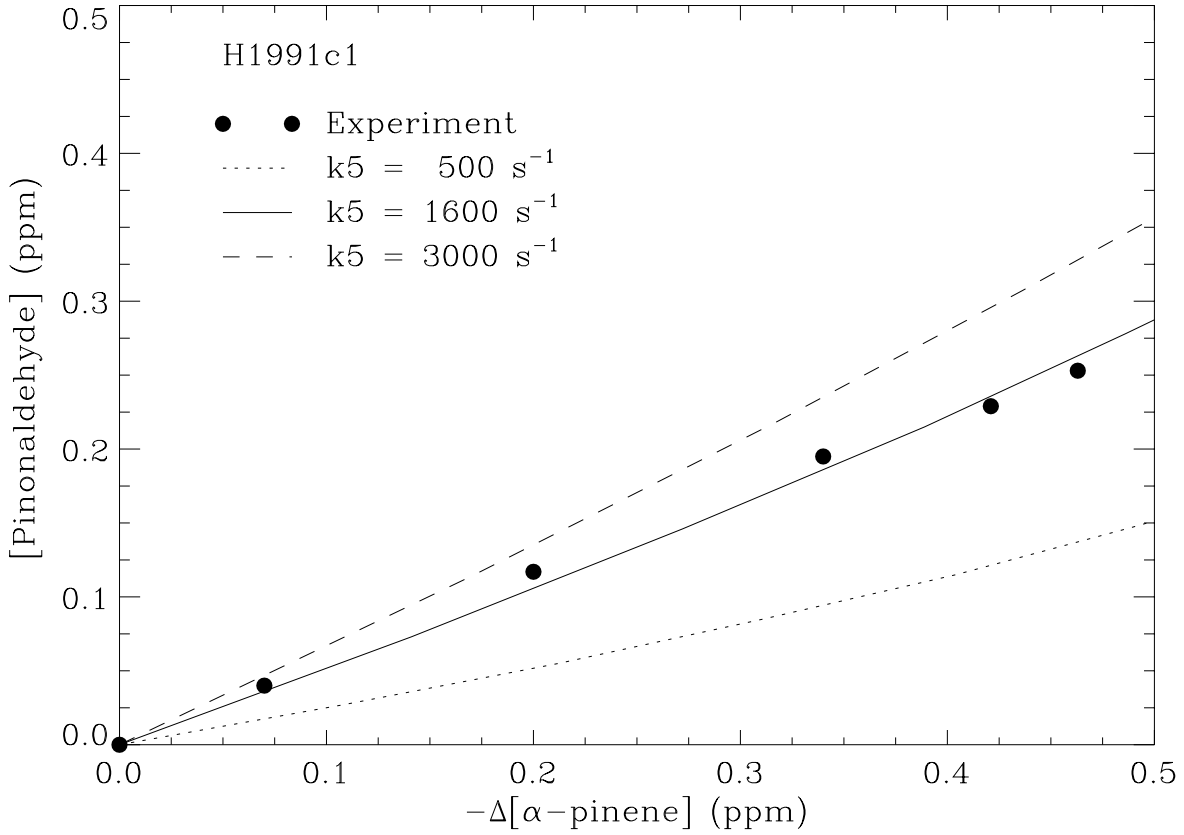

Figure 4.14: Dependence of pinonaldehyde production on the rate constant k5. Solid and broken lines are simulated profiles, filled circles are experimental values from the data set H1991c1.

above value for k5, a simulation was performed for the experiment H1991c2. Figure 4.15 shows that the simulated and observed time evolutions of α-pinene, NO, NO_2, and PALD are in excellent agreement, and well within experimental errors.

The model, however, did not give any appreciable aerosol yield under the experimental conditions of H1991d, in which a final yield of 23% was observed. Nitrogen was also found to be present in the aerosol mass, implying additional aerosol sources under very high NO_x concentrations. Interestingly, the model predicted about 11% pono2, and 62% PONO yields, either or both of which could have contributed to the observed aerosol mass. However, formation of these species is likely to be very small under typical atmospheric NO_x levels of a few ppbs, and can be safely neglected.

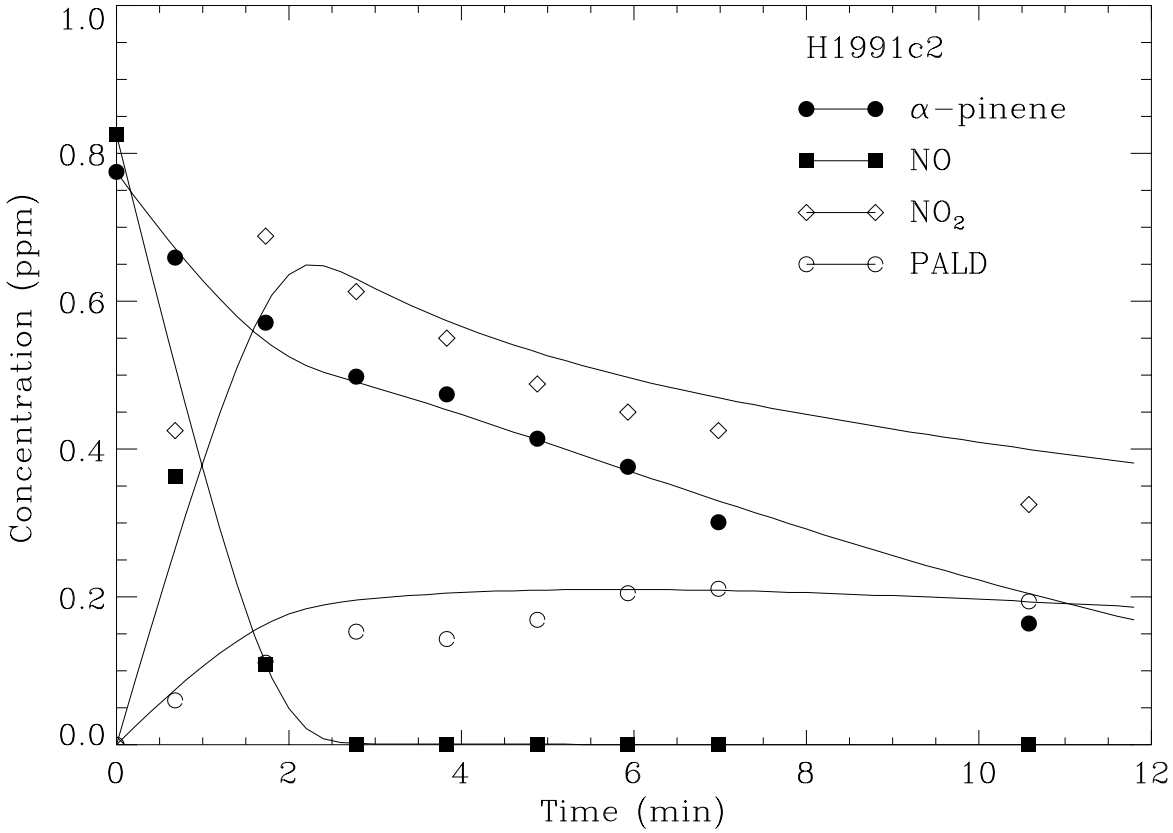

Figure 4.15: Simulated (lines), and experimental (symbols) time evolution of the major gaseous species in the reaction of α-pinene and OH in the presence of NO_x (data set H1991c2).

4.3 Summary and Remarks

This concludes the mechanism development and evaluation against the available experimental data in the literature. The final mechanism is simplified by lumping Reactions (R9) and (R10), and is listed in Table 4.5 with the recommended yields and rate constants. In summary, the newly developed mechanism, though somewhat speculative, can successfully explain a variety of experimental observations which includes OH and H_2O_2 formations from α-pinene-O_3 reaction. More importantly, the mechanism is able to accurately predict the different aerosol carbon yields observed under a range of reactant concentrations and operating conditions. In the proposed mechanism, only the reactions of α-pinene with OH and NO_3 lead to the formation of aerosol precursors, while that with ozone tends to enhance the rate of formation by generating reactive radicals such as OH and HO_2.

The proposed α-pinene-NO_3 scheme could be potentially important with respect to

Table 4.5: Proposed α-Pinene Photooxidation Mechanism

No.	Reaction			Rate Constant k [molecule-cm^3-s]
1.	APIN + O_3	$\xrightarrow{M}$	.19PCRIG + .57OH + .24HO_2 .49PCHO + .37HCHO .12CO + .45CO_2 + 0.226OGP	$2.37 \times 10^{-15} \exp(-904/T)$
2.	APIN + OH	$\xrightarrow{O_2}$	PO_2	$8.53 \times 10^{-12} \exp(550/T)$
3.	APIN + NO_3	$\longrightarrow$	$PO_2(ONO_2)$	6.1×10^{-12}
4.	PCRIG + H_2O	$\longrightarrow$	PALD + H_2O_2	1.6×10^{-17}
5.	PCRIG + NO	$\longrightarrow$	PALD + NO_2	$2.1 \times 10^{-9}\ T^{-1}$
6.	PCRIG + NO_2	$\longrightarrow$	PALD + NO_3	$2.1 \times 10^{-10}\ T^{-1}$
7.	PO_2 + HO_2	$\longrightarrow$	SOA	$7.7 \times 10^{-14} \exp(1300/T)$
8.	PO_2 + PO_2	$\longrightarrow$	1.1PO + 0.9OGP	4.0×10^{-14}
9.	PO_2 + NO	$\xrightarrow{O_2}$	PO + NO_2	$4.2 \times 10^{-12} \exp(180/T)$
10.	PO	$\xrightarrow{O_2}$	PALD + HO_2	$1.6 \times 10^{+3}$
11.	PO + NO	$\longrightarrow$	PONO	3.0×10^{-11}
12.	PO + NO_2	$\longrightarrow$	$PONO_2$	1.5×10^{-11}
13.	$PO_2(ONO_2)$ + HO_2	$\longrightarrow$	SONA	$7.7 \times 10^{-14} \exp(1300/T)$
14.	$PO_2(ONO_2)$ + NO	$\longrightarrow$	NO_2 + NITR	$4.2 \times 10^{-12} \exp(180/T)$
15.	$2PO_2(ONO_2)$	$\longrightarrow$	2NITR	1.1×10^{-14}
16.	PALD + OH	$\longrightarrow$	PCO_3	$1.16 \times 10^{-11} \exp(250/T)$
17.	PCHO + OH	$\longrightarrow$	PCO_3	$1.16 \times 10^{-11} \exp(250/T)$
18.	PALD + $h\nu$	$\longrightarrow$	ALD2 + OLE + 3PAR + AONE	j(ALD2)
19.	PALD + $h\nu$	$\longrightarrow$	QO_2 + HO_2 + CO	10 × j(ALD2)
20.	PCHO + $h\nu$	$\xrightarrow{O_2}$	ALD2 + OLE + 3PAR + AONE	j(ALD2)
21.	PCHO + $h\nu$	$\xrightarrow{O_2}$	QO_2 + HO_2 + CO	10 × j(ALD2)
22.	PCO_3 + NO	$\xrightarrow{O_2}$	QO_2 + NO_2 + CO_2	$3.5 \times 10^{-11} \exp(-180/T)$
23.	PCO_3 + NO_2	$\longrightarrow$	PNIT	$2.6 \times 10^{-12} \exp(-380/T)$
24.	PNIT	$\longrightarrow$	PCO_3 + NO_2	$2.0 \times 10^{16} \exp(-180/T)$
25.	QO_2 + NO	$\xrightarrow{O_2}$	ALD2 + 4PAR + AONE + NO_2 + HO_2	$4.2 \times 10^{-12} \exp(180/T)$

aerosol formation in the presence of NO_x, especially at nighttime, and certainly deserves experimental investigation. About 23% of the carbon atoms in the α-pinene-O_3 reaction are unaccounted for, and could be an important source of radicals via subsequent reactions. Also, other products including PCHO, QO_2, and PCO_3 need to be identified, and their recommended yields and reaction rate constants must be experimentally confirmed.

Most of the experiments considered to develop the mechanism were carried out at relatively high initial concentrations of both α-pinene and NO_x compared to typical concentrations found in the atmosphere. It is, therefore, necessary to evaluate the proposed mechanism under a variety of atmospheric conditions to better understand the role of monoterpenes (α-pinene) in the oxidant cycle and aerosol production. This becomes the topic of the next section.

4.4 Mechanism Evaluation Under Atmospheric Conditions

The mechanism compiled in Table 4.5 was incorporated into the CBM-Z along with the new isoprene chemistry developed in the previous chapter. It was then used to investigate the formation of H_2O_2, O_3, and aerosol under different scenarios. Since the focus was on the evaluation of the mechanism, a variable volume box-model was employed with prescribed diurnally varying mixing height. Realistic diurnally varying emissions of α-pinene and isoprene, and hypothetical emissions of NO_x and anthropogenic non-methane hydrocarbons (ANMHC) were also used. The meteorological and emission inputs, and the box-model formulation are described in the following subsection.

4.4.1 Box-Model Formulation and Inputs

The present box-model can be viewed as a well mixed boundary layer, uniform in the horizontal, but has variable volume which depends on the height of the mixed layer. The biogenic hydrocarbons are emitted at the surface, and are assumed to be instantly well mixed within the mixed-layer. Similary, NO_x emitted from soil, or transported from a nearby urban site within the box, is assumed to be instantly mixed in the box as shown in Figure 4.16 (Lurmann *et al.*, 1983).

The diurnal meteorological inputs to the box model include ambient temperature, and mixing height H_{ML}. Figure 4.17 illustrates the prescribed diurnal variations of H_{ML}, and

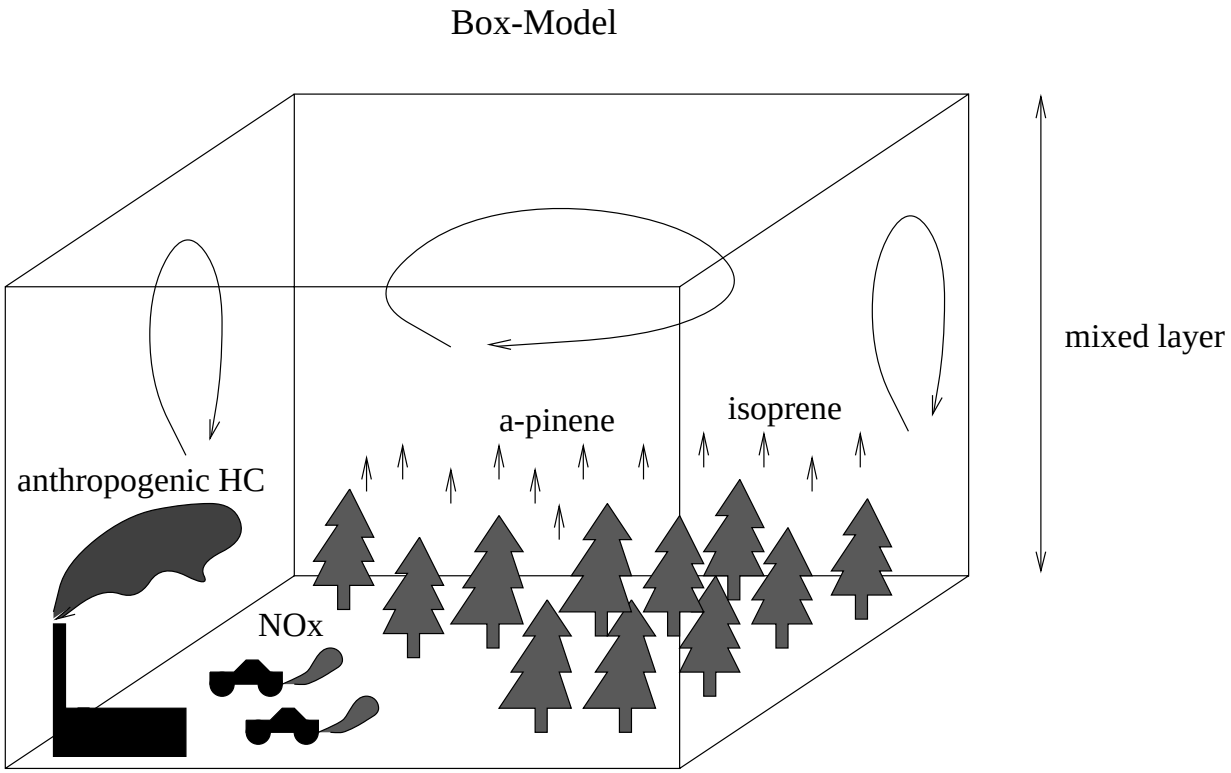

Figure 4.16: Schematic illustration of the box-model.

temperature is representative of a summertime continental boundary layer in high pressure regions. After sunrise as the mixing height increases, the boundary-layer air gets mixed with the air aloft usually causing dilution with respect to most species. Just before sunset, the turbulence in the mixed-layer decays rapidly, and the mixing height corresponds to the nocturnal boundary layer (NBL). Though the air is statically stable, sporadic turbulence occurring due to high wind shears in the air aloft can cause mixing throughout the NBL (Stull, 1988). These processes were incorporated in the box-model.

The growth of the mixed-layer height after sunrise was parameterized with the theoretical solar zenith angle at 40° N latitude, and was allowed to remain constant at a maximum height of about 1000 m from noon until sunset, after which a constant height of 200 m was used for the NBL until the following sunrise:

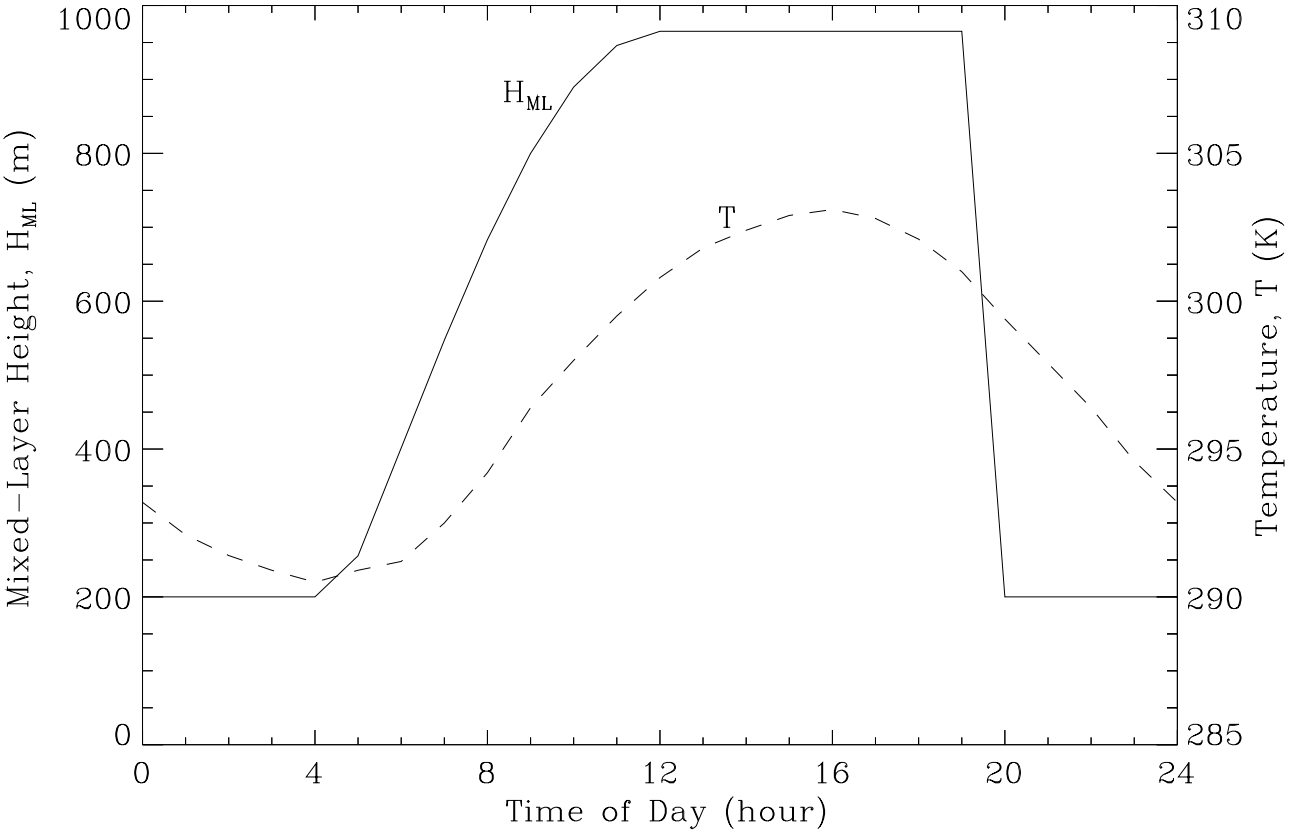

Figure 4.17: Prescribed diurnal variations of mixed-layer height, and temperature.

$$H_{ML} = H_1 \times \cos(\theta_z) + H_2, \tag{4.3}$$

where θ_z is the theoretical solar zenith angle, H_{ML} is the mixed-layer height, $H_1 = 800$ m, and $H_2 = 200$ m.

The typical emissions of α-pinene and isoprene for both coniferous and deciduous forests for the month of July were adopted from Lamb *et al.* (1993). Typical diurnal variations of the emission fluxes were parameterized with the solar zenith as before, using Equations (2.2) and (2.3). As seen from Figure 4.18 the parameter values given in Table 4.6 quite adequately reproduce the observed emission fluxes. It is also worth noting that while both the species exhibit a noon-time maxima, the isoprene emissions decrease to zero at night, but those of α-pinene tend to have minimum, non-zero base values.

Emissions of NO_x and ANMHC were prescribed over a wide range representing pristine rural conditions to a relatively polluted forest boundary layer influenced by a nearby urban

Table 4.6: Emission Flux Parameters for α-Pinene, and Isoprene for Fluxes over Deciduous and Coniferous Forests during July (based on Lamb *et al.*, 1993).

Species	Deciduous		Coniferous	
	E_1	E_2	E_1	E_2
	(μmol m^{-2} hr^{-1})			
Isoprene	91.5	0	3.2	0
α-Pinene	4.4	8.1	2.6	4.4

Table 4.7: Hypothetical Emissions Scenarios and Aloft-Air Concentrations.

Scenario	NO_x		NMOC / NO_x	Aloft[a] $[NO_2]$ (ppb)
	E_1	E_2		
	(μmol m^{-2} hr^{-1})			
C1 (coniferous)	0	0.8	0	0.5
C2 (coniferous)	4	1	5	1
C3 (coniferous)	16	4	10	2
D1 (deciduous)	0	0.8	0	0.5
D2 (deciduous)	4	1	5	1
D3 (deciduous)	16	4	10	2

[a] Aloft $[O_3]$ = 50 ppb, $[H_2O_2]$ = 1 ppb, [CO] = 100 ppb, and $[CH_4]$ = 1600 ppb for all scenarios.

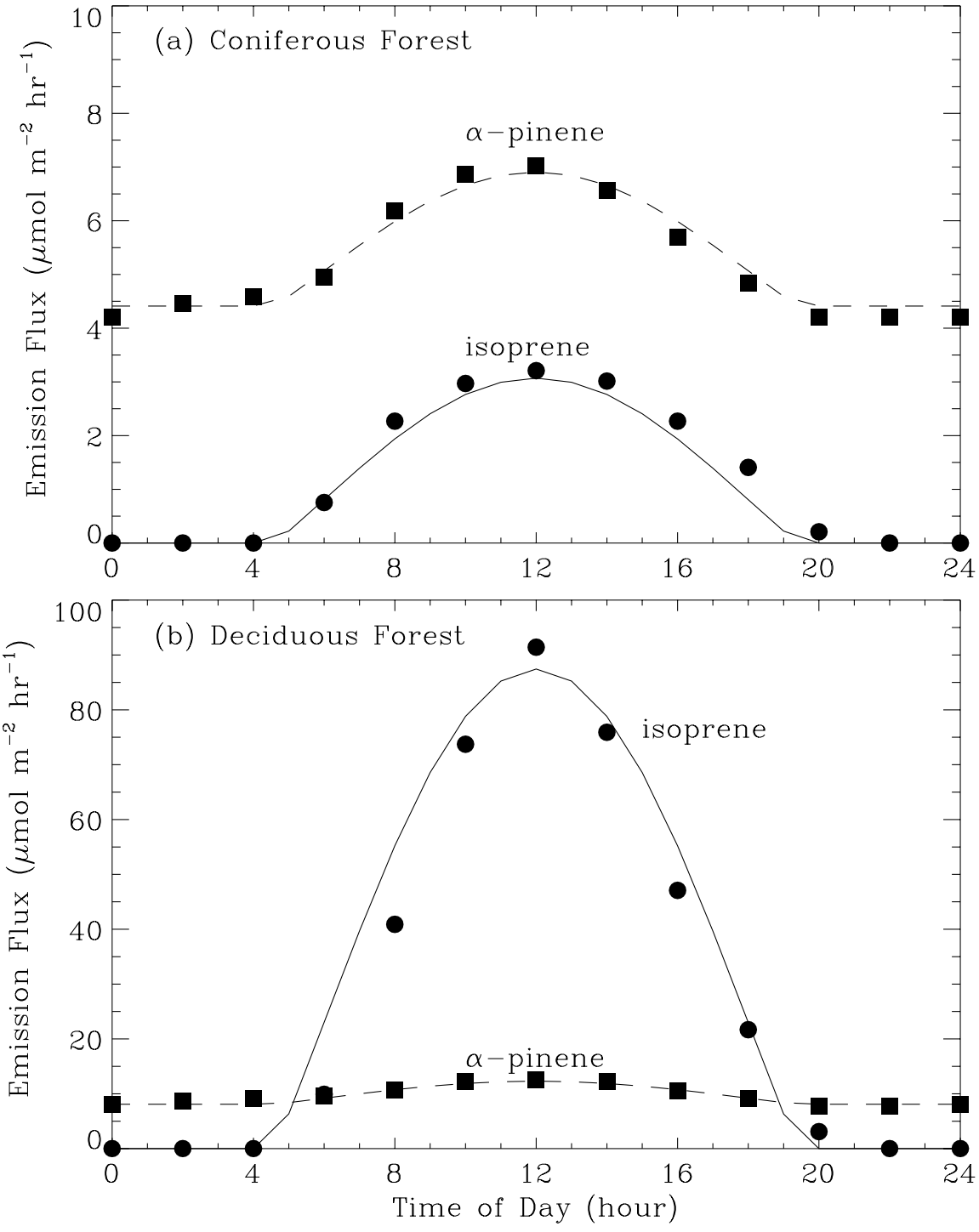

Figure 4.18: Parameterized (lines) and observed (symbols) emission fluxes of isoprene, and α-pinene for (a) coniferous forest, and (b) deciduous forest (from Lamb *et al.*, 1993).

center. In the pristine scenario, the natural NO_x emission flux from soil was kept at a constant value of 0.8 μmol m^{-2} hr^{-1} at all times. While the anthropogenic emissions are usually more difficult to prescribe, in this work the diurnal NO_x flux was also paramterized using Equations (2.2) and (2.3), such that the nighttime flux was constant at about 20% of the peak daytime value, the underlying reason being decreased anthropogenic activity at nighttime as compared to that at daytime peaking at noon. The ANMHC fluxes were calculated by a prescribed NMOC/NO_x ratio between 0 and 10 (Table 4.7). The urban NMOC composition was adopted from Stockwell *et al.* (1990), and the individual hydrocarbon species were partitioned into the CBM-Z species (see Tables 2.13 and 2.14).

The anthropogenic NO_x emissions were assumed to be 90% in the form of NO, and 10% as NO_2. Initial concentrations of α-pinene, isoprene, NO_x, and ANMHC species in the mixed layer were set to zero. Only the initial concentrations of O_3, CH_4, and CO were non-zero at 30, 100, and 1600 ppb, respectively, for all the scenarios. Also, non-zero aloft-air concentrations were prescibed for these species and for NO_2 and H_2O_2 based on pollution scenario, and are also listed in Table 4.7. Furthermore, a constant water vapor concentration of 3.81×10^{17} molecule cm^{-3} was assumed for all the runs, which corresponds to $\sim$50% RH at 298 K and 1 atm.

All diurnal model inputs including mixing height, temperature, and emission fluxes were updated every model hour during a simulation. Each simulation was allowed to run for 4 model days beginning midnight, July 1. Only the last two days were used for analysis so that the initial conditions were "forgotten".

4.4.2 Simulation Results and Mechanism Analysis

Scenarios C2 and D2 are selected as the two base cases representing suburban coniferous and deciduous forest settings, having moderate urban NO_x and hydrocarbon influences. Diurnal concentration variations of various species predicted during the last two days are shown in Figures 4.19 through 4.22 for the two base cases along with an additional run with the same conditions, but without the emissions of α-pinene and isoprene. The species plotted include α-pinene, isoprene, O_3, H_2O_2, OH, HO_2, NO_3, and NO_2.

Even though the emission fluxes for both α-pinene and isoprene peaked in the afternoon, their diurnal maxima and minima occurred at different times. For example, in scenario D2, the maxima of isoprene concentration occurred around 1600 hours, and the minima just

before sunrise as expected; however, the maxima of α-pinene concentration approximately coincided with the minima of isoprene concentration, and vice versa. This reverse dependence of concentration with respect to emission cycle is, actually, often observed in forest surface-layer air (Yokouchi *et al.*, 1983; Isidorov *et al.*, 1985; Riba *et al.*, 1987), and can be attributed to the diurnal variations in the mixing-height of the turbulent boundary layer.

Diurnal variation of ozone concentration exhibited distinct mid-afternoon maxima and early morning minima. This also is typically observed. Here, the increases in the ozone concentrations after sunrise are due to photochemical reactions as suggested by the differences in the maximas for the three cases. Clearly, the biogenic hydrocarbons appear to have a significant positive effect on the diurnal ozone cycle. Similar conclusions may also be drawn for H_2O_2. The H_2O_2 concentration reached a plateau by mid-afternoon in the case without biogenic hydrocarbons, while they continued to climb until sunrise in the presence of α-pinene and isoprene. The subsequent drop in the concentration was due to dilution of boundary layer air by vertical mixing. The enhanced H_2O_2 levels can be attributed to the direct formation from the α-pinene-O_3 reaction in the presence of water vapor, and also due to enhanced HO_2 radical production during photooxidation of both α-pinene and isoprene in the presence of NO_x.

Nighttime OH radical concentrations in both scenarios (C2 and D2) were significantly higher compared to the run without biogenic HCs. On the contrary, the daytime OH concentrations were the highest for the run without biogenics. Similar results were also found for HO_2. This suggests that α-pinene and isoprene could be important nighttime sources of free radicals. Reactions of α-pinene are especially important since its concentration peaks at nighttime. Lower daytime OH concentrations reflect vigorous scavenging by the biogenics and their products.

Influence of the biogenic HCs on the nighttime chemistry is most visible in the levels of NO_3 radical. The nighttime NO_3 levels are suppressed by two orders of magnitude due to the fast reaction with α-pinene. Nighttime NO_2 levels are also affected as a result.

Due to the complex nature of the coupled α-pinene-isoprene atmospheric chemistry, it should be useful if the relative importance of the initial reaction of each species were quantified. The following equation was employed on-line during the simulations to compute the relative percent depletion due to each initial reaction:

$$f_{i,j}(t) = \left(\frac{dC_{i,j}/dt}{dC_{i,tot}/dt} \right)_t , \tag{4.4}$$

where $f_{i,j}$ is the instantaneous fraction of species i depleted due to its reaction with species j at any given time t. Here, i can be α-pinene and isoprene, and j can be O_3, OH, and NO_3.

Instantaneous relative depletions of α-pinene and isoprene for the two base scenarios are shown in Figures 4.23 and 4.24. It is clearly evident that different initial reactions, for a given species, become dominant or diminish depending on the forest type and the time of day. For example, scavenging of both species due to OH radical generally gains importance during the daytime; however, its relative importance to the O_3 reaction is considerably different for the same species (especially α-pinene) between the two scenarios. Also, the reaction with NO_3 becomes important at nighttime, and its relative importance should be higher under higher pollution. This point is illustrated in Figure 4.25 which plots time averaged relative depletions for all scenarios. The overall daily loss of α-pinene due to NO_3 could be as high as 35% under the high NO_x scenarios C3 and D3, while the overall loss due to O_3 could be as high as 60% under the relatively cleaner scenarios, and as low as 40% under the dirty ones. The importance of OH reaction appears to be relatively steady between 25-30% under all scenarios.

Isoprene, on the other hand, is scavenged most efficiently by OH radical (55-80%) under all scenarios, followed by O_3($\sim$20%). However, the reaction of NO_3 with isoprene can successfully compete with O_3 under highly polluted scenarios (C3 and D3).

Having better understood the relative strengths of different scavenging pathways, it is now appropriate to analyze the aerosol formation potential of α-pinene under various scenarios. Again, the instantaneous aerosol carbon yields in the form of SOA or SONA can be expressed as

$$Y_i(t) = \left(\frac{d[C_i]/dt}{d[APIN]_{rxn}/dt} \right)_t , \tag{4.5}$$

where i may be SOA or SONA, and the rate of change of α-pinene concentration in the denominator is solely due to chemical reaction and does not include emissions. Figures 4.26 and 4.27 display the instantaneous aerosol carbon yields for scenarios C1, C2, and C3, and D1, D2, and D3, respectively.

As expected, the majority of the SOA forms during the daytime, while the SONA forms more efficiently during the nighttime hours. However, it is interesting to note the relative

contributions of both between the two forest types. Even though the overall relative depletion of α-pinene by OH is more or less constant (Figure 4.25), the SOA formation appears to be quite suppressed in the deciduous forest scenarios compared to the corresponding coniferous forest scenarios. This is probably due to lower HO_2 levels in the deciduous scenarios as a result of quite different radical chemistry in the presence of high concentrations of isoprene. Figure 4.28 shows the time averged SOA, SONA, and total aerosol carbon yields for all scenarios. The daily contribution of SONA to the total yield ranged from 5% under clean conditions to more than 10% for dirty conditions, while that of SOA ranged from 15% under clean conditions to about 6% under dirty conditions. Between the two forest types, the SOA yields under relatively clean coniferous scenarios (C1 and C2) were considerably lower than the corresponding deciduous cases (D1 and D2). As a result, the total aerosol carbon yields in a remote coniferous forest could be almost twice as high as that in a remote deciduous forest. The absolute amounts of aerosol carbon formed in the two forests would, however, depend on the absolute amounts of α-pinene reacted.

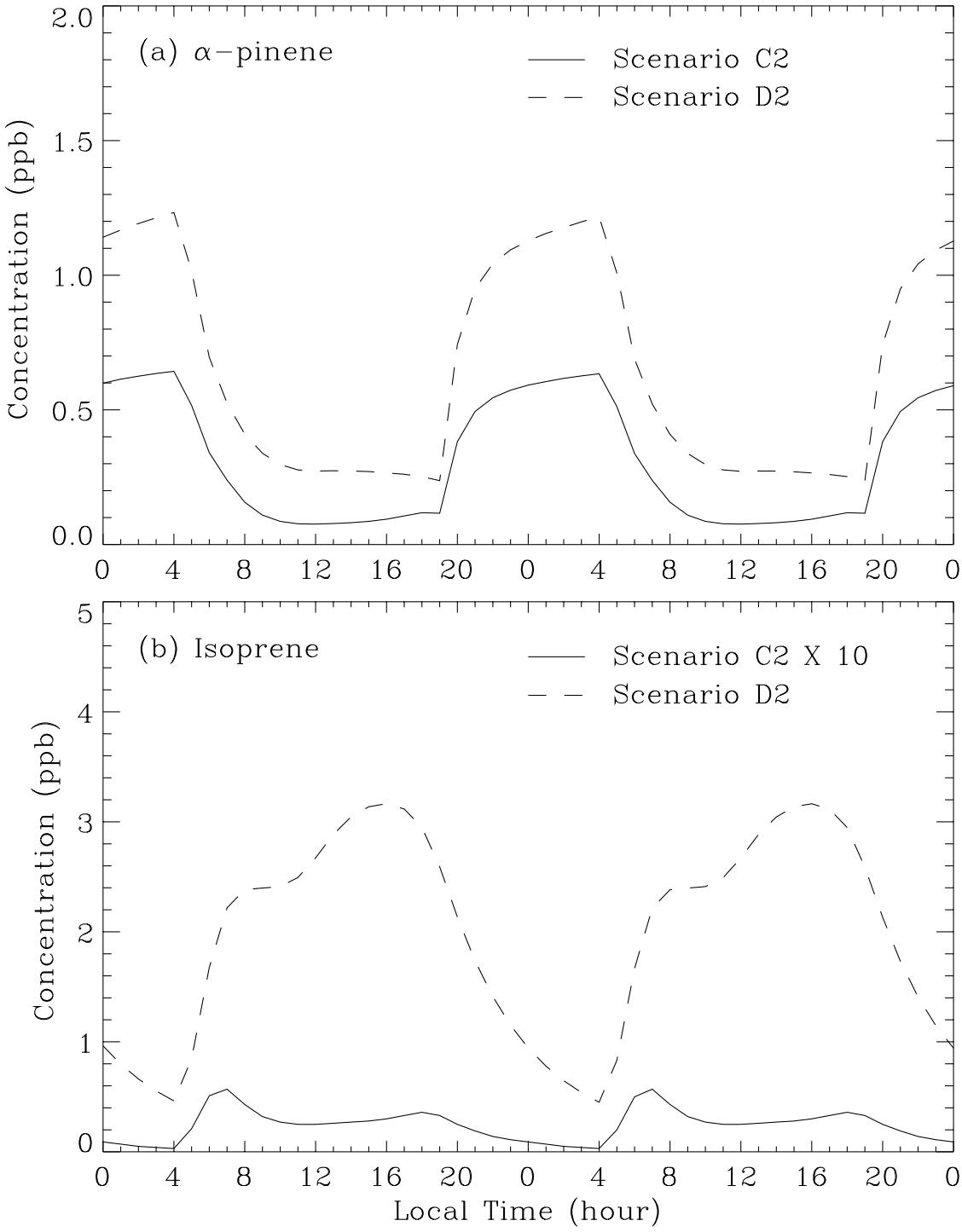

Figure 4.19: Diurnal concentration profiles for scenarios C2, D2 and without biogenic HCs: (a) α-pinene; (b) isoprene.

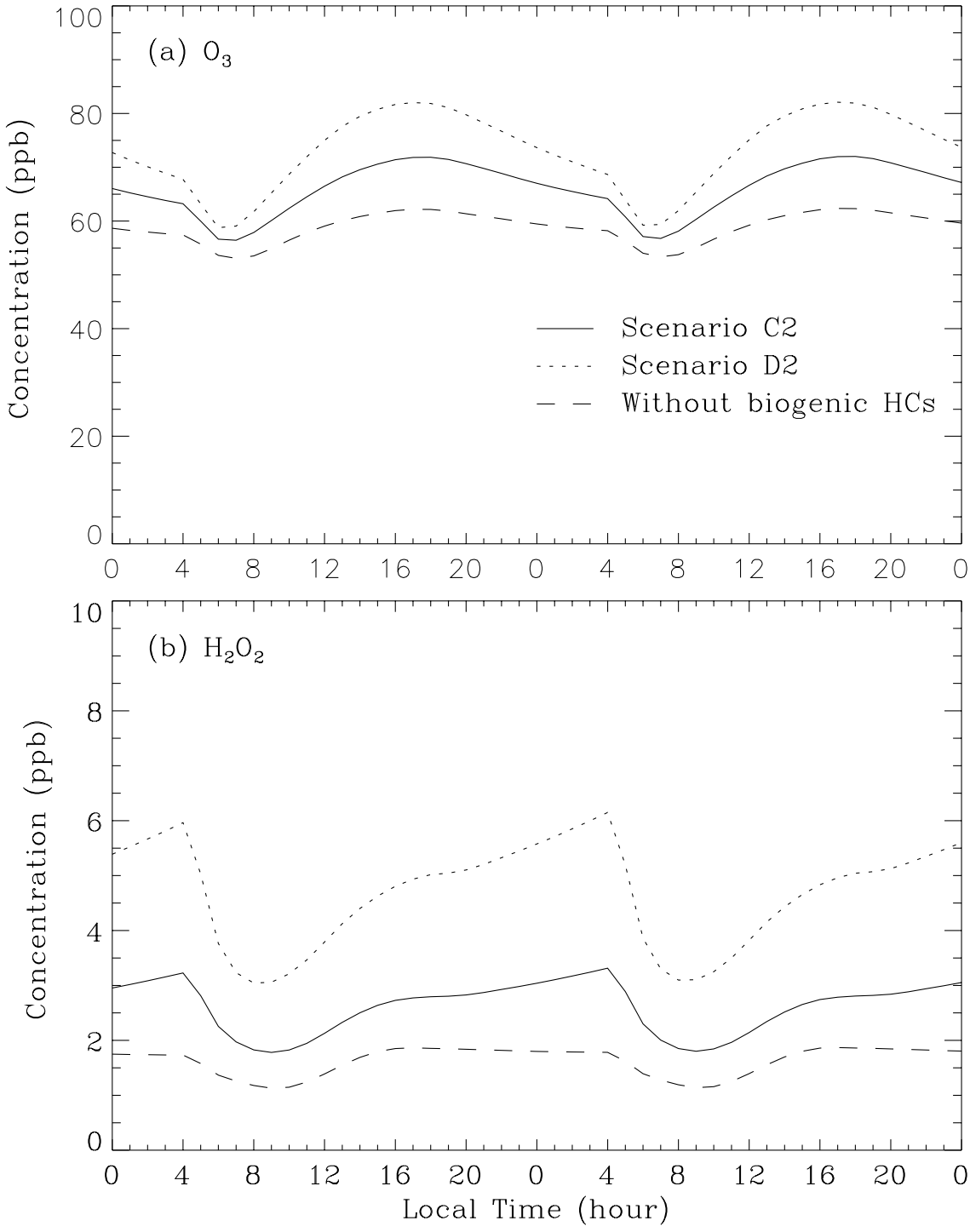

Figure 4.20: Diurnal concentration profiles for scenarios C2, D2 and without biogenic HCs: (a) O_3; (b) H_2O_2.

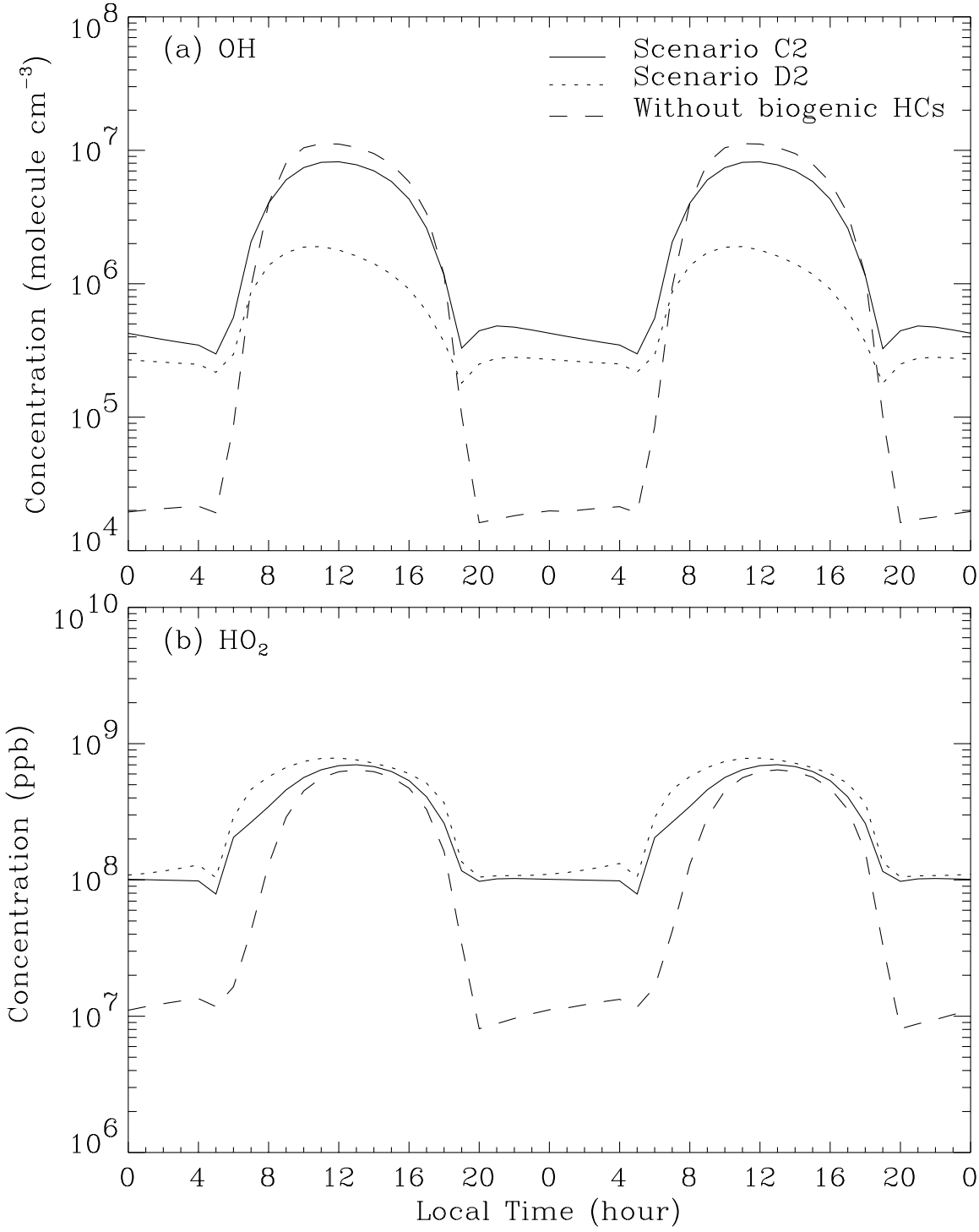

Figure 4.21: Diurnal concentration profiles for scenarios C2, D2 and without biogenic HCs: (a) OH; (b) NO_3.

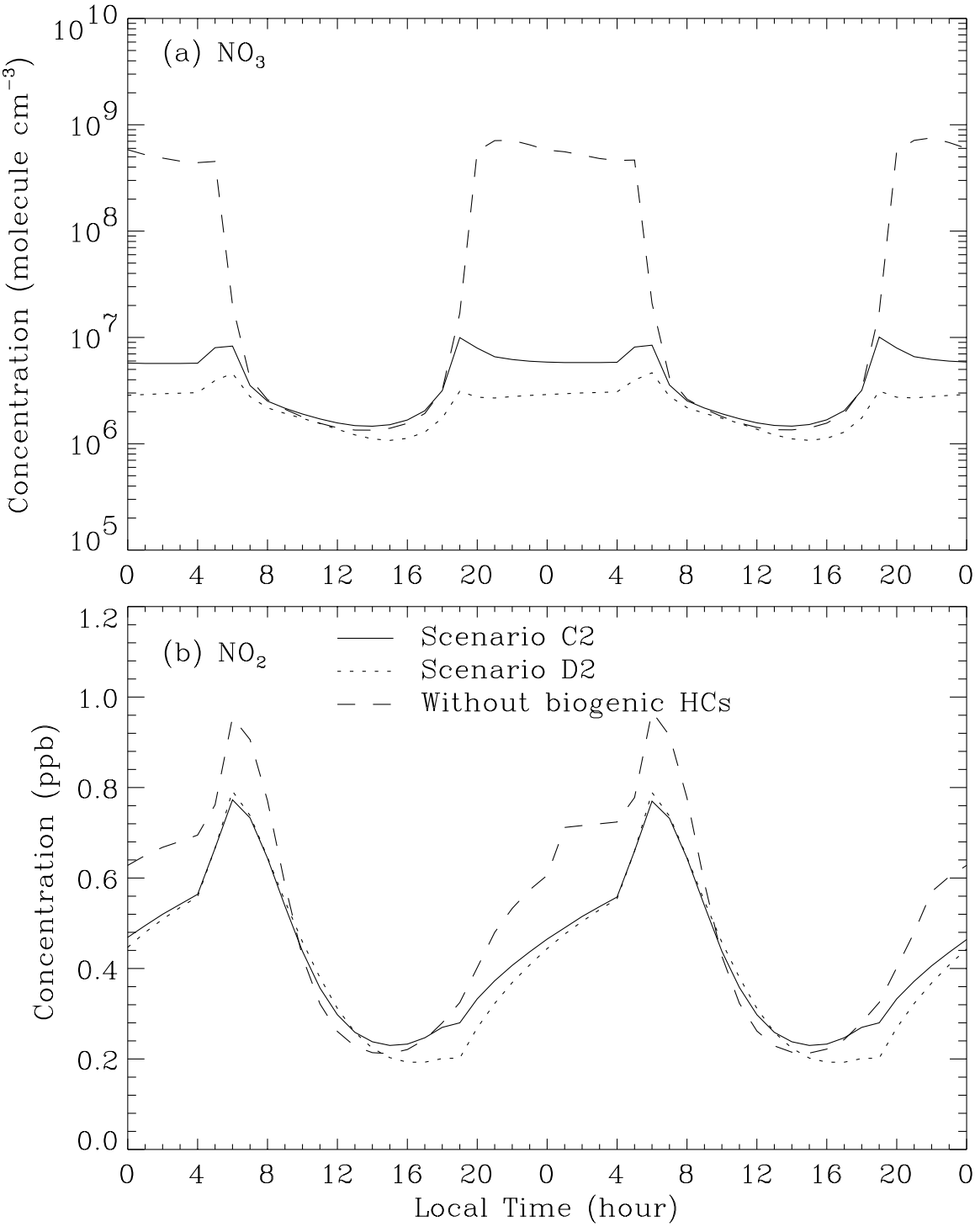

Figure 4.22: Diurnal concentration profiles for scenarios C2, D2 and without biogenic HCs: (a) NO_3; (b) NO_2.

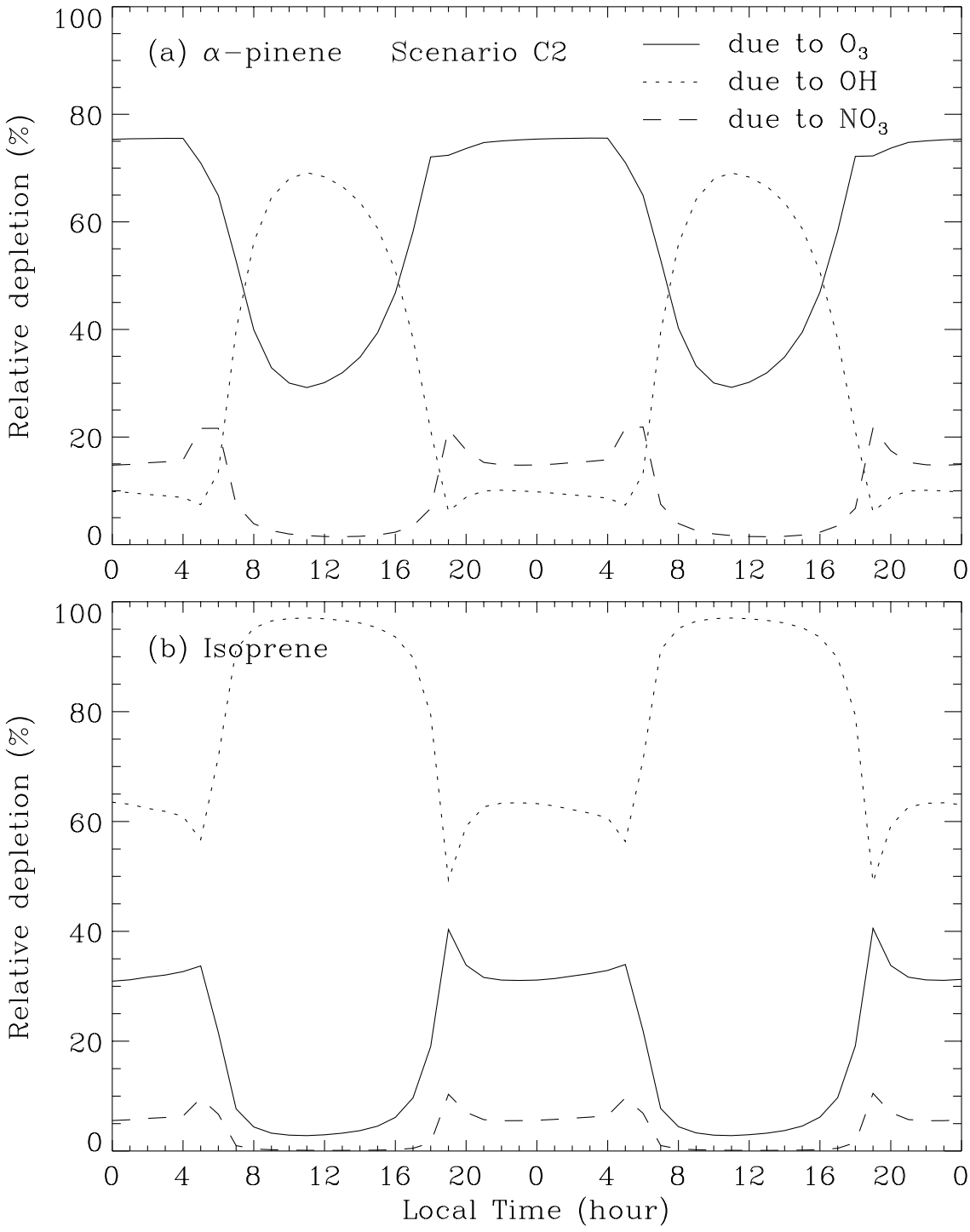

Figure 4.23: Diurnal relative depletion profiles of (a) α-pinene, and (b) isoprene due to reactions with O_3, OH and NO_3 for scenario C2.

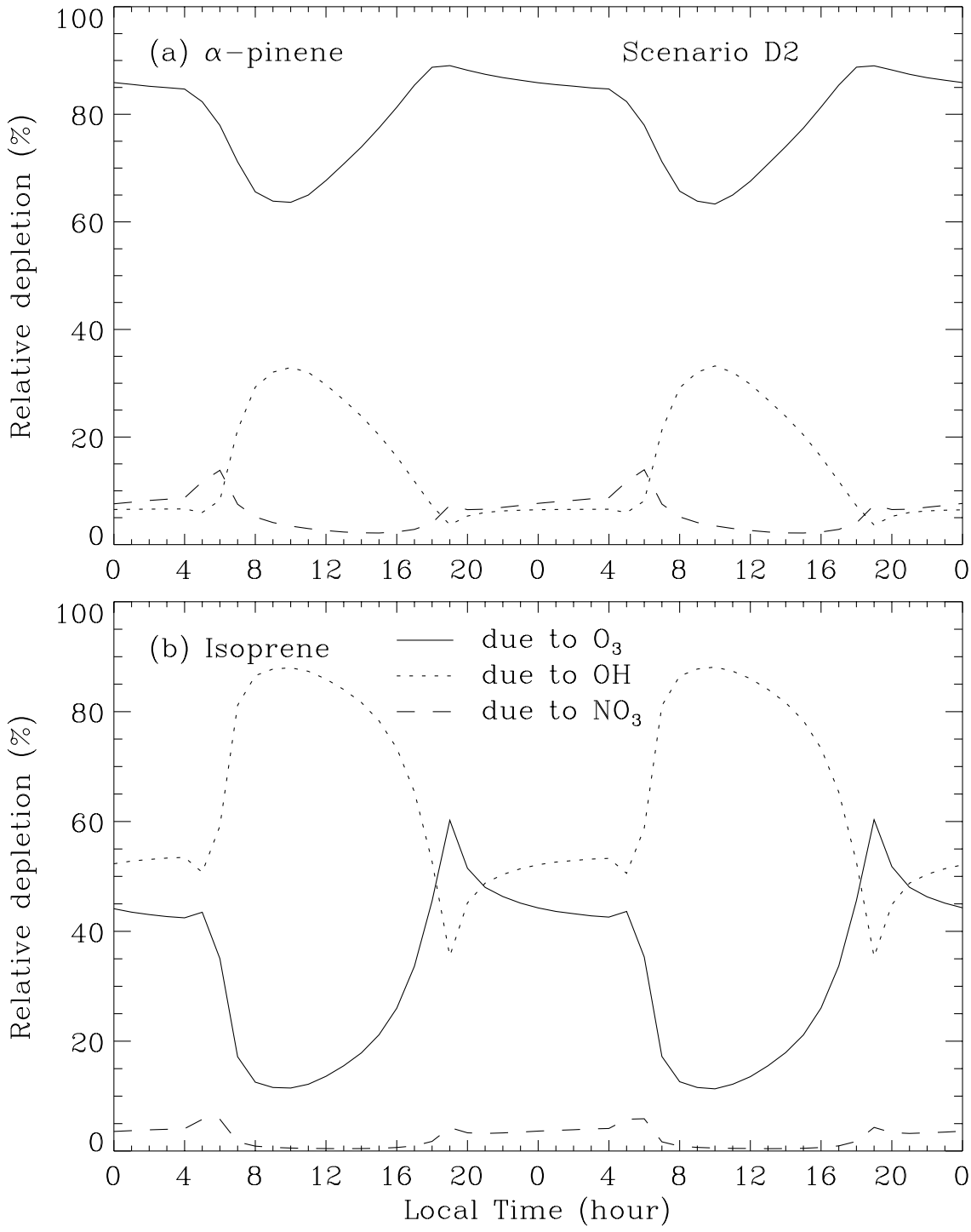

Figure 4.24: Diurnal relative depletion profiles of (a) α-pinene, and (b) isoprene due to reactions with O_3, OH and NO_3 for scenario D2.

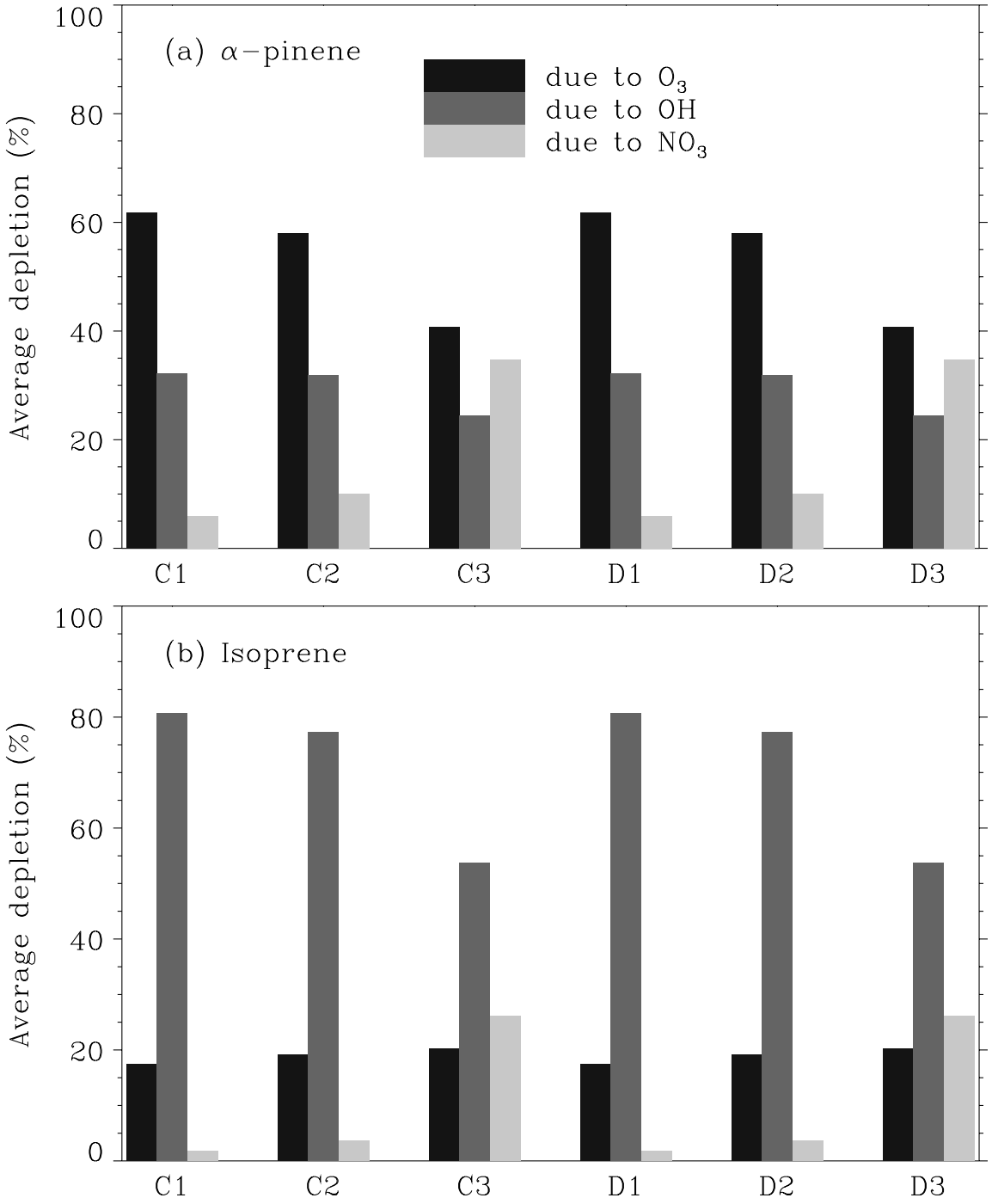

Figure 4.25: Daily average relative depletions of (a) α-pinene, and (b) isoprene due to reactions with O_3, OH, and NO_3.

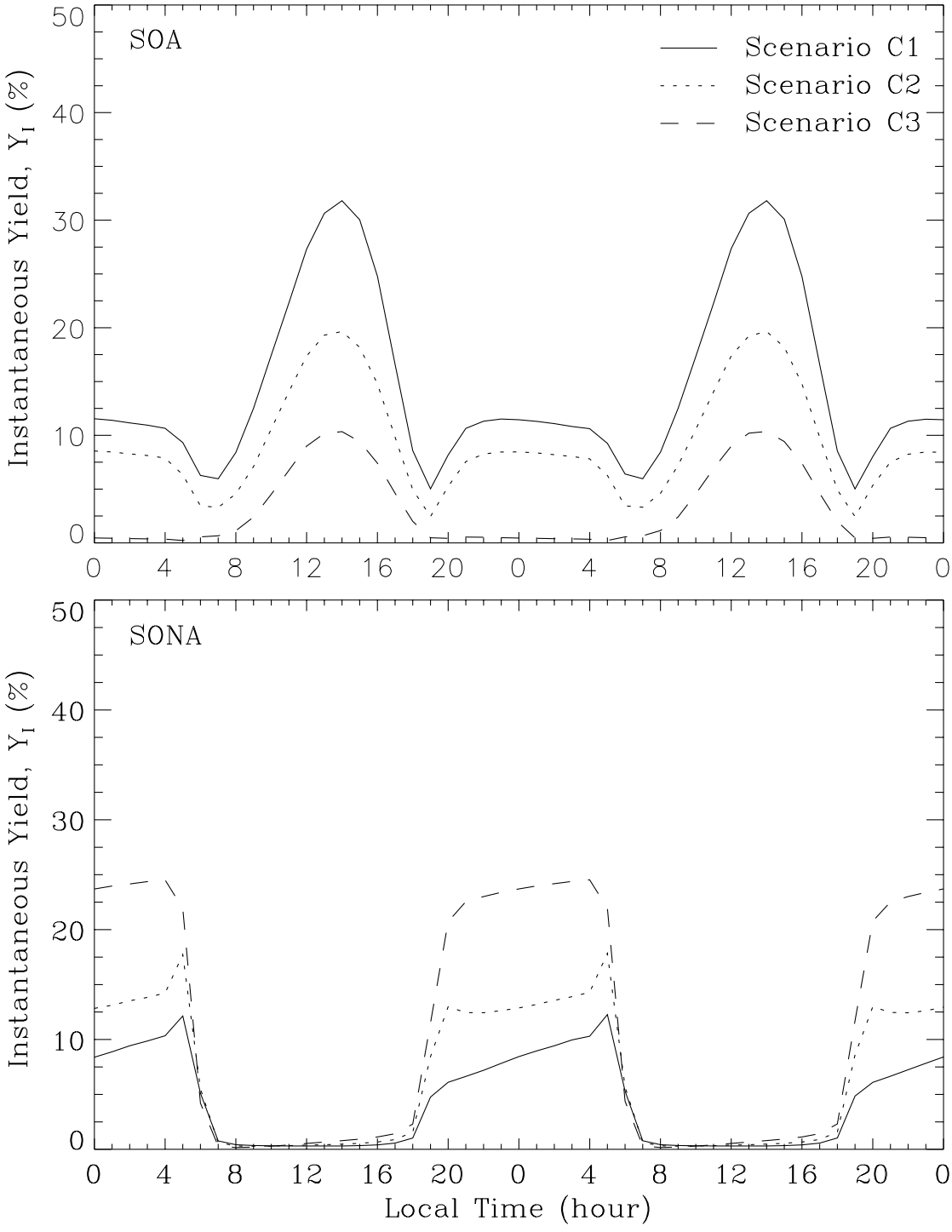

Figure 4.26: Diurnal instantaneous yields of (a) SOA, and (b) SONA with respect to APIN conversion for scenarios C1, C2, and C3.

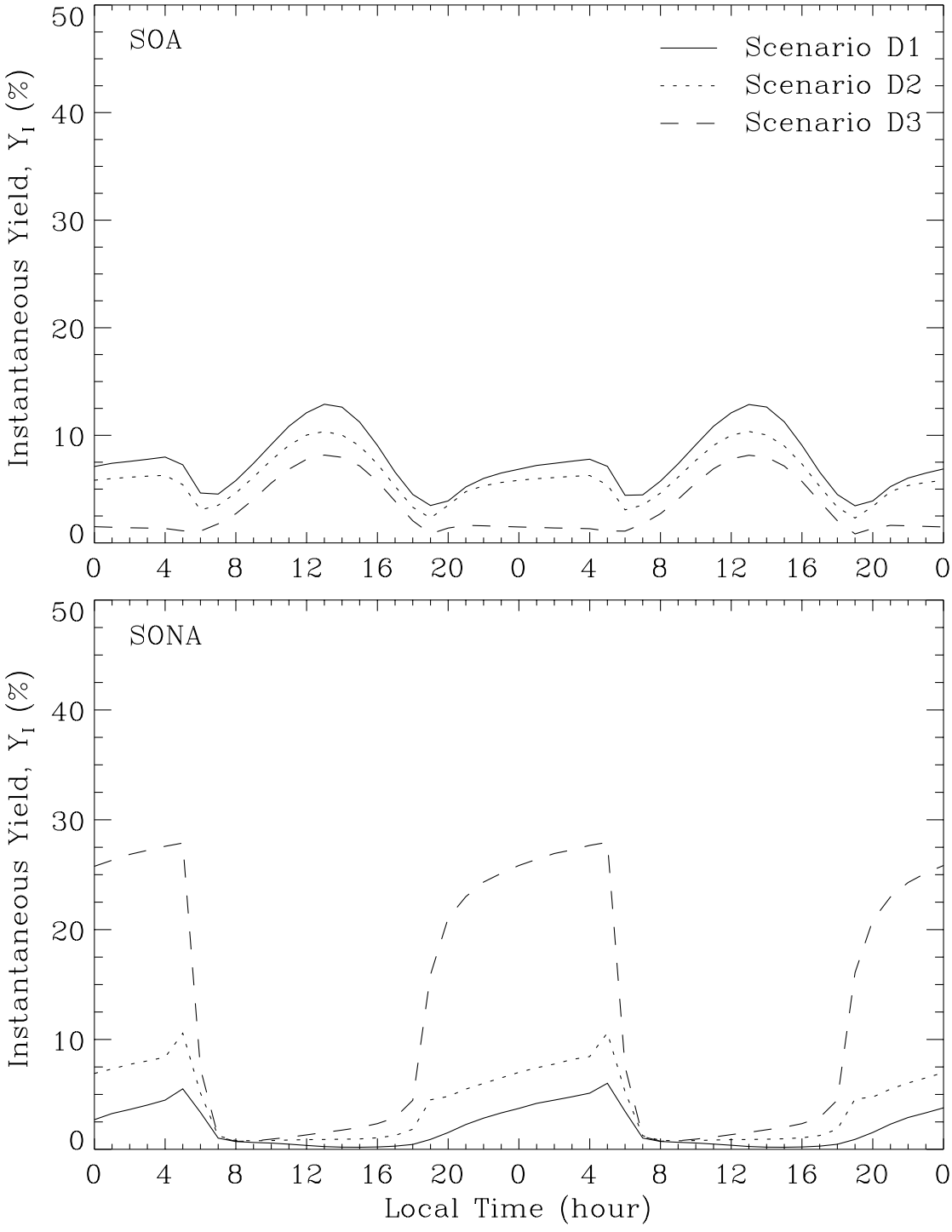

Figure 4.27: Diurnal instantaneous yields of (a) SOA, and (b) SONA with respect to APIN conversion for scenarios D1, D2, and D3.

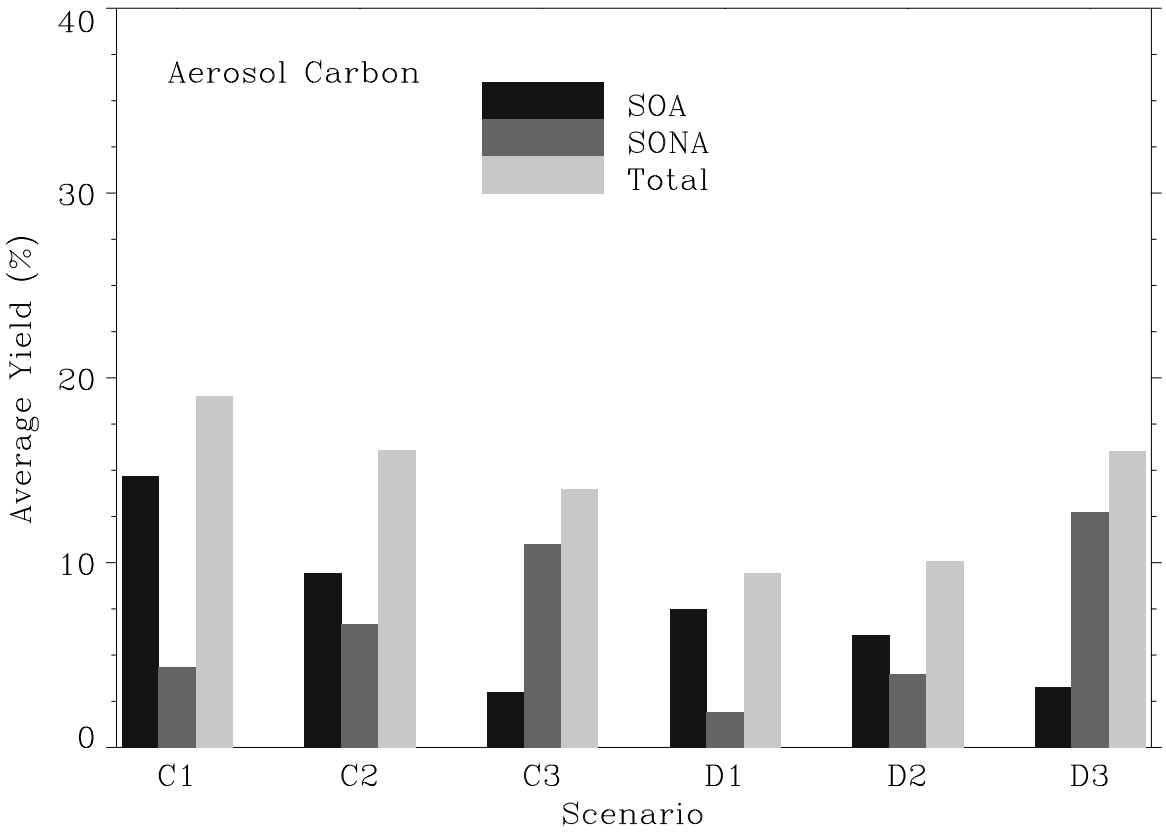

Figure 4.28: Daily average SOA, SONA, and total aerosol carbon yields for all scenarios.

4.5 Condensed Mechanism

The full α-pinene mechanism given in Table 4.5 consists of 15 species and 25 reactions. As mentioned earlier, this mechanism is developed using experiments which employed relatively high initial concentrations of α-pinene and NO_x. Therefore, it is possible that some of the reactions that were important under laboratory conditions may become less important under typical atmospheric conditions. As a result, it may be possible to condense the full mechanism into a more compact version. This is explored briefly in the present section.

Consider the three reactions of PCRIG with H_2O and NO_x. Ambient NO_x concentrations may reach about 10 ppb in urban areas, while they are usually less than 2-3 ppb in less polluted forested regions. Taking both [NO] and [NO_2] at a maximum of 10 ppb each would give the combined first order loss constant of PCRIG of 1.9 s^{-1}, while that due to a water vapor concentration of 3.8×10^{17} molecule cm^{-3} ($\equiv$ 50% RH at 298 K) is about 6.1. Thus, the loss of PCRIG due to NO_x reactions is likely to be small under the conditions of our interest, i.e., regional- and global-scale modeling. Hence, all three reactions are eliminated, and the PCRIG formed in the α-pinene-O_3 reaction is directly assumed to form PALD and H_2O_2.

Similarly, the reactions of PO with NO and NO_2 are of negligible importance under the above NO_x concentrations (1.9 s^{-1}), as compared to the decomposition reaction (1600 s^{-1}). Thus, all PO formed in the PO_2-PO_2 reaction is assumed to form PALD + HO_2.

Furthermore, PALD and PCHO were treated as separate species to interpret certain experimental data while developing the mechanism. However, since they both are assumed to undergo exactly indentical reactions, a common surrogate species, say PCHO, may be used. Also, the two photolytic reactions of PCHO could be lumped together by using appropriate product yields and a lumped rate constant.

Finally, since only the total organic aerosol mass will be used in the aerosol model, both SOA and SONA may be represented by only one species — SOA. Other unknown species such as PONO, $PONO_2$, OGP and NITR could also be eliminated since they do not react further in the present mechanism. With these modifications, the full mechanism was condensed to give a more efficient version listed in Tables 4.8 and 4.9. The condensed mechanism contains only 8 species and 15 reactions, and yields almost identical results under the six scenarios used for model evaluation.

Table 4.8: List Organic Species in Condensed α-pinene Mechanism.

No.	Species	Representation
1.	α-pinene	APIN
2.	β-hydroxyalkylperoxy radical	PO_2
3.	β-nitroxyalkylperoxy radical	$PO_2(ONO_2)$
4.	Surrogate for PALD and other aldehydes	PCHO
5.	Acetylperoxy like compound from PCHO	PCO_3
6.	Surrogate for 9 carbon peroxy radical	QO_2
7.	PAN like compound	PNIT
8.	Secondary organic aerosol precursor	SOA

Table 4.9: Condensed α-Pinene Photooxidation Mechanism

No.	Reaction			Rate Constant k [molecule-cm^3-s]
1.	APIN + O_3	$\xrightarrow{M}$	.68PCHO + .19H_2O_2 + .57OH + .24HO_2 + .37HCHO + .12CO	$2.37 \times 10^{-15} \exp(-904/T)$
2.	APIN + OH	$\xrightarrow{O_2}$	PO_2	$8.53 \times 10^{-12} \exp(550/T)$
3.	APIN + NO_3	$\longrightarrow$	$PO_2(ONO_2)$	6.1×10^{-12}
4.	PO_2 + HO_2	$\longrightarrow$	SOA	$7.7 \times 10^{-14} \exp(1300/T)$
5.	PO_2 + PO_2	$\longrightarrow$	1.1PCHO	4.0×10^{-14}
6.	PO_2 + NO	$\xrightarrow{O_2}$	PCHO + NO_2 + HO_2	$4.2 \times 10^{-12} \exp(180/T)$
7.	$PO_2(ONO_2)$ + HO_2	$\longrightarrow$	SOA	$7.7 \times 10^{-14} \exp(1300/T)$
8.	$PO_2(ONO_2)$ + NO	$\longrightarrow$	NO_2 + products	$4.2 \times 10^{-12} \exp(180/T)$
9.	$2PO_2(ONO_2)$	$\longrightarrow$	products	1.1×10^{-14}
10.	PCHO + OH	$\longrightarrow$	PCO_3	$1.16 \times 10^{-11} \exp(250/T)$
11.	PCHO + $h\nu$	$\longrightarrow$	.09ALD2 + .09OLE + .27PAR + .09AONE + .91QO_2 + .91HO_2 + .91CO	11 $\times$ j(ALD2)
12.	PCO_3 + NO	$\xrightarrow{O_2}$	QO_2 + NO_2 + CO_2	$3.5 \times 10^{-11} \exp(-180/T)$
13.	PCO_3 + NO_2	$\longrightarrow$	PNIT	$2.6 \times 10^{-12} \exp(-380)$
14.	PNIT	$\longrightarrow$	PCO_3 + NO_2	$2.0 \times 10^{+16} \exp(-180/T)$
15.	QO_2 + NO	$\xrightarrow{O_2}$	ALD2 + 4PAR + AONE + NO_2 + HO_2	$4.2 \times 10^{-12} \exp(180/T)$

4.6 Concluding Remarks

The α-pinene photooxidation mechanism developed in this chapter was applied under a range of conditions for two forest types — coniferous and deciduous. While considerable differences could be expected in the aerosol yields under different conditions, contributions of both SOA and SONA appear to be important. Also, coniferous forests, with relatively low isoprene emissions, could result in about twice as high aerosol carbon yields from α-pinene reactions compared to similar deciduous scenarios. The biogenic hydrocarbons were found to have significant influence on the oxidant cycle under all scenarios. Both daytime and nighttime chemistries could be significantly different in the presence of α-pinene and isoprene.

The proposed α-pinene mechanism was further condensed to yield a more compact mechanism, suitable for large-scale applications. The condensed version is, thus, recommended for the CBM-Z for global modeling.

Chapter 5

Marine Gas-Phase Chemistry: DMS

A global tropospheric chemistry model is incomplete without adequate representation of the marine air chemistry. Among other gases, oceanic emissions include natural sulfur compounds such as dimethylsulfide (DMS), hydrogen sulfide (H_2S), carbon disulfide (CS_2), and carbonyl sulfide (COS). Current estimates of their global emissions indicate that DMS may be the most dominant naturally occurring sulfur carrier at about 11-40 Tg S yr^{-1} (Spiro *et al.*, 1992). According to Andreae (1986), the global H_2S flux is about 3 Tg S yr^{-1}, while Saltzman and Cooper (1988) suggested an upper limit of 1 Tg S yr^{-1}; emissions of COS and CS_2 are thought to be even smaller (Spiro *et al.*, 1992).

Oceanic DMS originates from the cleavage of β-dimethylsulfoniopropionate (DMSP) which plays an important role in osmoregulation of phytoplankton cells (Vairavamurthy *et al.*, 1985). Other suggested roles include the bactericidal properties of the acrylic acid formed when DMSP is cleaved, and as a cryoprotectant for organisms living in very low temperature marine environments, such as polar waters and ice (Liss *et al.*, 1993, and references therein). Therefore, the seasonality in the level of biological activity therefore has a strong influence on the DMSP and DMS concentrations in the surface and near-surface temperate waters. Thus, the resulting ocean to atmosphere fluxes also exhibits a seasonal behavior. The emission flux is also dependent on the water temperature and surface wind speed. Based on the climatological surface wind speeds, Spiro *et al.* (1992) have constructed monthly global emission flux fields. Figures 5.1 and 5.2 show the average DMS emissions for July and January, respectively.

Marine boundary layer DMS concentrations are typically in the range of 50-500 ppt (Andreae *et al.*, 1985; Yvon *et al.*, 1996). Its oxidation in the atmosphere ultimately leads to the formation of SO_2, H_2SO_4, and methanesulfonic acid (MSA). Gaseous H_2SO_4 may deposit on pre-existing marine aerosols, or nucleate to form new particles under clean conditions. Since MSA is also relatively non-volatile, it also may deposit on pre-existing marine aerosols. Thus, although net global DMS emission is an order of magnitude lower than total anthropogenic SO_2 emission (Figure 5.3), it is still the major source of sub-micron size particles in the remote marine troposphere. An accurate mechanism of the DMS photochemistry is

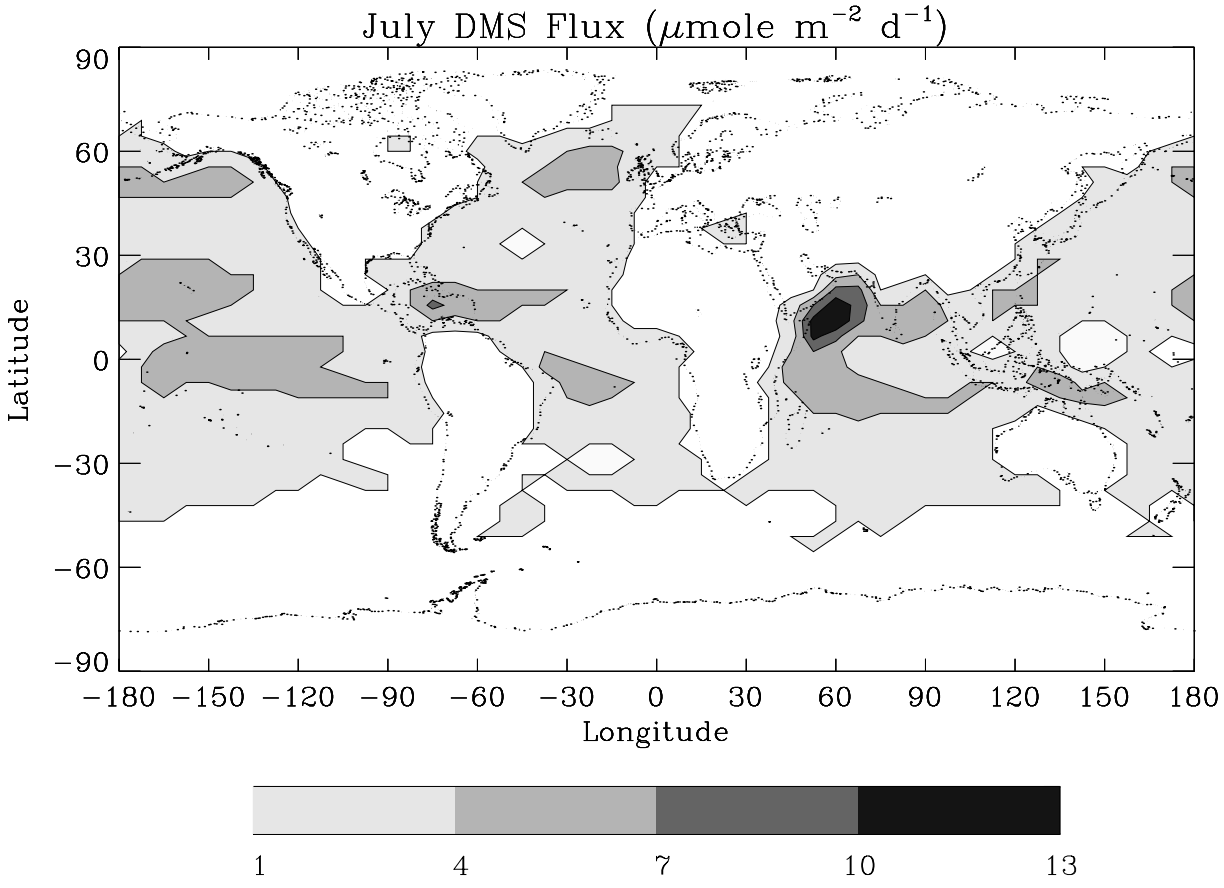

Figure 5.1: July DMS emission flux based on the global inventory of Spiro *et al.* (1992).

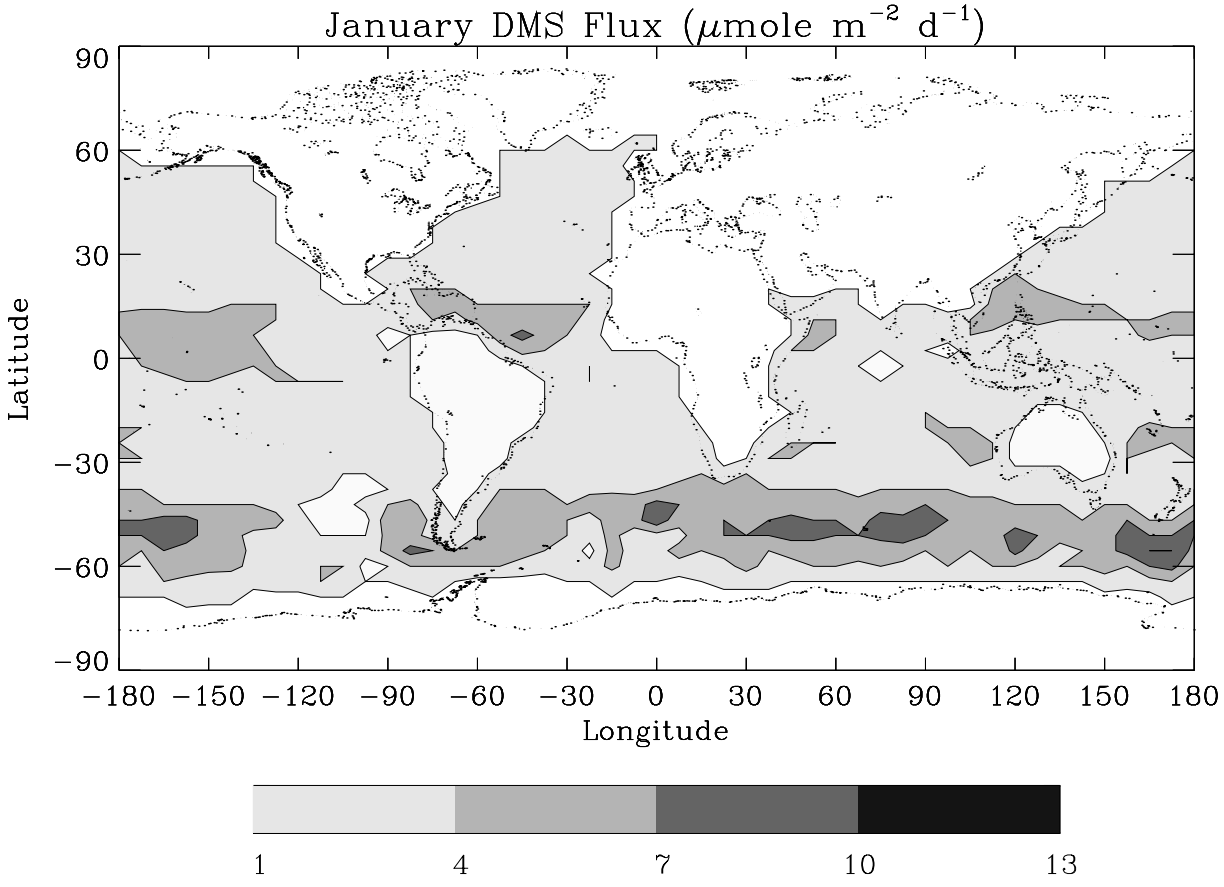

Figure 5.2: January DMS emission flux based on the global inventory of Spiro *et al.* (1992).

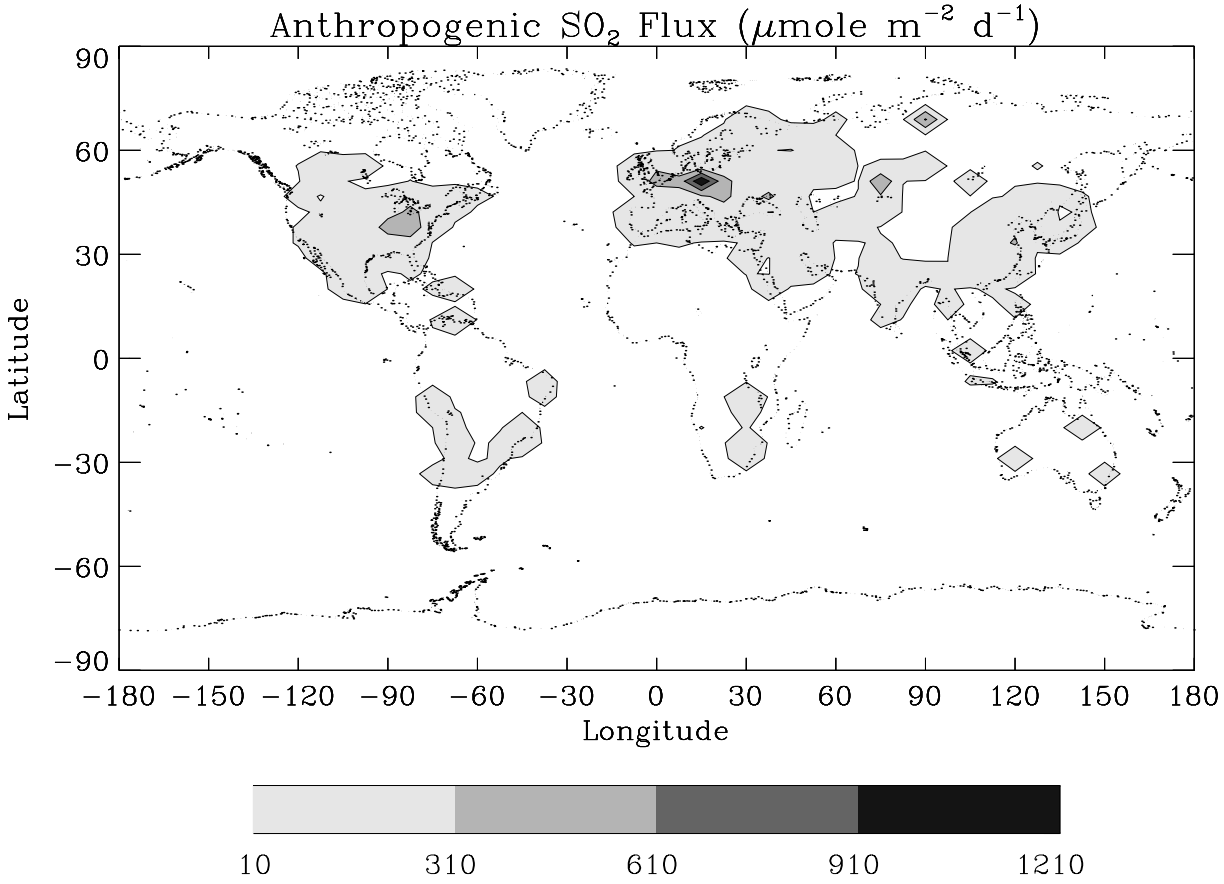

Figure 5.3: Anthropogenic SO_2 emission flux based on the global inventory of Spiro *et al.* (1992).

necessary to distinguish between H_2SO_4 vapor, which can form new aerosol particles through homogeneous nucleation, and MSA, which cannot. This chapter explores the available DMS photooxidation mechanisms for the global model and develops a simplified scheme for incorporation into a global tropospheric chemistry model.

5.1 Literature Review

Several research groups have investigated various aspects of the DMS photochemistry, and as result a relatively good understanding has been achieved regarding various oxidation pathways. (Wine *et al.*, 1981; Grosjean and Lewis, 1982; Hatakeyama *et al.*, 1982, 1985; Hatakeyama and Akimoto, 1983; Balla and Heicklen, 1985; Balla *et al.*, 1986; Hynes *et al.*, 1986; Wallington *et al.*, 1986a, 1986b; Barnes *et al.*, 1987, 1988, 1989, 1994, 1996; Dominé *et al.*, 1989; Tyndall and Ravishankara, 1989a,b; Yin *et al.*, 1990a,b; Jensen *et al.*, 1991, 1992; Van Dingenen *et al.*, 1994). While the above list of references is certainly not exhaustive, it probably represents the important developments and findings in the last fifteen years. Based on the available data then and their own experimental work, Yin *et al.* (1990a,b) carefully developed a comprehensive photooxidation mechanism of DMS, and evaluated it against a series of outdoor smog chamber experiments with a very good degree of success. The mechanism consists of about 40 sulfur containing species and 140 reactions, and is schematically illustrated in Figure 5.4.

In the ambient atmosphere, DMS is found to react with OH, NO_3, and $O(^3P)$. The reaction with OH can proceed in two ways — via abstraction of a hydrogen atom, or by addition of an OH radical to the sulfur atom. The branching ratio for this reaction is found to be temperature dependent such that the abstraction pathway dominates ($\sim$70%) at room temperature, while the addition pathway becomes increasingly important at temperatures below 280 K (see Figure 5.5, Hynes *et al.*, 1986). The addition pathway proceeds via methanesulfenic acid (CH_3SOH), dimethylsulfoxide (DMSO), dimethylsulfone ($DMSO_2$), methanesulfinic acid (CH_3SO_2H), and other radicals. Most reactions of these species lead to the formation of methanesulfonyl radical (CH_3SO_2).

On the other hand, the abstraction pathway proceeds via a series of intermediates including methanethiyl radical (CH_3S) and methanesulfinyl radical (CH_3SO), and ultimately leads to the formation of CH_3SO_2. The initial DMS reactions with NO_3 and $O(^3P)$ also lead to CH_3SO_2 via these intermediates. The fate of the CH_3SO_2 radical is important as it may

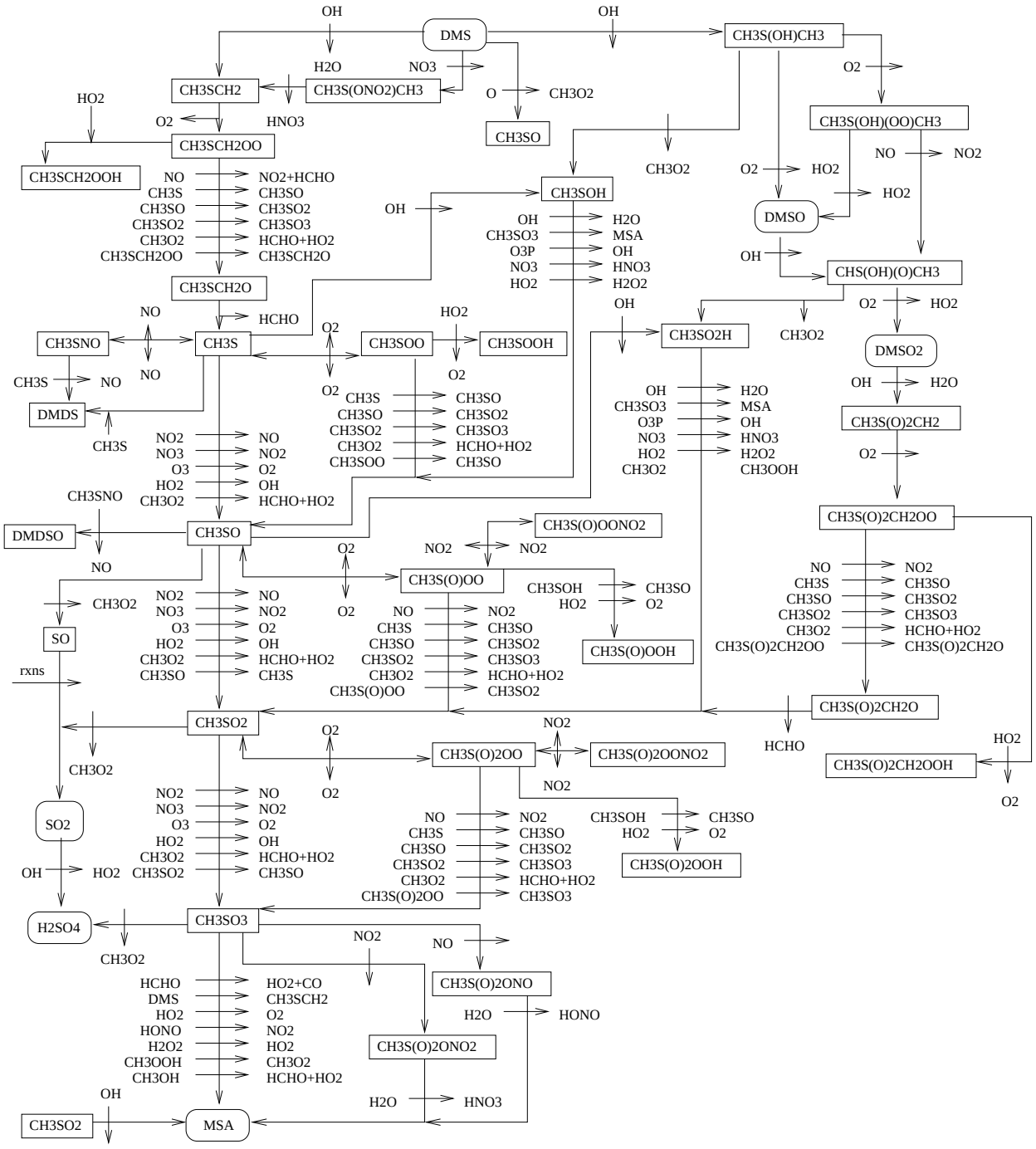

Figure 5.4: Comprehensive DMS photooxidation scheme proposed by Yin *et al.* (1990a).

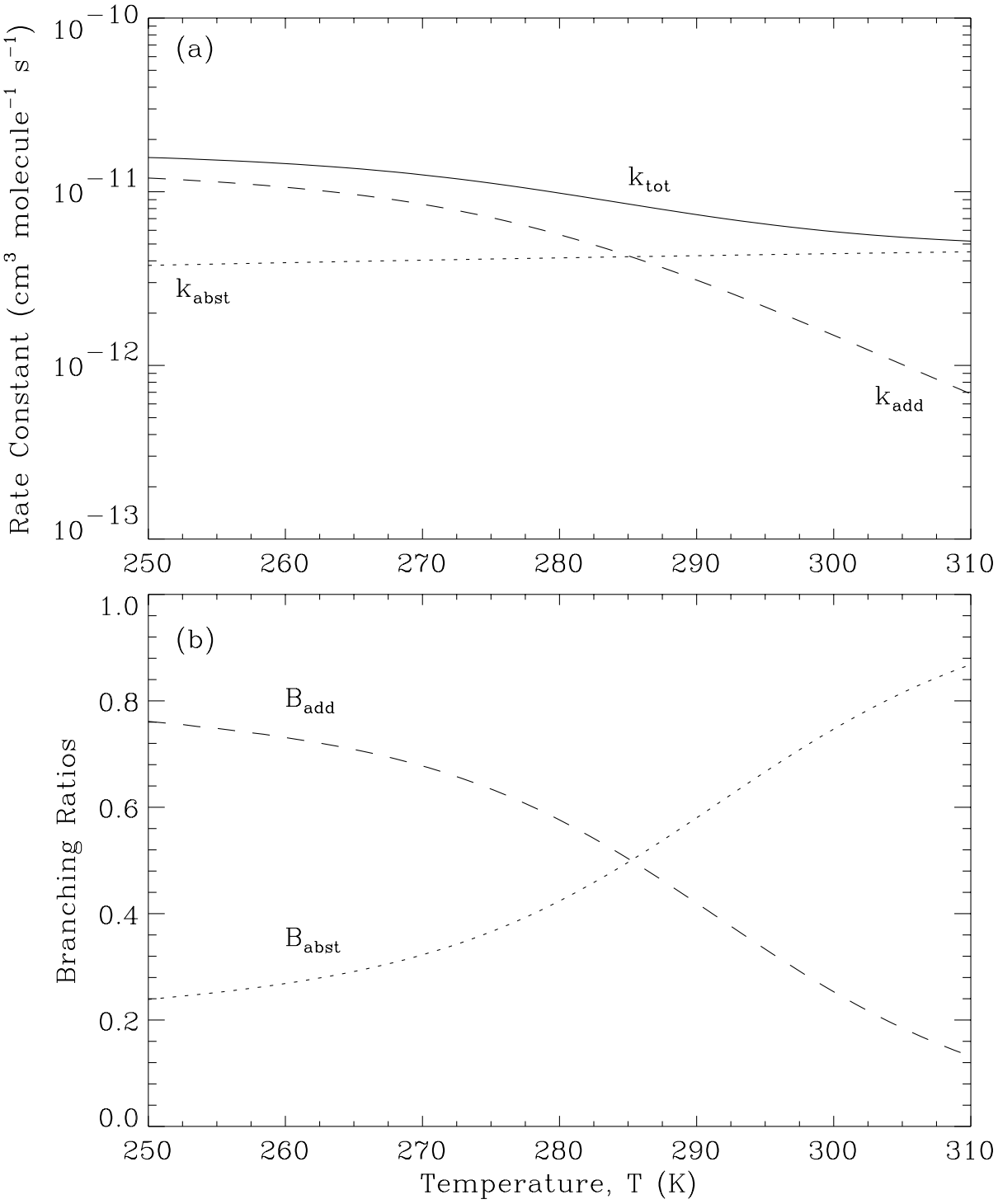

Figure 5.5: (a) Rate constants of the two initial DMS-OH reaction pathways, and (b) their branching ratios (after Hynes *et al.*, 1986).

rapidly decompose to give SO_2 or undergo further oxidation to form the CH_3SO_3 radical. Similarly, the CH_3SO_3 radical may decompose to give SO_3, which is assumed to react rapidly with water vapor forming gaseous H_2SO_4, or further react to form MSA.

Although Yin *et al.*'s mechanism can successfully simulate several experimental data, it fails to explain some of the observed MSA to non-sea salt sulfate (NSSS) ratios measured at several locations around the globe The MSA to non-sea-salt sulfate (NSSS) molar ratios have been found to gradually increase as one moves towards the poles, ranging from about 0.01 at the equator to more than 0.6 at higher latitudes. Figure 5.6a shows a composite of various field observations of the summertime MSA/NSSS ratio as a function of latitude (Saltzman *et al.*, 1983; Berresheim *et al.*, 1990; Galloway *et al.*, 1990; Mihalopoulos *et al.*, 1990; Bürgermeister and Georgii, 1991; Gillett *et al.*, 1993; Li *et al.*, 1993; Li and Barrie, 1993; Wylie and de Mora, 1996; Allen *et al.*, 1997). Temperature dependence of the MSA/NSSS ratio appears to be the most reasonable explanation for this latitudinal variation. On the other hand, long-term seasonal measurements (Figure 5.6b) at high latitude sites reveal that MSA/NSSS ratios experience a maxima during summer and a minima in winter (Gillett *et al.*, 1993; Allen *et al.*, 1997). This indicates that the temperature dependence may not be a simple one.

Yin *et al.*'s mechanism gives very little MSA ($< 0.5\%$) for temperatures ranging from 270 K to 310 K, and thus, fails to capture this important feature. As a result, several recent modeling studies have proposed and adopted alternate pathways for MSA formation (Koga and Tanaka, 1993, 1996; Hertel *et al.*, 1994). Although these alternate pathways are capable of predicting reasonable MSA concentrations, they may not necessarily be based on correct mechanistic information.

Three different mechanistic interpretations regarding the yields of SO_2, H_2SO_4 and MSA have been suggested. Each interpretation and its implication is described below, and a semi-quantitative attempt is made to evaluate it in the light of available information.

5.1.1 Initial DMS-OH Reaction

The temperature dependence of MSA/NSSS ratio has often been linked to the temperature dependence of the addition and abstraction branching ratio of the DMS-OH reaction. Since the OH-addition pathway becomes increasingly dominant at lower temperatures, it has been suggested this pathway is responsible for MSA formation (Berresheim, 1987; Berresheim

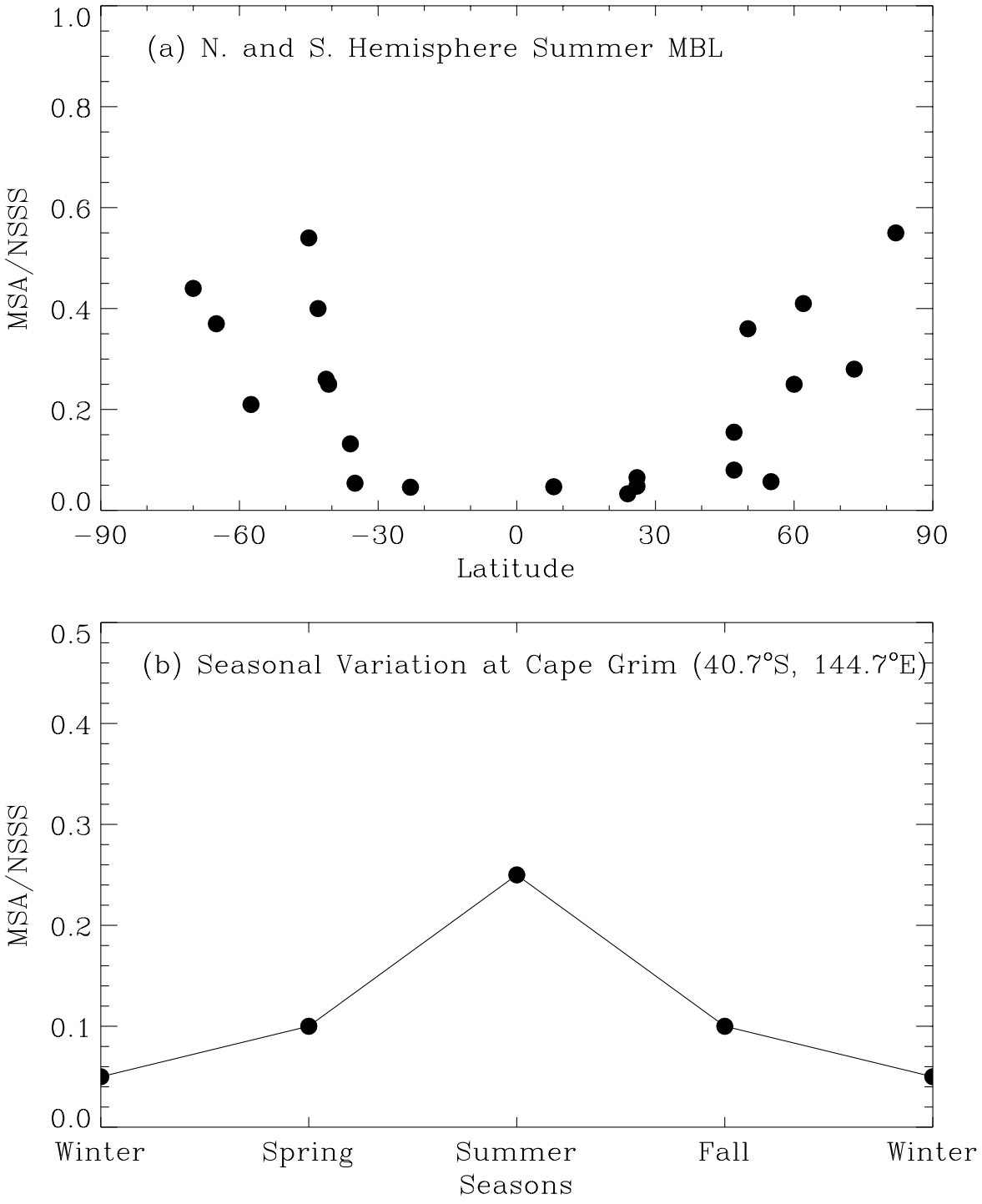

Figure 5.6: Observed MSA/NSSS ratios: (a) Latitudinal variation in summer; (b) Seasonal variation at Cape Grim (refer text for references).

et al., 1990). Recently, Koga and Tanaka (1993) proposed a condensed chemical mechanism in which the DMS-OH addition leg is comprised of the following reactions (the rate constants are expressed in molecule $-$ cm^3 $-$ s units):

$CH_3S(OH)CH_3 + O_2$	$\longrightarrow$	DMSO + HO_2	$k = 2 \times 10^{-12}$
$CH_3S(OH)CH_3 + O_2$	$\longrightarrow$	$CH_3SOH + CH_3O_2$	$k = 1 \times 10^{-12}$
$CH_3S(OH)CH_3 + O_2$	$\longrightarrow$	$CH_3S(OH)(OO)CH_3$	$k = 1 \times 10^{-12}$
$CH_3SOH + O_2$	$\longrightarrow$	MSA	$k = 1.7 \times 10^{-17}$
$CH_3S(OH)(OO)CH_3$	$\longrightarrow$	MSA	$k = 88.0$

Reactions on the DMS-OH addition leg were based on the mechanism of Yin *et al.* The mechanism was then able to predict latitudinal MSA/NSSS ratios in accordance with observations. However, the above scheme to produce MSA is inconsistent with the experimental work of Barnes *et al.* (1996) who estimated an overall yield of 30% for DMSO under NO_x-free experiments carried out in synthetic air at 296 K. This latter result is in excellent agreement with the mechanism of Yin *et al.*

Secondly, the above reaction of CH_3SOH with O_2 is not consistent with the structural difference between CH_3SOH and CH_3SO_3H (Penn *et al.*, 1978; Yin *et al.*, 1990a), and with the suggestion the similar reaction between DMS and O_2, if it occurred, would be faster because of the electrophilic nature of O_2. Thus, the hypothesized connection between MSA/NSSS, DMS-OH branching ratio, and temperature is probably erroneous; and it appears that the chemical fates of CH_3SO_2 and CH_3SO_3 will decide the yields of SO_2, H_2SO_4 and MSA.

5.1.2 Decomposition of the CH_3SO_2 Radical

Another suggestion was that the thermal decomposition of CH_3SO_2 may not be important (Hertel *et al.*, 1994). This means that most of the CH_3SO_2 radical would be oxidized to CH_3SO_3 which can thermally decompose to give H_2SO_4, or react further to form MSA. Two different values for the first order rate constant of CH_3SO_2 decomposition have been reported in the literature. Good and Thynne (1967) reported the following expression for the rate constant

$$k_{CH_3SO_2} = 10^{13} \times \exp(-11313/T) \quad s^{-1}, \tag{5.1}$$

which gives a value of 3.4×10^{-4} s^{-1} at 298 K. However, it should be noted that Good and Thynne (1967) mention that much reliance cannot be placed on their Arrhenius parameters

because of the limited temperature range over which they carried out the experiments, and of certain experimental difficulties involved in the measurement of small changes in SO_2 concentration.

More recently, Mellouki *et al.* (1988) also studied the decomposition of the CH_3SO_2 radical, and estimated $k_{CH_3SO_2}$ to be about 10 s^{-1} at room temperature and 0.33 Torr pressure. The two values, differing by a factor of 30,000, would predict completely different fates of the CH_3SO_2 radical, and as a result, completely different SO_2, H_2SO_4, and MSA yields under, otherwise, identical conditions. Therefore, the important question is that which estimate is closer to the actual value. The low value of $k_{CH_3SO_2}$ would give very little SO_2 under typical marine boundary layer conditions. This result may lend support to the observed low SO_2 concentrations (Bandy *et al.*, 1992) and the high average DMS/SO_2 ratios from 18 upto 32 (Huebert *et al.*, 1993).

On the other hand, Yin *et al.* observed high SO_2 yields (60-70%) in their smog chamber experiments. Similar yields have also been observed by Grosjean and Lewis (1982) and Barnes *et al.* (1988, 1996). While some experimental studies (Hatakeyama and Akimoto, 1983; Hatakeyama *et al.*, 1982, 1985; Niki *et al.*, 1983) suggest rather low SO_2 yields in the range of 20-30%, Yin *et al.* qualitatively showed that these differences could be attributed to the differences in the experimental conditions, such as initial reactant concentrations, temperature, and light intensity. Yin *et al.* had to employ a value of 11 s^{-1} for $k_{CH_3SO_2}$ to reproduce the high yields observed in their experiments. This is in complete agreement with the value estimated by Mellouki *et al.* (1988), and it appears that the actual value is probably closer to these estimates. Using the C-S bond dissociation energy (BDE) in CH_3SO_2 of about 17.2 kcal mol^{-1} as the activation energy, Yin *et al.* expressed the rate constant as

$$k_{CH_3SO_2} = 5.0 \times 10^{13} \times \exp(-8686/T) \quad s^{-1}. \tag{5.2}$$

5.1.3 Decomposition of the CH_3SO_3 Radical

The estimated C-S BDE in CH_3SO_3 is about 22 kcal mol^{-1}, and would, therefore, also rapidly decompose to give H_2SO_4 and CH_3O_2 in the presence of water vapor and O_2. Although the rate constant for this reaction has not been measured, a value of 0.16 s^{-1} was estimated by Yin *et al.* However, no activation energy was associated with it in their mechanism. Thermal decomposition of the CH_3SO_3 radical is in competition with its reaction with HO_2 to form MSA. Turnipseed and Ravishankara (1993) suggested that an activation

energy of about 25 kcal mol^{-1} for the decomposition reaction could explain the temperature dependence of the MSA/NSSS ratio. This is probably the most plausible hypothesis, and is investigated further in this work.

5.2 Condensed Mechanism

The comprehensive mechanism of Yin *et al.* is too large for practical applications in three-dimensional models, and therefore, must be condensed into a more tractable form. Although the comprehensive mechanism was developed and evaluated using laboratory experiments involving very high initial concentrations of DMS and NO_x (ppm levels), it is expected to be valid under relatively clean marine air conditions characterized by ppt levels of NO_x and DMS. Thus, many of the oxidation pathways, which are important at very high concentrations, may become less important or virtually negligible under actual ambient conditions. Following this reasoning, the comprehensive DMS scheme was augmented with the CBM-Z model, and was condensed by eliminating consistently unimportant reactions for several scenarios of varying NO_x, O_3, NMHC, temperature, and humidity. While reducing the number of reactions, this procedure does not change the number of species in the scheme.

Another approach used to reduce the total number of sulfur species and associated reactions was identification of the rate controlling steps or legs in the full mechanism, and careful lumping of the intermediate relatively faster legs (a leg refers to a set of parallel reaction pathways for a species being converted to another species). Only the legs which are always guaranteed to be fast under various simulated realistic conditions were eliminated by lumping: fast unimolecular decompositions, fast oxidations by oxygen molecules, and fast reactions with water vapor are specific examples. Both techniques are illustrated below.

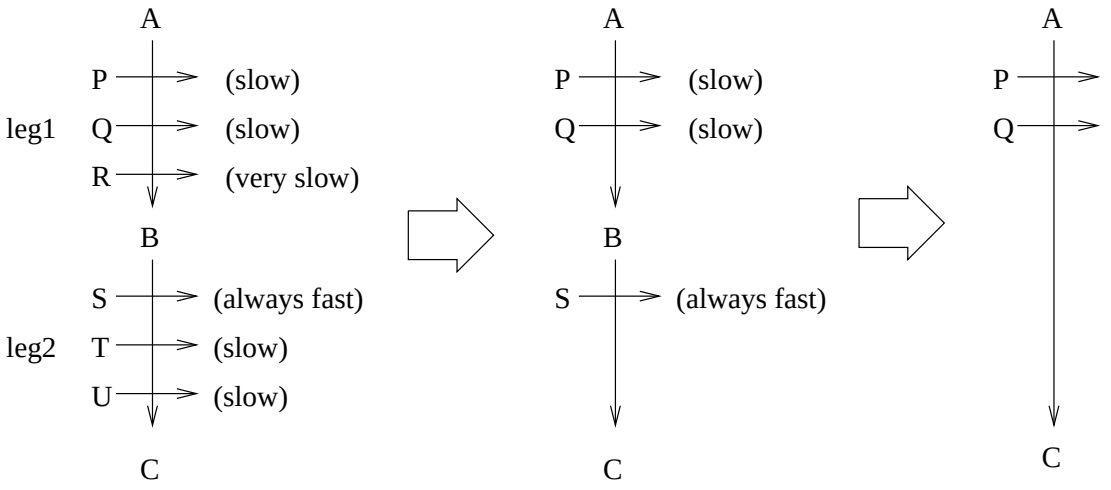

Examine all reactions | Eliminate relatively slow reactions | Keep the rate determining leg and lump the fast leg

The condensed DMS mechanism involves only 12 sulfur species and 33 reactions (refer to Figure 5.7). The important pathways have been preserved so that it can handle relatively polluted conditions as well. The condensed DMS mechanism is computationally about 40-50% faster with respect to the full mechanism, and predicts SO_2, H_2SO_4, MSA, DMSO, $DMSO_2$, NO_x, and O_3 concentrations within 5-15% deviations under a range of typical marine air conditions. The list of species and reactions in the condensed mechanism are shown in Tables 5.1 and 5.2, respectively.

Table 5.1: List Organic Species in Condensed DMS Mechanism.

No.	Species	Representation
1.	Dimethylsulfide (CH_3SCH_3)	DMS
2.	Methanesulfonic acid (CH_3SO_3H)	MSA
3.	Dimethylsulfoxide ($CH_3S(O)CH_3$)	DMSO
4.	Dimethylsulphone ($CH_3S(O)_2CH_3$)	$DMSO_2$
5.	Methanesulfinic acid (CH_3SO_2H)	CH_3SO_2H
6.	CH_3SCH_2OO	CH_3SCH_2OO
7.	methanesulfonyl radical (CH_3SO_2)	CH_3SO_2
8.	CH_3SO_3	CH_3SO_3
9.	$CH_3S(O)_2OO$	$CH_3S(O)_2OO$
10.	$CH_3S(O)_2CH_2OO$	$CH_3S(O)_2CH_2OO$

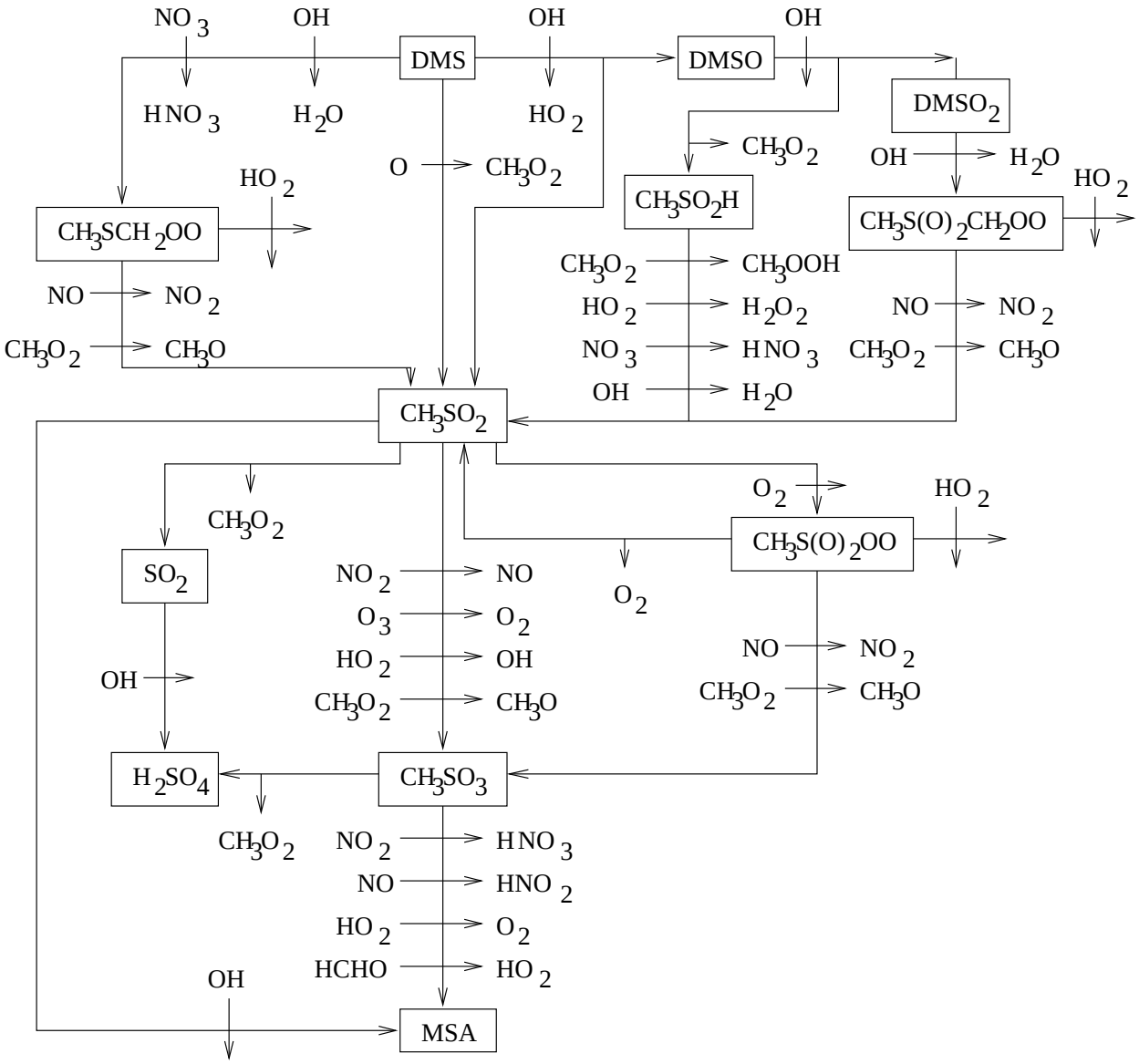

Figure 5.7: Condensed DMS photooxidation scheme (this work).

Table 5.2: Gas-Phase Condensed DMS Photooxidation Mechanism

No.	Reaction			Rate Constant k [molec-cc-s]
1.	DMS + OH	$\longrightarrow$	$CH_3SCH_2OO + H_2O$	$9.6 \times 10^{-12} \exp(-234/T)$
2.	DMS + NO_3	$\longrightarrow$	$CH_3SCH_2OO + HNO_3$	$1.4 \times 10^{-13} \exp(500/T)$
3.	DMS + $O(^3P)$	$\longrightarrow$	$CH_3SO_2 + CH_3O_2$	$1.3 \times 10^{-11} \exp(409/T)$
4.	DMS + OH	$\longrightarrow$	$\alpha CH_3SO_2 + \alpha CH_3O_2 + (1-\alpha)DMSO + (1-\alpha)HO_2$	1.7×10^{-12} [a]
5.	CH_3SCH_2OO + NO	$\longrightarrow$	CH_3SO_2 + HCHO + NO_2	8.0×10^{-12}
6.	$CH_3SCH_2OO + CH_3O_2$	$\longrightarrow$	CH_3SO_2 + 2HCHO + HO_2	1.8×10^{-13}
7.	DMSO + OH	$\longrightarrow$	$\beta CH_3SO_2H + \beta CH_3O_2 + (1-\beta)DMSO_2 + (1-\beta)HO_2$	5.8×10^{-11} [b]
8.	$DMSO_2$ + OH	$\longrightarrow$	$CH_3S(O)_2CH_2OO$	1.0×10^{-14}
9.	$CH_3S(O)_2CH_2OO$ + NO	$\longrightarrow$	CH_3SO_2 + HCHO + NO_2	5.0×10^{-12}
10.	$CH_3S(O)_2CH_2OO + CH_3O_2$	$\longrightarrow$	CH_3SO_2 + 2HCHO + HO_2	1.8×10^{-13}
11.	$CH_3SO_2H + HO_2$	$\longrightarrow$	$CH_3SO_2 + H_2O_2$	1.0×10^{-15}
12.	$CH_3SO_2H + NO_3$	$\longrightarrow$	$CH_3SO_2 + HNO_3$	1.0×10^{-13}
13.	$CH_3SO_2H + CH_3O_2$	$\longrightarrow$	$CH_3SO_2 + CH_3OOH$	1.0×10^{-15}
14.	CH_3SO_2H + OH	$\longrightarrow$	$CH_3SO_2 + H_2O$	1.6×10^{-11}
15.	$CH_3SO_2H + CH_3SO_3$	$\longrightarrow$	CH_3SO_2 + MSA	1.0×10^{-13}
16.	CH_3SO_2	$\xrightarrow{M}$	$SO_2 + CH_3O_2$	$2.5 \times 10^{13} \exp(-8686/T)$ [c]
17.	$CH_3SO_2 + NO_2$	$\longrightarrow$	CH_3SO_3 + NO	1.0×10^{-14}
18.	$CH_3SO_2 + O_3$	$\longrightarrow$	$CH_3SO_3 + O_2$	5.0×10^{-15}
19.	$CH_3SO_2 + HO_2$	$\longrightarrow$	CH_3SO_3 + OH	2.5×10^{-13}
20.	$CH_3SO_2 + CH_3O_2$	$\longrightarrow$	CH_3SO_3 + HCHO + HO_2	2.5×10^{-13}
21.	CH_3SO_2 + OH	$\longrightarrow$	MSA	5.0×10^{-11}
22.	$CH_3SO_2 + O_2$	$\xrightarrow{M}$	$CH_3S(O)_2OO$	2.6×10^{-18}
23.	$CH_3S(O)_2OO$	$\xrightarrow{M}$	$CH_3SO_2 + O_2$	3.3
24.	$CH_3S(O)_2OO$ + NO	$\longrightarrow$	$CH_3SO_3 + NO_2$	1.0×10^{-11}
25.	$CH_3S(O)_2OO + CH_3O_2$	$\longrightarrow$	CH_3SO_3 + HCHO + HO_2	5.5×10^{-12}
26.	CH_3SO_3	$\xrightarrow{M}$	$H_2SO_4 + CH_3O_2$	$2.0 \times 10^{17} \exp(-12626/T)$ [c]
27.	$CH_3SO_3 + NO_2$	$\xrightarrow{M}$	MSA + HNO_3	3.0×10^{-15}
28.	CH_3SO_3 + NO	$\longrightarrow$	MSA + HNO_2	3.0×10^{-15}
29.	$CH_3SO_3 + HO_2$	$\longrightarrow$	MSA + O_2	5.0×10^{-11}
30.	CH_3SO_3 + HCHO	$\xrightarrow{O_2}$	MSA + HO_2 + CO	1.6×10^{-15}

[a] $\alpha = 5 \times 10^5/(5 \times 10^5 + [O_2] \times 3 \times 10^{-12})$

[b] $\beta = 1.5 \times 10^7/(1.5 \times 10^7 + [O_2] \times 1.2 \times 10^{-12})$

[c] Revised in this work. See text in subsection 5.3.2 for a detailed explanation.

5.3 Model Evaluation Under Atmospheric Conditions

The sensitivity of the predicted MSA/NSSS ratio with respect to temperature and NO_x levels was investigated using a simple box model. Although the observed MSA/NSSS ratio in the fine-mode marine aerosol (submicrometer range particles) would depend on a number of chemical and physical processes occurring in the marine boundary layer (see Figure 5.8), the present analysis assumes that the long-term average MSA/NSSS ratios observed are comparable to the time-averaged MSA/NSSS ratios predicted by the model. The predicted MSA/NSSS ratios ignore any heterogeneous SO_2 to H_2SO_4 conversion in the cloud-phase followed by resuspension of the aerosol particles or on the surface of the fine-mode aerosol particles, and should, therefore, represent the upper limit. Any heterogeneous SO_2 to H_2SO_4 conversion will tend to lower this ratio in the aerosol-phase.

5.3.1 Model Inputs

A fixed marine boundary layer height of 500 m is assumed for all scenarios. Three hypothetical emission scenarios listed in Table 5.3 were prescribed based on the modeling study of Suhre and Rosset (1994). The chosen emission flux of DMS of 180 nmol m^{-2} h^{-1} lies in the range of observed values in the southern trade-wind region. The base case flux of NO of 5 nmol m^{-2} h^{-1} represents sea-air emission (Thompson and Zafiriou, 1983), while that of NO_2 is an ad-hoc production term representing long range transport of long-lived nitrogen species such as PAN. Subsequent scenarios represent increasing influences of continental pollution to the marine air mass. The non-methane hydrocarbon mix is based on the composition given in Table 2.13. Removal of species by dry deposition at the sea surface is included, while scavenging by aerosols is ignored. Each scenario was run for three model days for different temperatures ranging from 270 K to 300 K. The diurnal variation of the solar radiation was representative of July 1 conditions at 40°N latitude.

5.3.2 Results and Discussion

The third day simulation results were analyzed and are presented here. Figure 5.9 shows the diurnal concentration profiles of DMS and SO_2 for all three scenarios at 300 K. Also shown in the same figure are the field measurements made over the tropical South Pacific Ocean (12°S, 135°W) during March 1992 (Yvon and Saltzman, 1996). Due to differences

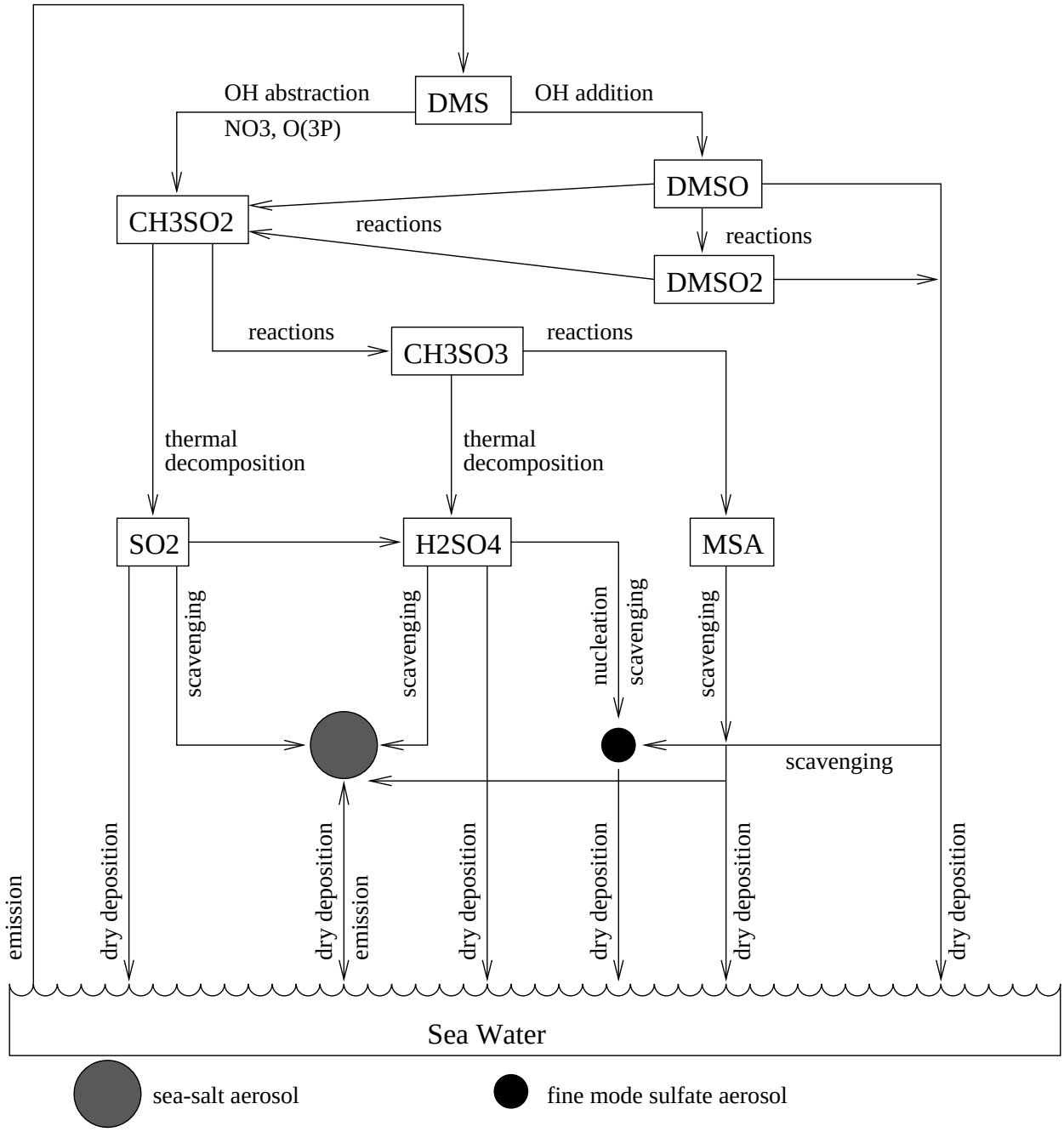

Figure 5.8: Production and loss of DMS-derived sulfur compounds in cloud-free marine boundary layer.

Table 5.3: Hypothetical Emissions Scenarios.

Scenario	Emission Flux (nmol m^{-2} h^{-1}) DMS	NO	NO_2	NMOC/NO_x	Initial Conc. $[CO]_0$ (ppb)	$[O_3]_0$ (ppb)
M1	180	5	0.05	0	60	10
M2	180	50	0.5	5	70	15
M3	180	500	5	10	80	20

$[DMS]_0 = 0.4$ ppb, $[CH_4]_0 = 1600$ ppb, $[C_2H_6]_0 = 0.8$ ppb and $[H_2O_2]_0 = 0.5$ ppb for all scenarios.
Dry deposition velocity for SO_2, DMSO and $DMSO_2$ assumed as 1 cm s^{-1}.

in the location and time of measurements and present simulations, only semi-quantitative comparisons between the two could be made. Clearly, the predicted shapes and amplitudes of the DMS concentration diurnal cycles for scenarios M1 and M2 are in good accord with the observed profile. Also, the observed diurnal cycle of SO_2 is in good agreement with the predicted profiles for the same two scenarios. Lack of discernible diurnal DMS concentration variation in scenario M3 indicates appreciable nighttime destruction by reaction with the NO_3 radical. The corresponding SO_2 cycle also looks different as a result.

Figure 5.10 shows the diurnal concentration cycles of DMSO and $DMSO_2$ for all three scenarios at 300 K. At this temperature, the yields of DMSO and $DMSO_2$ are quite low, and as a result, their predicted average concentrations were below 8 ppt in all scenarios. However, at lower temperatures, the DMS-OH addtion pathway becomes important, and should result in much higher concentrations of DMSO and $DMSO_2$. This is illustrated in Figure 5.11 which shows the concentration profiles of DMSO and $DMSO_2$ at 280 K. The average concentrations at this temperature more than doubled as compared to those at 300 K. Since DMSO and $DMSO_2$ have low vapor pressures and are highly soluble, they will be removed by dry deposition at the sea-surface, and will be efficiently scavenged before they are further oxidized to SO_2. Thus, lower yields of SO_2 should be observed at lower temperatures.

Since the thermal decomposition of the CH_3SO_2 radical has a large activation energy, the yield of SO_2 decreases even further at lower temperatures. This fact is reflected from the predicted average DMS/SO_2 ratios listed in Table 5.4. Similar high ratios were observed in clean marine air masses by Huebert *et al.* (1993) during the Soviet/American Gases and Aerosols (SAGA) 3 program in February and March 1991. The measurements were made

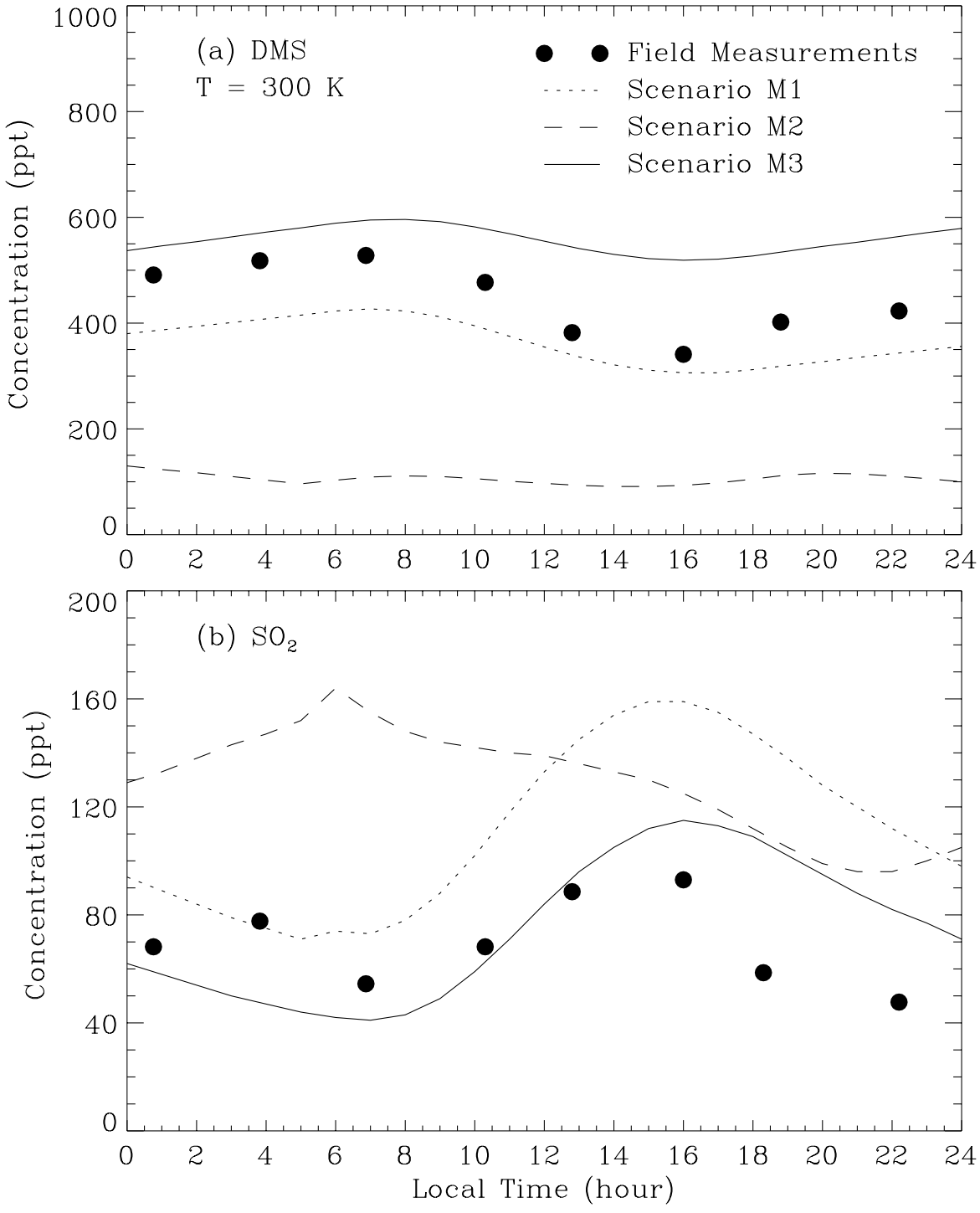

Figure 5.9: Diurnal concentration profiles for scenarios M1, M2 and M3 at 300 K: (a) DMS; (b) SO_2. Filled circles are field measurements from Yvon and Saltzman (1996).

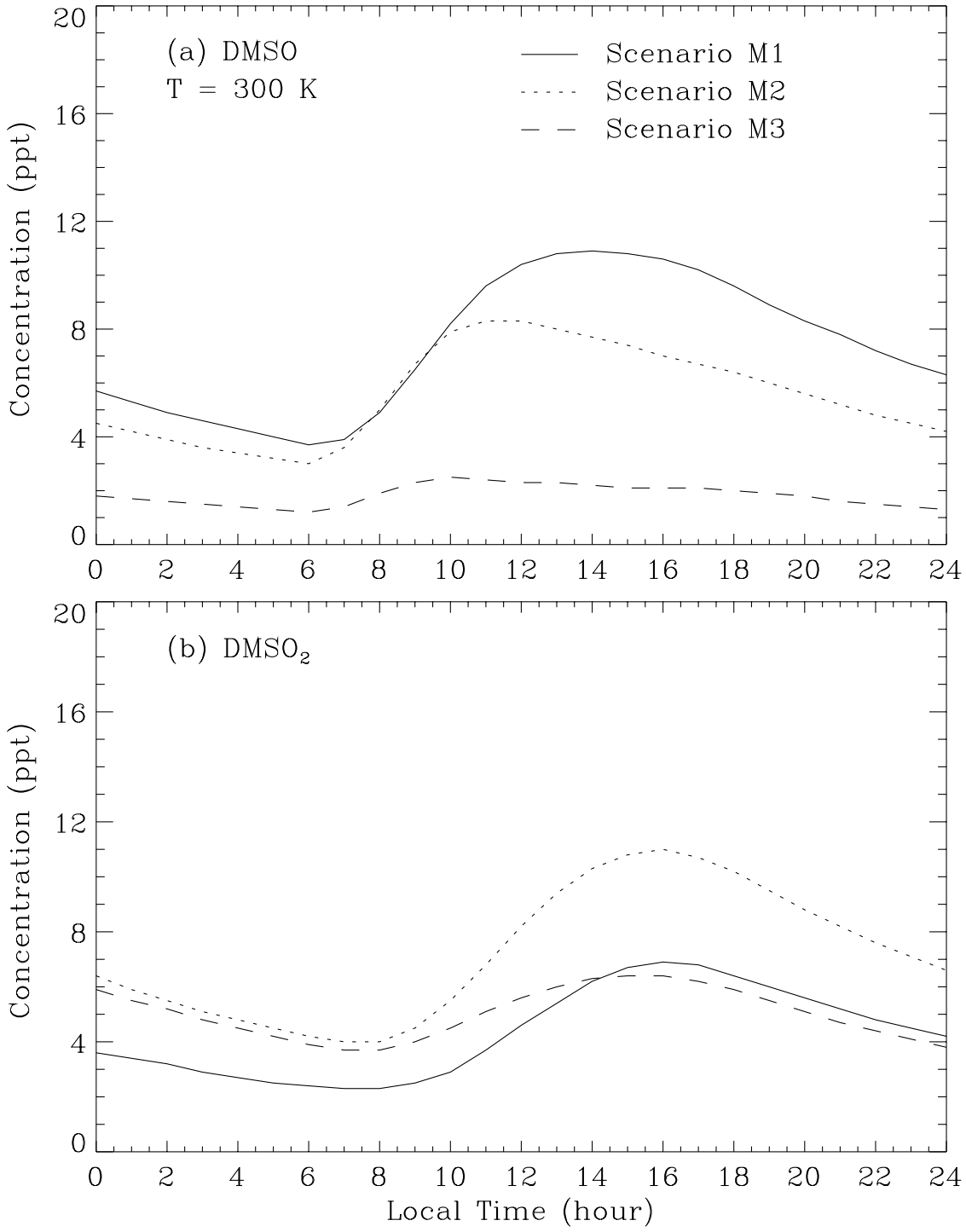

Figure 5.10: Diurnal concentration profiles for scenarios M1, M2 and M3 at 300 K: (a) DMSO; (b) $DMSO_2$.

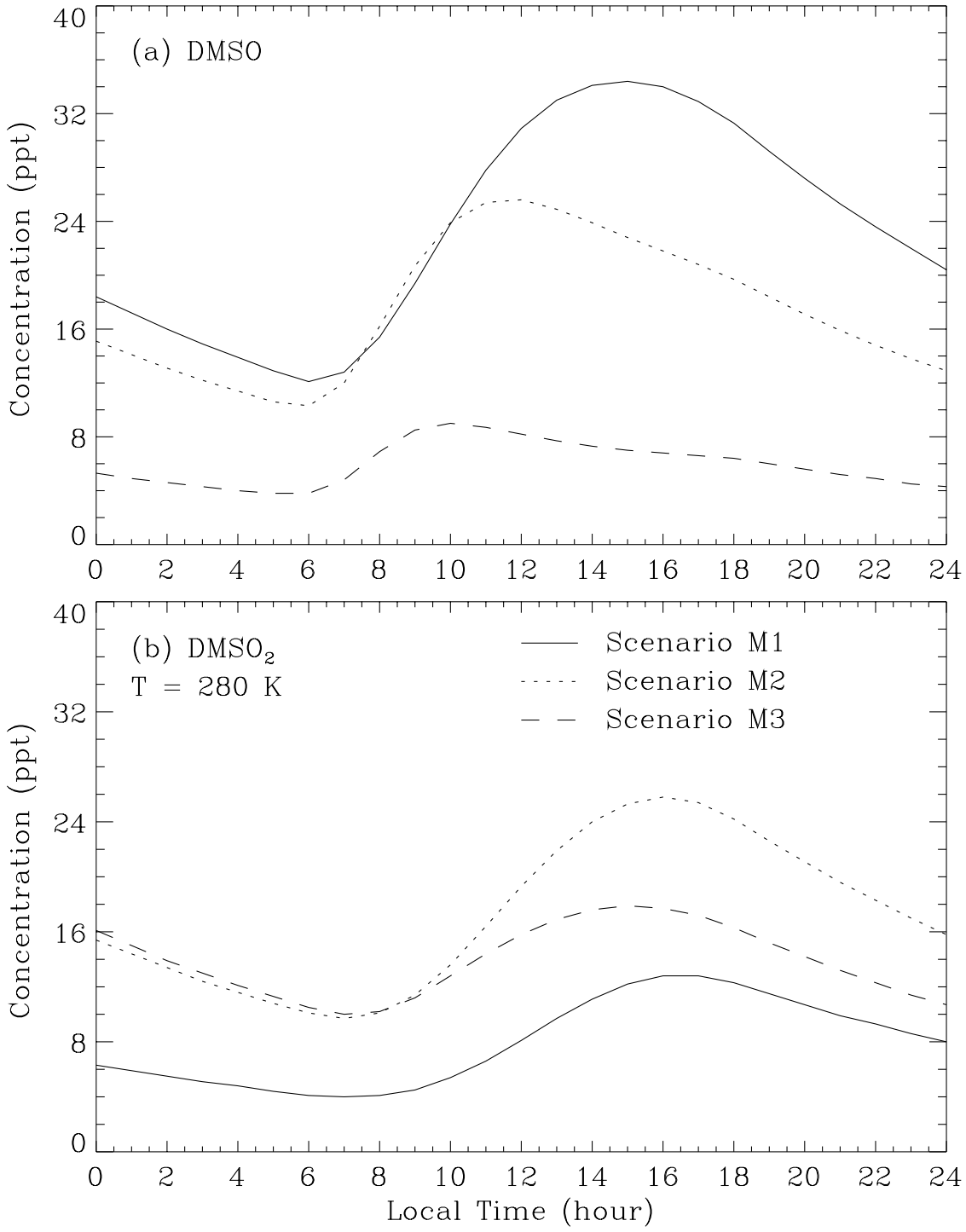

Figure 5.11: Diurnal concentration profiles for scenarios M1, M2 and M3 at 280 K: (a) DMSO; (b) $DMSO_2$.

Table 5.4: Predicted Average Gas-Phase DMS/SO_2 Concentration Ratios.

Temperature	DMS/SO_2 Molar Ratio		
(K)	Scenario M1	Scenario M2	Scenario M3
270	15.0	3.61	1.13
280	11.5	3.37	0.93
290	9.1	3.37	0.88
300	7.5	3.28	0.82

in equatorial Pacific marine boundary layers. Bandy *et al.* (1992) also observed DMS/SO_2 ratios close to 7 in the marine boundary layer of the northeast Pacific Ocean west of Seattle, Washington, during April 1991.

As discussed before, the most reasonable pathway for MSA formation appears to be via CH_3SO_3 reactions. Thermal decomposition of the CH_3SO_3 radical is expected to be quite fast; however, its rate constant is quite uncertain. Yin *et al.* (1990a,b) estimated a value of 0.16 s^{-1} at 298 K based on the measured yields for H_2SO_4 and MSA in their smog chamber studies. However, since these species can be lost quickly to the chamber walls, their measured yields have a certain degree of uncertainty. This uncertainty would propagate into the decomposition rate constant.

Using the C-S BDE in CH_3SO_3 of 22 kcal mol^{-1} as the activation energy, and the rate constant of 0.16 s^{-1} at 298 K, we get the following Arrhenius expression

$$k_{CH_3SO_3} = 4.0 \times 10^{17} \times \exp(-12626/T) \quad s^{-1}. \tag{5.3}$$

Assuming that the activation energy equation (1.3) is reasonable, the uncertainty would then mostly lie in the pre-exponential factor. Also, since the decomposition rate of the CH_3SO_2 radical indirectly affects the rate of MSA formation, a small error in $k_{CH_3SO_2}$ would be amplified, resulting in a large error in the final MSA yield. Again, by similar argument, the uncertainty in the expression for $k_{CH_3SO_2}$ would be in the pre-exponential factor.

The sensitivity of the MSA/NSSS ratio was investigated by reducing the values of the pre-exponential factors for $k_{CH_3SO_2}$ and $k_{CH_3SO_3}$ given in Equations 5.2 and 5.3. Average MSA/NSSS ratios for all three scenarios were computed at four different temperatures, and are listed in Table 5.5. Clearly, the MSA/NSSS ratios are a strong function of temperature. In all scenarios and for a given set of $k_{CH_3SO_2}$ and $k_{CH_3SO_3}$, the MSA/NSSS ratio increases with decreasing temperatures. Secondly, at any given temperature, the MSA/NSSS ratio

Table 5.5: Predicted Average MSA/NSSS Molar Concentration Ratios.

Temperature (K)	MSA/NSSS Molar Ratio			
	$k_{CH_3SO_2}$, $k_{CH_3SO_3}$	$.5k_{CH_3SO_2}$, $k_{CH_3SO_3}$	$k_{CH_3SO_2}$, $.5k_{CH_3SO_3}$	$.5k_{CH_3SO_2}$, $.5k_{CH_3SO_3}$
Scenario M1				
270	0.65	1.08	0.81	1.43
280	0.10	0.18	0.15	0.27
290	0.012	0.023	0.021	0.040
300	0.0015	0.0028	0.0026	0.0052
Scenario M2				
270	0.93	1.50	1.14	2.00
280	0.15	0.25	0.20	0.37
290	0.017	0.032	0.028	0.053
300	0.0018	0.0035	0.0032	0.0063
Scenario M3				
270	1.12	1.71	1.41	2.34
280	0.18	0.30	0.25	0.44
290	0.021	0.039	0.035	0.065
300	0.0021	0.0041	0.0039	0.0076

appears to increase with increasing NO_x emissions. And lastly, the MSA/NSSS ratio is a strong function of both $k_{CH_3SO_2}$ and $k_{CH_3SO_3}$. A lowering of either or both $k_{CH_3SO_2}$ and $k_{CH_3SO_3}$ by 50% results in proportional increase in the MSA/NSSS ratio. However, the DMS/SO_2 ratios remained nearly constant for all cases, which indicates that the yield of SO_2 is relatively insensitive to $k_{CH_3SO_2}$.

Although the observed MSA/NSSS ratios are highly variable, a 50% reduction in previously estimated values of both $k_{CH_3SO_2}$ and $k_{CH_3SO_3}$ appears to give MSA/NSSS ratios that resemble more closely some of the observed values. Thus, a 50% reduction in the pre-exponential factors of $k_{CH_3SO_2}$ and $k_{CH_3SO_3}$ is recommended in the present mechanism until more accurate values are determined experimentally.

5.4 Concluding Remarks

Thermal decomposition of the CH_3SO_2 and CH_3SO_3 radicals were identified as the most critical steps in determining the yields of SO_2, H_2SO_4, and MSA under typical atmospheric conditions. A highly condensed DMS photooxidation mechanism was first derived from the comprehensive mechanism of Yin *et al.* (1990a), and then evaluated under typical marine boundary layer scenarios. Based on the results of simple box-model simulations, it appears that the temperature dependence of the MSA/NSSS ratio can be captured by the temperature dependent reactions of the CH_3SO_2 and CH_3SO_3 radicals; however, a 50% reduction in their previously estimated thermal decomposition rate constants yields a better match with some of the observed MSA/NSSS ratios.

Although the temperature dependence of the MSA/NSSS ratios can be modeled by the present mechanism, the seasonal variation of the ratio at a given latitude still remains unexplained. Further work is needed to fully understand this behavior.

DMS/SO_2 ratios much greater than unity have been observed under remote marine boundary layer conditions, indicating that SO_2 may not be the major product of DMS photooxidation. This behavior is also well captured by the present model. However, under relatively polluted conditions and at higher temperatures, the DMS/SO_2 ratio can be less than one, thus explaining the variability of such ratios in various locations.

Chapter 6

Aerosol-Phase Chemistry

Proper treatment of direct and indirect radiative forcing by aerosols requires simulation of the aerosol physical size distribution. Direct radiative forcing is quite sensitive to particle size as the mass scattering efficiency peaks for particle sizes near the wavelength of light, whereas indirect forcing is sensitive to the number of particles active as cloud condensation nuclei (CCN). Aerosol size distributions vary widely since aerosols are emitted as primary particles or nucleated as secondary particles. These particles are then subjected to various processes such as growth by condensation of precursor gases and coagulation, activation as CCN, incorporation by clouds, resuspension, and scavenging by precipitation. For example, activation of aerosol particles to form cloud droplets followed by precipitation scavenging of the cloud droplets can remove 85% of the aerosol mass but only 15% of the aerosol number. The particles that remain have a much smaller size. Such changes in size distribution cannot be simulated in models that only treat aerosol mass. Simulation of a wide range of particle sizes is therefore required.

The chemical composition of an aerosol plays an important role in light scattering by affecting its water content and hence the actual wet size, and by its activation as a CCN. Among the various processes mentioned above, the chemical composition of an aerosol undergoes changes primarily due to condensation of various precursor gases such as H_2SO_4, HNO_3, HCl, NH_3, MSA, etc. Characteristic times for gas- and aerosol-phases to reach equilibrium may range from a few seconds to a few hours or even a day, depending on the ambient temperature, particle size, and number concentration (Wexler and Seinfeld, 1990; Meng and Seinfeld, 1996). Some field measurements appear to support the theoretically predicted time-scales (Allen and Harrison, 1989; Wexler and Seinfeld, 1992; Harrison and Msibi, 1994). Also, with several co-existing aerosol particles of different compositions, number concentrations, and diameters, the rates of condensation/evaporation to/from each will be different. This can result in preferential condensation of non-volatile gases such as sulfuric acid onto a particle of one size over another. This effect is experienced by semi-volatile species such as nitric and hydrochloric acids, along with inter-particle transfer, both governed by equilibrium constraints.

Thus, an accurate prediction of the competitive growth of different aerosol particles via condensation/evaporation processes requires a dynamic treatment, driven and constrained by multiphase equilibria. This chapter descibes the development of such a model for simulating aerosol ions by condensation (MOSAIC) suitable for our global-scale model. Wexler and Seinfeld (1991) first developed a dynamic multicomponent inorganic aerosol growth model; and more recently, Jacobson *et al.* (1996) also constructed a similar model to simulate tranfer between gas and aerosol. Although these models are quite sophisticated and capable of solving any number of equations describing the multiphase equilibria, they are also computationally very expensive due to the large number of iterations that must be performed for solving the equilibrium equations at every time step. The present model is designed to overcome this serious drawback.

Before presenting the dynamic aspects of the model, the assumptions and approximations that are made to reduce the complexity of the problem will be described. The major simplifications may be categorized into three parts: the chemical nature of various ambient aerosols, their physical characteristics, and their size distribution representation.

6.1 Aerosol Ions and Electrolytes

Although ambient aerosols are quite complex, containing a large number of chemical elements combined with each other to form an even larger suite of compounds, we will only treat a few major species as prognostic variables due to limited computational memory, time, and more importantly due to the scarcity of experimental data and field observations on all the species that may occur. Fortunately, most field experiments reveal that sulfate, nitrate, chloride, ammonium, and methanesulfonic acid (MSA) usually constitute the majority of the submicron size aerosol mass in both marine and continental atmospheres (Ferek *et al.*, 1983; Wolff, 1984; Hara *et al.*, 1989; Kopcewicz *et al.*, 1991; Arimoto *et al.*, 1992, Matsumoto and Tanaka, 1996). MSA usually constitutes a minor fraction of the sub-micron marine aerosol, but may become important at high latitudes, especially during summer. However, due to lack of necessary data, MSA is not included in the present model.

Coarse particles consist of sea-salt aerosol and wind-blown dust. Sea-salt aerosol can be assumed to be composed of the above mentioned ions in addition to sodium which is the dominant cation; other cations in sea-salt such as potassium and calcium are treated as equivalent sodium ions for simplicity. Similarly, minor quantities of other halides (bromide

and iodide) are also treated as chloride.

Dust is usually the most complex and difficult to characterize due to its large compositional variability across the globe. For this reason, dust is simply assumed as inert mass in the present model. Two other generic species that must be accounted for are the organic and black carbon masses. Organic carbon mass usually occurs as secondary aerosols, i.e., non-volatile organic vapors condensing on pre-existing particles, or homogeneously nucleating to form new particles. In the present model, the only source of secondary organic aerosol (SOA) precursor is from monoterpene photooxidation as described in Chapter 4. The black carbon mass (or soot) is always primary in nature, resulting mainly from smoke emissions from biomass burning. Both organic carbon and black carbon are treated as inert insoluble masses due to lack of relevant data for these. However, there is growing evidence that the presence of these species and other organics can alter the hygroscopicity of atmospheric aerosol (Saxena *et al.*, 1995), and deserves attention in the future.

As indicated later in the chapter, we will require the knowlegde of all possible electrolytes for a given set of concentrations of the individual generic species mentioned above. Depending on the ambient relative humidity, an electrolyte may exist as solid, liquid, or both. For a closed multiphase, multicomponent system at chemical equilibrium at constant temperature T and pressure P, the total Gibbs free energy of the system should be at a minimum, or equivalently (Denbigh, 1981; Kim *et al.*, 1993a)

$$\sum_{i} \nu_{ij} \mu_i = 0, \tag{6.1}$$

where ν_{ij} is the stoichiometric coefficient of the i^{th} species in the j^{th} reaction, and μ_i is the chemical potential of species i defined as

$$\mu_i = \mu_i^o(T) + RT \ln a_i. \tag{6.2}$$

Here, $\mu_i^o(T)$ is the standard chemical potential for the i^{th} species at temperature T, and a_i is the activity of the i^{th} species.

Combining (6.1) and (6.2) gives

$$\exp\left[-\frac{1}{RT}\sum_{i} \nu_{ij}\mu_i^o\right] = \prod_{i} a_i^{\nu_{ij}} = K_{ij} \tag{6.3}$$

where $K_j(T)$ is the equilibrium constant of the j^{th} reaction. Thus, one must minimize the Gibbs free energy by solving (6.1), or equivalently solve the set of equilibrium equations

described by (6.3) to determine the equilibrium concentrations of each species. Numerical solution of (6.3) is very simple except when there is one or more solid phases present in the system. In this case, the method for solving (6.3) is not so straightforward; one may resort to solving (6.1), which can be very expensive (Wexler and Seinfeld, 1991). As an alternative quick approach, Saxena *et al.* (1986) and Pilinis and Seinfeld (1987) divided the full domain of the total component concentrations, including gas-phase, into several sub-domains, depending on RH and molar ratio of ammonia to sulfate or ammonia and sodium to sulfate. Approximations concerning the concentrations of certain components were made to reduce the number of equilibrium reactions. However, these models were designed to simulate the final equilibrium state of the total gas/aerosol system, and could not handle size-segregated aerosols.

In this work, the approach of *a priori* determination of the concentrations of all possible electrolytes is further exploited, but limited only within the aerosol phase. At a given time step and any given generic species concentration, the electrolyte concentrations are determined as if they were all solids, except for H_2SO_4, HNO_3, and HCl. The electrolyte formation priority is based on the Gibbs free energy considerations under dry conditions. Solid phase activity is unity, and thus, the chemical potential of an electrolyte reduces to its standard chemical potential (i.e., $\mu_i = \mu_i^o(T)$). The temperature dependence of $\mu_i^o(T)$ can be calculated from (Denbigh, 1981):

$$\frac{\mu^o}{RT} = \frac{\Delta G_f^o}{RT_o} + \frac{\Delta H_f^o}{RT_o}\left[\frac{T_o}{T} - 1\right] + \frac{\Delta C_p^o}{R}\left[1 + \ln\left(\frac{T_o}{T}\right) - \frac{T_o}{T}\right] \tag{6.4}$$

where T_o is the standard-state temperature (298.15 K) and ΔG_f^o, ΔH_f^o, ΔC_p^o are the standard molar Gibbs free energy of formation, the standard molar enthalpy of formation, and the standard molar heat capacity at constant pressure, respectively, assumed constant over the temperature range of interest. Values of these thermodynamic quantities are given in Table 6.1 for some of the relevant ammonium and sodium salts.

For example, consider a mixture of 2 mol Na, 1 mol SULF (SULF = total sulfate), 2 mol NH_4^+, and 2 mol NO_3^-. One can form 1 mol Na_2SO_4 and 2 mol NH_4NO_3, which gives a total Gibbs free energy of the system as -1637.9 kJ at T = 298.15 K; or alternatively one can form 1 mol $(NH_4)_2SO_4$ and 2 mol $NaNO_3$, which gives a total Gibbs free energy of -1635.7 kJ. The former pair of electrolyes is favored over the latter since it has lower Gibbs free energy. Assuming typical relative concentrations of different species found in the atmospheric aerosols, one can determine the approximate priority of electrolyte formation.

Tables 6.2 and 6.3 show the electrolyte priority list under various regimes determined by various ratios such as [Na]/[SULF], ([Na] + [NH_4])/[SULF], etc. In any given column, one must try to form the electrolyte starting from top and move downwards until all generic species are considered. The resulting electrolytes should correspond to the lowest possible total Gibbs free energy of the system, and thus, the equilibrium state. This information is then used to determine the phases present in the aerosol as described in the next subsection.

Table 6.1: Thermodynamic Parameters for Typical Aerosol Electrolytes[a].

Electrolytes	ΔG_f^o (kJ mol^{-1})	ΔH_f^o (kJ mol^{-1})	ΔC_p^o (kJ mol^{-1})
$Na_2SO_{4(S)}$	-1270.16	-1387.08	128.20
$NaHSO_{4(S)}$	-922.80	-1125.50	85.00
$NaNO_{3(S)}$	-367.00	-467.85	92.88
$NaCl_{(S)}$	-384.14	-411.15	50.50
$(NH_4)_3H(SO_4)_{2(S)}$	-1730.00	-2207.00	315. 0
$(NH_4)_2SO_{4(S)}$	-901.67	-1180.85	187.5
$NH_4HSO_{4(S)}$	-823.00	-1026.96	127.5
$NH_4NO_{3(S)}$	-183.87	-365.56	139.3
$NH_4Cl_{(S)}$	-202.87	-314.43	84.10

[a] All values are taken from Kim *et al.* (1993a).

Table 6.2: Assumed Possible Electrolytes in Coarse-Mode Sea-Salt Aerosol.

$0 < X_{Na} < 2$				$2 \le X_{Na}$
$X_T < 1$	$1 \le X_T < X'_{Na}$	$X'_{Na} \le X_T < 2$	$2 \le X_T$	
$NaHSO_4$	NH_4HSO_4	Na_2SO_4	Na_2SO_4	Na_2SO_4
NH_4HSO_4	Na_2SO_4	For $1.5 \le X'_{NH_4} < 2$	$(NH_4)_2SO_4$	$NaNO_3$
H_2SO_4	$NaHSO_4$	$(NH_4)_2SO_4$	NH_4NO_3	$NaCl$
HNO_3	HNO_3	$(NH_4)_3H(SO_4)_2$	NH_4Cl	NH_4NO_3
HCl	HCl	For $1 \le X'_{NH_4} < 1.5$	HNO_3	NH_4Cl
		$(NH_4)_3H(SO_4)_2$	HCl	HNO_3
		NH_4HSO_4		HCl
		HNO_3		
		HCl		

Note: $X_{Na} = [Na^+]_T/[SULF]_T$, $X_{NH_4} = [NH_4^+]_T/[SULF]_T$, $X'_{Na} = 0.5X_{Na} + 1$, $X'_{NH_4} = (2X_{NH_4})/(2 - X_{Na})$. Subscript T denotes the total concentration of the generic species.

Table 6.3: Assumed Possible Electrolytes in Fine-Mode Sulfate Aerosol.

$X_{Na} = 0$			
$0 \le X_T < 1$	$1 \le X_T < 1.5$	$1.5 \le X_T < 2$	$2 \le X_T$
NH_4HSO_4	$(NH_4)_3H(SO_4)_2$	$(NH_4)_3H(SO_4)_2$	$(NH_4)_2SO_4$
H_2SO_4	NH_4HSO_4	$(NH_4)_2SO_4$	NH_4NO_3
HNO_3	HNO_3	HNO_3	NH_4Cl
HCl	HCl	HCl	HNO_3
			HCl

6.2 Phase-states and Deliquescence

At equilibrium, an electrolyte (salt) in its pure state will be completely solid if the ambient RH is below its deliquescence RH (DRH); at or above DRH it is completely dissolved. Thus, the DRH of a pure salt is a unique parameter specific of that salt. However, in a mixed-salt system, for example the $(NH_4)_2SO_4$-NH_4NO_3 system (Figure 6.1), both salts begin to dissolve partially at a particular RH lower than both the pure salt DRHs. This DRH is called the mutual DRH or MDRH, and the corresponding aqueous-phase composition is called the Eutonic point. However, each salt will be completely dissolved only when the ambient RH exceeds its pure-salt DRH. In the region between the MDRH of the system and the DRH of a salt, it will co-exist in both phases — liquid and solid. Although MDRH values for some two-salt mixtures are known (Wexler and Seinfeld, 1991), very little information exists for systems with more than two salts.

Several laboratory experiments with single levitated particles have shown that most salts of interest exhibit hysteresis during the drying cycle following complete dissolution (Tang and Munkelwitz, 1981, 1984, 1986, 1994a,b, 1997; Cohen *et al.*, 1987a,b; Chan *et al.*, 1992). In the absence of any nucleating surface, the salt droplet may become supersaturated when the ambient RH falls below its saturation or deliquescence RH. The onset of spontaneous crystallization in the metastable state is poorly understood, and is probably sensitive to the ambient conditions. Metastable aerosols have also been observed in the ambient atmosphere, with crystallization relative humidities between 10 an 45% (Rood *et al.*, 1989; Shaw and Rood, 1990)

Figure (6.2) shows the growth cycles of pure $(NH_4)_2SO_4$ and NH_4NO_3 particles (Chan *et al.*, 1992). Consider initially dry particles of both salts. On increasing the ambient RH, the NH_4NO_3 particles will abruptly deliquesce at 62% (D_1 in the figure), and reach an equilibrium state in which the water activity equals the fractional ambient RH. Above 62% RH, the NH_4NO_3 particles absorb more water such that equilibrium is maintained; the solution is sub-saturated. Similarly, at 80% RH (D_2), the $(NH_4)_2SO_4$ particle undergoes deliquescence. Now, upon slowly lowering the ambient RH, the sub-saturated droplets may not crystallize at their respective DRHs, but become supersaturated. Although different salts may spontaneously crystallize at different RHs, both particles are assumed to crystallize spontaneously at 35% RH (C) in the figure. A mixed $(NH_4)_2SO_4$-NH_4NO_3 particle will undergo deliquescence at some point below 62% RH, and form a two-phase saturated solution. All NH_4NO_3 will

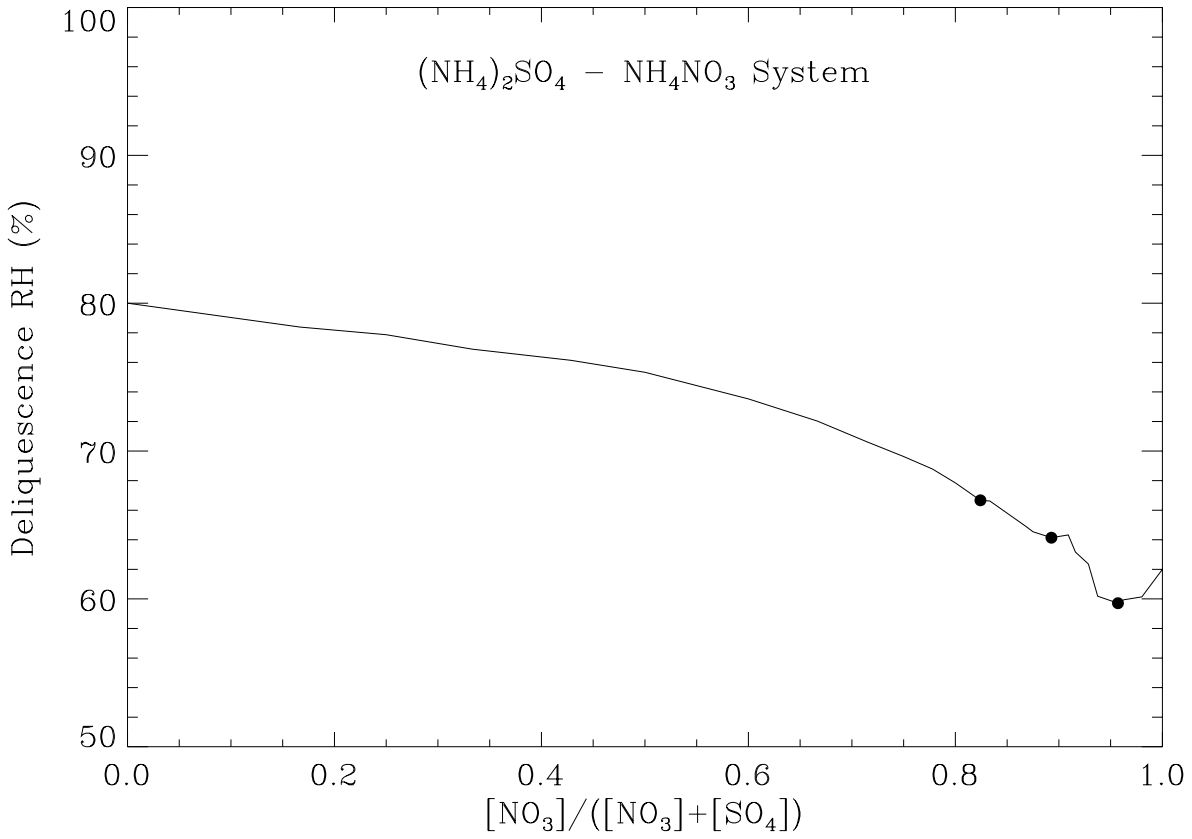

Figure 6.1: Variation of saturation water activity as a function of relative amounts of $(NH_4)_2SO_4$ and NH_4NO_3 in a mixed-salt system (based on the saturation data of Seidell and Linke (1965)). The filled circles indicate three eutonic points and the corresponding water activities are the mutual DRHs.

be dissolved at 62% RH, while $(NH_4)_2SO_4$ will only be partially dissolved. Only at the saturation RH for a given composition will all $(NH_4)_2SO_4$ be completely dissolved.

Thus, the actual physical state of an aerosol particle at any given ambient temperature and relative humidity depends on the composition, mutual deliquescence and crystallization relative humidities at that composition and temperature, and the particle's hysteresis history. Of these, the hysteresis leg is the easiest to model, provided we assume some reasonable mutual crystallization point. However, a mutual deliquescence point and the solid-liquid phase equilibria of any given salt mixture are very computationally intensive to determine (Potukuchi and Wexler, 1995a,b, 1997; Jacobson *et al.*, 1996).

Here, an alternative approach is proposed which eliminates the problems associated with

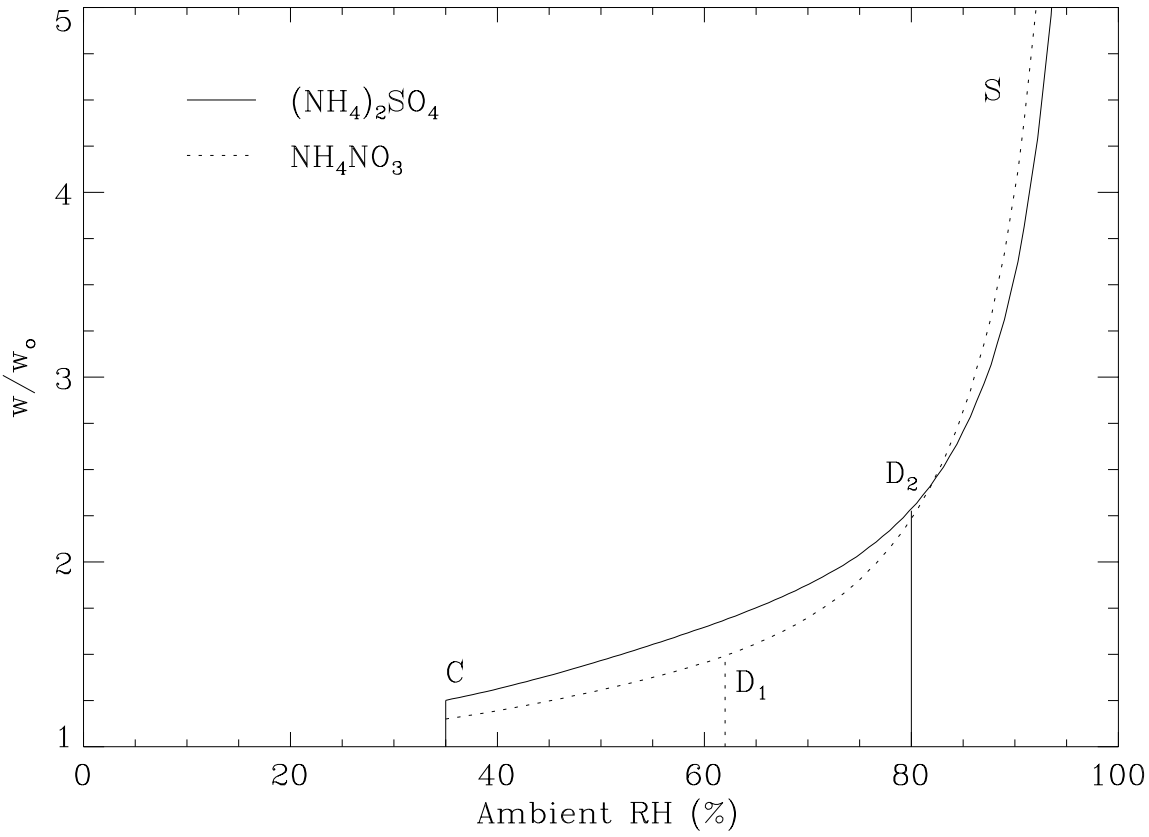

Figure 6.2: Growth cycle of various single-salt aerorol particles. The ratio w/w_o represents the ratio of the wet aerosol mass to the dry mass.

mixed-phase systems. Instead of calculating multiple phase-transitions with gradually increasing RH, a single average DRH is calculated, at or above which the entire particle is completely liquid. Our primary interest in aerosol deliquescence is to calculate the equilibrium water content, followed by new aerosol size distribution calculations. Thus, the average DRH should be weighted with fractional water content associated with each electrolyte at the given ambient RH. Assuming that the mutual DRH of a mixed salt is equal to the lowest individual salt DRH, and the saturation DRH corresponds to the RH where the salt (jsat) with the highest DRH dissolves completely, the average DRH is expressed as

$$\mathrm{DRH_{avg}} = \frac{\mathrm{W_{jsat}DRH_{sat}} + \cdots + \mathrm{W_j DRH_j}}{\mathrm{W_T}} \tag{6.5}$$

where $\mathrm{W_j}$ is the water content associated with the $\mathrm{j^{th}}$ electrolyte, $\mathrm{W_T}$ is the total water content assuming all aerosol salts are completely dissolved, and $\mathrm{DRH_j}$ is the deliquescence

RH of the j^{th} electrolyte. The saturation DRH of a mixed salt may be approximated by linear interpolation between the individual salt DRHs as

$$\mathrm{DRH_{sat}} = \mathrm{DRH_{max}} + \sum_{j} \mathrm{X_j}(\mathrm{DRH_j} - \mathrm{DRH_{max}}) \tag{6.6}$$

where $\mathrm{DRH_{max}}$ corresponds to the salt with the highest DRH, $\mathrm{X_j} = [\mathrm{salt_j}]/([\mathrm{salt_j}] + [\mathrm{salt_{max}}])$, and $\mathrm{DRH_j}$ is the DRH of salt j, e.g., for sulfate aerosol with $\mathrm{X_T} \geq 2$

$$\mathrm{DRH_{max}} = \mathrm{DRH_{(NH_4)_2SO_4}} \tag{6.7}$$

$$\mathrm{X_{NH_4NO_3}} = [\mathrm{NH_4NO_3}]/([\mathrm{NH_4NO_3}] + [(\mathrm{NH_4})_2\mathrm{SO_4}]) \tag{6.8}$$

$$\mathrm{X_{NH_4Cl}} = [\mathrm{NH_4Cl}]/([\mathrm{NH_4Cl}] + [(\mathrm{NH_4})_2\mathrm{SO_4}]) \tag{6.9}$$

Similarly for sea-salt aerosol with $\mathrm{X_{Na}} \geq 2$

$$\mathrm{DRH_{max}} = \mathrm{DRH_{Na_2SO_4}} \tag{6.10}$$

$$\mathrm{X_{NaNO_3}} = [\mathrm{NaNO_3}]/([\mathrm{NaNO_3}] + [\mathrm{Na2SO_4}]) \tag{6.11}$$

$$\mathrm{X_{NaCl}} = [\mathrm{NaCl}]/([\mathrm{NaCl}] + [\mathrm{Na2SO_4}]) \tag{6.12}$$

$$\mathrm{X_{NH_4NO_3}} = [\mathrm{NH_4NO_3}]/([\mathrm{NH_4NO_3}] + [\mathrm{Na_2SO_4}]) \tag{6.13}$$

$$\mathrm{X_{NH_4Cl}} = [\mathrm{NH_4Cl}]/([\mathrm{NH_4Cl}] + [\mathrm{Na_2SO_4}]) \tag{6.14}$$

DRHs of all electrolytes are non-zero except for the acids. Due to their relatively higher volatility, HNO_3 and HCl are not used in the above equation. If the resulting $\mathrm{DRH_{avg}}$ is higher than the ambient RH then the aerosol is treated as completely dry. In this case, HNO_3 and HCl, if present in the aerosol-phase, are simply put back into the gas-phase. On the other hand, if a liquid aerosol is predicted, then the total water content is recomputed using all the electrolytes present in the aerosol.

Total and individual electrolyte water contents can be easily calculated by the widely used empirical relationship, known as the ZSR equation (Zdanovskii, 1948; Stokes and Robinson, 1966). The ZSR equation states that the total water content is equal to the sum of water contents due to individual binary electrolytes at the same water activity as the multicomponent solution. Thus,

$$\mathrm{W_T} = \sum_{j} \mathrm{W_j} = \sum_{j} \frac{[\mathrm{E_j}]}{\mathrm{m_j^o}(\mathrm{a_w})} \tag{6.15}$$

where individual electrolyte concentration, $[\mathrm{E_j}]$, in the multicomponent solution is expressed as mol(in aerosol-phase) $\mathrm{m^{-3}}$(air), and $\mathrm{m_j^o}(\mathrm{a_w})$ is the equilibrium binary electrolyte molality

at the same water activity as the multicomponent solution. The binary electrolyte molalities as a function of water activity have been measured by several investigators and usually expressed as a polynomial function. In this work, the available polynomials from different sources have been re-fitted in terms of percent weight fraction for uniformity. The polynomial coefficients and procedure to calculate $m_j^o(a_w)$ are given in Appendix A.

The assumption of an average DRH seems reasonable if the minimum and maximum individual salt DRHs are not too far apart, and if one component of the mixed salt dominates over the other components. This is probably true of most submicron sized aerosols observed in the atmosphere. Ammonium salts of sulfate usually comprise the majority of the total inorganic mass in such aerosols. Volatile salts such as NH_4NO_3 and NH_4Cl are usually present in relatively smaller amounts. On the other hand, sea-salt aerosols are mainly composed of NaCl, Na_2SO_4 and $NaNO_3$, all of which have DRHs between 75 and 85%. Also, since both sulfate and sea-salt aerosols usually start out as completely aqueous (i.e., somewhere on the upper hysteresis leg as depicted in Figure 6.2), they must go through the crystallization point before they may form two-phase solutions upon further deliquescence (Binkowski and Shankar, 1995). Thus, the proposed approach appears to be well justified.

6.2.1 Illustration of the ZSR Model

The accuracy of the ZSR model is illustrated for mixed salt systems. Figures 6.3 to 6.5 show the equilibrium water content curves for the mixed NH_4^+ - SO_4^{2-} system with X_T ranging from 0.2 to 1.8. Clearly, the ZSR model is able to predict the equilibrium water content quite accurately over the whole range. The ZSR model has also been successfully applied to other mixed-salt systems such as $(NH_4)_2SO_4$-NH_4NO_3, Na_2SO_4-$NaNO_3$-NaCl, etc. (Chan *et al.*, 1992; Tang, 1997)

6.2.2 Temperature Effects

Temperature dependence of equilibrium binary electrolyte molalities at a given ambient RH (or water activity) is generally found to be small and may be neglected (Jacobson *et al.*, 1996). However, the temperature dependence of DRH cannot be ignored. Tang and Munkelwitz (1993) derived the following relation for temperature dependence based on solubility and the integral heat of solution data:

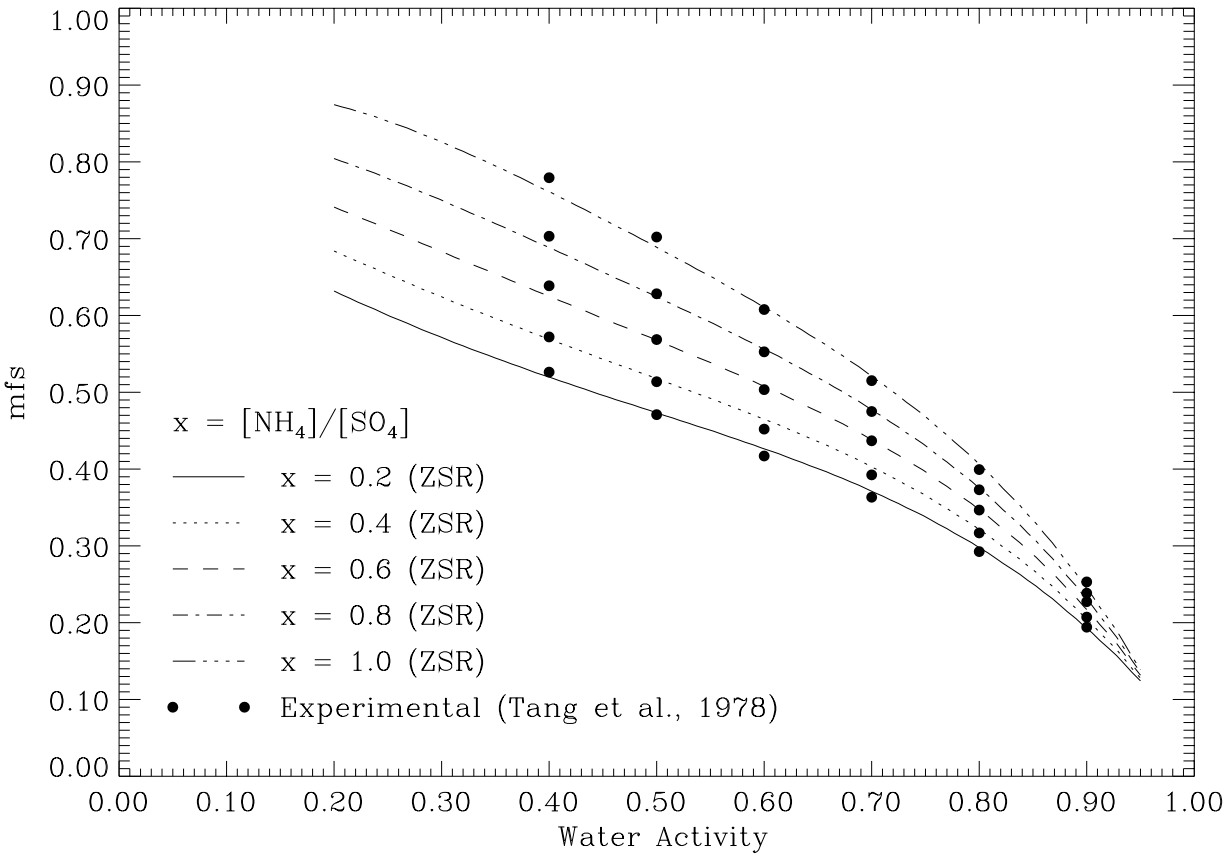

Figure 6.3: Mass fraction of solute (mfs) vs. water activity for NH_4^+ - SO_4^{2-} system with X_T ranging from 0.2 to 1.

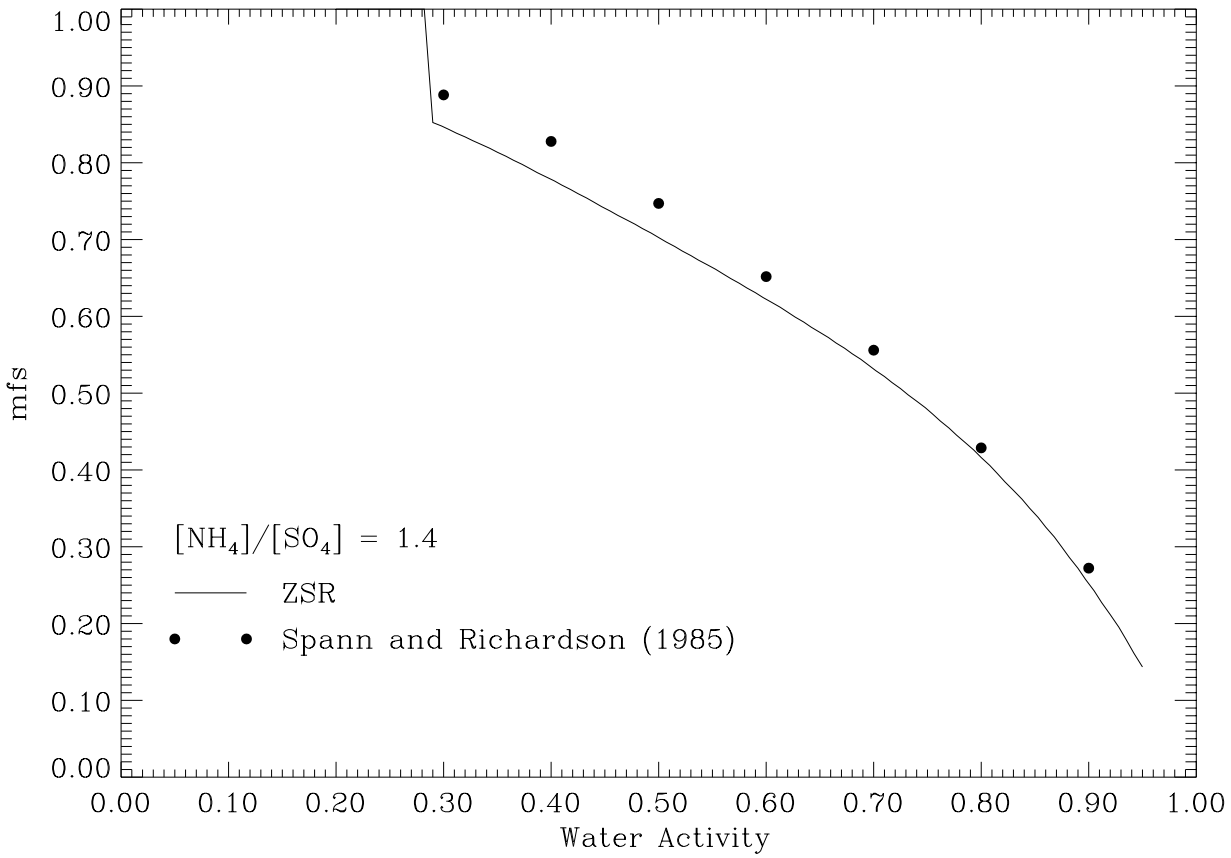

Figure 6.4: Mass fraction of solute (mfs) vs. water activity for NH_4^+ - SO_4^{2-} system with X_T = 1.4.

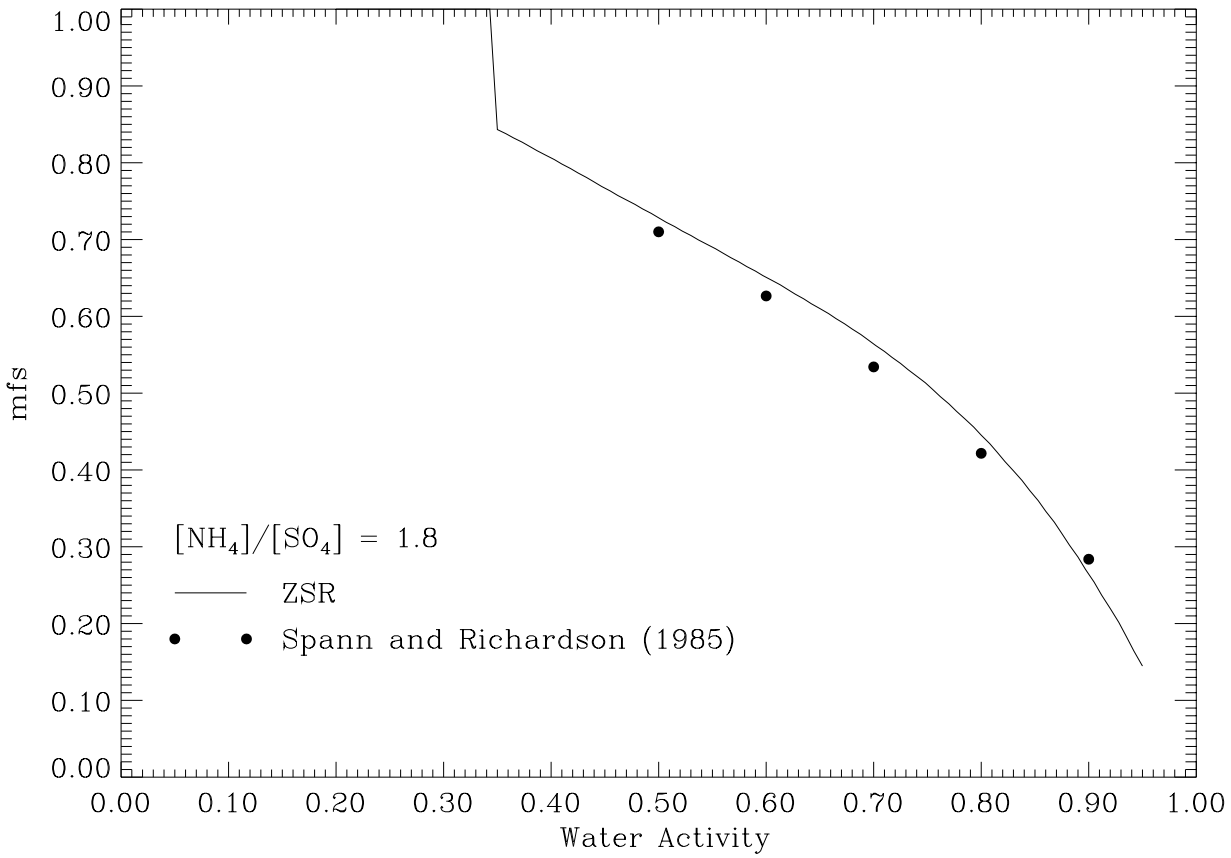

Figure 6.5: Mass fraction of solute (mfs) vs. water activity for NH_4^+ - SO_4^{2-} system with X_T = 1.8.

$$\ln \frac{\%\mathrm{DRH(T)}}{\%\mathrm{DRH(T_r)}} = \theta_s \left[\mathrm{A} \left(\frac{1}{\mathrm{T}} - \frac{1}{\mathrm{T_r}} \right) - \mathrm{B} \ln \frac{\mathrm{T}}{\mathrm{T_r}} - \mathrm{C(T - T_r)} \right], \tag{6.16}$$

where $\mathrm{T_r}$ is the reference temperature at which the DRH is known, here 298.15 K. The parameters θ_s, A, B, and C are given in Table A.2. Figure 6.6 illustrates the variation of DRH of various ammonium and sodium salts with temperature.

In certain regions of the atmosphere, especially towards the poles and at high altitudes, the ambient temperature can be considerably lower, causing the aerosol liquid water to freeze. In the present model, the frozen aerosol particles are simply treated as solid aerosols. The freezing point of a multicomponent solution is estimated by the following correlation (Zaytsev and Aseyev, 1992)

$$\mathrm{T_f} = \frac{10^7}{36608 - 32979 \log \mathrm{a_w^o} - 74302 (\log \mathrm{a_w^o})^2 - 607310 (\log \mathrm{a_w^o})^3}, \tag{6.17}$$

Here, the freezing point of a multicomponent electrolyte solution is correlated to its water activity at 298.15 K ($\mathrm{a_w^o}$). Figure 6.7 shows the variation of the solution freezing point as a function of water activity. Note that as water activity approaches unity, $\mathrm{T_f}$ approaches the freezing point of pure water at 273.15 K.

6.3 Aerosol Size Distributions

Simulating the aerosol physical size distribution requires numerical solution of the aerosol general dynamics equation (Friedlander, 1977). A number of solution techniques have been developed. The most direct technique involves discretization of the particle size range into a number of size bins and application of spline, sectional, or finite element solution techniques (Gelbard and Seinfeld, 1980). The number of prognostic aerosol fields with this approach is given by $\mathrm{N_{bins} N_{comp}}$, where $\mathrm{N_{bins}}$ is the number of size bins or sections (typically 20 or more), and $\mathrm{N_{comp}}$ is the number of chemical components. This becomes computationally burdensome in a three-dimensional atmospheric model,

The modal aerosol dynamics (MAD) approach (Giorgi, 1986) adopted for our model assumes that the aerosol population is composed of a set of log-normally distributed modes.

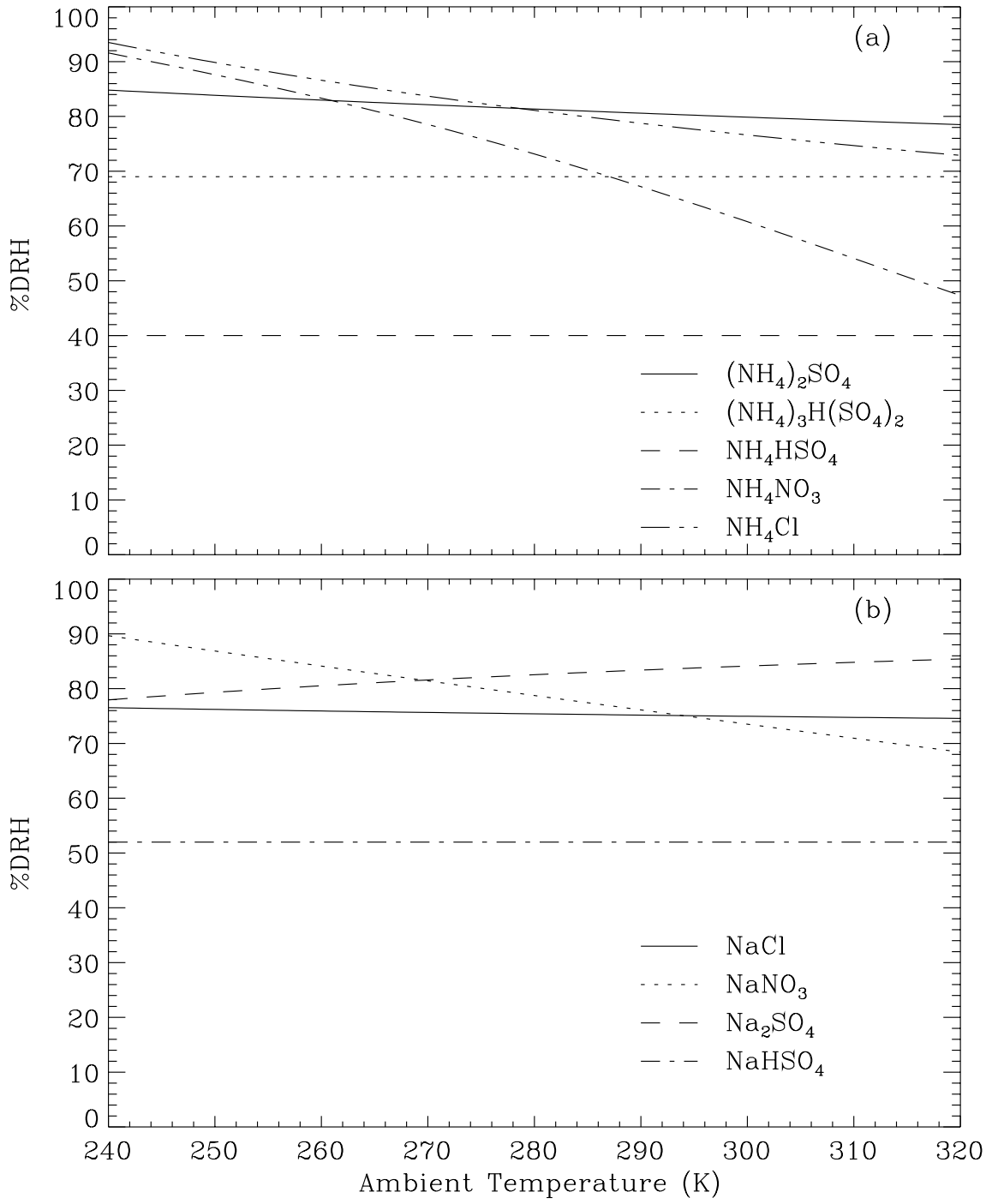

Figure 6.6: Variation of the deliquescence relative humidities with temperature based on the parameters given in Table A.2 for (a) ammonium salts, and (b) sodium salts.

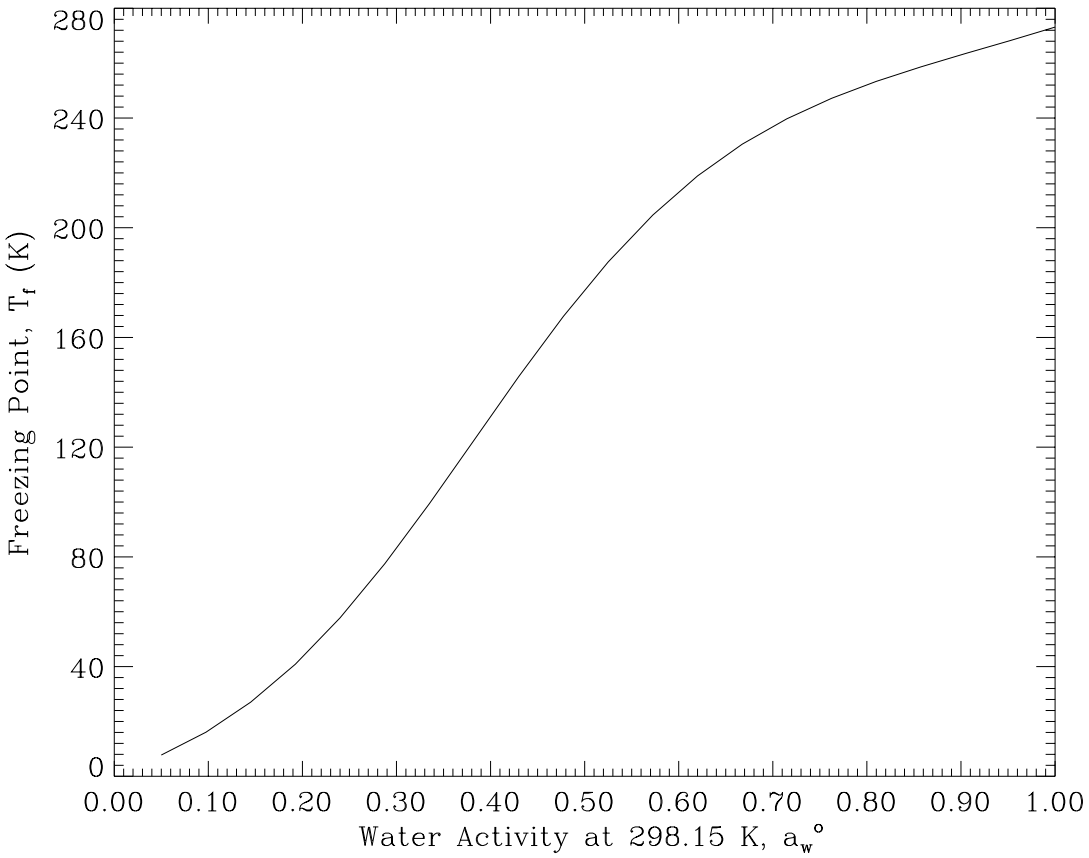

Figure 6.7: Variation of the freezing point of an electrolyte solution as a function of the solution water activity at 298.15 K.

The basis for this approach is that observed atmospheric aerosol size distributions are generally well characterized by the modal approach, and there is a theoretical basis for the existence of the different modes (Whitby 1978). Originally, three size modes were used to characterize the atmospheric aerosol, but recent observations extending to sizes below 10 nm diameter (Covert, 1996) have shown the existence of four size modes: nuclei (sizes below 10 nm), Aitken (previously referred to as nuclei), accumulation, and coarse.

Each mode is described by three distribution parameters: total number (N_T), geometric mean number diameter (D_{pgN}), and geometric standard deviation (σ_g). Aerosol components within each mode are assumed to be internally mixed (i.e., all particles in a given mode have the same average composition), while different modes are assumed to be externally mixed, having different compositions. The resulting number of prognostic aerosol fields is then $N_{modes}(N_{comp}+1)$, where N_{modes} is the number of modes, and the one extra variable is for aerosol water content. This method is, thus, computationally more efficient than the sectional method.

The log-normal particle size distribution for number concentration can be expressed as

$$\frac{dN}{d\ln D_p} = \frac{N_T}{\sqrt{2\pi}\ln\sigma_g}\exp\left[-\frac{(\ln D_p - \ln D_{pgN})^2}{2(\ln\sigma_g)^2}\right]. \tag{6.18}$$

The corresponding surface area, and volume (or mass) distribution can be easily written in terms of the number concentration distribution as

$$\frac{dS}{d\ln D_p} = \pi D_p^2 \times \frac{dN}{d\ln D_p} \tag{6.19}$$

$$\frac{dV}{d\ln D_p} = \frac{\pi}{6} D_p^3 \times \frac{dN}{d\ln D_p}. \tag{6.20}$$

The total surface area and total volume of a mode can also be expressed in terms of N_T and D_{pgN} as (Heintzenberg, 1994)

$$S_T = \pi D_{pgS}^2\ N_T\ \exp\left[-\frac{(\ln D_{pgS} - \ln D_{pgN})^2}{2(\ln\sigma_g)^2}\right] \tag{6.21}$$

$$V_T = \frac{\pi}{6} D_{pgV}^3\ N_T\ \exp\left[-\frac{(\ln D_{pgV} - \ln D_{pgN})^2}{2(\ln\sigma_g)^2}\right] \tag{6.22}$$

where D_{pgS} is the geometric mean surface diameter, and D_{pgV} is the geometric mean volume diameter, given by

$$D_{pgS} = D_{pgN} \exp[2(\ln \sigma_g)^2] \quad (6.23)$$

$$D_{pgV} = D_{pgN} \exp[3(\ln \sigma_g)^2] \quad (6.24)$$

Table 6.4 lists typical modal parameters (D_{pgN} and σ_g), and summarizes the chemical components treated in each mode. Figure 6.8 illustrates the normalized log-normal number, surface and volume distributions for various modes; the distributions are normalized with respect to the total number, surface and volume, respectively.

Table 6.4: Chemical and Physical Description of the Different Aerosol Modes.

i	Aerosol Modes	D_{pgN} (μm)	σ_g	Generic Components[a]
1	Ultrafine	variable	variable	SULF, NO_3^-, Cl^-, NH_4^+
2	Aitken	0.029	1.62	SULF, NO_3^-, Cl^-, NH_4^+, OC, BC
3	Accumulation	0.116	1.69	SULF, NO_3^-, Cl^-, NH_4^+, OC, BC
4	Sea-Salt	0.200	3.00	SULF, NO_3^-, Cl^-, NH_4^+, Na^+
5	Dust	0.400	2.50	DM, SULF, NO_3^-, NH_4^+, Cl^-

[a] SULF = SO_4^{2-} + HSO_4^-, DM = Dust Mass, OC = Organic Carbon, BC = Black Carbon, Na^+ = sum of all equivalent sea-salt alkali metal cations, Cl^- = sum of all sea-salt halides.

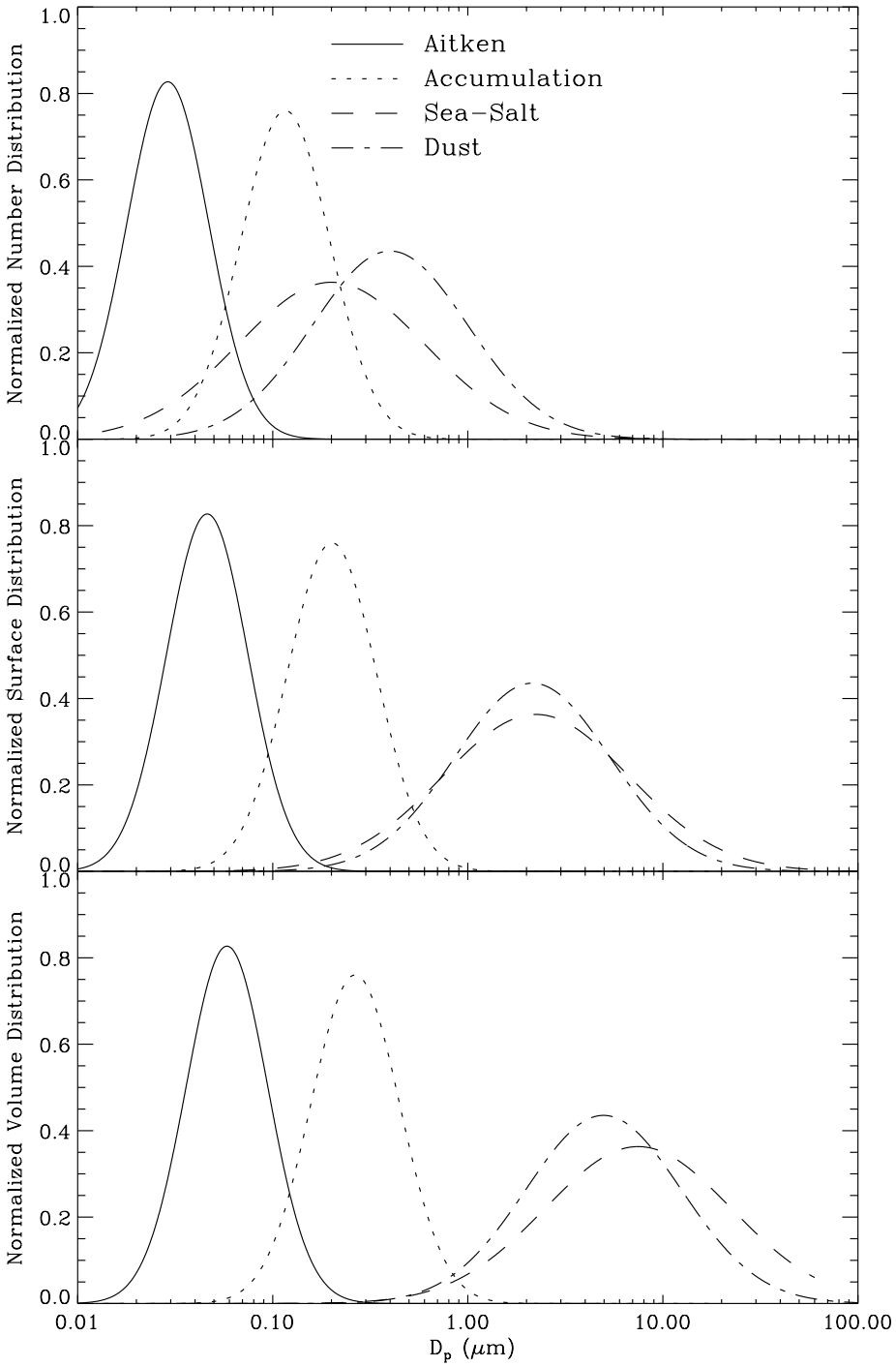

Figure 6.8: Normalized log-normal number, surface, and volume concentration distributions of different modes based on the number geometric mean diameters and geometric standard deviations listed in Table 6.4.

6.4 Dynamic Condensation Equations

The basic dynamic equations describing transfer of species A between gas- and aerosol-phases due to condensation or evaporation are:

$$\frac{\mathrm{d}}{\mathrm{dt}}[\mathrm{A}]_{\mathrm{G}} = -\sum_{\mathrm{i}=1}^{\mathrm{Nmodes}} \mathrm{K}^{1}_{\mathrm{A,i}} \left([\mathrm{A}]_{\mathrm{G}} - [\mathrm{A}]^{*}_{\mathrm{G,i}}\right) + \mathrm{R}_{\mathrm{G,A}} \tag{6.25}$$

$$\frac{\mathrm{d}}{\mathrm{dt}}[\mathrm{A}]_{\mathrm{p,i}} = \mathrm{K}^{1}_{\mathrm{A,i}} \left([\mathrm{A}]_{\mathrm{G}} - [\mathrm{A}]^{*}_{\mathrm{G,i}}\right) \tag{6.26}$$

where $[\mathrm{A}]_{\mathrm{G}}$ is the concentration of species A in the bulk gas phase (mol m^{-3} air); $[\mathrm{A}]^{*}_{\mathrm{G,i}}$ is the gas-phase concentration at the surface of the i^{th} mode aerosol particles and in equilibrium with the bulk aerosol-phase (mol m^{-3} air); $[\mathrm{A}]_{\mathrm{p,i}}$ is the average concentration of A in i^{th} aerosol mode, expressed as gas-phase concentration (mol m^{-3} air); and $\mathrm{K}^{1}_{\mathrm{A,i}}$ is the integral first-order mass-transfer coefficient for species A and i^{th} mode (s^{-1}). Again, the important underlying assumption is that a given mode is internally mixed.

The term $\mathrm{R}_{\mathrm{G,A}}$ lumps the production and destruction of A in the bulk gas-phase due to chemical reactions, emission, dry deposition, and other processes (mol m^{-3} s^{-1}). Assuming $\mathrm{R}_{\mathrm{G,A}}$ is known, we require the knowledge of the integral mass transfer coefficient and the equilibrium surface concentrations of the species of interest, namely, $\mathrm{H_2SO_4}$, $\mathrm{HNO_3}$, HCl, and $\mathrm{NH_3}$, at any given time. Determination of each of these is discussed next. The set of non-linear ordinary differential equations arising from (6.25) and (6.26) can be solved by LSODES.

6.4.1 Mass-Transfer Coefficient

The first order mass transfer coefficient for species A and mode i is calculated by integrating the product of the effective gas-side mass-transfer coefficient $\mathrm{k}_{\mathrm{G,A,i}}$ (m s^{-1}) and the surface area distribution over the whole range of the size distribution

$$\mathrm{K}^{1}_{\mathrm{A,i}} = \int_{0}^{\infty} \mathrm{k}_{\mathrm{G,A,i}}\, \pi \mathrm{D}_{\mathrm{p}}^{2} \left(\frac{\mathrm{dN_i}}{\mathrm{dD_p}}\right)\, \mathrm{dD_p}. \tag{6.27}$$

This assumes any internal resistance to mass transfer is negligible compared to that in the gas phase. According to the Maxwellian flux formula for a vapor diffusing to a sphere, the

mass-transfer coefficient is simply the ratio of the diffusivity of the vapor to the radius of the sphere. However, when the mean free path of the diffusing vapor molecules is of the same order as the particle diameter, as is the case here, the mass transfer phenomena is said to lie in the transition regime, and one cannot use the continuum-regime mass-transfer coefficient (Seinfeld, 1986). Fuchs and Sutugin (1971) obtained a Knudsen Number correction factor ($F_1(\mathrm{Kn})$) to the Maxwellian flux, based on the flux matching idea of Fuchs (1964). The Knudsen Number is defined as $\mathrm{Kn} = 2\lambda_\mathrm{A}/\mathrm{D_p}$, where λ_A is the mean free path of species A in air and $\mathrm{D_p}$ is the particle diameter. Another correction factor ($F_2(\mathrm{Kn}, \alpha_\mathrm{m})$) was derived to account for interfacial mass transport limitations characterized by the mass accomodation coefficient α_m (Hegg, 1990). Thus, the effective gas-side mass-transfer coefficient is written as

$$\begin{aligned} \mathrm{k_{G,A,i}} &= \frac{2\mathcal{D}_\mathrm{G,A}}{\mathrm{D_p}}\ F_1(\mathrm{Kn})\ F_2(\mathrm{Kn}, \alpha_\mathrm{m,A}) && (6.28) \\ F_1(\mathrm{Kn}) &= \frac{1+\mathrm{Kn}}{1+1.71\ \mathrm{Kn}+1.33\ \mathrm{Kn}^2} && (6.29) \\ F_2(\mathrm{Kn}, \alpha_\mathrm{m,A}) &= \left[1+1.33\ \mathrm{Kn}\ F_1(\mathrm{Kn})\ \left(\frac{1}{\alpha_\mathrm{m,A}}-1\right)\right]^{-1} && (6.30) \end{aligned}$$

The integral in (6.27) can be re-written in terms of $\ln \mathrm{D_p}$

$$\mathrm{K^1_{A,i}} = \int_{-\infty}^{\infty} \mathrm{k_{G,A,i}}\ \pi \mathrm{D_p^2} \left(\frac{\mathrm{dN_i}}{\mathrm{d}\ln \mathrm{D_p}}\right)\ \mathrm{d}\ln \mathrm{D_p} \tag{6.31}$$

Substituting the log-normal number concentration size-distribution from (6.18), and the expression for the mass-transfer coefficient from (6.28) in the above equation, we get

$$\mathrm{K^1_{A,i}} = \sqrt{2\pi}\ \frac{\mathrm{N_{T,i}}\mathcal{D}_\mathrm{G,A}}{\ln \sigma_\mathrm{g,i}} \int_{-\infty}^{\infty} \mathrm{D_p}\ F_1(\mathrm{Kn}) F_2(\mathrm{Kn}, \alpha_\mathrm{m,A})\ \exp\left[-\frac{(\ln \mathrm{D_p} - \ln \mathrm{D_{pgN,i}})^2}{2(\ln \sigma_\mathrm{g,i})^2}\right]\ \mathrm{d}\ln \mathrm{D_p} \tag{6.32}$$

The above integral can be converted, by variable transformation, into a form that can be numerically evaluated by the Gauss-Hermite quadrature. But before making the transformation, we multiply and divide the integrand by $(\mathrm{D_p})^\beta$. By choosing an appropriate value for β,

we can adjust the quadrature points to be centered around the maximum of the function that is used in the quadrature summation. Thus, employing the following variable transformation

$$\mathrm{x} = \frac{\ln \mathrm{D_p} - \ln \mathrm{D_{pgN,i}} - \beta(\ln \sigma_{\mathrm{g,i}})^2}{\sqrt{2} \ln \sigma_{\mathrm{g,i}}} \tag{6.33}$$

and after some algebraic manipulations, (6.32) can be written as

$$\mathrm{K^1_{A,i}} = 2\sqrt{\pi}\ \mathrm{N_{T,i}} \mathcal{D}_{\mathrm{G,A}} \exp\left[\beta \ln \mathrm{D_{pgN,i}} + \frac{1}{2}(\beta \ln \sigma_{\mathrm{g,i}})^2\right] \int_{-\infty}^{\infty} f(\mathrm{x}) \exp(-\mathrm{x}^2)\ \mathrm{dx} \tag{6.34}$$

where

$$f(\mathrm{x}) = \left[\exp\left(\sqrt{2} \ln \sigma_{\mathrm{g,i}}\ \mathrm{x} + \ln \mathrm{D_{pgN,i}} - \beta(\ln \sigma_{\mathrm{g,i}})^2\right)\right]^{(1-\beta)} F_1(\mathrm{Kn}) F_2(\mathrm{Kn}, \alpha_{\mathrm{m,A}}) \tag{6.35}$$

The integral in (6.34) is now amenable for numerical integration by the Gauss-Hermite Quadrature (Beyer, 1987); and by setting $\beta = 2$, just the second-order quadrature formula gives adequate accuracy (Easter, 1996).

6.5 Equilibrium Surface Concentrations for Dry Aerosol

As discussed earlier, in the present model the aerosol can be either completely dry (solid) or completely dissolved. Procedures for calculating equilibrium surface concentration for dry and wet aerosols are somewhat different, and are, therefore, presented separately. This section develops an algorithm for dry aerosols, while liquid aerosols are discussed in the next section.

Table 6.5 lists some of the important multiphase equilibrium reactions that will be used to calculate the surface concentrations. Additionally, some irreversible reactions must also be considered in the case of dry aerosols, and are listed in Table 6.6. Due to lack of kinetic data on gas-solid reactions, they are assumed to be mass-transfer limited. Thus, if a gas-soild reaction does occur, its rate constant is equal to the integral mass-transfer coefficient of the condensing vapor. Since H_2SO_4 is extremely non-volatile with vapor pressures over partially neutralized solutions in the range of 0.05 to 0.5 ppt (Marti *et al.*, 1997), its surface concentration is assumed equal to zero for both wet and dry aerosols. Relaxing this assumption in the future should cause only minor changes in the algorithms presented here. Thus, we must determine surface concentrations of only HNO_3, HCl, and NH_3. Furthermore, this must be done without violating the salt formation hierarchies listed in Tables 6.2 and 6.3, which in

fact, provide the necessary constraints for closure. Since the fine-mode aerosol is relatively less complex, it is considered first.

Table 6.5: Equilibrium Reactions Involved with Aerosols.

No.	Equilibrium Reaction			Equilibrium Constant			
				Symbol	$K(T_r)$	a	b
	Solid-Gas						
1.	$NH_4NO_{3(S)}$	$\rightleftharpoons$	$NH_{3(G)} + HNO_{3(G)}$	$K_{NH_4NO_3}$	5.746×10^{-17}	-74.38	6.12
2.	$NH_4Cl_{(S)}$	$\rightleftharpoons$	$NH_{3(G)} + HCl_{(G)}$	K_{NH_4Cl}	1.086×10^{-16}	-71.00	2.40
	Liquid-Liquid						
3.	HSO_4^-	$\rightleftharpoons$	$SO_4^{2-} + H^+$	K_{HSO_4}	1.015×10^{-2}	8.85	25.14
4.	$NH_{3(L)} + H_2O_{(L)}$	$\rightleftharpoons$	$NH_4^+ + OH^-$	K_{NH_3}	1.805×10^{-5}	-1.50	26.92
5.	$H_2O_{(L)}$	$\rightleftharpoons$	$H^+ + OH^-$	K_w	1.01×10^{-14}	-22.52	26.92
	Gas-Liquid						
6.	$NH_{3(G)}$	$\rightleftharpoons$	$NH_{3(L)}$	$\mathcal{H}_{NH_3}$	5.764×10^{1}	13.79	-5.39
7.	$HNO_{3(G)}$	$\rightleftharpoons$	$NO_3^- + H^+$	$\mathcal{H}_{HNO_3}$	2.511×10^{6}	29.17	16.83
8.	$HCl_{(G)}$	$\rightleftharpoons$	$Cl^- + H^+$	$\mathcal{H}_{HCl}$	1.971×10^{6}	30.20	19.91
9.	$H_2O_{(G)}$	$\rightleftharpoons$	$H_2O_{(L)}$	$K_{Kel.}$			

Note: All equilibrium constants are taken from Kim *et al.* (1993), and are expressed in mol-kg-atm units. Constants a and b are used in $K(T) = K(T_r)\ \exp[a(T'-1)+b(1+\ln(T')-T')]$, where $T' = T_r/T$, and $T_r = 298.15$ K.

Table 6.6: Irreversible Reactions Involved with Dry Aerosols.

No.	Reaction			Rate Constant s^{-1}
1.	$2NaCl_{(S)} + H_2SO_{4(G)}$	$\longrightarrow$	$Na_2SO_{4(S)} + 2HCl_{(G)}\uparrow$	$K^1_{H_2SO4}$
2.	$NaCl_{(S)} + HNO_{3(G)}$	$\longrightarrow$	$NaNO_{3(S)} + HCl_{(G)}\uparrow$	$K^1_{HNO_3}$
3.	$2NaNO_{3(S)} + H_2SO_{4(G)}$	$\longrightarrow$	$Na_2SO_{4(S)} + 2HNO_{3(G)}\uparrow$	$K^1_{H_2SO4}$

6.5.1 Fine-Mode Aerosol

Case 1 ($X_T < 2$)

According to the first criteria in Table 6.3, no NH_4NO_3 or NH_4Cl can form or should be present if $X_T < 2$, in which case fluxes of HNO_3 and HCl must be zero. Also, since the aerosol has excess sulfate, the surface concentration of NH_3 may be assumed zero. Thus, we have

$$[NH_3]^*_{(G)} = 0 \tag{6.36}$$

$$[HNO_3]^*_{(G)} = [HNO_3]_{(G)} \tag{6.37}$$

$$[HCl]^*_{(G)} = [HCl]_{(G)} \tag{6.38}$$

Case 2 ($X_T \geq 2$)

According to the gas-solid equilibria shown in Table 6.5, solid NH_4NO_3 can form if the gas-phase product $[NH_3]_{(G)}[HNO_3]_{(G)} > K_{NH_4NO_3}$. Both gases will deposit and react at the surface to form $NH_4NO_{3(S)}$, such that at equilibrium the bulk gas-phase satisfies $[NH_3]_{(G)}[HNO_3]_{(G)} = K_{NH_4NO_3}$. Consequently, at the total system equilibrium, the surface concentrations should be the same as the bulk gas phase. Similar behavior is expected of the NH_3-HCl-NH_4Cl system. Thus, at equilibrium we have

$$[NH_3]^*_{(G)}[HNO_3]^*_{(G)} = K_{NH_4NO_3} \tag{6.39}$$

$$[NH_3]^*_{(G)}[HCl]^*_{(G)} = K_{NH_4Cl} \tag{6.40}$$

However, if the initial gas-phase concentrations of NH_3 and HNO_3 in a closed system are such that $[NH_3]_{(G)}[HNO_3]_{(G)} < K_{NH_4NO_3}$, and there is no solid-phase NH_4NO_3 to begin with, then no reaction can take place, and the system is already at equilibrium. Again, the equilibrium surface concentrations of NH_3 and HNO_3 should be the same as bulk gas phase concentrations, but

$$[NH_3]^*_{(G)}[HNO_3]^*_{(G)} < K_{NH_4NO_3} \tag{6.41}$$

One must, therefore, check for these conditions before using the gas-solid equilibria for calculating equilibrium surface concentrations. In the present system, four different scenarios are possible:

Scenario 1: Both NH_4NO_3 and NH_4Cl have potential to form or evaporate

If the gas-phase concentrations of NH_3, HNO_3, and HCl are favorable, or if there already exists some NH_4NO_3 or NH_4Cl in the aerosol phase, then NH_4NO_3 and NH_4Cl may form or evaporate such that the net flux of ammonia equals the sum of the net equivalent fluxes of nitrate, chloride, and sulfate, thus maintaining the electroneutrality of the particle. Mathematically, this can be expressed as

$$\begin{aligned} K^1_{NH_3}\left([NH_3]_{(G)} - [NH_3]^*_{(G)}\right) &= K^1_{HNO_3}\left([HNO_3]_{(G)} - [HNO_3]^*_{(G)}\right) \\ &+ K^1_{HCl}\left([HCl]_{(G)} - [HCl]^*_{(G)}\right) \\ &+ 2K^1_{H_2SO_4}\left([H_2SO_4]_{(G)} - [H_2SO_4]^*_{(G)}\right) \end{aligned} \tag{6.42}$$

Assuming $[H_2SO_4]^*_{(G)} = 0$, we can solve equations (6.39), (6.40), and (6.42) simultaneously to obtain the equilibrium surface concentrations

$$[NH_3]^*_{(G)} = \frac{-b + \sqrt{b^2 + 4c}}{2} \tag{6.43}$$

$$[HNO_3]^*_{(G)} = \frac{K_{NH_4NO_3}}{[NH_3]^*_{(G)}} \tag{6.44}$$

$$[HCl]^*_{(G)} = \frac{K_{NH_4Cl}}{[NH_3]^*_{(G)}} \tag{6.45}$$

where the parameters b and c are

$$b = \frac{K^1_{HNO_3}}{K^1_{NH_3}}[HNO_3]_{(G)} + \frac{K^1_{HCl}}{K^1_{NH_3}}[HCl]_{(G)} + 2\frac{K^1_{H_2SO_4}}{K^1_{NH_3}}[H_2SO_4]_{(G)} - [NH_3]_{(G)} \tag{6.46}$$

$$c = \left(\frac{K^1_{HNO_3}K_{NH_4NO_3}}{K^1_{NH_3}}\right) + \left(\frac{K^1_{HCl}K_{NH_4Cl}}{K^1_{NH_3}}\right) \tag{6.47}$$

Again, the above expressions for b and c are for the case when there exists some NH_4NO_3 and NH_4Cl in the aerosol phase, or if the gas-phase concentrations are favorable for salt formation (i.e., both HNO_3 and HCl are significant in the simulataneous solution for surface concentrations). If under given conditions, the calculated surface concentrations predict

evaporation of a salt, and the salt concentration is zero, then the parameters b and c must be modified by neglecting the terms pertaining to that salt/acid.

Scenario 2: Potential for only NH_4Cl to form or evaporate

If no $NH_4NO_{3(S)}$ exists, and the gas-phase concentrations of HNO_3 and NH_3 do not favor salt formation but the gas-phase HCl and NH_3 concentrations favor NH_4Cl formation, or if some NH_4Cl $_{(S)}$ pre-exists, then the expressions for b and c in (6.46) and (6.47) must be modified by neglecting the terms containing to $K^1_{HNO_3}$

Scenario 3: Potential for only NH_4NO_3 to form or evaporate

Similarly, if there is potential for $NH_4NO_{3(S)}$ to degas or form, but not for NH_4Cl , then the terms in b and c containing K^1_{HCl} must be neglected.

Scenario 4: No potential for either salt to form or evaporate

If, however, both $K^1_{HNO_3}$ and K^1_{HCl} containing terms must be neglected under a given set of conditions, then the surface concentrations are given by

$$[NH_3]^*_{(G)} = \max(-b, 0) \tag{6.48}$$

$$[HNO_3]^*_{(G)} = [HNO_3]_{(G)} \tag{6.49}$$

$$[HCl]^*_{(G)} = [HCl]_{(G)} \tag{6.50}$$

6.5.2 Sea-Salt Aerosol

The algorithm for determining equilibrium surface concentrations over dry sea-salt aerosol is similar to that discussed for fine-mode particles; however, one must first use the irreversible reactions of depositing H_2SO_4 vapor with NaCl and $NaNO_3$ or HNO_3 with NaCl to reach the assumed equilibrium state as depicted in Table 6.2. Additionally, one must make certain assumptions to overcome some specific situations.

For example, consider a sea-salt aerosol containing $NaCl_{(S)}$, $NaNO_{3(S)}$, and NH_4Cl $_{(S)}$, and the gas-phase containing H_2SO_4 vapor. Furthermore, assume that NH_4Cl $_{(S)}$ forms the outermost layer of the particle. Condensing H_2SO_4 vapor will first react with NH_4Cl , causing HCl vapor to degas at the same rate as H_2SO_4 deposits. The question is whether to degas

NH_3, or react it with H_2SO_4 to form $(NH_4)_2SO_4$. Degassing NH_3 along with HCl would leave deposited H_2SO_4 unreacted, while forming $(NH_4)_2SO_4$ in the presence of NaCl and $NaNO_3$ would not result in minimum Gibbs free energy. In reality, the final equilibrium state will be probably reached via either of the pathways; however, this phenomena cannot be modeled unless we have data on the actual gas-solid reaction rate constants. Similar problems arise in an aerosol containing $NaNO_3$, NH_4NO_3, and NH_4Cl . Such situations can be overcome by instantly evaporating the volatile ammonium salts — NH_4Cl and NH_4NO_3 — if present. This is done by simply putting appropriate amounts of NH_3, HCl, and HNO_3 into the gas phase, and subtracting them from the aerosol-phase.

Irreversible reactions of H_2SO_4 and HNO_3 with NaCl can be used to calculate the surface concentrations as follows:

$$[NH_3]^*_{(G)} = [NH_3]_{(G)} \tag{6.51}$$

$$[HNO_3]^*_{(G)} = 0 \tag{6.52}$$

$$[HCl]^*_{(G)} = [HCl]_{(G)} + \frac{(2K^1_{H_2SO_4}[H_2SO_4]_{(G)} + K^1_{HNO_3}[HNO_3]_{(G)})}{K^1_{HCl}} \tag{6.53}$$

Similarly, with any reaction of H_2SO_4 with $NaNO_3$, the surface concentrations are

$$[NH_3]^*_{(G)} = [NH_3]_{(G)} \tag{6.54}$$

$$[HCl]^*_{(G)} = [HCl]_{(G)} \tag{6.55}$$

$$[HNO_3]^*_{(G)} = [HNO_3]_{(G)} + \frac{(2K^1_{H_2SO_4}[H_2SO_4]_{(G)})}{K^1_{HNO_3}} \tag{6.56}$$

Volatile salts of ammonium may only form according to the hierarchies for sea-salt aerosol when no H_2SO_4 is present in the gas-phase. Algorithms developed in the previous section are equally applicable under those conditions.

6.6 Equilibrium Surface Concentrations for Liquid Aerosol

Calculation of equilibrium surface concentrations over a completely liquid aerosol is relatively straightforward, and involves three basic steps:

1. Determination of aerosol water content by the ZSR equation together with the Kelvin Effect.

2. Solution of the non-ideal aqueous-phase multicomponent ionic equilibria.

3. Determination of the equilibrium gas-phase surface concentration using Henry's Law.

6.6.1 Water Content and Kelvin Effect

Equilibrium water activity of a multicomponent solution is equal to the relative humidity above it if the air/solution interface is a flat surface. However, the equilibrium partial pressure of water over a curved interface is modfied due to the surface tension of the solution through a phenomenon known as the Kelvin Effect. At any given temperature, a convex aqueous surface, a water droplet for example, experiences a higher partial pressure of water above it than over a flat surface at same droplet-phase water activity. But since the partial pressure of water at the surface of a droplet at equilibrium is in fact the same as the ambient atmospheric water partial pressure, the resulting equilibrium water activity of the droplet solution is lower than the ambient relative humidity. The effect becomes increasingly pronounced with decreasing radius of the droplet as governed by the equation (Pruppacher and Klett, 1978):

$$\mathrm{RH} = \mathrm{a_w} \exp\left(\frac{4\mathrm{M_w}\ \sigma_\mathrm{L}}{\mathcal{R}\mathrm{T}\rho_\mathrm{w}\ \mathrm{D_{pmV}}}\right) \tag{6.57}$$

where $\mathrm{a_w}$ is the aerosol water activity, $\mathrm{M_w}$ is the molecular weight of water, σ_L is the surface tension of the multicomponent solution, $\mathcal{R}$ is the gas constant, ρ_w is the water density, and $\mathrm{D_{pmV}}$ is the particle mean volume diameter. The particle mean volume diameter is defined as

$$\mathrm{D_{pmV}} = \left(\frac{6\mathrm{V_T}}{\pi \mathrm{N_T}}\right)^{1/3} \tag{6.58}$$

where the total volume V_T is the ratio of the total mass to the multicomponent solution density ρ_L. The total aerosol mass is the sum of the mass of water and individual electrolytes, i.e., $V_T = W_T + \sum M_j[E_j]$. Invoking the ZSR equation for water content (6.15) yields

$$V_T = \frac{1}{\bar{\rho_L}} \sum_{j=1}^{Ne} \left\{ [E_j] \left(\frac{1}{m_k^o(a_w)} + M_j \right) \right\} \tag{6.59}$$

Thus, D_{pmV} is an implicit function of a_w. Moreover, the multicomponent solution surface tension and density are also related to a_w, thus, requiring an iterative procedure to compute the value of a_w in equilibrium with the ambient RH.

The resulting water content, W_T, at equilibrium is used for solving ionic equilibria. Since absorption or evaporation of water only changes the volume of the aerosol, and not the number, we can calculate the new equilibrium D_{pgN} by keeping σ_g constant.

$$D_{pgN} = D_{pmV} \ \exp\left[-\frac{3}{2} (\ln \sigma_g)^2 \right] \tag{6.60}$$

This value is used to compute the new mass-transfer coefficients.

6.6.2 Multicomponent Ionic Equilibria

For a single-electrolyte solution containing an i-j ion pair, the molal-scale activity is expressed as (Robinson and Stokes, 1959; Kim *et al.*, 1993)

$$\begin{aligned} a_{ij} &= a_i^{\nu_i} \ a_j^{\nu_j} \\ &= \gamma_i^{\nu_i} m_i^{\nu_i} \ \gamma_j^{\nu_j} m_j^{\nu_j} \\ &= \gamma_{ij}^{\nu} m_i^{\nu_i} m_j^{\nu_j} \qquad (6.61) \\ \nu &= \nu_i + \nu_j \qquad (6.62) \end{aligned}$$

where m_i is the molality of ion i, ν_i is the number of moles of ion species i per mol of i-j ion pair electrolyte dissociating completely, and γ_{ij} is the mean ionic activity coefficient of an i-j ion pair electrolyte. Thus, individual ion activity coefficients are related to the mean ionic activity coefficient as

$$\gamma_{ij}^{\nu} = \gamma_i^{\nu_i} \ \gamma_j^{\nu_j} \tag{6.63}$$

In our model, all aerosol-phase concentrations are expressed as mol m^{-3} air, while water content W_T is in kg m^{-3} air. The liquid-phase equilibrium equations (Table 6.5) in terms of molality can be written, therefore, as

$$W_T\ [HSO_4^-] = C_1\ [H^+]\ [SO_4^{2-}] \quad (6.64)$$

$$W_T\ a_w\ [NH_3]_L = C_2\ [NH_4^+]\ [OH^-] \quad (6.65)$$

$$[H^+]\ [OH^-] = C_3\ W_T^2\ a_w \quad (6.66)$$

where C_1, C_2, and C_3 are defined in terms of mean ionic activity coefficient as

$$C_1 = \frac{\gamma_{H\cdot SO_4}}{\gamma_{H\cdot HSO_4}\ K_{HSO_4}} \quad (6.67)$$

$$C_2 = \frac{\gamma_{NH_4\cdot OH}}{\gamma_{NH_3}\ K_{NH_3}} \quad (6.68)$$

$$C_3 = \frac{K_w}{\gamma_{H\cdot OH}} \quad (6.69)$$

Furthermore, the following electroneutrality condition must be satisfied at all times

$$[H^+] + [Na^+] + [NH_4^+] = [HSO_4^-] + 2[SO_4^{2-}] + [OH^-] + [NO_3^-] + [Cl^-] \quad (6.70)$$

Using mass conservation to close the above equations, we have

$$[SULF]_T = [HSO_4^-] + [SO_4^{2-}] \quad (6.71)$$

$$[NO_3^-]_T = [NO_3^-] \quad (6.72)$$

$$[Cl^-]_T = [Cl^-] \quad (6.73)$$

$$[NH_4^+]_T = [NH_4^+] + [NH_3]_L \quad (6.74)$$

$$[Na^+]_T = [Na^+] \quad (6.75)$$

where all terms on the LHS are the total concentrations of the generic prognostic species. These are initialized at time t = 0, and are known at any given time step by solving the dynamic condensation differential equations. The above nine unknowns and nine equations can be easily reduced to a single equation in $[H^+]$, which can be numerically solved by the Newton-Ralphson method or the bisection method. Either method requires about 10-15 iterations per solution. Upon converging on a value of $[H^+]$, concentrations of all other ions

can be calculated and used for calculating the equilibrium gas-phase surface concentrations, expressed as

$$[H_2SO_4]_g^* = 0 \tag{6.76}$$

$$[NH_3]_g^* = \frac{\gamma_{NH_4\cdot HSO_4}^2}{\gamma_{H\cdot HSO_4}^2} \frac{[NH_4^+]}{a_w\,[H^+]} \frac{K_w}{K_{NH_3}\mathcal{H}_{NH_3}} \tag{6.77}$$

$$[HNO_3]_g^* = \frac{\gamma_{H\cdot NO_3}^2 [H^+][NO_3^-]}{\mathcal{H}_{HNO_3} W_T^2} \tag{6.78}$$

$$[HCl]_g^* = \frac{\gamma_{H\cdot Cl}^2 [H^+][Cl^-]}{\mathcal{H}_{HCl} W_T^2} \tag{6.79}$$

Estimation of the multicomponent mean ionic activity coefficients is discussed next.

6.6.3 Activity Coefficient

Several methods exist for calculating mean ionic activity coefficients in a multicomponent solution (Kim *et al.*, 1993a,b). In this work, the method of Meissner and Kusik (1978) has been selected because of its relatively good accuracy and high computational efficiency. The original method was meant only for strong electrolytes that dissiociate almost completely in aqueous solutions. In the present system, all electrolytes are strong, except for HSO_4^- ion, which does not dissociate completely under acidic conditions (low pH). Thus, it appears that the method has been somewhat incorrectly applied in the past for estimating mean activity coefficients in concentrated aqueous aerosols (Kim *et al.*, 1993a,b).

According to the original method,

$$\begin{aligned} \log \gamma_{12} &= \frac{z_2}{(z_1+z_2)I} \left[m_2 \left(\frac{z_1+z_2}{2} \right)^2 \log \gamma_{12}^o + m_4 \left(\frac{z_1+z_4}{2} \right)^2 \log \gamma_{14}^o + \cdots \right] \\ &+ \frac{z_1}{(z_1+z_2)I} \left[m_1 \left(\frac{z_1+z_2}{2} \right)^2 \log \gamma_{12}^o + m_3 \left(\frac{z_3+z_2}{2} \right)^2 \log \gamma_{32}^o + \cdots \right] \end{aligned} \tag{6.80}$$

where odd and even subscripts denote cations and anions, respectively; and γ_{ij}^o is the mean binary ionic activity coefficient for an electrolyte ion pair i-j alone in aqueous solution. For a strong 1-2 electrolyte in aqueous solution alone, the RHS of the above equation for multicomponent system simplifies to $\log \gamma_{12}^o$. Since $H^+ - HSO_4^-$, or $H^+ - SO_4^{2-}$ ion pairs

cannot exist alone in aqueous H_2SO_4 solutions, the above method would fail to recover the mean binary ionic activity coefficients for these ion pairs.

The original method was, therefore, modified to overcome this drawback for weak acid HSO_4^-. The modified Meissner and Kusik multicomponent activity coefficient model is as follows:

$$\begin{aligned}
\log \gamma_{\mathrm{H\cdot NO_3}} &= \frac{1}{2\mathrm{IW}}([\mathrm{NO_3^-}] \log \gamma^{\circ}_{\mathrm{H\cdot NO_3}} + [\mathrm{Cl^-}] \log \gamma^{\circ}_{\mathrm{H\cdot Cl}} + [\mathrm{HSO_4^-}] \log \gamma^{\circ}_{\mathrm{H\cdot HSO_4}} \\
&+ \frac{9}{4}[\mathrm{SO_4^{2-}}] \log \gamma^{\circ}_{\mathrm{2H\cdot SO_4}} + [\mathrm{H^+}] \log \gamma^{\circ}_{\mathrm{H\cdot NO_3}} + [\mathrm{NH_4^+}] \log \gamma^{\circ}_{\mathrm{NH_4\cdot NO_3}} \\
&+ [\mathrm{Na^+}] \log \gamma^{\circ}_{\mathrm{Na\cdot NO_3}}) \qquad (6.81)
\end{aligned}$$

$$\begin{aligned}
\log \gamma_{\mathrm{H\cdot Cl}} &= \frac{1}{2\mathrm{IW}}([\mathrm{NO_3^-}] \log \gamma^{\circ}_{\mathrm{H\cdot NO_3}} + [\mathrm{Cl^-}] \log \gamma^{\circ}_{\mathrm{H\cdot Cl}} + [\mathrm{HSO_4^-}] \log \gamma^{\circ}_{\mathrm{H\cdot HSO_4}} \\
&+ \frac{9}{4}[\mathrm{SO_4^{2-}}] \log \gamma^{\circ}_{\mathrm{2H\cdot SO_4}} + [\mathrm{H^+}] \log \gamma^{\circ}_{\mathrm{H\cdot Cl}} + [\mathrm{NH_4^+}] \log \gamma^{\circ}_{\mathrm{NH_4\cdot Cl}} \\
&+ [\mathrm{Na^+}] \log \gamma^{\circ}_{\mathrm{Na\cdot Cl}}) \qquad (6.82)
\end{aligned}$$

$$\begin{aligned}
\log \gamma_{\mathrm{H\cdot HSO_4}} &= \frac{1}{2\mathrm{IW}} \left([\mathrm{H^+}] + [\mathrm{NH_4^+}] + [\mathrm{Na^+}] + [\mathrm{HSO_4^-}] + 4[\mathrm{SO_4^{2-}}]\right) \log \gamma^{\circ}_{\mathrm{H\cdot HSO_4}} \\
&+ \frac{1}{2\mathrm{IW}} \left([\mathrm{NO_3^-}] \log \gamma^{\circ}_{\mathrm{H\cdot NO_3}} + [\mathrm{Cl^-}] \log \gamma^{\circ}_{\mathrm{H\cdot Cl}}\right) \qquad (6.83)
\end{aligned}$$

$$\begin{aligned}
\log \gamma_{\mathrm{2H\cdot SO_4}} &= \frac{1}{2\mathrm{IW}} \left([\mathrm{H^+}] + [\mathrm{NH_4^+}] + [\mathrm{Na^+}] + [\mathrm{HSO_4^-}] + 4[\mathrm{SO_4^{2-}}]\right) \log \gamma^{\circ}_{\mathrm{2H\cdot SO_4}} \\
&+ \frac{1}{2\mathrm{IW}} \left([\mathrm{NO_3^-}] \log \gamma^{\circ}_{\mathrm{H\cdot NO_3}} + [\mathrm{Cl^-}] \log \gamma^{\circ}_{\mathrm{H\cdot Cl}}\right) \qquad (6.84)
\end{aligned}$$

$$\begin{aligned}
\log \gamma_{\mathrm{NH_4\cdot HSO_4}} &= \frac{1}{2\mathrm{IW}} \left([\mathrm{H^+}] + [\mathrm{NH_4^+}] + [\mathrm{Na^+}] + [\mathrm{HSO_4^-}] + 4[\mathrm{SO_4^{2-}}]\right) \log \gamma^{\circ}_{\mathrm{NH_4\cdot HSO_4}} \\
&+ \frac{1}{2\mathrm{IW}} \left([\mathrm{NO_3^-}] \log \gamma^{\circ}_{\mathrm{NH_4\cdot NO_3}} + [\mathrm{Cl^-}] \log \gamma^{\circ}_{\mathrm{NH_4\cdot Cl}}\right) \qquad (6.85)
\end{aligned}$$

$$\begin{aligned}
\log \gamma_{\mathrm{NH_4\cdot OH}} &= \frac{1}{2\mathrm{IW}} \left(([\mathrm{NH_4^+}] + 4[\mathrm{SO_4^{2-}}]) \log \gamma^{\circ}_{\mathrm{NH_4\cdot OH}} + [\mathrm{Na^+}] \log \gamma^{\circ}_{\mathrm{Na\cdot OH}}\right) \\
&+ \frac{1}{2\mathrm{IW}}([\mathrm{NO_3^-}] \log \gamma^{\circ}_{\mathrm{NH_4\cdot NO_3}} + [\mathrm{Cl^-}] \log \gamma^{\circ}_{\mathrm{NH_4\cdot Cl}} \\
&+ [\mathrm{HSO_4^-}] \log \gamma^{\circ}_{\mathrm{NH_4\cdot HSO_4}}) \qquad (6.86)
\end{aligned}$$

$$\begin{aligned}\log\gamma_{\mathrm{Na\cdot OH}} &= \frac{1}{2\mathrm{IW}}([\mathrm{OH^-}]\log\gamma^{\circ}_{\mathrm{Na\cdot OH}} + [\mathrm{NO_3^-}]\log\gamma^{\circ}_{\mathrm{Na\cdot NO_3}} + [\mathrm{Cl^-}]\log\gamma^{\circ}_{\mathrm{Na\cdot Cl}} \\ &+ [\mathrm{HSO_4^-}]\log\gamma^{\circ}_{\mathrm{Na\cdot HSO_4}} + \frac{9}{4}[\mathrm{SO_4^{2-}}]\log\gamma^{\circ}_{\mathrm{2Na\cdot SO_4}} \\ &+ [\mathrm{Na^+}]\log\gamma^{\circ}_{\mathrm{Na\cdot OH}} + [\mathrm{NH_4^+}]\log\gamma^{\circ}_{\mathrm{NH_4\cdot OH}}) \end{aligned} \tag{6.87}$$

$$\gamma^2_{\mathrm{H\cdot OH}} = \frac{\gamma^2_{\mathrm{NH_4\cdot OH}}\ \gamma^2_{\mathrm{H\cdot HSO_4}}}{\gamma^2_{\mathrm{NH_4\cdot HSO_4}}} \tag{6.88}$$

$$\gamma^2_{\mathrm{H\cdot OH}} = \frac{\gamma^2_{\mathrm{Na\cdot OH}}\ \gamma^2_{\mathrm{H\cdot HSO_4}}}{\gamma^2_{\mathrm{Na\cdot HSO_4}}} \tag{6.89}$$

The binary activity coefficients are expressed as a polynomial function of fractional ionic strength as,

$$\log\gamma^{\circ}_{\mathrm{A\cdot B}} = \mathrm{b_1}\sqrt{\mathrm{I_f}} + \mathrm{b_2 I_f} + \mathrm{b_3 I_f^2} + \mathrm{b_4 I_f^3} + \mathrm{b_5 I_f^4} \tag{6.90}$$

where the ionic strength is defined as,

$$\mathrm{I} = \frac{1}{2\mathrm{W}}\left([\mathrm{H^+}] + [\mathrm{NH_4^+}] + [\mathrm{Na^+}] + [\mathrm{HSO_4^-}] + 4[\mathrm{SO_4^=}] + [\mathrm{NO_3^-}] + [\mathrm{Cl^-}] + [\mathrm{OH^-}]\right) \tag{6.91}$$

and fractional ionic strength as

$$\mathrm{I_f} = \frac{\mathrm{I}}{\mathrm{I} + 1000/\mathrm{M_w}} \tag{6.92}$$

The mean binary activity coefficients for $\mathrm{H^+ - HSO_4^-}$, $\mathrm{2H^+ - SO_4^{2-}}$, and $\mathrm{NH_4^+ - HSO_4^-}$ ion pairs were calculated by the model of Clegg and Brimblecombe (1995) over the entire range of composition and ionic strengths from 0 to 100 mol $\mathrm{kg^{-1}}$. The results were fit into polynomials, and the coefficients, $\mathrm{b_1}, \ldots, \mathrm{b_5}$, were tabulated as a function of the parameter $\mathrm{X_b}$, varied at an interval of 0.02 between 0.0 and 2.0, where

$$\mathrm{X_b} = \frac{[\mathrm{NH_4^+}] + [\mathrm{Na^+}]}{[\mathrm{SULF}]} \tag{6.93}$$

Although Clegg and Brimblecombe's model only treats the ammonium and sulfuric acid system, the sodium and sulfuric acid system is assumed to behave in an identical manner due to lack of data. The mean binary ionic activity coefficients can be conveniently interpolated for any intermediate value of $\mathrm{X_b}$. However, the parameter $\mathrm{X_b}$ must be restricted to values equal to or less than 2.0 even if the actual value may be slightly greater than two. Values of b's for other species are given in Table (A.3).

6.7 Test Simulations

The purpose of this section is to demonstrate the performance of various algorithms implemented in MOSAIC in response to various initial and ambient conditions. To keep the analysis simple, only single mode results are presented with arbitrary realistic values of mass transfer coefficients chosen for the condensing species ($K^1_{NH_3} = 0.3$ h^{-1}, $K^1_{HNO_3} = 0.2$ h^{-1}, $K^1_{HCl} = 0.2$ h^{-1}, $K^1_{H_2SO_4} = 0.1$ h^{-1}). Also, the Kelvin Effect was neglected in these simulations. Each simulation was run for a 10 h period. Since the mass-transfer coefficients were arbitrary, the chosen length of simulation is merely for convenience in illustrating the dynamics of the model, and bears no physical significance.

Table 6.7 lists the initial concentrations and ambient conditions for the six different test cases. The first three cases represent fine-mode sulfate aerosols, and the remaining three represent the sea-salt mode. Figures 6.9 through 6.20 show the evolutions of various species in the gas and aerosol phases. Growth curves, characterized by two different mass ratios are also shown for each case. The mass ratios are defined as

$$\frac{W_{tot}(t)}{W_{dry}(t)} = \frac{\text{total aerosol mass at time t}}{\text{dry aerosol mass at time t}}$$

$$\frac{W_{dry}(t)}{W_{dry}(0)} = \frac{\text{dry aerosol mass at time t}}{\text{initial dry aerosol mass}}$$

Table 6.7: Hypothetical Test Cases

Case	RH	T	Gas-Phase				Aerosol-Phase[a]					X_T
	(%)	(K)	$[H_2SO_4]$	$[HNO_3]$	[HCl]	$[NH_3]$	[SULF]	$[NO_3^-]$	$[Cl^-]$	$[NH_4^+]$	$[Na^+]$	
			(ppb)				(ppb)					
A1	30	290	3	4	0	4	1	0	2	4	0	4
A2	80	290	3	4	0	4	1	0	2	4	0	4
A3	65	290	4	4	3	1	2	0	0	4	0	2
A4	45	280	5	5	0	4	1	0	3	0	5	5
A5	80	280	5	5	0	4	1	0	3	0	5	5
A6	65	280	6	5	3	1	2	0	0	0	4	2

[a] The aerosol ions are generic species, and do not indicate the phase of the system. The phase is determined according to the average DRH of the mixed salt, the ambient RH, and the hysteresis history of the particle. Also, note that aerosol-phase concentrations are expressed as gas-phase ppb units for easy comparison.

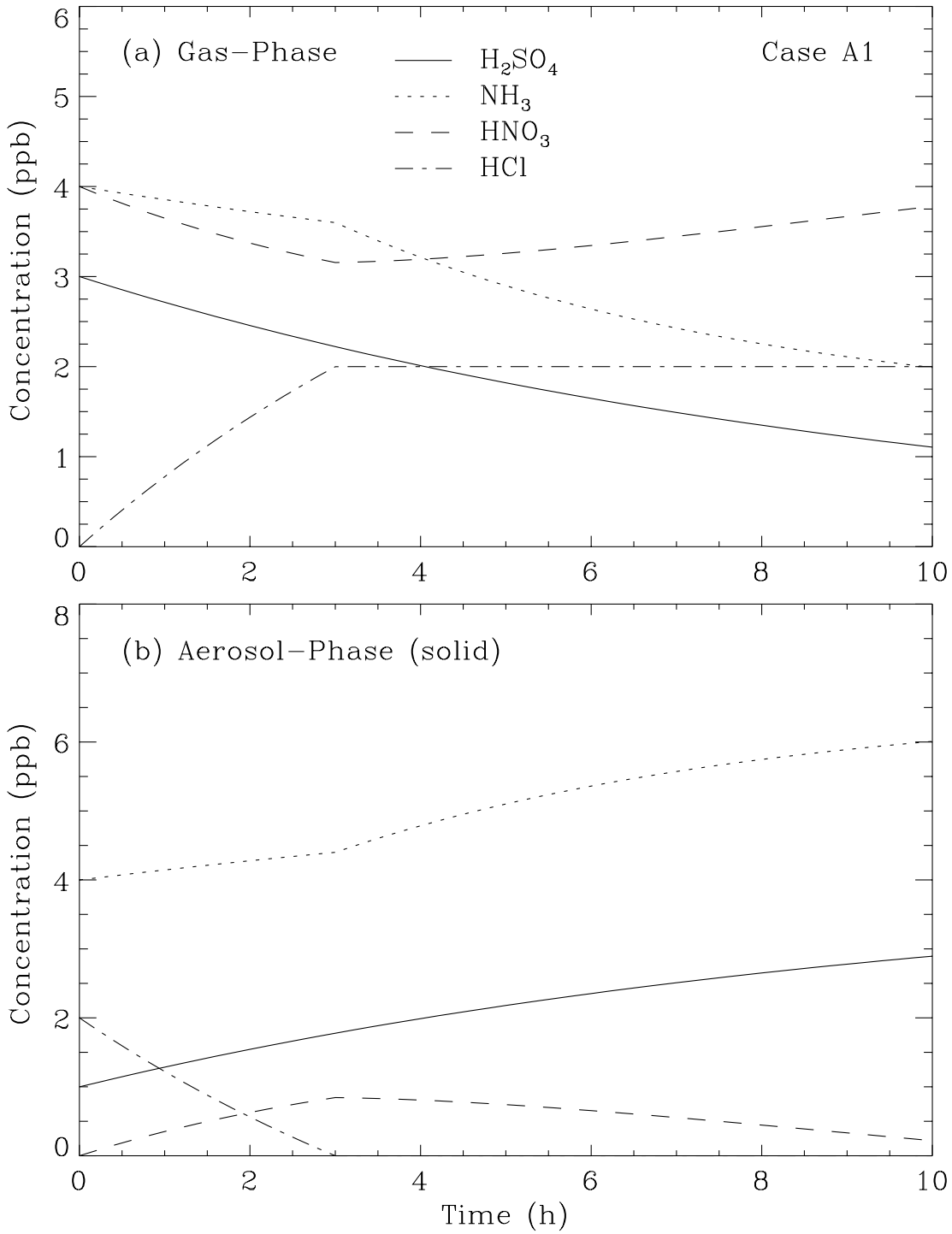

Figure 6.9: Concentration evolution profiles for case A1: (a) gas-phase species; (b) corresponding aerosol-phase generic species.

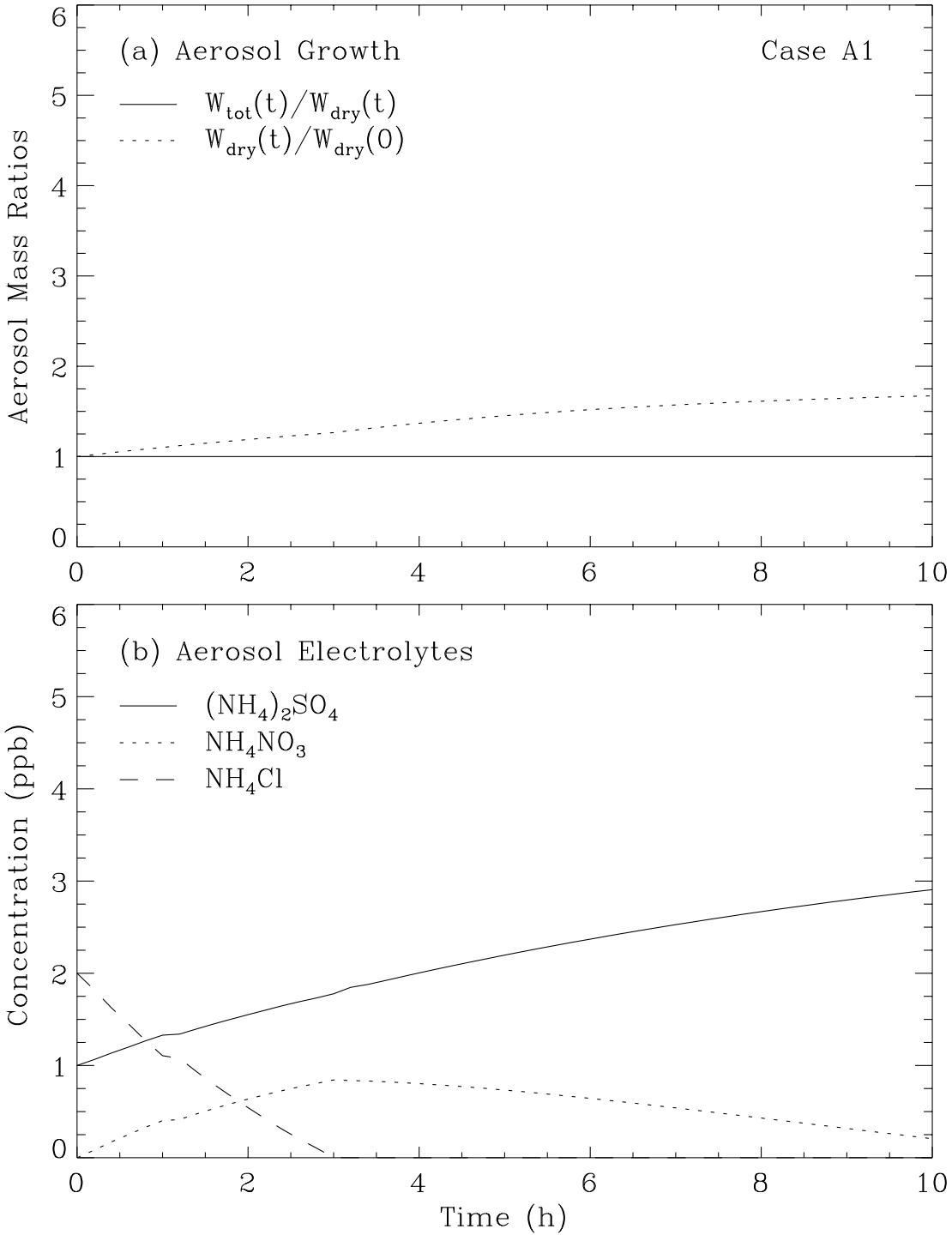

Figure 6.10: (a) Aerosol growth curves for case A1; (b) evolution of individual electrolytes in the aerosol phase.

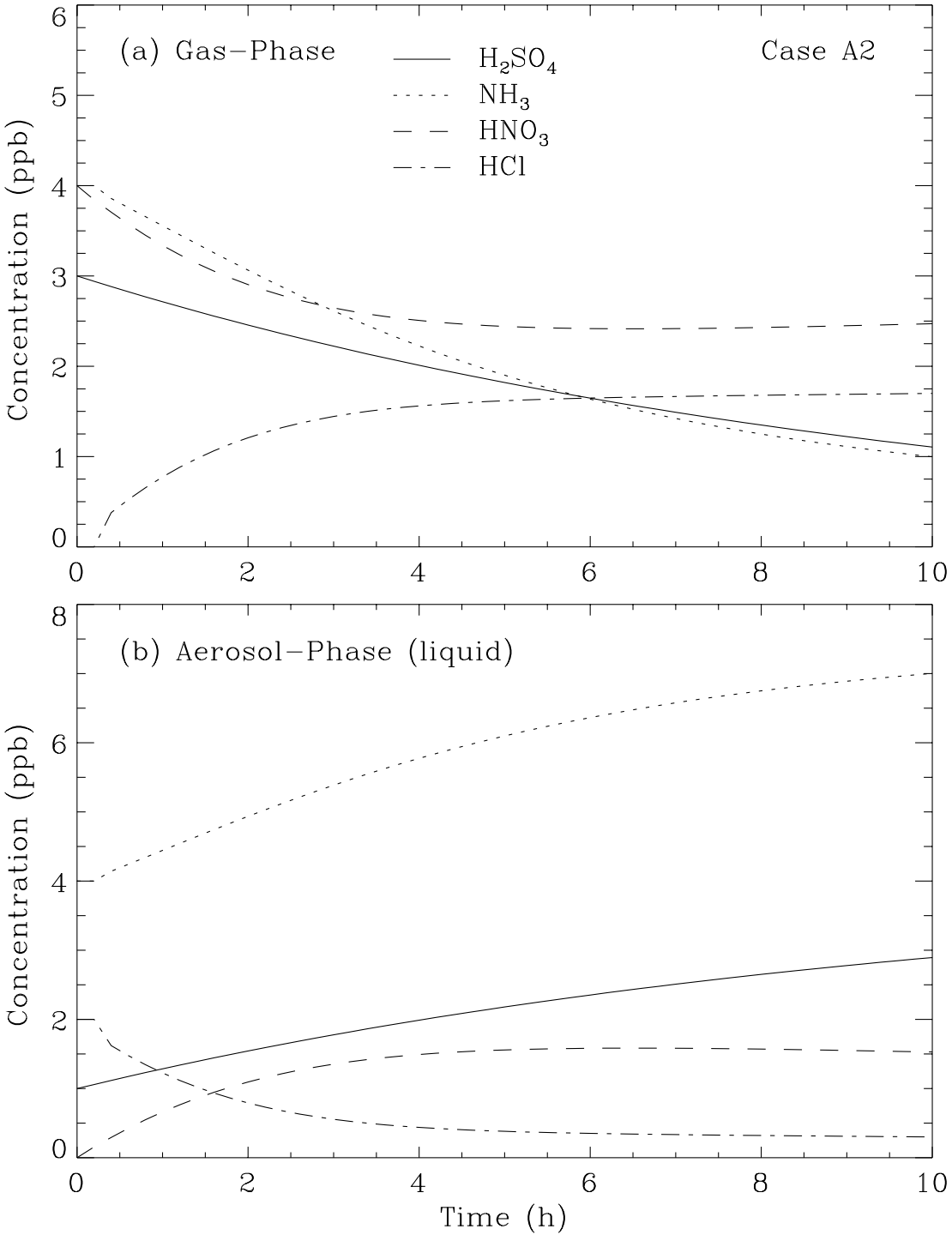

Figure 6.11: Concentration evolution profiles for case A2: (a) gas-phase species; (b) corresponding aerosol-phase generic species.

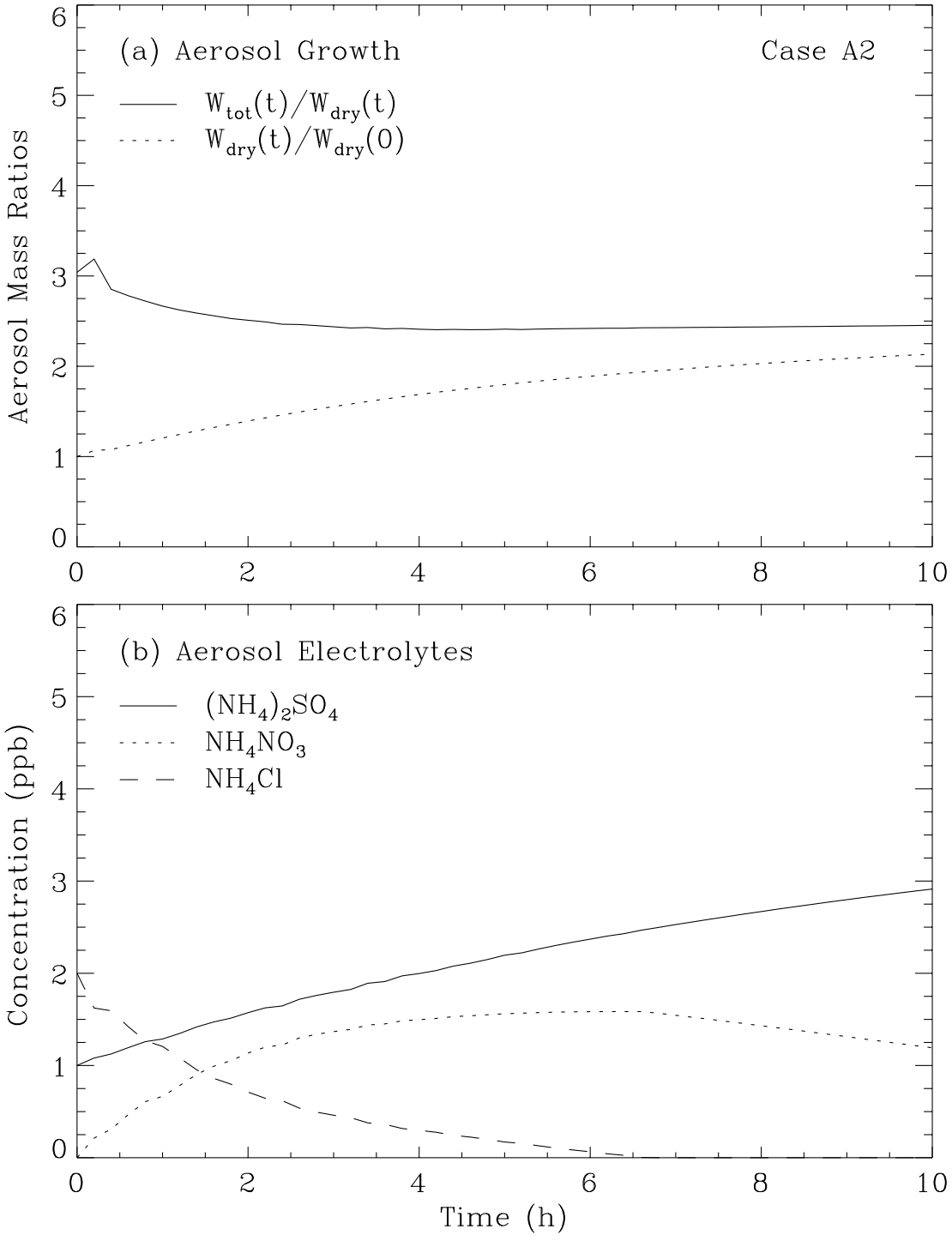

Figure 6.12: (a) Aerosol growth curves for case A2; (b) evolution of individual electrolytes in the aerosol phase.

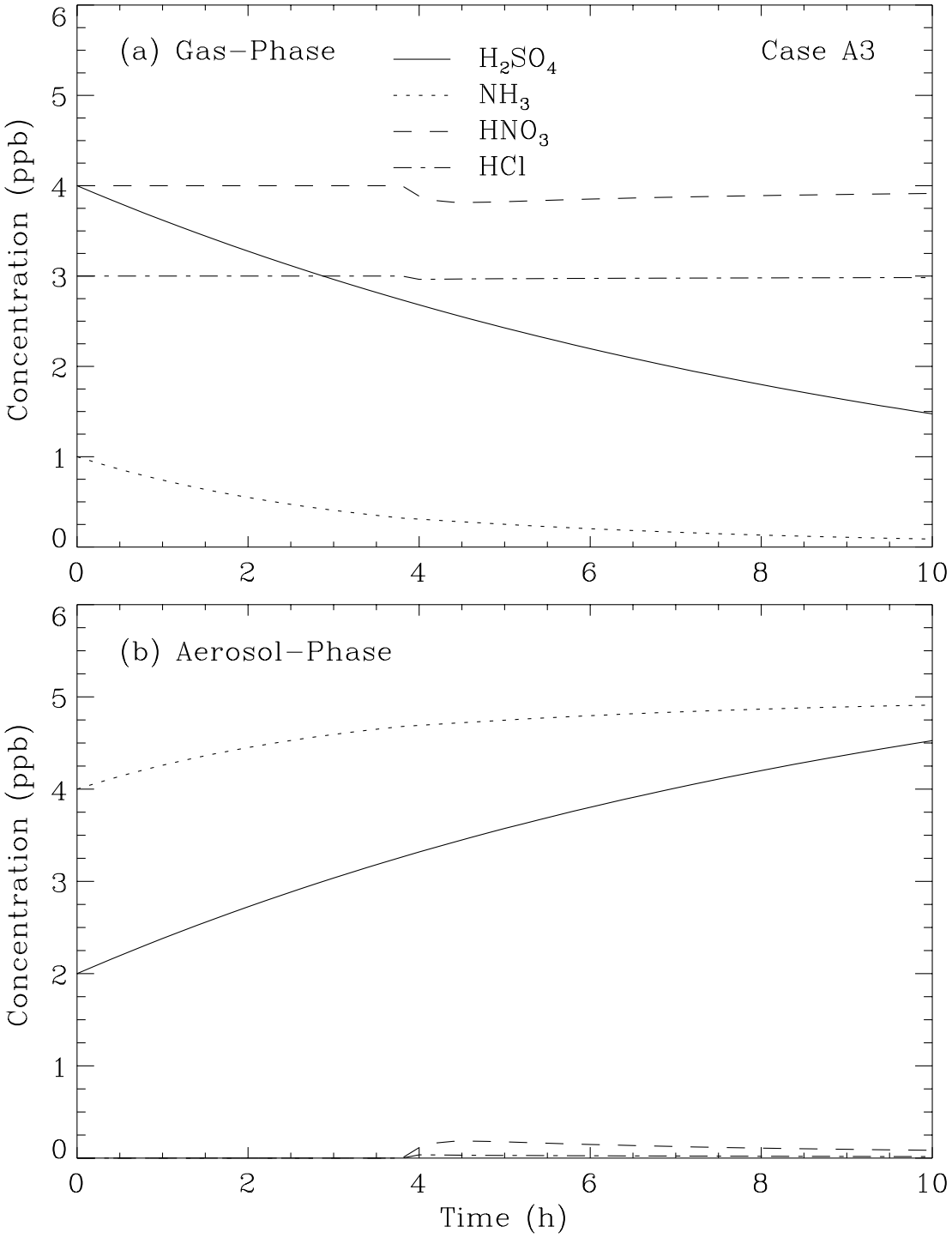

Figure 6.13: Concentration evolution profiles for case A3: (a) gas-phase species; (b) corresponding aerosol-phase generic species.

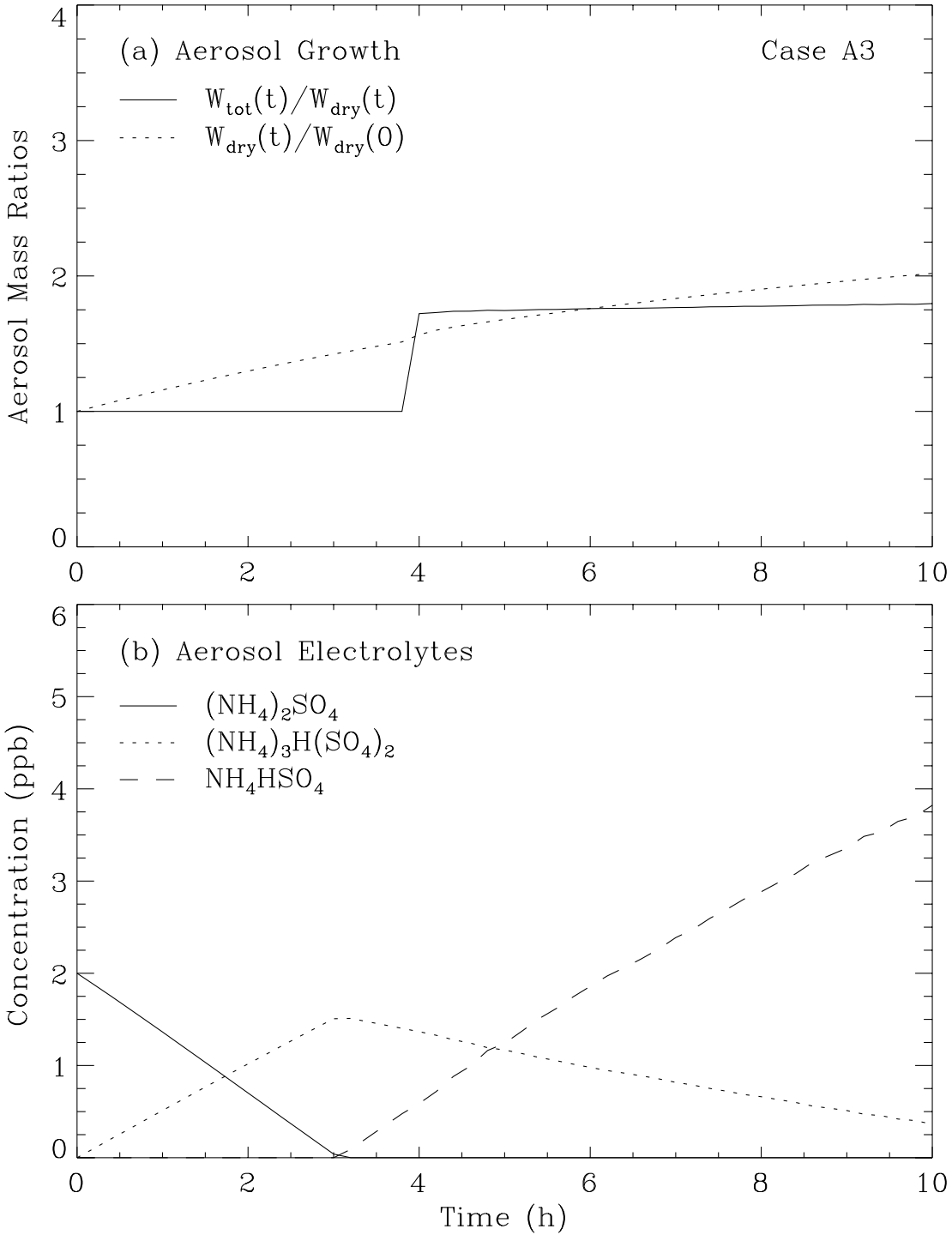

Figure 6.14: (a) Aerosol growth curves for case A3; (b) evolution of individual electrolytes in the aerosol phase.

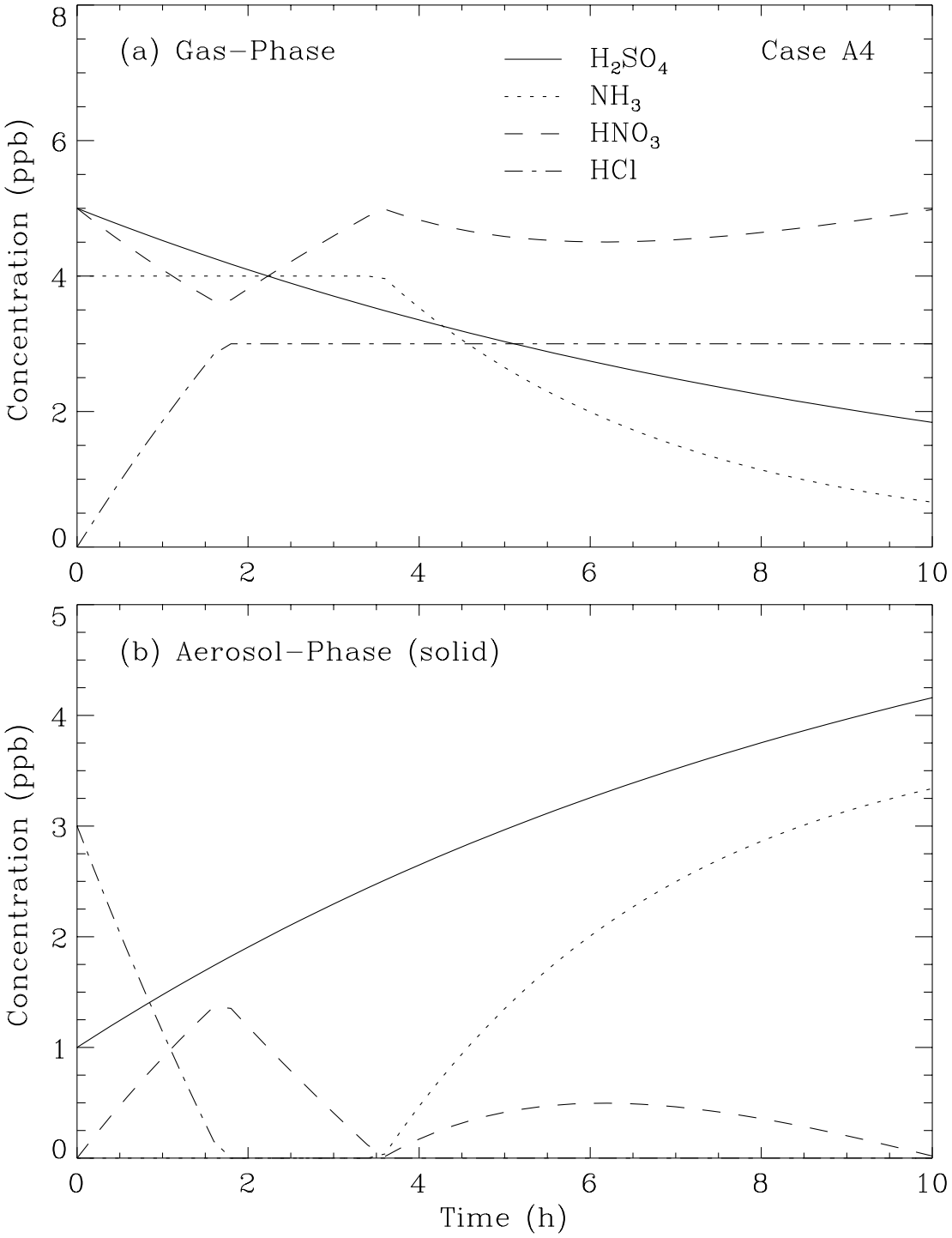

Figure 6.15: Concentration evolution profiles for case A4: (a) gas-phase species; (b) corresponding aerosol-phase generic species.

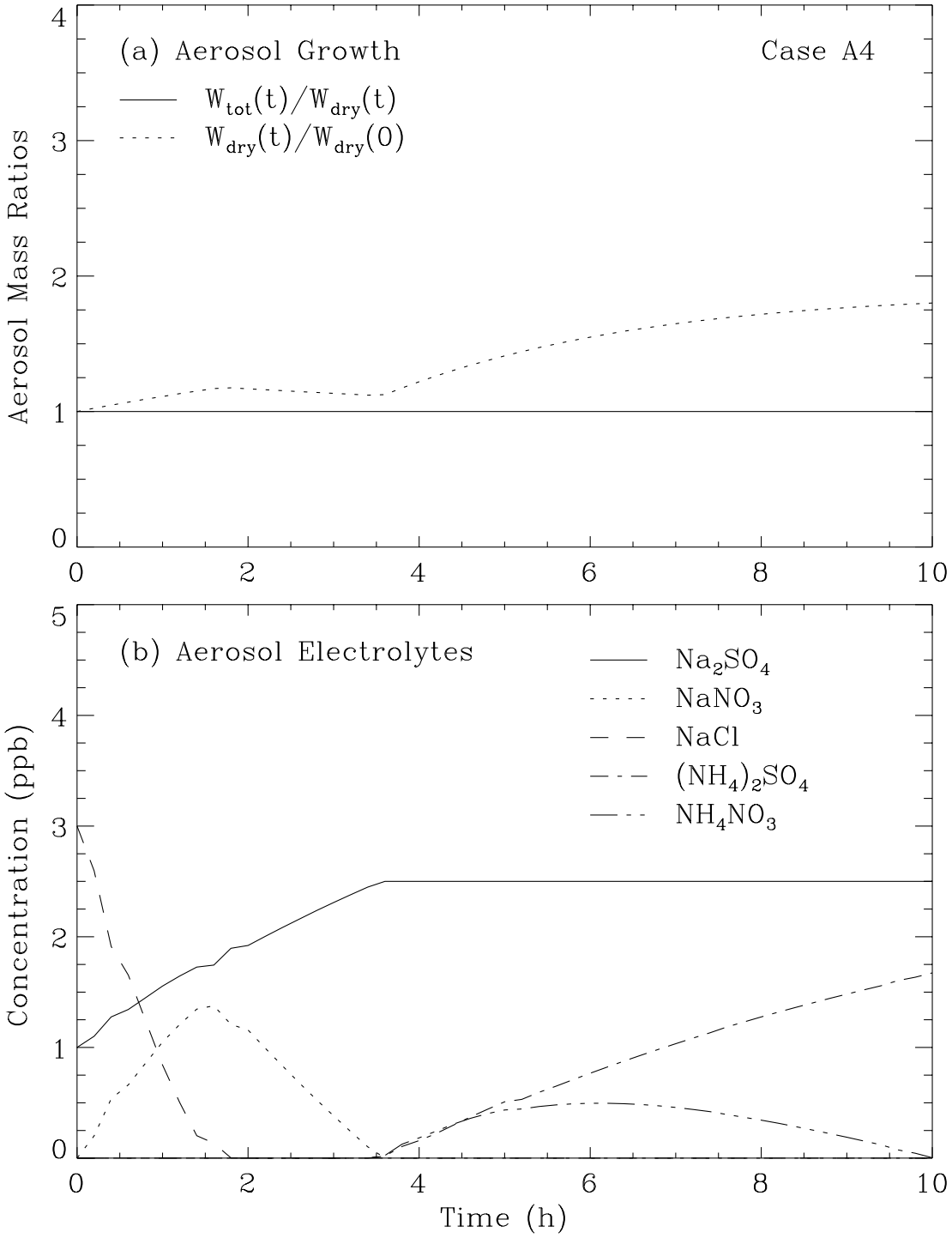

Figure 6.16: (a) Aerosol growth curves for case A4; (b) evolution of individual electrolytes in the aerosol phase.

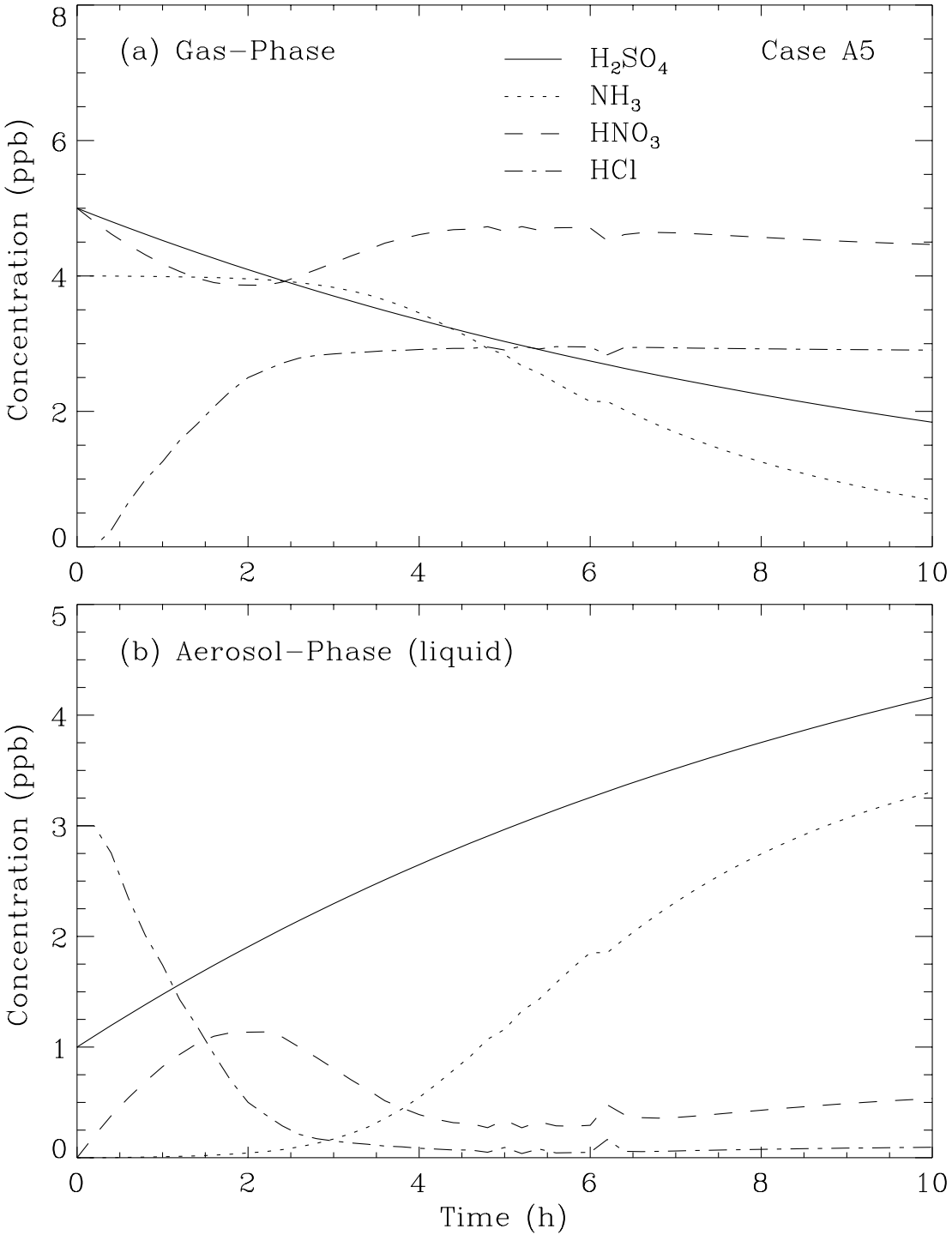

Figure 6.17: Concentration evolution profiles for case A5: (a) gas-phase species; (b) corresponding aerosol-phase generic species.

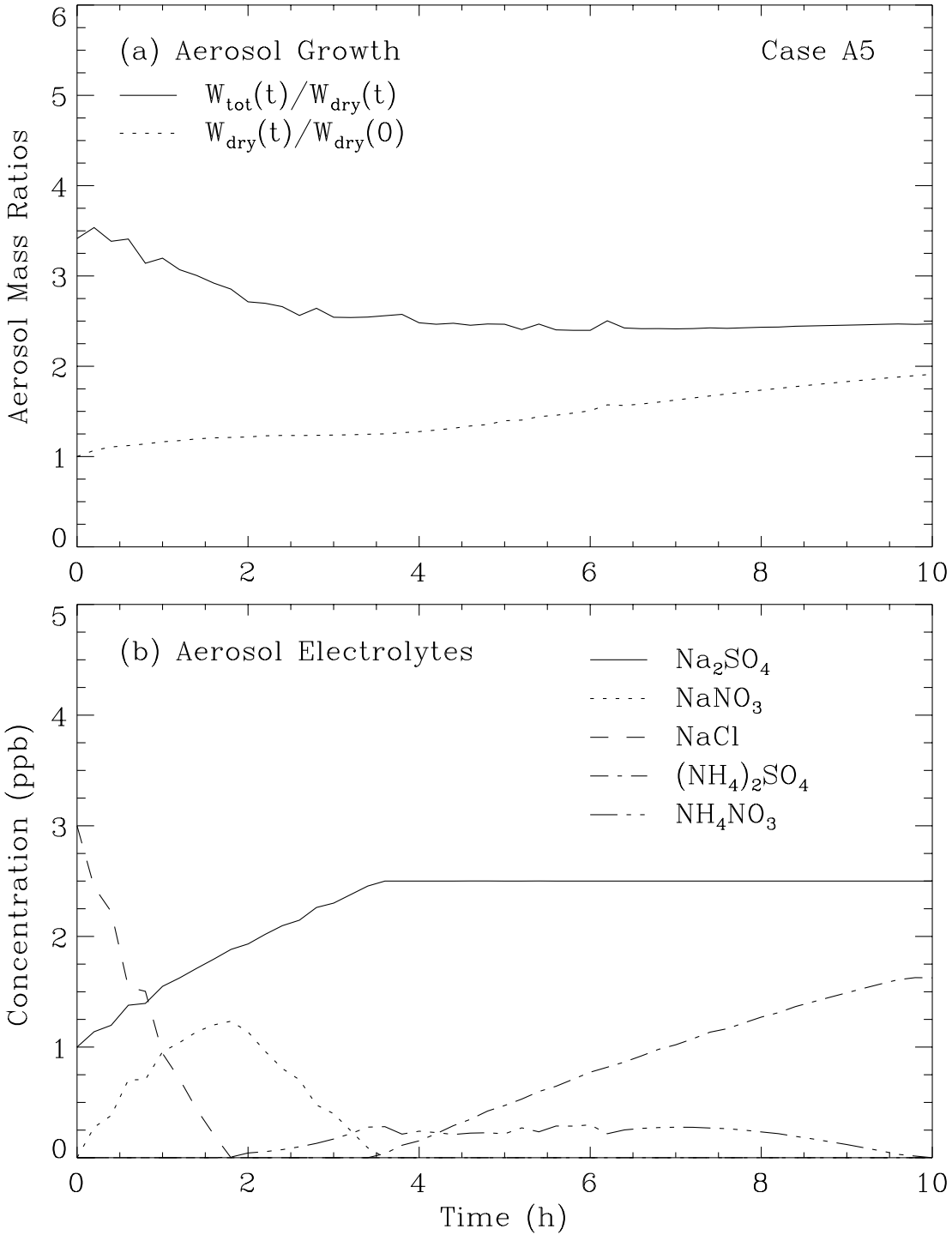

Figure 6.18: (a) Aerosol growth curves for case A5; (b) evolution of individual electrolytes in the aerosol phase.

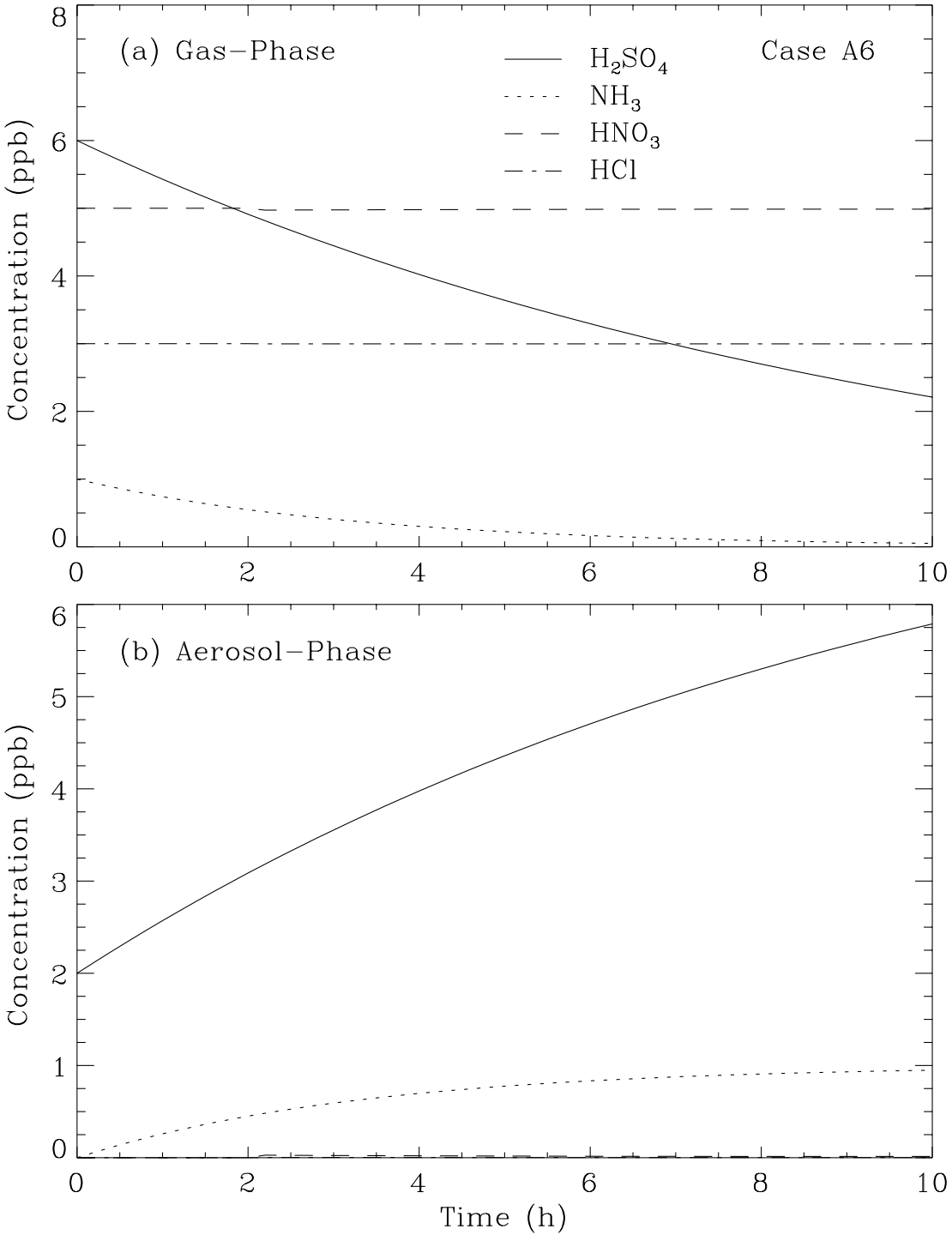

Figure 6.19: Concentration evolution profiles for case A6: (a) gas-phase species; (b) corresponding aerosol-phase generic species.

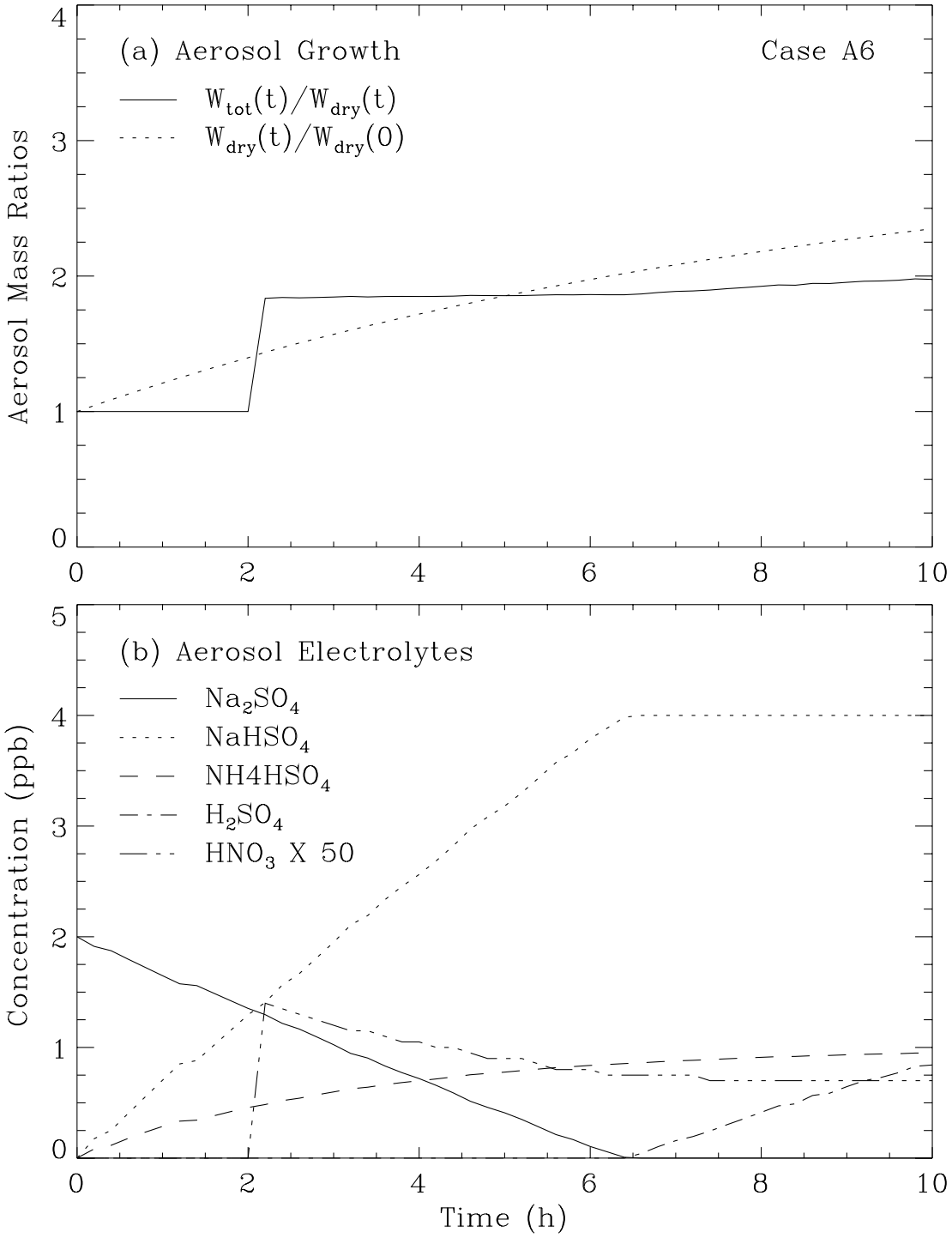

Figure 6.20: (a) Aerosol growth curves for case A6; (b) evolution of individual electrolytes in the aerosol phase.

The cases A1 and A2 have identical initial conditions except for the ambient RH. At 30% RH, all electrolytes predicted in case A1 are dry. In Figures 6.9 and 6.10, observe that HNO_3 initially condenses along with H_2SO_4 and NH_3, forming NH_4NO_3, but partially evaporates back into the gas-phase as the NH_3 concentration in the gas-phase decreases during the later stages of the run. On the other hand, all NH_4Cl in the aerosol rapidly decomposes to release HCl, while the corresponding NH_3 remains in the aerosol phase to react with condensing HNO_3 and H_2SO_4. This explains the slower deposition rate of NH_3 during the early stages of the run. The corresponding evolution profiles in the case A2 are markedly different at 80% RH, where the initial aerosol is predicted to be completely dissolved (Figures 6.11 and 6.12). Interestingly, the aerosol-phase NH_4Cl evaporates less rapidly, while considerably higher NH_4NO_3 forms in the aerosol. As expected, the H_2SO_4 profiles are identical in these two cases.

In the case A3, the aerosol is initially completely dry at 65% RH, but deliquesces around t = 4 h when appreciable NH_4HSO_4 is predicted in the aerosol-phase (refer to Figures 6.13 and 6.14). This is marked by the sudden increase in the total growth ratio. Since the aerosol phase is relatively acidic, very little HNO_3 and HCl were absorbed due to the common ion effect of H^+.

The sea-salt aerosol cases A4 and A5 are relatively more complex. In the case A4, the aerosol is predicted to be completely dry at 45% RH. The most interesting behavior is displayed by HNO_3 (Figure 6.15). Initially it forms solid $NaNO_3$ by the irreversible reaction with NaCl. However, when all NaCl was exhausted, the condensing H_2SO_4 vapors reacted with the crystalline $NaNO_3$, releasing HNO_3 gas. When all sodium was converted to Na_2SO_4, the HNO_3 vapors re-condensed in the aerosol phase as solid NH_4NO_3. This also points to the marked the onset of $(NH_4)_2SO_4$ formation in the aerosol-phase. Interestingly, the most significant growth in the aerosol mass also occurred beyond this point, as reflected by the dry mass growth curve (see Figure 6.16).

The case A5 is identical to A4 except for the ambient RH. Again, at 80% RH, the sea-salt aerosol was predicted to be completely liquid. Here, the time evolutions of both HNO_3 and HCl concentrations are similar to the dry case, except that the profiles lack the characteristic discontinuities associated with gas-solid dynamics (Figure 6.17). It is interesting to note that the total mass growth ratio gradually decreased with increase in the inorganic mass of the aerosol, indicating differences in the hygroscopicities of various salts.

Finally, the composition and ambient RH in the case A6 were chosen such that the sea-salt aerosol deliquesced at t = 2 h, after initially starting out as completely dry. Since the resulting aqueous solution is acidic, very little HNO_3 and HCl partitioned into the aerosol phase (Figures 6.19 and 6.20).

With regards to computational efficiency, the aqueous-phase cases required almost twice as much time as the dry cases, most likely due to repeated iterative solution needed for solving the multicomponent ionic equilibria. However, the CPU time requirements for the 10 h simulations were very small when compared to a typical 10 h gas-phase chemistry run.

6.8 Concluding Remarks

A comprehensive yet highly efficient model (MOSAIC) was developed for simulating dynamic aerosol growth due to condensation of inorganic gases. The first version of the model presented in this chapter treats various ammonium and sodium salts of sulfate, nitrate, and chloride. Additional species such as methanesulfonic acid could be easily incorporated into the model with some modifications in the algorithms.

The model is designed to handle any reasonable scenario typically found in the atmosphere, and requires that the user-supplied initial aerosol-phase compositions conform to the ones assumed for the model. Furthermore, the model assumes that an aerosol is either completely dry, or completely dissolved, based on a weighted average deliquescence relative humidity and the ambient RH. This eliminates the computationally expensive solid-liquid equilibrium calculations. The CPU time requirements of MOSAIC are negligible compared to the gas-phase chemistry calculations, thus making it suitable for large-scale atmospheric chemistry models.

The model currently treats condensing organic vapors as inert mass, and does not take into account the potential hydrophobic effects of high molecular weight organic molecules on the overall hygroscopicity of the aerosol. Such effects are being investigated by various research groups in the aerosol research community, and may possibly be included in future versions of MOSAIC.

Chapter 7

Cloud-Phase Chemistry

Clouds are efficient atmospheric reactors where reactions may proceed at much higher rates than corresponding gas-phase rates. Additionally, it may even open-up alternate reaction pathways, thus accelerating oxidation rates of several species of interest. Apart from the nucleating aerosol ions, the major sources of acidity in cloud water include absorption of acidic gases such as H_2SO_4, HNO_3, CO_2, and HCOOH formed as a result of gas-phase photochemical reactions. Also, absorption of various precursor gases such as SO_2, NO_x, and HCHO, followed by in-situ aqueous-phase oxidation by various dissolved oxidants such as O_3, H_2O_2, HO_2, OH, and NO_3 can be important (Seigneur and Saxena, 1984; Lelieveld and Crutzen, 1991). Several modeling studies have estimated that in-cloud processes are responsible for at least 50 to 60% of the total SO_2 to sulfate conversion (Hegg, 1985; Luria and Sievering, 1991). Precipitating clouds can effectively remove the dissolved species from the atmosphere, while non-precipitating ones tend to increase the aerosol mass upon evaporation (Nair and Peters, 1989). The latter phenomenon is called "cloud processing". Thus, there is a keen interest in simulating the atmospheric cloud-phase chemistry.

Absorption of the acid vapors, their precursors, and the oxidants vary widely depending upon their gas-phase diffusivity, interfacial mass accommodation coefficient, effective aqueous-phase solubility, aqueous-phase diffusivity, and effective aqueous-phase first-order reaction rate constant. When the effective characteristic reaction time of a dissolved species is much higher than its characteristic mass transfer time, it is reasonable to assume its concentration to be in equilibrium with the gas-phase as dictated by Henry's Law. However, when the two time-scales are comparable, or if the reverse is true, then there exist some limitations to the rate of reaction since the aqueous-phase concentration will be lower than the equilibrium value (Schwartz, 1986, 1988b; Shi and Seinfeld, 1991).

In this chapter, the analytical solution to the simultaneous diffusion and reaction in a cloud droplet is examined and interpreted in terms of the classical two-film model, and subsequently applied to a comprehensive aqueous-phase reaction mechanism to determine the potential for mass transfer limitation for various species. A condensed mechanism is also derived for use in a global-scale model.

7.1 Mass Transfer with Chemical Reaction

Schwartz and Freiberg (1981), Schwartz (1986, 1988b), and more recently Shi and Seinfeld (1991) have performed detailed analysis on mass-transport limitation for reactive absorption in micron-size cloud droplets, and have presented generalized criteria for the onset of such a limitation. They have also shown that there is negligible mass-transport limitation for a simple SO_2-H_2O_2-O_3 aqueous-phase reaction system. However, little or no information exists on the potential for mass-transfer limitation of other species, especially in a dynamic coupled gas-aqueous chemistry system.

In the following sections, the previous work on the coupled diffusion-reaction problem is reconciled with the classical two-resistance model — a form more convenient for analysis and implementation in a computer model.

7.1.1 Theory

Observed drop size spectra of various types of clouds indicate that most droplets are concentrated in the range from 1 to 30 μm diameter (Pruppacher and Klett, 1978). According to the criteria of Kronig and Brink (1950), mass-transport in droplets of diameter below 40 μm may be assumed to be entirely due to molecular diffusion. The governing transient differential equation for the aqueous-phase concentration of species i diffusing and reacting in a spherical droplet is (Shi and Seinfeld, 1991)

$$\frac{\partial \mathrm{A_i}}{\partial \mathrm{t}} = \mathrm{D_{L,i}} \frac{1}{\mathrm{r}^2} \frac{\partial}{\partial \mathrm{r}} \left(\mathrm{r}^2 \frac{\partial \mathrm{A_i}}{\partial \mathrm{r}} \right) - \mathrm{k_i^1 A_i}, \tag{7.1}$$

with the boundary conditions

B.C. 1:

$$\mathrm{D_{L,i}} \left(\frac{\partial \mathrm{A_i}}{\partial \mathrm{r}} \right)_{\mathrm{r=a^-}} + \mathrm{k_{G,i}} \frac{\mathrm{A_i(a,t)}}{\mathcal{H}_\mathrm{i}} = \mathrm{k_{G,i}} \bar{\mathrm{G}}_\mathrm{i}(\mathrm{t}), \tag{7.2}$$

B.C. 2:

$$\left(\frac{\partial \mathrm{A_i}}{\partial \mathrm{r}} \right)_{\mathrm{r=0}} = 0, \tag{7.3}$$

where, $\mathrm{A_i}$ is the aqueous-phase concentration of species i; $\mathrm{D_{L,i}}$ is the diffusivity of species i in the liquid-phase; $\mathrm{k_i^1}$ is the liquid-phase effective first-order reaction rate constant for species i; a is the droplet radius; $\mathcal{H}_\mathrm{i}$ is the Henry's Law constant; $\bar{\mathrm{G}}_\mathrm{i}$ is the bulk gas-phase

concentration of i; and $k_{G,i}$ is the effective gas-side mass-transfer coefficient combining gas-phase and interfacial mass transfer effects, defined as

$$\frac{1}{k_{G,i}} = \frac{a}{D_{G,i}} + \frac{4}{\alpha_i \bar{v}}. \tag{7.4}$$

In Equation 7.4, α_i is the mass accommodation coefficient, and $\bar{v}$ is the mean molecular speed in the gas-phase. The quasi steady-state solution of (7.1) is

$$A_i^{ss}(r,t) = A_i^{ss}(a,t)\ \frac{a}{r}\ \frac{\sinh(q_i r/a)}{\sinh q_i}, \tag{7.5}$$

where q is a diffuso-reactive parameter, and $A_i^{ss}(a,t)$ is the quasi steady-state concentration at the droplet surface, defined as

$$q_i = a\sqrt{\frac{k_i^1}{D_{L,i}}} \tag{7.6}$$

$$A_i^{ss}(a,t) = \frac{k_{G,i}\bar{G}_i(t)}{\frac{D_{L,i}}{a}(q_i \coth q_i - 1) + \frac{k_{G,i}}{\mathcal{H}_i}} \tag{7.7}$$

The volume average concentration of the steady-state concentration profile $A_i^{ss}(r,t)$ is obtained by integrating it over the radius a and dividing the result by the volume of the droplet $4\pi a^3/3$

$$\frac{\bar{A}_i(t)}{A_i^{ss}(a,t)} = 3\left(\frac{q_i \coth q_i - 1}{q_i^2}\right) = Q_i(q). \tag{7.8}$$

Following the above results, a simple differential equation for the aqueous-phase concentration adjacent to the interface was proposed

$$\frac{d}{dt}A_i^{ss}(a,t) = \frac{1}{Q_i(q)\tau_i}[\mathcal{H}_i\bar{G}_i(t) - A_i^{ss}(a,t)] - k_i^{(1)}A_i(a,t), \tag{7.9}$$

where $\tau_i = \frac{a\mathcal{H}_i}{3k_{G,i}}$ [1]. Using Equation (7.8) in (7.9) one obtains the species differential equation in terms of bulk-phase concentrations as

$$\frac{d}{dt}\bar{A}_i(t) = \frac{1}{\tau_i}\left(\mathcal{H}_i\bar{G}_i(t) - \frac{\bar{A}_i(t)}{Q_i(q)}\right) - k_i^1\bar{A}_i(t). \tag{7.10}$$

[1] τ_i defined by Shi and Seinfeld as $\frac{a}{3\mathcal{H}_i k_{G,i}}$ appears to be incorrect

At steady-state, we can express the ratio of the bulk aqueous-phase concentration to the bulk gas-phase concentration as

$$\frac{\bar{A}_i(t)}{\bar{G}_i(t)} = \mathcal{H}_i \left(\frac{a\mathcal{H}_i k_i^1}{3k_{G_i}} + \frac{q_i^2}{3(q_i \coth q_i - 1)} \right)^{-1} \tag{7.11}$$

7.1.2 Two-Film Model

Applying the classical two-film mass-transfer model (Astarita, 1967) to describe the bulk aqueous-phase concentration, we get

$$\frac{d}{dt}\bar{A}_i(t) = K_{L_i}\frac{3}{a}[H_i\bar{G}_i(t) - \bar{A}_i(t)] - k_i^{(1)}\bar{A}_i(t) \tag{7.12}$$

where $K_{L,i}$ is the overall mass-transfer coefficient based on liquid side, defined as

$$\frac{1}{K_{L,i}} = \frac{1}{k_{L,i}} + \frac{\mathcal{H}_i}{k_{G,i}} \tag{7.13}$$

The parameter $k_{L,i}$ is the liquid-side mass-transfer coefficient with chemical reaction, defined as

$$k_{L,i} = \frac{D_{L,i}}{\delta_{L,i}} \tag{7.14}$$

where $\delta_{L,i}$ is the hypothetical liquid-side film thickness in which all the mass-transfer resistance is assumed to be present. Again, at pseudo-state, Equation (7.12) can be rearranged to

$$\frac{\bar{A}_i(t)}{\bar{G}_i(t)} = \mathcal{H}_i \left(\frac{K_{L,i}\frac{3}{a}}{K_{L,i}\frac{3}{a} + k_i^1} \right) \tag{7.15}$$

In practice, it is not convenient to measure the liquid-side film thickness since it is a model construct. However, it can be theoretically estimated by equating the right-hand-sides of Equations (7.11) and (7.15), since they both represent the ratio of the bulk gas-phase concentration to the bulk aqueous-phase concentration. Thus, after some algebraic manipulations, we obtain an expression for film thickness as

$$\delta_{L,i} = a\left(\frac{1 - Q_i(q)}{q_i \coth q_i - 1} \right) \tag{7.16}$$

As the effective first-order rate constant $k_i^1 \longrightarrow 0$, $q_i \longrightarrow 0$, $\coth q_i \longrightarrow \infty$, and $Q_i(q) \longrightarrow 1$. We can obtain an expression for the film thickness in the absence of reaction (δ_L^o) by taking a limit of (7.16) as $q_i \longrightarrow 0$

$$\begin{aligned} \delta_{L,i}^o &= \lim_{q_i \to 0} \delta_{L,i} \\ &= a \lim_{q_i \to 0} \left(\frac{1 - Q_i(q)}{q_i \coth q_i - 1} \right) \\ \delta_{L,i}^o &= \frac{a}{5} \end{aligned} \tag{7.17}$$

Thus, in the absence of reactions and internal circulations, the film-model suggests that the majority of the concentration gradient of a diffusing species is confined within an outer film, about 20% of the droplet diameter thickness. Interestingly, the diffusive film thickness is independent of the diffusivity of the species. In the presence of chemical reactions, the film thickness decreases as governed by Equation (7.16).

The corresponding liquid-side mass-transfer coefficients in the absence and presence of chemical reactions are

$$k_{L,i}^o = 5\frac{D_{L,i}}{a} \tag{7.18}$$

$$k_{L,i} = \frac{D_{L,i}}{a} \frac{(q_i \coth q_i - 1)}{1 - Q_i(q)} \tag{7.19}$$

We now define an enhancement factor, Φ, as the ratio of the reactive liquid side mass-transfer coefficient to the physical liquid mass-transfer coefficient (Astarita, 1967; Doraiswamy and Sharma, 1984),

$$\Phi_i = \frac{k_{L,i}}{k_{L,i}^o} = \frac{1}{5} \left(\frac{q_i \coth q_i - 1}{1 - Q_i(q)} \right) \tag{7.20}$$

Note that $\lim_{q_i \to 0} \Phi_i = 1$ and for $q_i > 0$, $\Phi_i > 1$. Figure (7.1) shows the variation of Φ with q. The curve will eventually reach a maximum asymptotic value Φ_a for instantaneous reactions,

$$\Phi_{a,i} = \left(1 + \frac{\bar{A}_j D_{L,j}}{A_i^* D_{L,i}} \right) \tag{7.21}$$

where $A_i^* = \bar{G}_i \mathcal{H}_i$, and $\bar{A}_j$ is the bulk aqueous-phase concentration of the species j reacting with the species i. The following condition must be satisfied for the instantaneous reaction regime to be operative

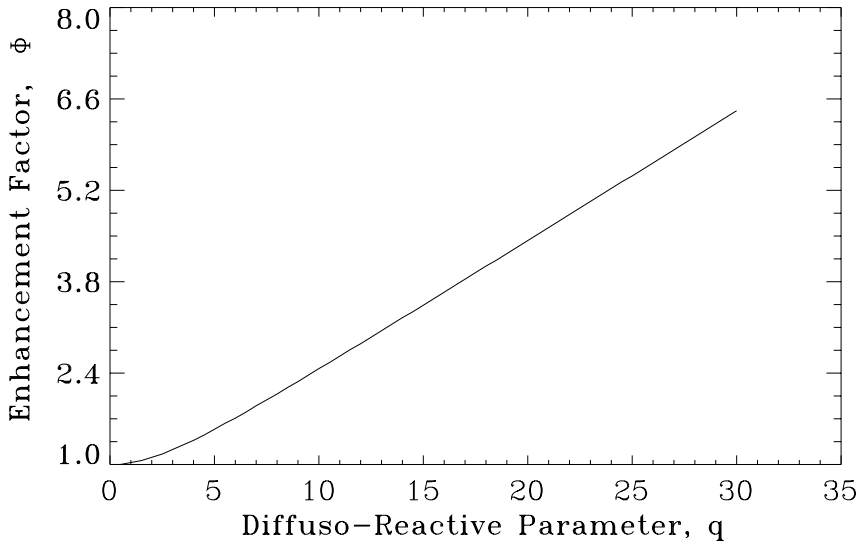

Figure 7.1: Variation of enhancement factor as a function of diffuso-reactive parameter

$$\frac{\sqrt{D_{L,i}k_i^1}}{k_{L,i}^o} \gg \frac{\bar{A}_j}{A_i^*}\sqrt{\frac{D_{L,j}}{D_{L,i}}} \tag{7.22}$$

where $k_i^1 = k_{rxn}\bar{A}_j$ (k_{rxn} is the actual second order rate constant for the reaction of species i and j). However, Equation (7.20) is valid provided the condition given by (7.22) is not satisfied, which is probably the case for most species of our interest.

7.1.3 Dynamic Coupled Phase Equations

Finally, the general sets of coupled non-linear ordinary differential equations for any number of species reacting in both gas and aqueous-phases can be written as:
aqueous-phase

$$\frac{d}{dt}\bar{A}_i(t) = P_i^a - L_i^a\,\bar{A}_i(t) + K_{L,i}\frac{3}{a}[\mathcal{H}_i\bar{G}_i(t) - \bar{A}_i(t)] \qquad i = 1, 2, \ldots, NLIQ \tag{7.23}$$

gas-phase

$$\frac{d}{dt}\bar{G}_i(t) = P_i^g - L_i^g\,\bar{G}_i(t) - K_{L,i}\frac{3}{a}V_c\left[\mathcal{H}_i\bar{G}_i(t) - \bar{A}_i(t)\right] \qquad i = 1, 2, \ldots, NGAS \tag{7.24}$$

where V_c is the volumetric cloud water content expressed as m^3 (water) m^{-3} (air); P_i^a and P_i^g are the production rates of species i in aqueous and gas-phases, respectively; and L_i^a and L_i^g are the respective net loss rate constants. The effective first-order rate constant k_i^1 is the same as the loss rate constant L_i^a for species with no aqueous-phase production. However, when a species is both produced and destroyed in the aqueous-phase due to *in-situ* chemical reactions, the effective first-order rate constant must be defined as

$$k_i^1 = L_i^a - \frac{P_i^a}{\bar{A}_i(t)}, \qquad \text{for } \bar{A}_i > 0, \text{ and } k_i^1 \geq 0 \tag{7.25}$$

This definition of the effective first-order rate constant gives the net aqueous-phase destruction frequency of an absorbing species, and should be used for the purpose of calculation of the enhancement factor. Physically, the quantity $P_i^a/\bar{A}_i(t)$ could be thought of as a production rate constant for the species i. Note that the effective rate constant approaches zero when the production and reaction rates become equal, implying no enhancement in the absorption rate. In such conditions the aqueous-phase concentration will be in equilibrium with the gas phase even though the actual reaction rate constant may be very high.

Furthermore, we define a new parameter Λ for measuring overall mass-transfer limitation.

$$\Lambda_i = \frac{K_{L,i}\frac{3}{a}}{K_{L,i}\frac{3}{a} + k_i^1} \tag{7.26}$$

This quantity also appears in Equation (7.15), and tends to lower the bulk aqueous-phase concentration of the species i in the presence of reaction at a given gas-phase concentration.

7.2 Comprehensive Mechanism

We now turn to the chemistry occurring in the aqueous phase. Pandis and Seinfeld (1989) proposed a comprehensive aqueous-phase mechanism involving 34 aqueous-phase species and 116 reactions, and condensed it to 60 reactions by conducting a sensitivity study for a typical scenario. Here, the comprehensive mechanism is primarily derived from the work of Pandis and Seinfeld, with some additional reactions incorporated to represent the aqueous-phase DMS chemistry for completeness. The comprehensive mechanism was coupled to the gas-phase CBM-Z mechanism to investigate the mass transfer aspects of the coupled gas-aqueous system. It was then further condensed with respect to the nitrate and sulfate producing

reactions. The mass transfer results are presented here, and the condensed mechanism is presented in the next subsection.

The full mechanism is given in Table 7.1, and the associated equilibrium reactions are listed in Tables 7.2 and 7.3. The other necessary physico-chemical data including gas- and liquid-phase diffusivities and mass accomodation coefficients are given in Table A.4. Table 7.4 shows the six hypothetical test scenarios that were used to evaluate reactive mass-transfer coefficients, as well as for condensing the mechanism. The non-methane hydrocarbon compositions were based on the mix given in Table 2.13. Each simulation was initiated at noon and allowed to run for 80 min under March conditions at 30° latitude. The cloud phase was activated after 20 min into the run, and was present until the end of the simulation. The resulting non-linear ordinary differential equations were solved by LSODES.

The aqueous-phase effective rate constants were calculated for all absorbing aqueous-phase species at every LSODES internal time-step, and were used to calculate the overall mass-transfer coefficient. The theoretical mass transfer limitation parameters (Λ_T) were calculated using Equation (7.26), and were compared to the predicted values (Λ_p) from the evolving bulk gas- and aqueous-phase concentrations as

$$\Lambda_{P,i} = \frac{\bar{A}_i}{\mathcal{H}_i \bar{G})_i} \tag{7.27}$$

The two independently calculated values for the same quantity were in excellent agreement, indicating that the numerical solution of the coupled-phase differential equations was accurate.

For most species, mass transfer limitations were not observed; i.e., the values of Λ_p were close to unity. However, considerable mass transfer limitations were found for the OH, NO_3, and HO_2 radicals. The mass-transfer and aqueous-phase reaction parameters for these species were averaged over the time during which the cloud phase was present, and are reported in Tables 7.5, 7.6, and 7.7. Under all scenarios, the effective first-order rate constant for OH was one to two orders of magnitude larger than the overall mass-transfer rate constant $K_L \frac{3}{a}$, resulting in very small values of Λ_p. Comparison of individual gas and liquid-side mass transfer rate constants reveal that mass transport is gas-phase diffusion controlled rather than aqueous-phase diffusion limited. As a result neglecting the enhancement in liquid-side mass transfer coefficient would result in only 10 to 20% error in the bulk aqueous-phase OH concentration.

Table 7.1: Comprehensive Aqueous-Phase Mechanism (Based on Pandis and Seinfeld, 1989).

No.	Reaction			Rate Constant k $[M^n s^{-1}]$
	Oxygen-Hydrogen Chemistry			
1.	$H_2O_2 + h\nu$	$\longrightarrow$	$2OH$	Radiation dependent
2.	$O_3 + h\nu$	$\longrightarrow$	H_2O_2	Radiation dependent
3.	$OH + HO_2$	$\longrightarrow$		$1.1 \times 10^{12} \exp(-1500/T)$
4.	$OH + O_2^-$	$\longrightarrow$	OH^-	$1.5 \times 10^{12} \exp(-1500/T)$
5.	$OH + H_2O_2$	$\longrightarrow$	HO_2	$8.1 \times 10^{9} \exp(-1700/T)$
6.	$HO_2 + HO_2$	$\longrightarrow$	H_2O_2	$2.4 \times 10^{9} \exp(-2365/T)$
7.	$HO_2 + O_2^-$	$\xrightarrow{H_2O}$	$H_2O_2 + OH^-$	$1.5 \times 10^{10} \exp(-1500/T)$
8.	$O_2^- + O_2^-$	$\xrightarrow{H_2O}$	$H_2O_2 + 2OH^-$	< 0.3
9.	$HO_2 + H_2O_2$	$\longrightarrow$	OH	0.5
10.	$O_2^- + H_2O_2$	$\longrightarrow$	$OH + OH^-$	0.13
11.	$OH + O_3$	$\longrightarrow$	HO_2	2.0×10^{9}
12.	$HO_2 + O_3$	$\longrightarrow$	OH	$<1.0 \times 10^{4}$
13.	$O_2^- + O_3$	$\longrightarrow$	$OH + OH^-$	$2.3 \times 10^{11} \exp(-1500/T)$
14.	$OH^- + O_3$	$\longrightarrow$	$O_2^- + HO_2$	70
15.	$HO_2^- + O_3$	$\longrightarrow$	$OH + O_2^-$	2.8×10^{6}
16.	$H_2O_2 + O_3$	$\longrightarrow$		$7.8 \times 10^{-3}[O_3]^{-0.5}$
	Carbonate Chemistry			
17.	$HCO_3^- + OH$	$\longrightarrow$	$CO_3^- + H_2O$	$9.1 \times 10^{9} \exp(-1910/T)$
18.	$HCO_3^- + O_2^-$	$\longrightarrow$	$CO_3^- + HO_2^-$	1.5×10^{6}
19.	$CO_3^- + O_2^-$	$\xrightarrow{H_2O}$	$HCO_3^- + OH^- + O_2$	$6.1 \times 10^{10} \exp(-1500/T)$
20.	$CO_3^- + H_2O_2$	$\longrightarrow$	$HCO_3^- + HO_2$	$1.0 \times 10^{10} \exp(-2820/T)$
	Chlorine Chemistry			
21.	$Cl^- + OH$	$\longrightarrow$	$ClOH^-$	$6.6 \times 10^{11} \exp(-1910/T)$
22.	$ClOH^-$	$\longrightarrow$	$Cl^- + OH$	6.1×10^{9}
23.	$ClOH^-$	$\xrightarrow{H^+}$	Cl	$2.1 \times 10^{10}[H^+]$
24.	Cl	$\xrightarrow{H_2O}$	$ClOH^-$	1.3×10^{3}
25.	$Cl_2^- + HO_2$	$\longrightarrow$	$2Cl^- + H^+$	$6.9 \times 10^{11} \exp(-1500/T)$
26.	$Cl_2^- + O_2^-$	$\longrightarrow$	$2Cl^- + O_2$	$1.5 \times 10^{11} \exp(-1500/T)$
27.	$Cl + HO_2$	$\longrightarrow$	$Cl^- + H^+$	$4.8 \times 10^{11} \exp(-1500/T)$
28.	$Cl_2^- + H_2O_2$	$\longrightarrow$	$2Cl^- + HO_2 + H^+$	$1.1 \times 10^{10} \exp(-3370/T)$
29.	$Cl + H_2O_2$	$\longrightarrow$	$Cl^- + HO_2 + H^+$	4.5×10^{7}
30.	$Cl_2^- + OH^-$	$\longrightarrow$	$2Cl^- + OH$	$1.0 \times 10^{10} \exp(-2160/T)$

continued on next page

Table 7.1: (*continued*)

	Nitrogen Chemistry			
31.	$NO + NO_2$	$\xrightarrow{H_2O}$	$2NO_2^- + 2H^+$	$3.1 \times 10^{10} \exp(-1500/T)$
32.	$NO_2 + NO_2$	$\xrightarrow{H_2O}$	$NO_2^- + NO_3^- + 2H^+$	$1.5 \times 10^{10} \exp(-1500/T)$
33.	$NO + OH$	$\longrightarrow$	$NO_2^- + H^+$	$3.1 \times 10^{12} \exp(-1500/T)$
34.	$NO_2 + OH$	$\longrightarrow$	$NO_3^- + H^+$	$2.0 \times 10^{11} \exp(-1500/T)$
35.	$HNO_2 + h\nu$	$\longrightarrow$	$NO + OH$	Radiation Dependent
36.	$NO_2^- + h\nu$	$\longrightarrow$	$NO + OH + OH^-$	Radiation Dependent
37.	$HNO_2 + OH$	$\longrightarrow$	NO_2	$1.5 \times 10^{11} \exp(-1500/T)$
38.	$NO_2^- + OH$	$\longrightarrow$	$NO_2 + OH^-$	$1.5 \times 10^{11} \exp(-1500/T)$
39.	$HNO_2 + H_2O_2$	$\xrightarrow{H^+}$	$NO_3^- + 2H^+$	$3.7 \times 10^{13} \exp(-6700/T)[H^+]$
40.	$NO_2^- + O_3$	$\longrightarrow$	NO_3^-	$6.7 \times 10^{15} \exp(-6950/T)$
41.	$NO_2^- + CO_3^-$	$\longrightarrow$	$NO_2 + HCO_3^-$	4.0×10^5
42.	$NO_2^- + Cl_2^-$	$\longrightarrow$	$NO_2 + 2Cl^-$	$3.8 \times 10^{10} \exp(-1500/T)$
43.	$NO_2^- + NO_3$	$\longrightarrow$	$NO_2 + NO_3^-$	$1.8 \times 10^{11} \exp(-1500/T)$
44.	$NO_3^- + h\nu$	$\xrightarrow{H_2O}$	$NO_2 + OH + OH^-$	Radiation dependent
45.	$NO_3 + h\nu$	$\longrightarrow$	NO	Radiation Dependent
46.	$NO_3 + HO_2$	$\longrightarrow$	$NO_3^- + H^+$	$6.9 \times 10^{11} \exp(-1500/T)$
47.	$NO_3 + O_2^-$	$\longrightarrow$	NO_3^-	$1.5 \times 10^{11} \exp(-1500/T)$
48.	$NO_3 + H_2O_2$	$\longrightarrow$	$NO_3^- + HO_2 + H^+$	$1.2 \times 10^{10} \exp(-2800/T)$
49.	$NO_3 + Cl^-$	$\longrightarrow$	$NO_3^- + Cl$	$1.5 \times 10^{10} \exp(-1500/T)$
	Methane Oxidation Chain			
50.	$CH_2(OH)_2 + OH$	$\xrightarrow{O_2}$	$HCOOH + HO_2$	$3.1 \times 10^{11} \exp(-1500/T)$
51.	$CH_2(OH)_2 + O_3$	$\longrightarrow$	products	0.1
52.	$HCOOH + OH$	$\xrightarrow{O_2}$	HO_2	$2.5 \times 10^{10} \exp(-1500/T)$
53.	$HCOOH + H_2O_2$	$\longrightarrow$	product	$1.6 \times 10^2 \exp(-5180/T)$
54.	$HCOOH + NO_3$	$\xrightarrow{O_2}$	$NO_3^- + H^+ + HO_2$	$9.7 \times 10^9 \exp(-3200/T)$
55.	$HCOOH + O_3$	$\longrightarrow$	$OH + HO_2$	5.0
56.	$HCOOH + Cl_2^-$	$\xrightarrow{O_2}$	$HO_2 + 2Cl^- + H^+$	$1.2 \times 10^{10} \exp(-4300/T)$
57.	$HCOO^- + OH$	$\xrightarrow{O_2}$	$HO_2 + OH^-$	$3.8 \times 10^{11} \exp(-1500/T)$
58.	$HCOO^- + O_3$	$\longrightarrow$	$OH + O_2^-$	100
59.	$HCOO^- + NO_3$	$\xrightarrow{O_2}$	$NO_3^- + HO_2$	$9.2 \times 10^9 \exp(-1500/T)$
60.	$HCOO^- + CO_3^-$	$\xrightarrow{H^+}$	$HO_2 + HCO_3^- + OH^-$	$9.9 \times 10^9 \exp(-3400/T)$
61.	$HCOO^- + Cl_2^-$	$\xrightarrow{O_2}$	$HO_2 + 2Cl^-$	$1.2 \times 10^{10} \exp(-2600/T)$
62.	$CH_3O_2 + HO_2$	$\longrightarrow$	CH_3OOH	$1.0 \times 10^{10} \exp(-3000/T)$
63.	$CH_3O_2 + O_2^-$	$\xrightarrow{H^+}$	$CH_3OOH + OH^-$	$1.1 \times 10^{10} \exp(-1600/T)$
64.	$CH_3OOH + h\nu$	$\xrightarrow{O_2}$	$HCHO + OH + HO_2$	Radiation Dependent
65.	$CH_3OOH + OH$	$\longrightarrow$	CH_3O_2	$8.1 \times 10^9 \exp(-1700/T)$

continued on next page

Table 7.1: (*continued*)

66.	$CH_3OH + OH$	$\longrightarrow$	$HCHO + HO_2$	$6.9 \times 10^8 \exp(-1500/T)$
67.	$CH_3OH + CO_3^-$	sO	$HCHO + HO_2 + HCO_3^-$	$9.4 \times 10^9 \exp(-4500/T)$
68.	$CH_3OH + Cl_2^-$	$\longrightarrow$	$HCHO + HO_2 + H^+ + 2Cl^-$	$9.0 \times 10^9 \exp(-4400/T)$
69.	$CH_3OOH + OH$	$\longrightarrow$	$HCHO + OH$	$8.0 \times 10^9 \exp(-1800/T)$
70.	$CH_3OH + NO_3$	$\xrightarrow{O_2}$	$NO_3^- + HCHO + HO_2 + H^+$	$1.2 \times 10^{10} \exp(-2800/T)$
	Sulfur Chemistry			
71.	$H_2SO_3 + O_3$	$\longrightarrow$	S(VI)	2.4×10^4
72.	$HSO_3^- + O_3$	$\longrightarrow$	S(VI)	$4.2 \times 10^{13} \exp(-5530/T)$
73.	$SO_3^{2-} + O_3$	$\longrightarrow$	S(VI)	$7.4 \times 10^{16} \exp(-5280/T)$
74.	$HSO_3^- + H_2O_2$	$\xrightarrow{H^+}$	$S(VI) + H_2O$	See note
75.	$HSO_3^- + H_2O_2$	$\xrightarrow{HX}$	$S(VI) + H_2O$	See note
76.	$S(IV) + O_2$	$\xrightarrow{Mn,Fe}$	S(VI)	See note
77.	$SO_3^{2-} + OH$	$\xrightarrow{O_2}$	$SO_5^- + OH^-$	$7.1 \times 10^{11} \exp(-1500/T)$
78.	$HSO_3^- + OH$	$\xrightarrow{O_2}$	SO_5^-	$6.4 \times 10^{11} \exp(-1500/T)$
79.	$SO_5^- + HSO_3^-$	$\xrightarrow{O_2}$	$HSO_5^- + SO_5^-$	8.6×10^3
80.	$SO_5^- + SO_3^{2-}$	$\xrightarrow{O_2}$	$HSO_5^- + SO_5^-$	2.1×10^5
81.	$SO_5^- + O_2^-$	$\xrightarrow{H_2O}$	$HSO_5^- + OH^-$	$1.5 \times 10^{10} \exp(-1500/T)$
82.	$SO_5^- + HCOOH$	$\xrightarrow{O_2}$	$HSO_5^- + HO_2$	$1.1 \times 10^{10} \exp(-5300/T)$
83.	$SO_5^- + HCOO^-$	$\xrightarrow{O_2}$	$HSO_5^- + O_2^-$	$9.5 \times 10^9 \exp(-4000/T)$
84.	$SO_5^- + SO_5^-$	$\longrightarrow$	$2SO_4^-$	$3.1 \times 10^{10} \exp(-1500/T)$
85.	$HSO_5^- + HSO_3^-$	$\xrightarrow{H^+}$	$2SO_4^{2-} + 3H^+$	$6.3 \times 10^{14} \exp(-4750/T)$
86.	$HSO_5^- + OH$	$\longrightarrow$	SO_5^-	$1.0 \times 10^{10} \exp(-1900/T)$
87.	$HSO_5^- + SO_4^-$	$\longrightarrow$	$SO_5^- + SO_4^{2-} + H^+$	$<1.0 \times 10^5$
88.	$HSO_5^- + NO_2^-$	$\longrightarrow$	$HSO_4^- + NO_3^-$	$1.5 \times 10^9 \exp(-6650/T)$
89.	$HSO_5^- + Cl^-$	$\longrightarrow$	SO_4^{2-} + product	$3.4 \times 10^7 \exp(-7050/T)$
90.	$SO_4^- + HSO_3^-$	$\xrightarrow{O_2}$	$SO_4^{2-} + H^+ + SO_5^-$	$2.0 \times 10^{11} \exp(-1500/T)$
91.	$SO_4^- + SO_3^{2-}$	$\xrightarrow{O_2}$	$SO_4^{2-} + SO_5^-$	$8.1 \times 10^{10} \exp(-1500/T)$
92.	$SO_4^- + HO_2$	$\longrightarrow$	$SO_4^{2-} + H^+$	$7.7 \times 10^{11} \exp(-1500/T)$
93.	$SO_4^- + O_2^-$	$\longrightarrow$	SO_4^{2-}	$7.7 \times 10^{11} \exp(-1500/T)$
94.	$SO_4^- + OH^-$	$\longrightarrow$	$SO_4^{2-} + OH$	$1.2 \times 10^{10} \exp(-1500/T)$
95.	$SO_4^- + H_2O_2$	$\longrightarrow$	$SO_4^{2-} + HO_2 + H^+$	$9.9 \times 10^9 \exp(-2000/T)$
96.	$SO_4^- + NO_2^-$	$\longrightarrow$	$SO_4^{2-} + NO_2$	$1.4 \times 10^{11} \exp(-1500/T)$
97.	$SO_4^- + HCO_3^-$	$\longrightarrow$	$SO_4^{2-} + H^+ + CO_3^-$	$1.0 \times 10^{10} \exp(-2100/T)$
98.	$SO_4^- + HCOO^-$	$\xrightarrow{O_2}$	$SO_4^{2-} + HO_2$	$2.6 \times 10^{10} \exp(-1500/T)$
99.	$SO_4^- + Cl^-$	$\longrightarrow$	$SO_4^{2-} + Cl$	$3.1 \times 10^{10} \exp(-1500/T)$
100.	$SO_4^- + HCOOH$	$\xrightarrow{O_2}$	$SO_4^{2-} + HO_2 + H^+$	$1.2 \times 10^{10} \exp(-2700/T)$
101.	$HSO_3^- + CH_3OOH$	$\xrightarrow{H^+}$	S(VI) + Products	$6.6 \times 10^{12} \exp(-3800/T)$

continued on next page

Table 7.1: (*continued*)

102.	$S(IV) + HO_2$	$\longrightarrow$	$S(VI) + OH$	1.0×10^6
103.	$S(IV) + O_2^-$	$\xrightarrow{H_2O}$	$S(VI) + OH + OH^-$	1.0×10^5
104.	$SO_4^- + CH_3OH$	$\xrightarrow{O_2}$	$SO_4^{2-} + HCHO + H^+ + HO_2$	$1.1 \times 10^{10} \exp(-1800/T)$
105.	$2HSO_3^- + NO_3$	$\xrightarrow{O_2}$	$NO_3^- + SO_4^{2-} 2H^+ SO_4^-$	1.0×10^8
106.	$HSO_3^- + 2NO_2$	$\xrightarrow{H_2O}$	$SO_4^{2-} + 3H^+ + 2NO_2^-$	2.0×10^6
107.	$HCHO + HSO_3^-$	$\longrightarrow$	$HOCH_2SO_3^-$	$4.0 \times 10^9 \exp(-4900/T)$
108.	$HCHO + SO_3^{2-}$	$\xrightarrow{H_2O}$	$HOCH_2SO_3^-$	$1.1 \times 10^{10} \exp(-1800/T)$
109.	$HOCH_2SO_3^- + OH^-$	$\longrightarrow$	$SO_3^{2-} + HCHO$	$1.3 \times 10^{10} \exp(-4500/T)$
110.	$HOCH_2SO_3^- + OH$	$\xrightarrow{O_2}$	$SO_5^- + HCHO$	$2.2 \times 10^{11} \exp(-1500/T)$
111.	$HSO_3^- + Cl_2^-$	$\xrightarrow{O_2}$	$SO_5^- + 2Cl^- + H^+$	$5.2 \times 10^{10} \exp(-1500/T)$
112.	$SO_3^{2-} + Cl_2^-$	$\xrightarrow{O_2}$	$SO_5^- + 2Cl^-$	$2.5 \times 10^{10} \exp(-1500/T)$
113.	$DMS + OH$	$\longrightarrow$	$0.5DMSO + 0.5DMS$	1.9×10^{10}
114.	$DMS + H_2O_2$	$\longrightarrow$	$DMSO$	3.5×10^{-2}
115.	$DMS + O_3$	$\longrightarrow$	$DMSO$	$6.7 \times 10^{15} \exp(-4832/T)$
116.	$DMSO + O_3$	$\longrightarrow$	$DMSO_2$	5.7

Note:

$k(74) = \frac{2.9 \times 10^{10}[H^+]}{1+16[H^+]} \exp(-1950/T)$

$k(75) = 3.53 \times 10^7 \exp(-1720/T)[HCOOH] + 1.91 \times 10^8 \exp(-2620/T)[CH_3COOH]$

$k(76) = 2.6 \times 10^3[Fe^{3+}] + 7.5 \times 10^2[Mn^{2+}] + 1.0 \times 10^{10}[Fe^{3+}][Mn^{2+}]$, $pH \leq 5$

$k(76) = 7.5 \times 10^2[Mn^{2+}] + 2.0 \times 10^{10}[Fe^{3+}][Mn^{2+}]$, $pH > 5$

Additional references: k(76), Martin and Good (1991); k(79) and k(80), Buxton *et al.* (1996); k(113), Bonifacic *et al.* (1975); k(114), Adewuyi (1989); k(115) and k(116), Lee and Zhou (1994).

Table 7.2: Gas-Liquid Interfacial Dissolution Equilibria (from Pandis and Seinfeld, 1989).

No.	Equilibrium Reaction			Henry's Law Constant, $\mathcal{H}$ $[M_{(L)}/M_{(G)})]$
1.	$HNO_{3(G)}$	$\rightleftharpoons$	$HNO_{3(L)}$	$5.1 \times 10^6 \exp[8700(\frac{1}{T} - \frac{1}{298})]$
2.	$HNO_{2(G)}$	$\rightleftharpoons$	$HNO_{2(L)}$	$1.2 \times 10^3 \exp[4780(\frac{1}{T} - \frac{1}{298})]$
3.	$SO_{2(G)}$	$\rightleftharpoons$	H_2SO_3	$3.0 \times 10^1 \exp[3120(\frac{1}{T} - \frac{1}{298})]$
4.	$H_2SO_{4(G)}$	$\rightleftharpoons$	$H_2SO_{4(L)}$	1.0×10^3
5.	$HCl_{(G)}$	$\rightleftharpoons$	$HCl_{(L)}$	$1.8 \times 10^4 \exp[2020(\frac{1}{T} - \frac{1}{298})]$
6.	$HCOOH_{(G)}$	$\rightleftharpoons$	$HCOOH_{(L)}$	$9.0 \times 10^4 \exp[5700(\frac{1}{T} - \frac{1}{298})]$
7.	$CH_3COOH_{(G)}$	$\rightleftharpoons$	$CH_3COOH_{(L)}$	1.0×10^3
8.	$CO_{2(G)}$	$\rightleftharpoons$	H_2CO_3	$8.3 \times 10^{-1} \exp[2420(\frac{1}{T} - \frac{1}{298})]$
9.	$CH_3SO_3H_{(G)}$	$\rightleftharpoons$	$CH_3SO_3H_{(L)}$	1.0×10^3
10.	$NH_{3(G)}$	$\rightleftharpoons$	NH_4OH	$1.4 \times 10^3 \exp[4181(\frac{1}{T} - \frac{1}{298})]$
11.	$HO_{2(G)}$	$\rightleftharpoons$	$HO_{2(L)}$	$4.9 \times 10^4 \exp[6640(\frac{1}{T} - \frac{1}{298})]$
12.	$H_2O_{2(G)}$	$\rightleftharpoons$	$H_2O_{2(L)}$	$2.4 \times 10^1 \exp(\frac{7514}{T} - 13.63)^a$
13.	$HCHO_{(G)}$	$\rightleftharpoons$	$HCHO_{(L)}$	$1.5 \times 10^5 \exp[6460(\frac{1}{T} - \frac{1}{298})]$
14.	$NO_{2(G)}$	$\rightleftharpoons$	NO_2(aq	$2.4 \times 10^{-1} \exp[2500(\frac{1}{T} - \frac{1}{298})]$
15.	$NO_{3(G)}$	$\rightleftharpoons$	$NO_{3(L)}$	3.7×10^2
16.	$O_{3(G)}$	$\rightleftharpoons$	$O_{3(L)}$	$2.8 \times 10^{-1} \exp[2300(\frac{1}{T} - \frac{1}{298})]$
17.	$OH_{(G)}$	$\rightleftharpoons$	$OH_{(L)}$	$6.1 \times 10^2 \exp[5280(\frac{1}{T} - \frac{1}{298})]$
18.	$CH_3O_{2(G)}$	$\rightleftharpoons$	$CH_3O_{2(L)}$	$1.5 \times 10^2 \exp[5600(\frac{1}{T} - \frac{1}{298})]$
19.	$CH_3OH_{(G)}$	$\rightleftharpoons$	$CH_3OH_{(L)}$	$5.4 \times 10^3 \exp[4900(\frac{1}{T} - \frac{1}{298})]$
20.	$CH_3OOH_{(G)}$	$\rightleftharpoons$	$CH_3OOH_{(L)}$	$5.6 \times 10^3 \exp[5610(\frac{1}{T} - \frac{1}{298})]$
21.	$DMS_{(G)}$	$\rightleftharpoons$	$DMS_{(L)}$	$1.2 \times 10^{-4} \exp(3480/T)^b$
22.	$DMSO_{(G)}$	$\rightleftharpoons$	$DMSO_{(L)}$	2.5×10^{7b}
23.	$DMSO_{2(G)}$	$\rightleftharpoons$	$DMSO_{2(L)}$	1.0×10^{3b}
24.	$N_2O_{5(G)}$	$\longrightarrow$	$2HNO_{3(L)}$	Instantaneous reaction

[a] From Staffelbach and Kok (1993).

[b] From Lee and Zhou (1994) and references therein.

Table 7.3: Aqueous-Phase Dissociation Equilibria (from Pandis and Seinfeld, 1989).

No.	Equilibrium Reaction			Equilibrium Constant, K [M]
1.	H_2O	$\rightleftharpoons$	$OH^- + H^+$	$1.0 \times 10^{-14} \exp[-6716(\frac{1}{T} - \frac{1}{298})]$
2.	$HO_{2(L)}$	$\rightleftharpoons$	$O_2^- + H^+$	3.5×10^{-5}
3.	$H_2O_{2(L)}$	$\rightleftharpoons$	$HO_2^- + H^+$	$2.2 \times 10^{-12} \exp[-3730(\frac{1}{T} - \frac{1}{298})]$
4.	H_2CO_3	$\rightleftharpoons$	$HCO_3^- + H^+$	$4.5 \times 10^{-7} \exp[-1000(\frac{1}{T} - \frac{1}{298})]$
5.	HCO_3^-	$\rightleftharpoons$	$CO_3^{2-} + H^+$	$4.5 \times 10^{-11} \exp[-1760(\frac{1}{T} - \frac{1}{298})]$
6.	$HNO_{3(L)}$	$\rightleftharpoons$	$NO_3^- + H^+$	1.5×10^{1}
7.	$HNO_{2(L)}$	$\rightleftharpoons$	$NO_2^- + H^+$	$5.1 \times 10^{-4} \exp[-1260(\frac{1}{T} - \frac{1}{298})]$
8.	NH_4OH	$\rightleftharpoons$	$NH_4^+ + OH^-$	$1.8 \times 10^{3} \exp[-450(\frac{1}{T} - \frac{1}{298})]$
9.	$HCHO_{(L)}$	$\rightleftharpoons$	$CH_2(OH)_2$	$1.8 \times 10^{3} \exp[4020(\frac{1}{T} - \frac{1}{298})]$
10.	H_2SO_3	$\rightleftharpoons$	$HSO_3^- + H^+$	$1.2 \times 10^{-2} \exp[1960(\frac{1}{T} - \frac{1}{298})]$
11.	HSO_3^-	$\rightleftharpoons$	$SO_3^{2-} + H^+$	$6.6 \times 10^{-8} \exp[1500(\frac{1}{T} - \frac{1}{298})]$
12.	$H_2SO_{4(L)}$	$\rightleftharpoons$	$HSO_4^- + H^+$	1.0×10^{3}
13.	HSO_4^-	$\rightleftharpoons$	$SO_4^{2-} + H^+$	$1.0 \times 10^{-2} \exp[2720(\frac{1}{T} - \frac{1}{298})]$
14.	$HCl_{(L)}$	$\rightleftharpoons$	$Cl^- + H^+$	$1.8 \times 10^{6} \exp[6900(\frac{1}{T} - \frac{1}{298})]$
15.	Cl_2^-	$\rightleftharpoons$	$Cl + Cl^-$	5.3×10^{-6}
16.	$HCOOH_{(L)}$	$\rightleftharpoons$	$HCOO^- + H^+$	$1.8 \times 10^{-4} \exp[-20(\frac{1}{T} - \frac{1}{298})]$
17.	$CH_3COOH_{(L)}$	$\rightleftharpoons$	$CH_3COO^- + H^+$	1.0×10^{-4}
18.	$CH_3SO_3H_{(L)}$	$\rightleftharpoons$	$CH_3SO_3^- + H^+$	1.6×10^{1} [a]

[a] Streitweiser and Heathcock (1976).

Table 7.4: Hypothetical Test Scenarios.

Scenario	Gas-Phase				Aqueous-Phase	
	$[SO_2]_0$ (ppb)	$[NO_x]_0$ (ppb)	$\frac{[NMOC]_0}{[NO_x]_0}$	$[HCl]_0$ (ppb)	$[Fe^{+3}]$ [M]	$[Mn^{+2}]$ [M]
C1	0.5	0.5	10	0	0	0
C2	1.0	1.0	20	0	0	0
C3	2.0	2.0	30	0	0	0
C4	3.0	4.0	10	1.0	4×10^{-7}	2×10^{-7}
C5	4.0	8.0	20	1.0	4×10^{-7}	2×10^{-7}
C6	5.0	16.0	30	1.0	4×10^{-7}	2×10^{-7}

$[O_3]_0 = 50$ ppb, $[H_2O_2]_0 = 3$ ppb, $[NH_3]_0 = 0.5$ ppb, $[CO]_0 = 100$ ppb, $[CH_4]_0 = 1600$ ppb, $[CO_2]_0 = 340$ ppm, $V_c = 4 \times 10^{-7}$ cm^3 (water) cm^{-3} (air), a = 10 μm, T = 280 K, RH = 100%.

In the case of the aqueous NO_3 radical, the overall mass-transfer rate constant was comparable to the effective first-order rate constant in the first three scenarios. This caused about 50% reduction in its bulk-phase concentration; however, in the presence of Cl^- ions in the last three cases, the mass-transfer limitations increased by an order of magnitude. Moreover, both gas- and liquid-phase transport limitations are appreciable, and neglecting the enhancement in liquid-side mass transfer coefficient would result in lower NO_3 concentrations, an error of about 40% in the present cases.

The HO_2 radical was found to experience some mass-transfer limitation under relatively less polluted scenarios, with gas-side diffusion being the rate limiting step in the two-film model. All other absorbing species may be assumed to be in equilibrium with their aqueous-phase counterparts. For such species, we can effectively lump the gas and aqueous differential equations by eliminating the inter-phase mass transfer terms; i.e., Equations 7.23 and 7.24 may be combined as

$$\frac{d}{dt}[\bar{G}_i(t) + V_c \bar{A}_i(t)] = P_i^g - L_i^g \bar{G}_i(t) + [P_i^a - L_i^a \bar{A}_i(t)]V_c \tag{7.28}$$

At any given time-step, we can calculate the aqueous-phase concentrations by solving only the gas-aqueous equilibrium equations.

Table 7.5: Comparison of Mass-Transfer and Reaction Rate Constants for OH[a].

Scenario	Φ (-)	$k_L \frac{3}{a}$ (s^{-1})	$\frac{k_G}{\mathcal{H}} \frac{3}{a}$ (s^{-1})	$K_L \frac{3}{a}$ (s^{-1})	k^1 (s^{-1})	Λ_P (-)	Λ_P^o (-)	Error (%)
C1	2.1	1430	151	136	2924	0.045	0.040	11.1
C2	2.8	1968	151	139	6688	0.021	0.018	14.3
C3	4.1	2833	151	143	15749	0.0096	0.0077	19.8
C4	4.8	3310	151	144	22275	0.0068	0.0055	19.1
C5	6.2	4263	151	146	42466	0.0035	0.0029	17.1
C6	6.4	4420	151	146	65475	0.0023	0.0018	21.7

[a] All values are 1 h averages; Λ_P^o is calculated using $k_L^o \frac{3}{a} = 681\ s^{-1}$; Error $= 100 \times (\Lambda_P - \Lambda_P^o)/\Lambda_P$.

Table 7.6: Comparison of Mass-Transfer and Reaction Rate Constants for NO_3[a].

Scenario	Φ (-)	$k_L \frac{3}{a}$ (s^{-1})	$\frac{k_G}{\mathcal{H}} \frac{3}{a}$ (s^{-1})	$K_L \frac{3}{a}$ (s^{-1})	k^1 (s^{-1})	Λ_P (-)	Λ_P^o (-)	Error (%)
C1	1.27	462	434	224	269	0.45	0.42	6.7
C2	1.25	453	434	222	243	0.48	0.45	6.3
C3	1.21	439	434	218	199	0.52	0.50	3.8
C4	3.97	1440	434	334	7566	0.042	0.026	38.1
C5	3.97	1440	434	334	7557	0.042	0.026	38.1
C6	3.97	1440	434	334	7576	0.042	0.025	38.1

[a] All values are 1 h averages; Λ_P^o is calculated using $k_L^o \frac{3}{a} = 364\ s^{-1}$; Error $= 100 \times (\Lambda_P - \Lambda_P^o)/\Lambda_P$.

Table 7.7: Comparison of Mass-Transfer and Reaction Rate Constants for HO_2[a].

Scenario	Φ (-)	$k_L \frac{3}{a}$ (s^{-1})	$\frac{k_G}{\mathcal{H}} \frac{3}{a}$ (s^{-1})	$K_L \frac{3}{a}$ (s^{-1})	k^1 (s^{-1})	Λ_P (-)
C1	1.0	498	0.87	0.87	0.66	0.57
C2	1.0	498	1.14	1.14	0.51	0.69
C3	1.0	498	1.26	1.26	0.37	0.77
C4	1.0	498	1.32	1.32	0.07	0.95
C5	1.0	498	1.33	1.33	0.11	0.93
C6	1.0	498	1.33	1.33	0.15	0.89

[a] All values are 1 h averages.

7.3 Condensed Mechanism

The comprehensive aqueous-phase mechanism is extremely large for use in large-scale models. Using the techniques employed for condensing the comprehensive gas-phase DMS mechanism, the full aqueous-phase mechanism was condensed to 42 reactions. The main criteria for condensation were based on the performance of the mechanism with respect to sulfate, nitrate, and formic acid productions. The major effort of mechanism condensation was spent in the reactions of S(IV) species to sulfate. Figure 7.2 illustrates the sulfur reaction pathways in the full mechanism.

According to the recent experimental study on the reactivity of oxysulfur-radical anions, the free-radical chain oxidation of S(IV) may be of less significance in the oxidation of S(IV) in cloud droplets than previously estimated (Buxton *et al.*, 1996). The newly recommended rate constant for the reaction between SO_5^- and HSO_3^- is two orders of magnitude smaller (at pH = 4) than that used by Pandis and Seinfeld (1989). As a result, the dominating reaction pathways for sulfate formation were via H_2O_2 and O_3 oxidation. Metal catalyzed reactions were also important. The competing oxysulfur radical ion reactions were found to be relatively unimportant, and were eliminated. The resulting condensed sulfur scheme is depicted in Figure 7.3, and the entire mechanism is given in Table 7.8.

Figures 7.4, 7.5, and 7.6 compare the performance of the condensed mechanism to the full mechanism with respect to H_2SO_4, HNO_3, and HCOOH productions. Clearly, the condensed mechanism performs quite well for H_2SO_4 and HNO_3 under all test scenarios. However, minor deviations are observed with respect to HCOOH performance. Also, the concentration evolutions of O_3 and H_2O_2 in the aqueous phase are almost identical in both comprehensive and condensed mechanisms (see Figures 7.7 and 7.8, respectively).

Importance of the aqueous-phase DMS chemistry requires more detailed simulations of the cloudy marine boundary layer, and are not attempted in this study.

The condensed mechanism is about 30-40% faster than the full mechanism. However, it is still quite slow compared to the gas-phase mechanism. The computational time requirements were especially large under neutral to low acidic conditions. The cause of this behavior is not clear, and certainly deserves more attention.

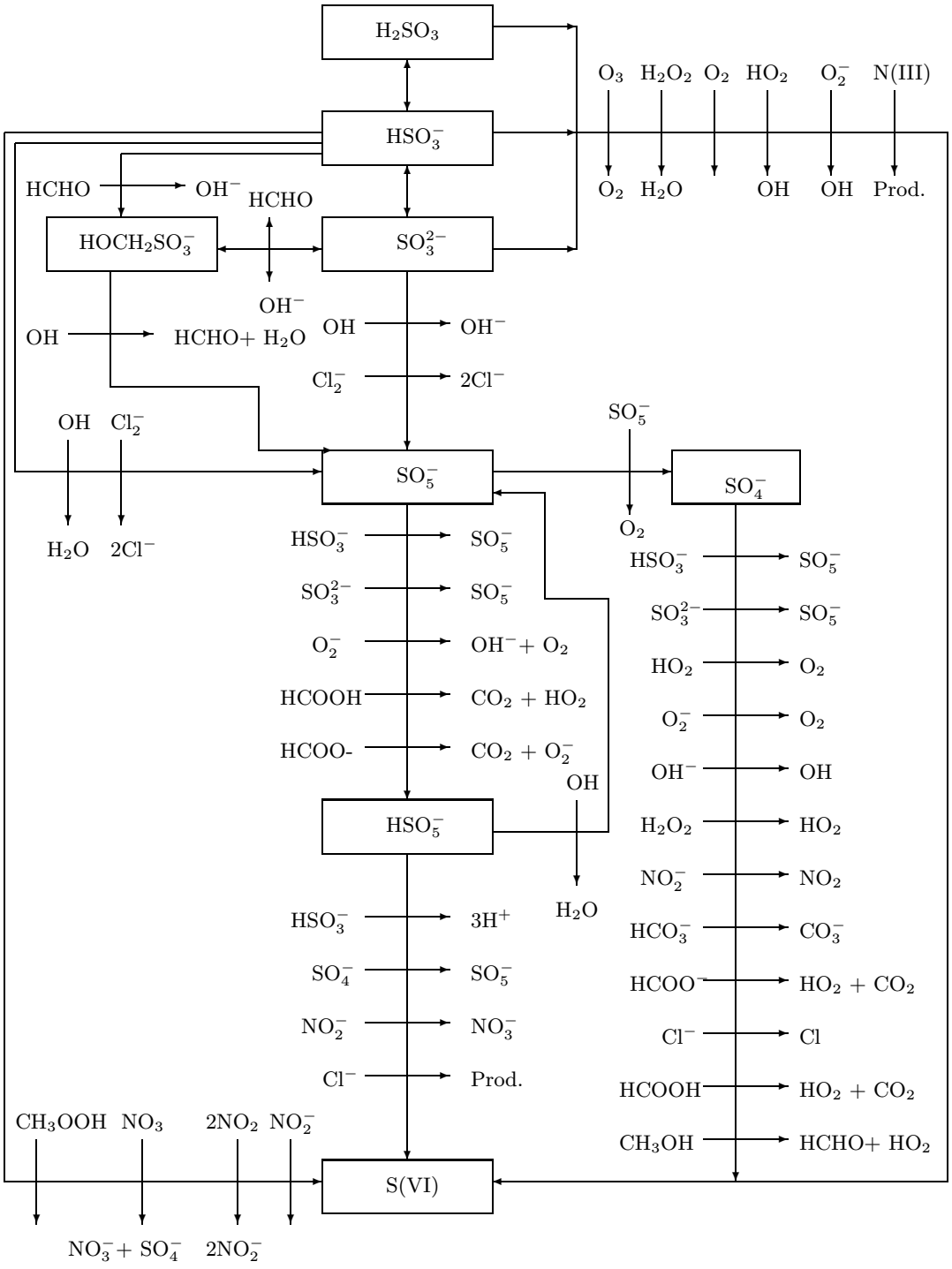

Figure 7.2: Comprehensive aqueous-phase S(IV) to S(VI) conversion pathways

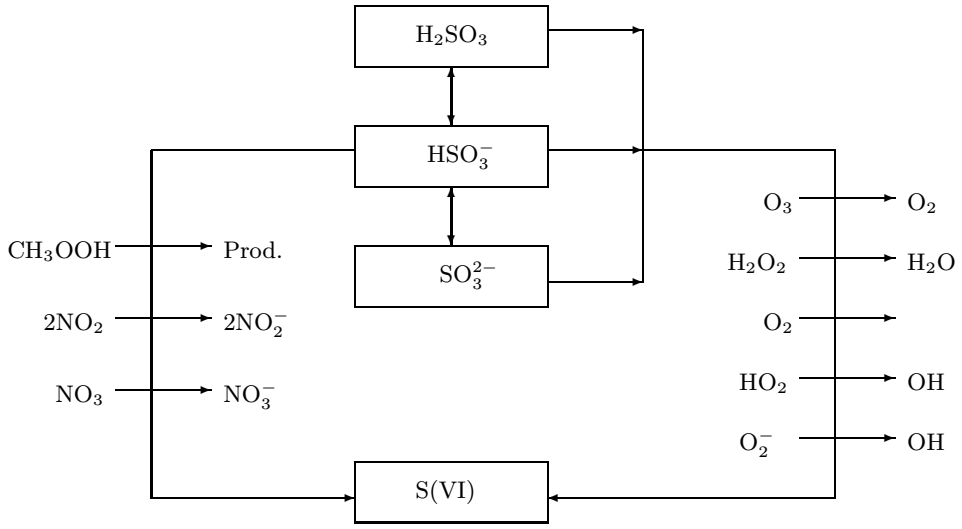

Figure 7.3: Condensed aqueous-phase S(IV) to S(VI) conversion pathways

Table 7.8: Condensed Aqueous-Phase Mechanism

No.	Reaction			Rate Constant k $[M^n s^{-1}]$
	Oxygen-Hydrogen Chemistry			
1.	$H_2O_2 + h\nu$	$\longrightarrow$	2OH	Radiation dependent
2.	$OH + HO_2$	$\longrightarrow$	$H_2O + O_2$	$1.1 \times 10^{12} \exp(-1500/T)$
3.	$OH + O_2^-$	$\longrightarrow$	$OH^- + O_2$	$1.5 \times 10^{12} \exp(-1500/T)$
4.	$OH + H_2O_2$	$\longrightarrow$	$HO_2 + H_2O$	$8.1 \times 10^{9} \exp(-1700/T)$
5.	$HO_2 + HO_2$	$\longrightarrow$	$H_2O_2 + O_2$	$2.4 \times 10^{9} \exp(-2365/T)$
6.	$HO_2 + O_2^-$	$\xrightarrow{H_2O}$	$H_2O_2 + O_2 + OH^-$	$1.5 \times 10^{10} \exp(-1500/T)$
7.	$O_2^- + O_3$	$\longrightarrow$	$OH + 2O_2 + OH^-$	$2.3 \times 10^{11} \exp(-1500/T)$
	Carbonate Chemistry			
8.	$HCO_3^- + OH$	$\longrightarrow$	$CO_3^- + H_2O$	$9.1 \times 10^{9} \exp(-1910/T)$
9.	$HCO_3^- + O_2^-$	$\longrightarrow$	$CO_3^- + HO_2^-$	1.5×10^{6}
10.	$CO_3^- + O_2^-$	$\xrightarrow{H_2O}$	$HCO_3^- + OH^- + O_2$	$6.1 \times 10^{10} \exp(-1500/T)$
11.	$CO_3^- + H_2O_2$	$\longrightarrow$	$HCO_3^- + HO_2$	$1.0 \times 10^{10} \exp(-2820/T)$
	Chlorine Chemistry			
12.	$Cl^- + OH$	$\xrightarrow{H^+}$	Cl	$2.1 \times 10^{10}[H^+]$
13.	$Cl_2^- + O_2^-$	$\longrightarrow$	$2Cl^- + O_2$	$1.5 \times 10^{11} \exp(-1500/T)$
14.	$Cl_2^- + H_2O_2$	$\longrightarrow$	$2Cl^- + HO_2 + H^+$	$1.1 \times 10^{10} \exp(-3370/T)$

continued on next page

Table 7.8: (*continued*)

15.	$Cl + H_2O_2$	$\longrightarrow$	$Cl^- + HO_2 + H^+$	4.5×10^7
	Nitrogen Chemistry			
16.	$NO_3^- + h\nu$	$\xrightarrow{H_2O}$	$NO_2 + OH + OH^-$	Radiation dependent
17.	$NO_3 + O_2^-$	$\longrightarrow$	$NO_3^- + O_2$	$1.5 \times 10^{11} \exp(-1500/T)$
18.	$NO_3 + Cl^-$	$\longrightarrow$	$NO_3^- + Cl$	$1.5 \times 10^{10} \exp(-1500/T)$
	Methane Oxidation Chain			
19.	$CH_2(OH)_2 + OH$	$\xrightarrow{O_2}$	$HCOOH + HO_2 + H_2O$	$3.1 \times 10^{11} \exp(-1500/T)$
20.	$HCOOH + OH$	$\xrightarrow{O_2}$	$HO_2 + CO_2 + H_2O$	$2.5 \times 10^{10} \exp(-1500/T)$
21.	$HCOO^- + OH$	$\xrightarrow{O_2}$	$HO_2 + CO_2 + OH^-$	$3.8 \times 10^{11} \exp(-1500/T)$
22.	$HCOO^- + CO_3^-$	$\xrightarrow{H^+}$	$HO_2 + CO_2 + HCO_3^-$	$9.9 \times 10^9 \exp(-3400/T)$
23.	$HCOO^- + Cl_2^-$	$\xrightarrow{O_2}$	$HO_2 + CO_2 + 2Cl^-$	$1.2 \times 10^{10} \exp(-2600/T)$
24.	$CH_3O_2 + HO_2$	$\longrightarrow$	$CH_3OOH + O_2$	$1.0 \times 10^{10} \exp(-3000/T)$
25.	$CH_3O_2 + O_2^-$	$\xrightarrow{H^+}$	$CH_3OOH + O_2 + OH^-$	$1.1 \times 10^{10} \exp(-1600/T)$
26.	$CH_3OOH + OH$	$\longrightarrow$	$CH_3O_2 + H_2O$	$8.1 \times 10^9 \exp(-1700/T)$
27.	$CH_3OOH + OH$	$\longrightarrow$	$HCHO + OH + H_2O$	$8.0 \times 10^9 \exp(-1800/T)$
28.	$CH_3OH + OH$	$\longrightarrow$	$HCHO + HO_2 + H_2O$	$6.9 \times 10^8 \exp(-1500/T)$
	Sulfur Chemistry			
29.	$H_2SO_3 + O_3$	$\longrightarrow$	S(VI)	2.4×10^4
30.	$HSO_3^- + O_3$	$\longrightarrow$	S(VI)	$4.2 \times 10^{13} \exp(-5530/T)$
31.	$SO_3^{2-} + O_3$	$\longrightarrow$	S(VI)	$7.4 \times 10^{16} \exp(-5280/T)$
32.	$HSO_3^- + H_2O_2$	$\xrightarrow{H^+}$	S(VI) + H_2O	See Table 7.1
33.	$HSO_3^- + H_2O_2$	$\xrightarrow{HX}$	S(VI) + H_2O	See Table 7.1
34.	S(IV) + O_2	$\xrightarrow{Mn,Fe}$	S(VI)	See Table 7.1
35.	$HSO_3^- + CH_3OOH$	$\xrightarrow{H^+}$	S(VI) + Products	$6.6 \times 10^{12} \exp(-3800/T)$
36.	S(IV) + HO_2	$\longrightarrow$	S(VI) + OH	1.0×10^6
37.	S(IV) + O_2^-	$\xrightarrow{H_2O}$	S(VI) + OH + OH^-	1.0×10^5
38.	$HSO_3^- + 2NO_2$	$\xrightarrow{H_2O}$	$SO_4^{2-} + 3H^+ + 2NO_2^-$	2.0×10^6
39.	DMS + OH	$\longrightarrow$	0.5DMSO + 0.5DMS	1.9×10^{10}
40.	DMS + H_2O_2	$\longrightarrow$	DMSO	3.5×10^{-2}
41.	DMS + O_3	$\longrightarrow$	DMSO	$6.7 \times 10^{15} \exp(-4832/T)$
42.	DMSO + O_3	$\longrightarrow$	$DMSO_2$	5.7

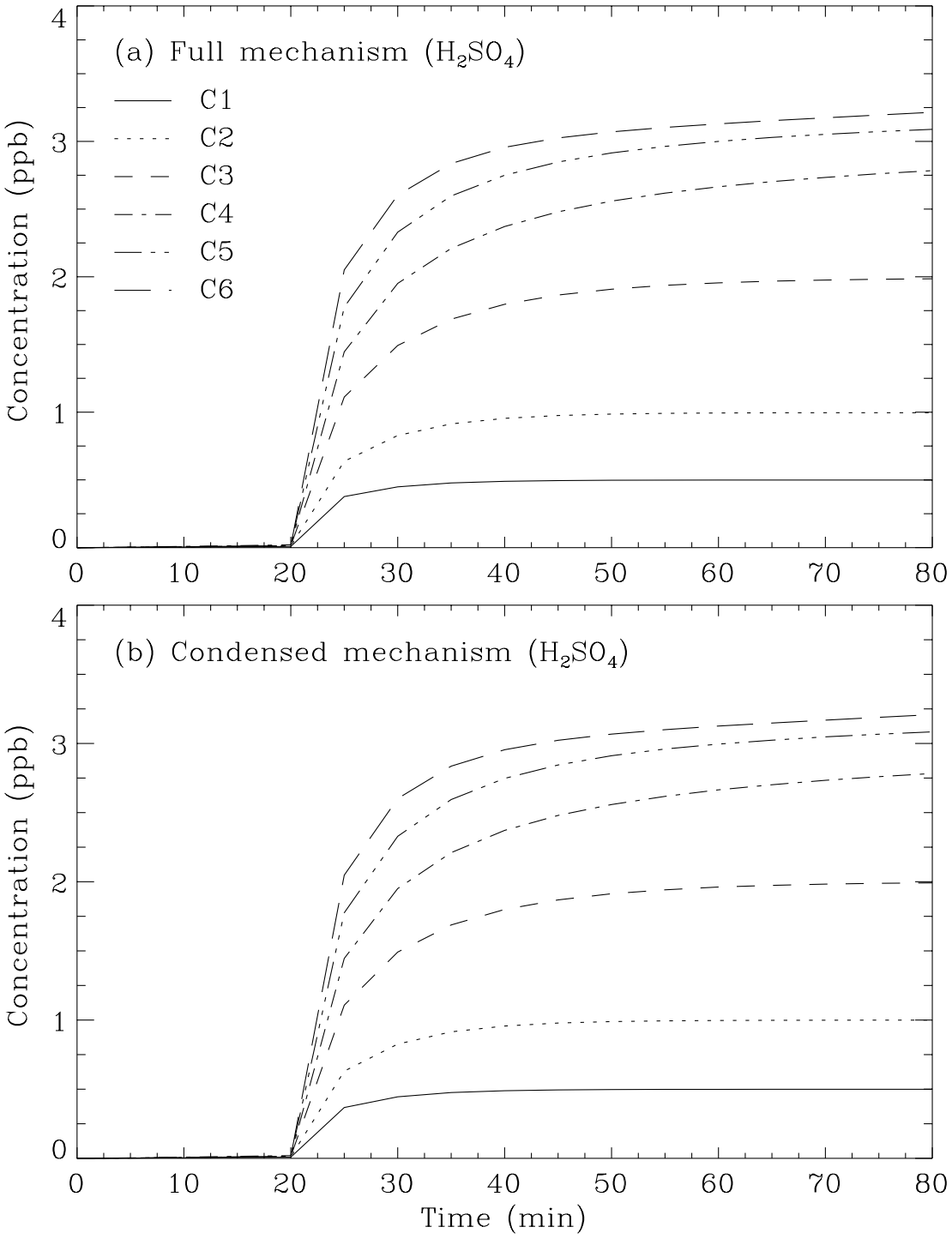

Figure 7.4: Total sulfate evolution from: (a) full aqueous-phase mechanism of Pandis and Seinfeld; (b) condensed mechanism derived in this work.

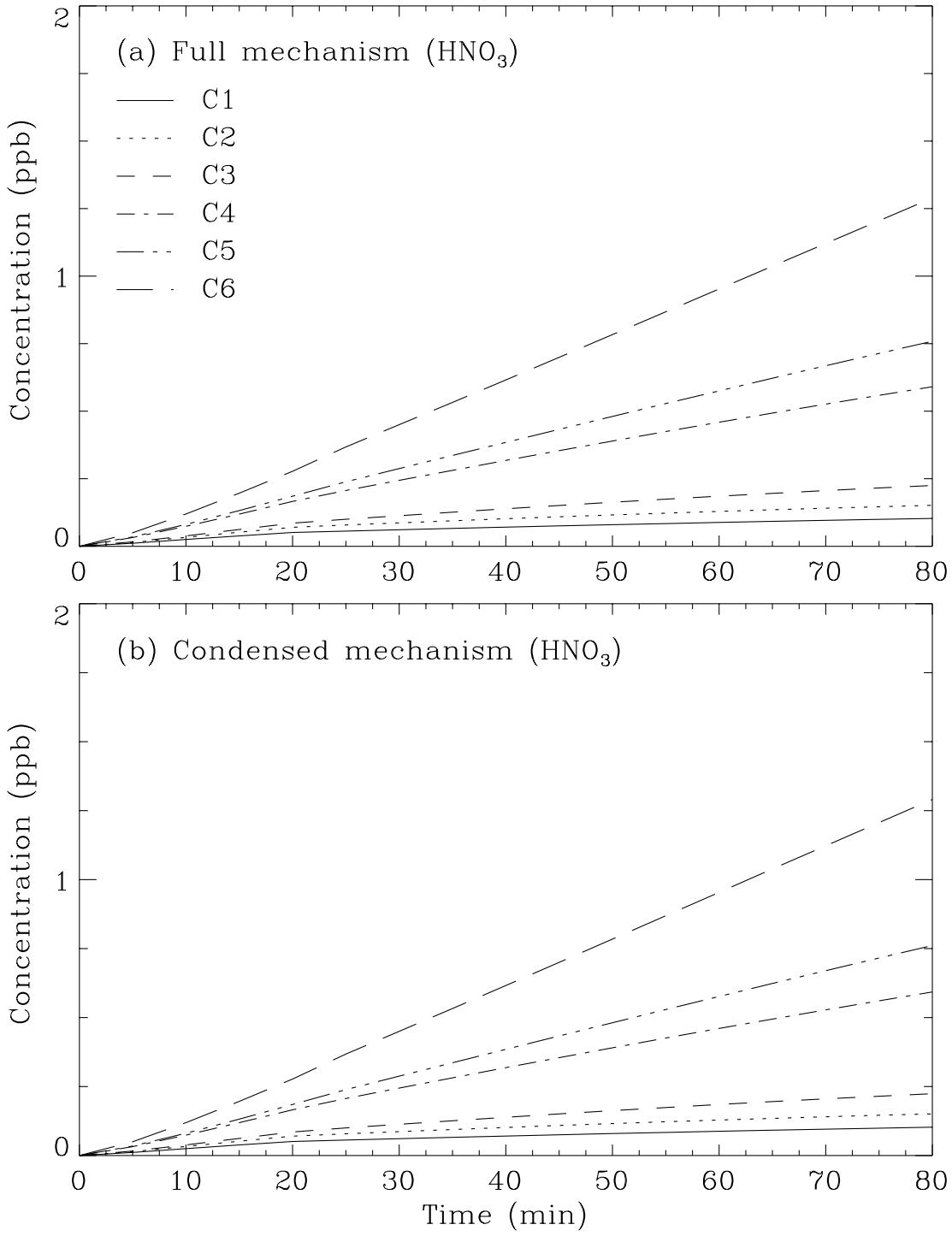

Figure 7.5: Total nitrate evolution from: (a) full aqueous-phase mechanism of Pandis and Seinfeld; (b) condensed mechanism derived in this work.

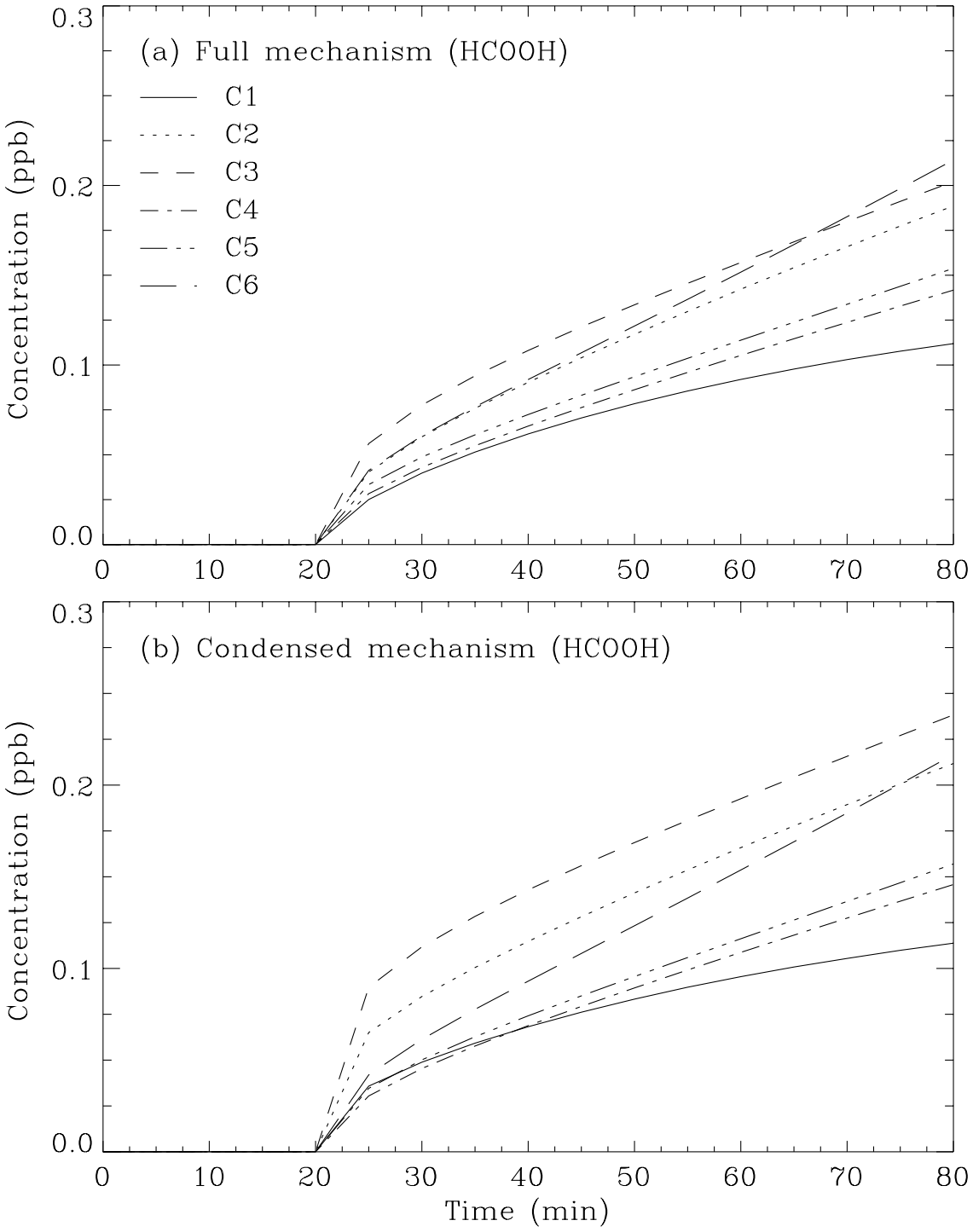

Figure 7.6: Total formic acid evolution from: (a) full aqueous-phase mechanism of Pandis and Seinfeld; (b) condensed mechanism derived in this work.

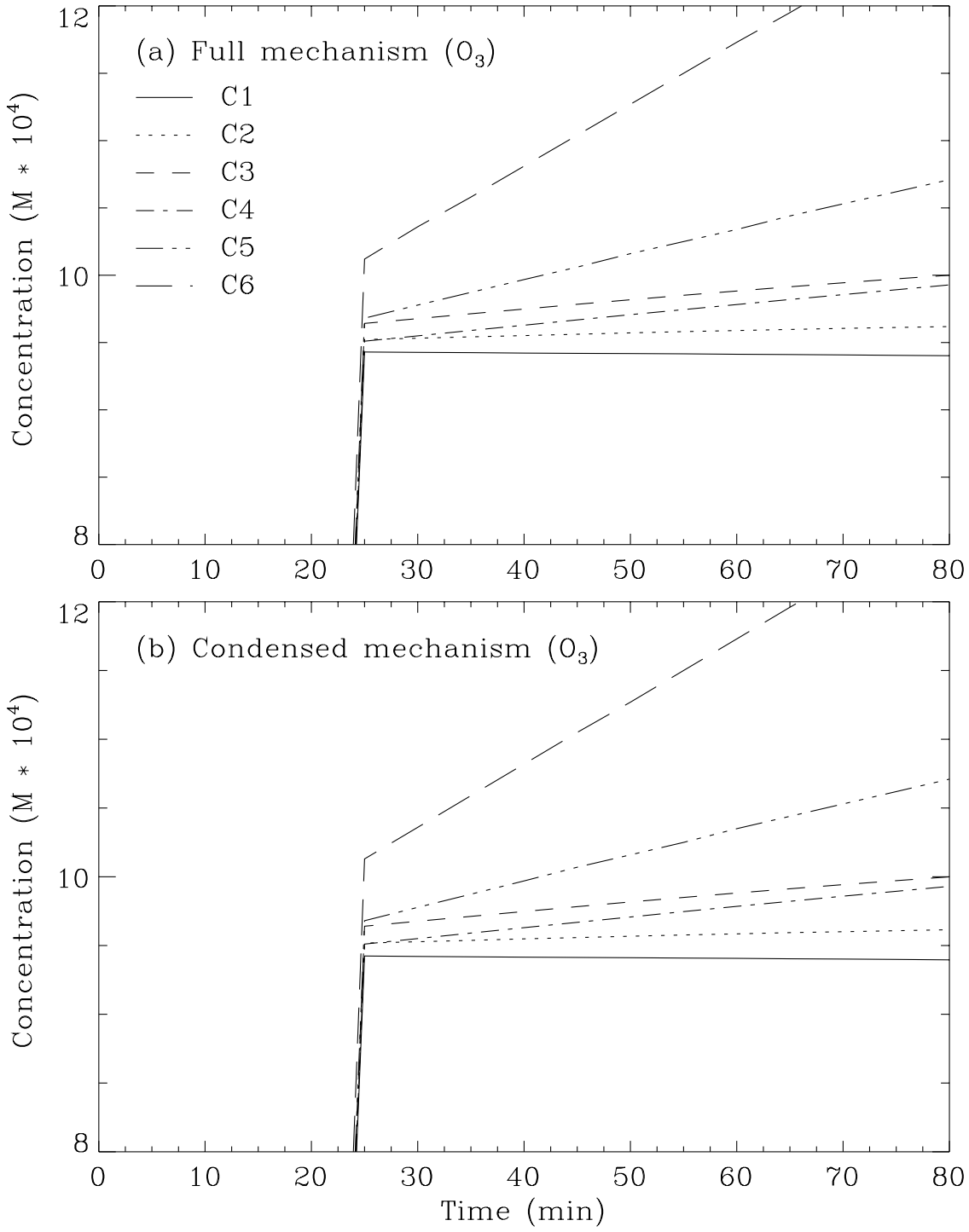

Figure 7.7: Aqueous-phase O_3 evolution from: (a) full aqueous-phase mechanism of Pandis and Seinfeld; (b) condensed mechanism derived in this work.

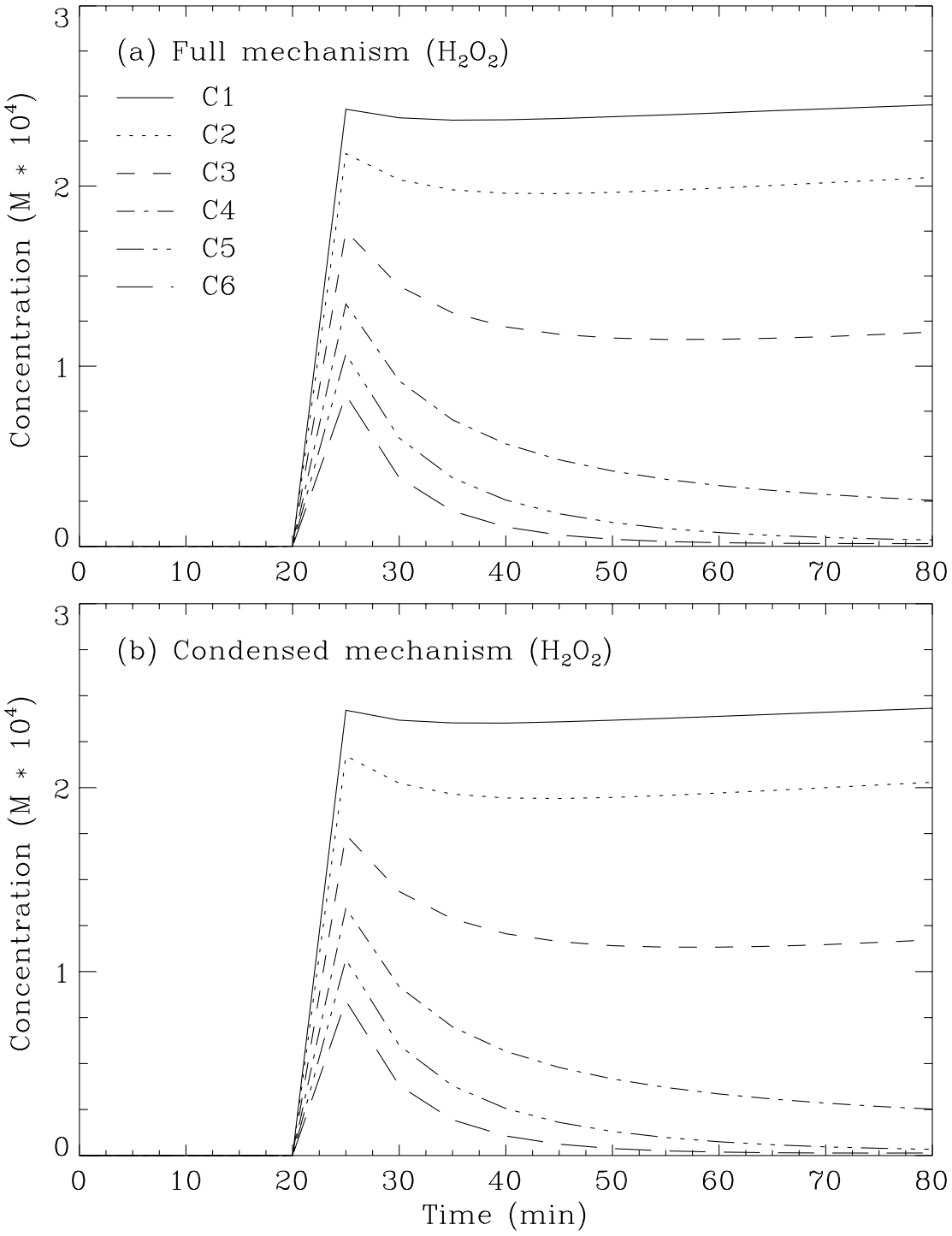

Figure 7.8: Aqueous-phase H_2O_2 evolution from: (a) full aqueous-phase mechanism of Pandis and Seinfeld; (b) condensed mechanism derived in this work.

7.4 Concluding Remarks

The analytical results for simultaneous diffusion and reaction in a spherical cloud droplet were re-interpreted in terms of the classical two-film theory of mass transfer with chemical reaction, and theoretical expressions for liquid-side film thickness and mass-transfer enhancement factor were derived.

The mass transfer aspects in a coupled phase system applied to cloud droplets were investigated using this two-film model. Under the employed test scenarios, only OH, NO_3, and HO_2 were found to have appreciable mass transfer limitation to their aqueous-phase reactions. All other absorbing species were practically in equilibrium with their aqueous counterparts.

Furthermore, a highly condensed mechanism was derived for use in the global-scale model with a primary interest in simulating sulfate, nitrate, and formic acid. As a result, the condensed mechanism is highly accurate for these species. The comprehensive and condensed mechanisms also agree well with respect to predicting O_3, and H_2O_2.

Chapter 8

Summary

The need for a comprehensive and efficient tropospheric chemistry model is addressed via systematic development of the various sub-models/mechanisms representing the gas-, aerosol-, and cloud-phase chemistries. The tropospheric chemistry model is designed for applications in regional- and global-scale studies on radiative impacts of tropospheric aerosols, as well as studies on global cycles of various trace chemicals in the atmosphere. The results of such studies should prove useful in improving the current global warming estimates, and the modeling system should eventually offer policymakers and governments a valuable tool in developing cost-effective solutions related to fossil fuel management. The comprehensive chemistry model can also be used for national and global acid deposition studies, tropospheric ozone budgets, and other regional-scale problems such as ground-level ozone concentrations and forest damage issues.

The model development was primarily driven by the lack of detailed, yet computationally efficient models of the gas, aerosol, and cloud phases. The important features, results, and conclusions of each mechanism/model are summarized here

8.1 Gas-Phase

Background and urban hydrocarbon chemistry

The proposed CBM-Z developed from the published CBM-IV is in very good agreement with the detailed RADM2 mechanism with respect to the predictions of all important oxidants and other species of interest. The published and revised inorganic chemistry versions of CBM-IV are, however, in relatively poor agreement with RADM2 in general, and especially with respect to H_2O_2 predictions. The improvement in the predictions of CBM-Z are due to: (1) use of identical inorganic reactions and rate constants as used in the RADM2 calculations, and (2) an explicit treatment for the lesser reactive alkanes, methane and ethane, and their intermediates, methyl and ethylperoxy radicals. The CBM-Z is still much more efficient than the RADM2 mechanism, which makes it attractive for use in large-scale models.

Isoprene chemistry

The gas-phase isoprene chemistry in the published CBM-IV was found to give large errors in O_3, H_2O_2, and NO_3 concentrations as compared to the RADM-C predictions. These errors tend to propagate back to isoprene by affecting its depletion, and as a result, the deviations in the concentrations of most species including isoprene, O_3, H_2O_2, and NO_x gradually grow with time. The proposed CBM-Z (new) isoprene mechanism is in excellent agreement with its equivalent mechanism RADM-C. The deviations in the concentrations of all important oxidants are marginal, and sometimes even negligible. Moreover, the CPU time requirements are also only marginally higher than for the original isoprene chemistry.

Monoterpene (α-pinene) chemistry

The gas-phase chemistry of the most dominant monoterpene, α-pinene, was developed using the available experimental data in the literature. Although somewhat speculative, the proposed mechanism can successfully explain a variety of experimental observations which include OH and H_2O_2 formation from the α-pinene-O_3 reaction. More importantly, the mechanism is able to accurately predict the different aerosol carbon yields observed under a range of reactant concentrations and operating conditions. In the proposed mechanism, only the reactions of α-pinene with OH and NO_3 lead to the formation of aerosol precursors, while that with ozone tends to enhance the rate of formation by generating reactive radicals such as OH and HO_2. The proposed α-pinene-NO_3 scheme could be potentially important with respect to aerosol formation in the presence of NO_x, especially at nighttime, and certainly deserves experimental investigation. About 23% of the carbon atoms in the α-pinene-O_3 reaction are unaccounted for, and could be an important source of radicals via subsequent reactions. Also, other products, probably higher aldehydes and alkylperoxy radicals lumped as PCHO, QO_2 and PCO_3, need to be identified, and their recommended yields and reaction rate constants must be experimentally confirmed.

While considerable differences could be expected in the aerosol yields under different atmospheric conditions, contributions from both the α-pinene-OH and α-pinene-NO_3 reactions appear to be important. The proposed α-pinene mechanism was further condensed to yield a more compact mechanism, suitable for large-scale applications.

Dimethylsulfide chemistry

The literature on DMS photooxidation mechanisms is critically examined in light of various field and laboratory experiments. Thermal decomposition of the CH_3SO_2 and CH_3SO_3 radicals are identified as the most critical steps in determining the yields of SO_2, H_2SO_4, and MSA under typical atmospheric conditions. A highly condensed DMS photooxidation mechanism is first derived from the comprehensive mechanism of Yin *et al.* (1990a), and then evaluated under typical marine boundary layer scenarios. Based on the results of simple box-model simulations, it appears that the temperature dependence of the MSA/NSSS ratio can be captured by the temperature dependent reactions of the CH_3SO_2 and CH_3SO_3 radicals; however, a 50% reduction in their previously esimated thermal decomposition rate constants yields a better match with some of the observed MSA/NSSS ratios. Although the temperature dependence of the MSA/NSSS ratios can be modeled by the present mechanism, the seasonal variation of the ratio at a given latitude still remains unexplained, and further work is needed to fully understand this behavior.

DMS/SO_2 ratios much greater than unity have been observed under remote marine boundary layer conditions, indicating that SO_2 may not be the major product of DMS photooxidation. This behavior is also well captured by the present model. However, under relatively polluted conditions and at higher temperatures, the DMS/SO_2 ratio can be less than one, thus explaining the variability of such ratios in various locations.

8.2 Condensed-Phases

Aerosol chemistry

A comprehensive yet highly efficient model (MOSAIC) was developed for simulating dynamic aerosol growth due to condensation of inorganic gases. The first version of the model presented in this chapter treats various ammonium and sodium salts of sulfate, nitrate, and chloride. Additional species such as methanesulfonic acid could be easily incorporated into the model with some modifications in the algorithms.

The model is designed to handle any reasonable scenario typically found in the atmosphere, and requires that the user-supplied initial aerosol-phase compositions conform to the ones assumed for the model. Furthermore, the model assumes that an aerosol is either completely dry or completely dissolved, based on a weighted average deliquescence relative

humidity and the ambient RH. This eliminates the computationally expensive solid-liquid equilibrium calculations. The CPU time requirements of MOSAIC are negligible compared to the gas-phase chemistry calculations, thus making it suitable for large-scale atmospheric chemistry models.

The model currently treats condensing organic vapors as inert mass, and does not take into account the potential hydrophobic effects of high molecular weight organic molecules on the overall hygroscopicity of the aerosol. Such effects are being investigated by various research groups in the aerosol research community, and may possibly be included in future versions of MOSAIC.

Cloud chemistry

The analytical results for simultaneous diffusion and reaction in a spherical cloud droplet are reinterpreted in terms of the classical two-film theory of mass transfer with chemical reaction, and a theoretical expression for liquid-side film thickness and mass-transfer enhancement factor are derived.

The mass transfer aspects in a coupled phase system applied to cloud droplets are investigated using this two-film model. Under the employed test scenarios, only OH, NO_3, and HO_2 are found to have appreciable mass transfer limitation to their aqueous-phase reactions. All other absorbing species are practically in equilibrium with their aqueous counterparts.

Furthermore, a highly condensed mechanism is derived for use in the global-scale model with a primary interest in simulating sulfate, nitrate, and formic acid. As a result, the condensed mechanism is highly accurate for these species. The comprehensive and condensed mechanisms also agree well with respect to predicting $O_3$and H_2O_2.

The total number of chemical species and reactions in each mechanism/model is summarized in Table 8.1.

Table 8.1: Summary of Various Chemistry Models/Mechanisms.

	Model/Mechanism	No. of Species	No. of Reactions
I	**Gas-phase**		
	Core mechanism		
	Inorganic	20	41
	Hydrocarbons	41	56
	Continental rural		
	Isoprene	7	19
	α-pinene	8	15
	Remote marine		
	Dimethylsulfide	10	30
II	**Aerosol-phase**[a]		
	Sulfate aerosol	6 + 1	—
	Sea-salt aerosol	5 + 1	—
	Dust	5 + 1	—
III	**Cloud-phase**	23	42

[a] Additional species in each aerosol mode represents water.

8.3 Future Work

The comprehensive mechanisms and models presented in this dissertation will be incorporated into the three-dimensional framework of the coupled Global Chemistry Model (GChM) - Community Climate Model (CCM2) being developed at Battelle Pacific Northwest National Laboratories. The coupled CCM2-GChM modeling system will be first evaluated against various available field observations, and then used to generate global aerosol distribution maps, and estimate the radiative impact of anthropogenic sulfur emissions.

Bibliography

Adewuyi Y. G. (1989) Oxidation of boigenic sulfur compounds in aqueous media: kinetics and environmental implications. *ACS symposium series,* New Orleans, LA, 30 August - 4 September, 1987. Eds. Saltzman E.S. and Cooper W.J., pp. 529-559, American Chemical Society, Washington D.C.

Akimoto H., Hoshino M., Inoue G., Sakamaki F., Bandow H. and Okuda M. (1978) Formation of propylene glycol-1,2-dinitrate in the photooxidation of a propylene - nitrogen oxides - air system. *J. Environ. Sci. Health* **A13(9)**, 677.

Akimoto H., Bandow H., Sakamaki F., Inoue G., Hoshino M. and Okuda M. (1980) Photooxidation of the propylene-NO_x-air system studied by Long-Path Fourier Transform Infrared Spectrometry. *Envir. Sci. Technol.* **14**, 172.

Allen, A. G. and R. M. Harrison (1989) Field measurements of the dissociation of ammonium nitrate and ammonium chloride aerosols. *Atmospheric Environment* **23**, 1591-1599.

Allen A. G., Dick A. L. and Davidson B. M. (1997) Sources of atmospheric methanesulphonate non-sea-salt sulphate, nitrate and related species over the temperate South Pacific. *Atmospheric Environment* **31**, 191-205.

Andreae M. O., Ferek R. J., Bermond F., Byrd K. P., Engstorm R. T., Hardin S., Houmere P. D., LeMarrec F., Raemdonck H. and Chatfield R. B. (1985) Dimethyl sulfidein the marine atmosphere. *J. Geophys. Res.* **90**, 891-900.

Andreae M. O. (1986) The ocean as a source of atmospheric sulfur compounds, in P. Buat-Menard (ed.), *The Role of Air-Sea Exchange in Geochemical Cycling,* D. Reidel, Dordrecht, pp. 331-362.

Andronache C., Chameides W. L., Rodger M. O., Martinez J., Zimmerman P. and Greenberg J. (1994) Vertical distribution of isoprene in the lower boundary layerof the rural and urban southern United States. *J. Geophys. Res.* **99**, 16,989-16,999.

Arimoto R., Duce R. A., Savoie D. L., Prospero J. N. (1992) Trace elements in aerosol particles from Bermuda and Barbados: concentrations, sources and relationships to aerosol sulfate. *J. Atmos. Chem.* **14**, 439-457.

Arnts R. R. and Gay B. W. (1979) Photochemistry of some naturally emitted hydrocarbons.

EPA-600/3-79-081, Research Triangle Park, NC.

Arnts R. R., Gay B. W. and Bufalini J. J. (1981) Photochemical oxidant potential of the biogenic hydrocarbons, in *Atmospheric Biogenic Hydrocarbons,* Vol. 2, Ambient Concentrations and Atmospheric Chemistry (edited by Bufalini J. J. and Arnts R. R.), Ann Arbor Science, Ann Arbor, MI, pp. 117-137.

Aschmann S. and Atkinson R. (1994) Formation yields of methyl vinyl ketone and methacrolein from the gas-phase reaction of O_3 with isoprene. *Envir. Sci. Technol.* **28**, 1539-1542.

Astarita G. (1967) *Mass transfer with chemical reaction.* Elsevier, New York.

Atkinson R., Llyod A. C. and Winges L. (1982a) An updated chemical mechanism for hydrocarbon/NO_x/SO_2 photooxidations suitable for inclusion in atmospheric simulation models. *Atmospheric Environment* **16**, 1341-1355.

Atkinson R., Winer A. M. and Pitts, Jr. J. N. (1982b) Rate constants for the gas phase reactions of O_3 with the natural hydrocarbons isoprene and α- and β-pinene. *Atmospheric Environment* **16**, 1017-1020.

Atkinson R. and Lloyd A. C. (1984) Evaluation of kinetic and mechanistic data for modelling of photochemical smog. *J. Phys. Chem. Ref. Data* **13**, 315-444.

Atkinson R., Aschmann S. M., Winer A. M. and Pitts, Jr. J. N. (1985) Kinetics and atmospheric implications of the gas-phase reactions of NO_3 radicals with a series of monoterpenes and related organics at 294 $\pm$ 2 K. *Envir. Sci. Technol.* **19**, 159-163.

Atkinson R. (1986) Kinetics and mechanisms of the gas-phase reactions of the hydroxyl radical with organic compounds under atmospheric conditions. *Chem. Rev.* **86**, 69-201.

Atkinson R. (1987) A structure-activity relationship for the estimation of rate constants for the gas-phase reactions of OH radicals with organic compounds. *Int. J. Chem. Kinet.* **19**, 799-828.

Atkinson R., Hasegawa D. and Aschmann S. M. (1990) Rate constants for the gas-phase reactions of O_3 with a series of monoterpenes and related compounds at 296$\pm$2 K. *Int. J. Chem. Kinet.* **22**, 871-887.

Atkinson R. and Aschmann S. M. (1992) OH radical reaction rate constants for polycyclic alkanes: Effects of ring strain and consequences for estimation methods. *Int. J. Chem. Kinet.* **24**, 983-989.

Atkinson R., Aschmann S. M., Arey J. and Shorees B. (1992) Formation of OH radicals in the gas phase reactions of O_3 with a series of terpenes. *J. Geophys. Res.* **97**, 6065-6073.

Atkinson R. (1994) Gas-phase tropospheric chemistry of organic compounds. *J. Phys. Chem. Ref. Data, Monograph* **2**, 1-216.

Balla R. J. and Heicklen J. (1985) Oxidation of sulfur compounds III: The photosynthesis of DMS in the presence of O_2. *J. Photochem.* **29**, 297-310.

Balla R. J., Nelson H. H. and McDonald J. R. (1986) Kinetics of the reaction of CH_3S with NO, NO_2 and O_2. *Chem. Phys.* **109**, 101-107.

Bandy A. R., Scott D. L., Blomquist B. W., Chen S. M. and Thornton D. C.(1992) Low yields of SO_2 from dimethyl oxidation in the marine boundary layer. *Geophys. Res. Lett.* **19**, 1125-1127.

Bandow H, Okuda M. and Akimoto H. (1980) Mechanism of the gas-phase reactions of C_3H_6 and NO_3 radicals. *J. Phys. Chem.* **84**, 3604.

Barnes I., Bastian V., Becker K. H. and Niki H. (1987b) FTIR spectroscopic studies of the CH_3S + NO_2 reaction under atmospheric conditions. *Chem. Phys. Lett.* **140**, 451-457.

Barnes I., Bastian V., Becker K. H. (1988) Kinetics and mechanisms of the reaction of OH radicals with dimethyl sulfide. *Int. J. Chem. Kinet.* **20**, 415-431.

Barnes I., Bastian V., Becker K. H. and Martin D. (1989). Fourier transform IR studies of the reactions of dimethyl sulfoxide with OH, NO_3, Cl radicals, In *Biogenic Sulfur in the Environment* (edited by Saltzman E. S. and Cooper W. J.), pp. 476-488, American Chemical Society, Washington, DC.

Barnes I., Becker K. H. (1994) An FTIR study of the photooxidation of dimethyl disulfide. *J. Atmos. Chem.* **18**, 267-289.

Barnes I., Becker K. H. and Patroescu I. (1996) FTIR product of the OH initiated oxidation of dimethyl sulphide: Observation of carbonyl sulphide and dimethyl sulphoxide. *Atmospheric Environment* **30**, 1805-1814.

Bates T. S., Calhoun J. A. and Quinn P. K. (1992) Variations in the methanesulfonate to sulfate molar ratio in submicrometer marine aerosol particles over the South Pacific Ocean. *J. Geophys. Res.* **97**, 9859-9865.

Berresheim H. (1987) Biogenic sulfur emissions from the Subantarctic and Antarctic Oceans. *J. Geophys. Res.* **92**, 13,245-13,262.

Berresheim H., Andreae M. O., Ayers G. P., Gillett R. W., Merril J. T., Davis V. J. and Chameides W. L. (1990) Airborne measurements of dimethylsulfide, sulfur dioxide, and aerosol ions overthe southern ocean south of Austalia. *J. Atmos. Chem.* **10**, 341-370.

Beyer W. H. (1987) *CRC Standard Mathematical Tables.* 28th ed., CRC Press, Boston.

Binkowski F. S. and Shankar U. (1995) The regional particulate matter model 1. Model description and preliminary results. *J. Geophys. Res.* **100**, 26,191-26,209.

Bonifacic M., Moeckel H., Bahenmann D. and Asmus K. -D. (1975) Formation of positive ions and other primary species in the oxidation of sulphides by hydroxyl radicles. *J. Chem. Soc. Perkin Trans.* **2**, 675-685.

Bürgermeister S. and Georgii H. -W. (1991) Distribution of methanesulfonate, NSS sulfate and dimethysulfide over the Atlantic and the North Sea. *Atmospheric Environment* **25A**, 587-595.

Buxton G. V., McGowan S., Salmon G. A., Williams G. E. and Wood N. D. (1996) A study of the spectra and reactivity of oxysulphur-radical anions in the chain oxidation of S(IV): a pulse and γ-radiolysis study. *Atmospheric Environment* **30**, 2483-2493.

Calvert J. G. and Pitts J. N. Jr. (1966) In *Photochemistry,* Wiley, New York.

Carter W. P. L. (1996) Condensed atmospheric photooxidation mechanisms for isoprene. *Atmospheric Environment* **30**, 4275-4290.

Carter W. P. L. and Atkinson R. (1996) Development and evaluation of a detailed mechanism for the atmospheric reactions of isoprene and NO_x. *Int. J. Chem. Kinet.* **28**, 497-530.

Carter W. P. L. and Lurmann F. W. (1989) *Evaluation of the RADM gas phase chemical mechanism.* EPA/600/3-90/001.

Carter W. P. L., Lurmann F. W., Atkinson R. and Llyod A. C. (1986) Development and testing of a surrogate species chemical reaction mechanism. *Rep. EPA/600/3-86/031,* U.S. Enviro. Prot. Agency, Research Triangle Park, N. C.

Chan C. K., Flagan R. C. and Seinfeld J. H. (1992) Water activities of $NH_4NO_3/(NH_4)_2SO_4$ solutions. *Atmospheric Environment* **26A**, 1661-1673.

Charlson R. J, Langner J. and Rodhe H. (1990) Sulphate aerosol and climate. *Nature* **348**, 22.

Charlson R. J., Langner J., Rodhe H., Leovy C. B. and Warren S. G. (1991) Perturbation of the northern hemisphere radiative balance from anthropogenic sulfate aerosols. *Tellus* **43A-B**, 152-163.

Charlson R. J., Schwartz J. M., Hales J. M., Cess R. D., Coakley J. A., Hansen J. E. and Hofmann D. J. (1992) Climate forcing by anthropogenic aerosols. *Science* **225**, 423-430.

Charlson R. J. and Wigley T. M. L. (1994) Sulfate aerosol and climatic change. *Scientific*

American **270**, 48-57.

Chin M., Jacob D. J., Gardener G. M., Foreman-Fowler M. S., Spiro P. A. and Savoie D. L. (1996) A global three-dimensional model of tropospheric sulfate. *J. Geophys. Res.* **101**, 18,667-18,690.

Clegg S. and Brimblecombe P. (1990) Equilibrium partial and pressures and mean activity and osmotic coefficients of 0-100% nitric acid as a function of temperature. *J. Phys. Chem.* **94**, 5369-5380.

Clegg S.L. and Brimblecombe P. (1995) A generalized multicomponent thermodynamic model applied to the $(NH_4)_2SO_4$-H_2SO_4-H_2O system to high supersaturation and low relative humidity at 298.15 K. *J. Atmos. Sci.* **26**, 19-38.

Cohen D. M., Flagan C. R. and Seinfeld J. H. (1987) Studies of concentrated electrolyte solutions using the electrodynamic balance. 1. Water activities for single-electrolyte solutions. *J. Phys. Chem.* **91**, 4563-4574.

Cohen D. M., Flagan C. R. and Seinfeld J. H. (1987) Studies of concentrated electrolyte solutions using the electrodynamic balance. 1. Water activities for single-electrolyte solutions. *J. Phys. Chem.* **91**, 4563-4574.

Covert D. S., Wiedensohler A., Aalto P., Heintzenberg J., McMurry P. H. and Leck C. (1996) Aerosol number size distributions from 3 to 500 nm diameter in the Arctic marine boundary layer during summer and autumn. *Tellus* **48B**, 197-212.

Denbigh K. (1981) *The Principles of Chemical Equilibrium,* 4th ed. Cambridge University Press, Cambridge.

DeMore W. B., Sander S. P., Molina M. J., Golden D. M., Hampson R. F., Kurylo M. J., Howard C. J. and Ravishankara A. R. (1988). *Chemical Kinetics and Photochemical Data for Use in Stratospheric Modeling, Evaluation Number 8,* National Aeronautics and Space Administration, Jet Propulsion Laboratory, California Institute of Technology, Pasadena.

Dingenen R. V., Jensen N. R., Hjorth J. and Raes F. (1994) Peroynitrate formation during the night-time oxidation of dimethylsulfide: Its role as a resevoir species for aerosol formation. *J. Atmos. Chem.* **18**, 211-237.

Dodge M. C. (1977) Combined use of modeling techniques and smog chamber data to derive ozone-precursor relationships. *Rep. EPA-600/3-77-001a,* U.S. Environ. Prot. Agency, Research Triangle Park, N.C.

Dodge M. C. (1989) A comparison of three photchemical oxidant mechanisms. *J. Geophys.*

Res. **94**, 5121-5136.

Dominé F., Ravishankar A. R. and Howard C. J. (1989) Atmospheric reactions of some reduced sulfur radicals. *Trans. Am. Geophys. Union.* **70**, 1008.

Doraiswamy L.K. and Sharma M.M. (1984) *Heterogeneous reactions: analysis, examples, and reactor Design,* Vol. 2: fluid-fluid-solid reactions. Wiley-Interscience, New York.

Easter R. C. (1996) Personal communication.

Erickson D. J., III, walton J. J., Ghan S. J. and Penner J. E. (1991) Three-dimensional modeling of the global atmospheric sulfur cycle: a first step. *Atmospheric Environment* **25A**, 2513-2520.

Ferek R. J., Lazrus A. L., Winchester J. W. (1983) Electron microscopy of acidic aerosols collected over the northeastern United States. *Atmospheric Environment* **17**, 1545-1561.

Feichter J., Kjellstrom E., Rodhe H., Dentener F., Lelieveld J. and Roelofs G. -J. (1996) Simulation of the tropospheric sulfur cycle in a global climate model. *Atmospheric Environment* **30**, 1693-1707.

Finlayson-Pitts B. J. and Pitts J. N. (1986) Atmospheric Chemistry: Fundamentals and Experimental Techniques. John Wiley and Sons, New York.

Friedlander, S. K., (1977) *Smoke, Dust and Haze.* John Wiley and Sons, New York.

Fuchs N. A. and Sutugin A. G. (1971) High-Dispersed Aerosols, in *Topics in Current Aerosol Research,* G. M. Hidy and J. R. Brock (Eds.), Pergamon, New York, 1-60.

Fuller E. N., Schettler P. D. and Giddings J. C. (1966) A new method for prediction of binary gas-phase diffusion coefficient. *Ind. Eng. Chem.* **58**, 19-27.

Galloway J. N., Keene W. C., Pszenny A. A. P., Whelpdale D. M., Sievering H., Merrill J. T. and Boatman J. F. (1990) Sulfur in the Western North Atlantic Ocean atmosphere: Results from a summer 1988 ship/aircraft experiment. *Global Biogeochem. Cycles* **4** 349-365.

Gardner J. A., Watson L. R., Adewuyi Y. G., Davidovits P., Zahniser M. S., Worsnop D. R. and Kolb C. E. (1987) Measurement of the mass accommodation coefficient of SO_2(g) n water droplets. *J. Geophys. Res.* **92**, 10,887-10,895.

Gelbard, F. and J. H. Seinfeld (1980) Simulation of multicomponent aerosol dynamics. *J. Colloid Interface Sci.* **78**, 485-501.

Gery M. W., Whitten G. Z., Killus J. P. and Dodge M. C. (1989) A photochemical kinetics

mechanism for urban and regional scale computer modeling. *J. Geophys. Res.* **94**, 12,925-12,956.

Gillett R. W., Ayers G. P., Ivey J. P and Gras J. L. (1993), In *Dimethylsulfide: Oceans, Atmosphere and Climate* (edited by Restelli G. and Angletti G.), pp. 117-128. Kluwer, Dordrecht.

Giorgi, F. (1986) *Development of an atmospheric model for studies of global budgets and effects of airborne particulate material.* Ph.D. Thesis, Cooperative Thesis No. 102, Georgia Institude of Technology, Atlanta, GA, and National Center for Atmospheric Research, Boulder, Colorado.

Good A. and Thynne J. C. J. (1967) Reaction of free radicals with sulfur dioxide. Part 1.-Methyl Radicals. *J. Chem. Soc. Faraday Trans.* **63**, 2708-2727.

Gorzelska K. and Galloway J. N. (1990) Amine nitrogen in the atmospheric environment over the North Atlantic ocean. *Global Biogeochem. Cycles* **4**, 309-333.

Graedel T. E. (1979) Terpenoids in the atmosphere. *Rev. Geophys. Space Phys.* **17**, 939-947.

Grimsrud E. P., Westberg H. H. and Rasmussen R. A. (1975) Atmospheric reactivity of monoterpene hydrocarbons, NO_x photoxidation and ozonolysis. *Int. J. Chem. Kinet. Symp.* **1**, 183-195.

Grosjean D. and Lewis R. (1982) Atmospheric photooxidation of methyl sulfide. *Geophys. Res. Lett.* **9**, 1203-1206.

Grosjean D., Williams II E. L. and Grosjean E. (1993) Atmospheric chemistry of Ioprene and of its carbonyl products. *Envir. Sci. Technol.* **27**, 830-840.

Guenther A. B., Monson R. K. and Fall R. (1991) Isoprene and monoterpene emission rate variability: Observations with eucalyptus and emission rate algorithm development. *J. Geophys. Res.* **96**, 10,799-10,808.

Guenther A. B., Zimmerman P. R. and Harley P. C. (1993) Isoprene and monoterpene emission rate variability: Model evaluations and sensivity analyses. *J. Geophys. Res.* **98**, 12,609-12,617.

Guenther A. B., Zimmerman P. R. and Wildermuth M. (1994) Natural volatile organic compound emission rate estimates for U.S. woodland landscapes. *Atmospheric Environment* **28**, 1197-1210.

Guenther A., Nicholas Hewitt C., Erickson D., Fall R., Geron C., Graedel T., Harley P.,

Klinger L., Lerdau M., McKay W. A., Pierce T., Scholes B., Steinbrecher R., Tallamraju R., Taylor J. and Zimmerman P. (1995) A global model of natural volatile organic compound emissions. *J. Geophys. Res.* **100**, 8873-8892.

Hakola H., Arey J., Aschmann S. M. and Atkinson R. (1994) Product formation from the gas-phase reactions of OH radicals and O_3 with a series of monoterpenes. *J. Atmos. Chem.* **18**, 75-102.

Hanson D. R., Burkholder J. B., Howard C. J. and Ravishankara A. R. (1992) Measurement of OH and HO_2 radical uptake coefficients on water and sulfuric acid surfaces. *J. Phys. Chem.* **96**, 4979-4985.

Hasselmann K. (1997) Are we seeing global warming? *Science* **276**, 914-915.

Hara H., Kato T., Matsushita H. (1989) The mechanism of seasonal variation in the size distributions of atmospheric chloride and nitrate aerosol in Tokyo. *Bull. Chem. Soc. Japan* **62**, 2643-2649.

Harrison R. M. and Msibi I. M. (1994) Validation of techniques for fast response measurement of HNO_3 and NH_3 and determination of the $[NH_3][HNO_3]$ concentration product. *Atmospheric Environment* **28**, 247-255.

Hatakeyama S., Okuda M. and Akimoto H. (1982)Formation of sulfur dioxide and methanesulfonic acid in the photooxidation of dimethyl sulfide in the air. *Geophys. Res. Lett.* **9**, 583-586.

Hatakeyama S. and Akimoto H. (1983) Reactions of OH radicals with methanethiol, dimethyl sulfide, and dimethyl disulfide in air. *J. Phys. Chem.* **87**, 2387-2395.

Hatakeyama S., Izumi K. and Akimoto H. (1985) Yield of SO_2 and formation in the photooxidation of DMS under atmospheric conditions. *Atmospheric Environment* **19**, 135-141.

Hatakeyama S., Izumi K., Fukuyama T. and Akimoto H. (1989) Reactions of ozone with α-pinene and β-pinene air: Yields of gaseous and particulate products. *J. Geophys. Res.* **94**, 13,013-13,024.

Hatakeyama S., Izumi K., Fukuyama T., Akimoto H. and Washida N. (1991) Reactions of OH with α-pinene and β-pinene in air: Estimate of global CO production from the atmospheric oxidation of terpenes. *J. Geophys. Res.* **96**, 947-958.

Hatakeyama S. (1997) Private communication.

Hegg D. A. (1985) The importance of liquid-phase oxidation of SO_2 in the troposphere. *J. Geophys. Res.* **90**, 3773-3779.

Hegg D. A. (1990) Heterogeneous production of cloud condensation nuclei in the marine atmosphere. *Geophys. Res. Lett.* **17**, 2165-2168.

Heintzenberg J. (1994) Properties of the log-normal particle size distribution. *Aerosol Sci. Technol.* **21**, 46-48.

Herron J. T., Martinez R. I. and Huie R. E. (1982) Kinetics and energetics of the Criegee intermediate in the gas phase. I. The Criegee intermediate in ozone-alkene reactions. *Int. J. Chem. Kinet.* **14**, 201-224.

Hertel O. and Christensen J. (1994) Modelling of the end products of the chemical decomposition of DMS in the marine boundary layer. *Atmospheric Environment* **28**, 2431-2449.

Hindmarsh A. C. (1983) ODEPACK: a systematized collection of ode solvers. In *Scientific Computing* (R. S. Stepleman, ed.), pp. 55-64. North-Holland Press, Amsterdam.

Hooker C. L., Westberg H. H. and Sheppard J. C. (1985) Determination of carbon balances for smog chamber terpene oxidation experiments using a ^{14}C tracer technique. *J. Atmos. Chem.* **2**, 307-320.

Hough A. M. (1987) A computer modelling study of the chemitry occuring during cloud formation over hills. *Atmospheric Environment* **21**, 1073-1095.

Höv O., Schjoldager J. and Wathne B. M. (1983) Measurements and modeling of the concentrations of terpens in coniferous forest air. *J. Geophys. Res.* **88**, 10,679-10,668.

Huebert B. J., Howell S., Laj P., Johnson J. E., Quinn P. K., Yegorov V., Clarke A. D. and Porter J. N. (1993) Observations of the atmospheric sulfur cycle on SAGA 3. *J. Geophys. Res.* **98**, 16,985-16, 995.

Hull L. A. (1981) Terpene ozonolysis products, in *Atmospheric Biogenic Hydrocarbons,* Vol. 2, Ambient Concentrations and Atmospheric Chemistry (edited by Bufalini J. J. and Arnts R. R.), Ann Arbor Science, Ann Arbor, MI, pp. 161-186.

Hynes A. J., Wine P. H. and Semmes D. H. (1986) Kinetics and mechanism of OH reactions with organic sulfides. *J. Phys. Chem.* **90**, 4148-4156.

Isidorov V. A., Zenkevich I. G. and Ioffe B. V. (1985) Volatile organic compounds in the atmosphere of forests. *Atmospheric Environment* **19**, 1-8.

Jacobson M. Z., Tabazadeh A. and Turco R. P. (1996) Simulating equilibrium within aerosols and nonequilibrium between gases and aerosols. *J. Geophys. Res.* **101**, 9079-9091.

Jacobson M. Z. (1997) Development and application of a new air pollution modelling system-II. Aerosol module structure and design. *Atmospheric Environment* **31**, 131-144.

Jensen N. R., Hjorth J., Lohse C., Skov H. and Restelli G. (1991) Products and mechanism of the reaction between NO3 and dimethylsulfide in air. *Atmospheric Environment* **25A**, 1897-1904.

Jensen N. R., Hjorth J., Lohse C., Skov H. and Restelli G. (1992) Products and mechanism of the gas phase reactions of $NO_3$with CH_3SCH_3, CD_3SCD_3, CH_3SH and CH_3SSCH_3. *J. Atmos. Chem.* **14**, 95-108.

Jones C., and Rasmussen R. A. (1975) Production of Isoprene by leaf tissue. *Plant Physiol.* **55**, 982-987.

Jonson J. E. and Isaksen I. S. (1993) Tropospheric ozone chemistry. The impact of cloud chemistry. *J. Atmos. Chem.* **16**, 99-122.

Kaiserman M. J. and Corse E. W. (1981) Aerosols and carbon balance in the pinene-NO_x photochemical system, in *Atmospheric Biogenic Hydrocarbons,* Vol. 2, Ambient Concentrations and Atmospheric Chemistry (edited by Bufalini J. J. and Arnts R. R.), Ann Arbor Science, Ann Arbor, MI, pp. 139-159.

Kamens R. M., Jeffries H. E., Gery M. W., Wiener R. W., Sexton K. G. and Howe G. B. (1981) The impact of α-pinene on urban smog formation: An outdoor smog chamber study. *Atmospheric Environment* **15**, 969-981.

Kamens R. M., Gery M. W., Jeffries H. E., Jackson M. and Cole E. I. (1982) Ozone-isoprene reactions: product formation and aerosol potential. *Int. J. Chem. Kinet.* **14**, 995-975.

Keene W. C., Pszenny A. A. P., Jacob D. J., Duce R. A., Galloway J. N., Schultz-Tokos J. J., Sievering H. and Boatman J. F. (1990) The geochemical cycling of reactive chlorine through the marine troposphere. *Global Biogeochem. Cycles* **4**, 407-430.

Kerr J. A. and Calvert J. G. (1985) Chemical transformation modules for Eulerian acid deposition models, vol. I, The gas-phase chemistry. *Rep. EPA-600/3-85-015,* U.S. Enviro. Prot. Agency, Research Triangle Park, N. C.

Killus J. P. and Whitten G. Z. (1982) A new carbon-bond mechanism for air quality modeling. *Rep. EPA-600/3-82-041,* U.S. Environ. Prot. Agency, D. C.

Kim P. Y., Seinfeld J. H. and Saxena P. (1993a) Atmospheric gas-aerosol equilibrium I. Thermodynamic model. *Aerosol Sci. Technol.* **19**, 157-181.

Kim P. Y., Seinfeld J. H. and Saxena P. (1993b) Atmospheric gas-aerosol equilibrium II. Analysis of common apprroximations and activity coefficient calculation methods. *Aerosol Sci. Technol.* **19**, 182-198.

Kirchner F. and Stockwell W. R. (1996) Effect of peroxy radical reactions on the predicted concentrations of ozone, nitrogenous compounds, and radicals. *J. Geophys. Res.* **101**, 21,007-21,022.

Koga S. and Tanaka H. (1993) Numerical study of the oxidation process of dimethylsulfide in the marine atmosphere. *J. Atmos. Chem.* **17**, 201-228.

Koga S. and Tanaka H. (1996) Simulations of seasonal variatons of sulfur compounds in the remote marine atmosphere. *J. Atmos. Chem.* **23**, 163-192.

Kopcewicz B., Nagamoto C., Parungo F., Harris J., Miller J., Sievering H. and Rosinski J. (1991) Morphological studies of sulfate and nitrate particles on the east coast of North America and over the North Atlantic Ocean. *Atmospheric Research* **26**, 245-271.

Kotzias D., Nicollin B. and Duane M. (1991) Carbonyls in the forest atmosphere — evidence for the monoterpene /ozone reaction. *Naturwissenschaften* **78**, 38-40.

Kronig R. and Brink J. C. (1950) On the theory of extraction from falling droplets. *Appl. Sci. Res.* **A2**, 142-154.

Lamb B., Gay D., Westberg H. and Pierce T. (1993) A biogenic hydrocarbon emission inventory for the U.S.A. using a simple forest canopy model. *Atmospheric Environment* **27A**, 1673-1690.

Langner J. and Rodhe H. (1991) A global three-dimensional model of the tropospheric sulfur cycle. *J. Atmos. Chem.* **13**, 225-263.

Langner J., Rodhe H., Crutzen P. J. and Zimmerman P. (1992) Anthropogenic influence on the distribution of tropospheric sulphate aerosol. *Nature* **359**, 712-716.

Lee J. H. and Tang I. N. (1988) Accommodation coefficient of gaseous NO_2 on water surfaces. *Atmospheric Environment* **22**, 1147-1151.

Lee Y. -N. and Zhou X. (1994) Aqueous reaction kinetics of ozone and dimethylsulfide and its atmospheric implications. *J. Geophys. Res.* **99**, 3597-3605.

Lelieveld J. and Crutzen P.J. (1991) The role of clouds in tropospheric photochemistry. *J. Atmos. Chem.* **12**, 229-267.

Leone J. A. and Seinfeld J. H. (1985) Comparative analysis of chemical reaction mechanisms for photochemical smog. *Atmospheric Environment* **19**, 437-464.

Li S. -M., Barrie L. A., Talbot R. W., Harris R. C., Davidson C. I. and Jaffrezo J. -L. (1993) Seasonal and geographic variations of methanesulfonic acid in the Artic troposphere. *Atmospheric Environment* **27A**, 3011-3024.

Li S. -M. and Barrie L. A. (1993) Biogenic sulfur aerosol in the Artic troposphere: 1. Contributions to total sulfate. *J. Geophys. Res.* **98**, 20,613-20,622.

Liss P. S., Malin G. and Turner S. M. (1993) Production of DMS by marine phytoplankton, In *Dimethylsulfide: Oceans, Atmosphere and Climate* (edited by Restelli G. and Angletti G.), pp. 1-14. Kluwer, Dordrecht.

Llyod A. C., Atkinson R., Lurmann F. W. and Nitta B. (1983) Modelingpotential ozone impacts from natural hydrocarbons-I. Development and testing of a chemical mechanism for the NO_x-air photooxidations of isoprene and α-pinene under ambient conditions. *Atmospheric Environment* **17** 1931-1950.

Luecken D. J., Berkowitz C. M. and Easter R. C. (1991) Use of a three-dimensional cloud-chemistry model to study the transatlantic transport of soluble species. *J. Geophys. Res.* **96**, 22,477-22,490.

Luria M., Van Valin C. C., Gunter R. L., Wellman D. L., Keene W. C., Galloway J. N., Sievering H. and Boatman J. F. (1990) sulfur dioxide over the western North Atlantic ocean during GCE/CASE/WATOX. *Global Biogeochem. Cycles* **4**, 381-393.

Luria M. and Sievering H. (1991) Heterogeneous and homogeneous oxidation of SO_2 in the remote marine atmosphere. *Atmospheric Environment* **25A**, 1489-1496.

Lurmann F. W., Llyod A. C. and Nitta B. (1983) Modeling potential ozone impacts from natural hydrocarbons-II. Hypothetical biogenic HC emission scenario modeling. *Atmospheric Environment* **17**, 1951-1963.

Lurmann F.W., Carter W. P. L. and Coyner L. A. (1987) A surrogate species chemical reaction mechanism for urban-scale air quality simulation models. *Rep. EPA/600/3-87/014,* U.S. Environ. Prot. Agency, Research Triangle Park, N.C.

Marti J. J., Jefferson A., Cai P. X., Richert C., McMurry P. H. andEisele F. (1997) H_2SO_4 vapor pressure of sulfuric acid and ammoniumsulfate solutions. *J. Geophys. Res.* **102**, 3725-3735.

Martin L. R. and Good T. W. (1991) Catalyzed oxidation of sulfur dioxide in solution: the iron-manganese synergism. *Atmospheric Environment* **25A**, 2395-2399.

Martin R. S., Westberg H., Allwine E., Ashman L., Farmer J. C. and Lamb B. (1994) Measurements of isoprene and its atmospheric oxidation products in a central Pennsylvania deciduous forest. *J. Atmos. Chem.* **28**, 1539-1542.

Matsumoto K. and Tanaka H. (1996) Formation and dissociation of atmospheric particulate

nitrate and chloride: an approach based on phase equilibrium. *Atmospheric Environment* **30**, 639-648.

McRae G. J., Goodin W. R. and Seinfeld J. H. (1982) Development of a second-generation mathematical model for urban air pollution, I. *Atmospheric Environment* **16**, 16,679-16,696.

Meissner H. P. and Kusik C. L. (1978) Electrolyte activity coefficients in inorganic processing. *AIChE Symp. Ser.* **173**, 14-20.

Mellouki A., Jourdain J. L. and Le Bras G. (1988) Discharge flow study of the $CH_3S + NO_2$ reaction mechanism using $Cl + CH_3SH$ as the CH_3S source. *Chem. Phys. Lett.* **148**, 231-236.

Meng Z. and Seinfeld J. (1996) Time scales to achieve atmospheric gas-aerosol equilibrium for volatile species. *Atmospheric Environment* **16**, 2889-2900.

Middleton P., Stockwell W. R. and carter W. P. L. (1990) Aggregation of volatile organic compound emissions for regional modeling. *Atmospheric Environment* **6**, 1107-1133.

Mihalopoulous N., Nyugen B. C., Biossard C., Campin J. M., Putaud J. P., Belviso S., Barnes I. and Becker K. H. (1992) Field study of dimethylsulfide oxidation in the boundary layer: Variations of dimethylsulfide, methanesulfonic acid, sulfur dioxide, non-sea-salt sulfate and Aitken nuclei at a coastal site. *J. Atmos. Chem.* **14**, 459-477.

Mozurkewich M. and Calvert J. G. (1988) Reaction probability of N_2O_5 on aqueous aerosols. *J. Geophys. Res.* **93**, 15,889-15,896.

Nair S. K. and Peters L. K. (1989) Studies on non-precipitating cumulus cloud acidification. *Atmospheric Environment* **23**, 1399-1423.

Niki H., Maker P. D., Savage C. M. and Breitenbach L. P. (1983b) An FITR study of the mechanism for the reaction $HO + CH_3SCH_3$. *Int. J. Chem. Kinet.* **15**, 647-654.

Odum J. R., Hoffmann T., Bowman F., Collins D., Flagan R. C. and Seinfeld J. H. (1996) Gas/particle partitioning secondary organic aerosol yields. *Envir. Sci. Technol.* **30**, 2580-2585.

Pandis S. N., Paulson S. E., Seinfeld J. H. and Flagan R. C. (1991) Aerosol formation in the photooxidation of isoprene and β-pinene. *Atmospheric Environment* **25A**, 997-1008.

Pandis S. N., Harley R. A., Cass G. R., and Seinfeld J. H. (1992) Secondary organic aerosol formation and transport. *Atmospheric Environment* **26A**, 2269-2282.

Pandis S.N. and Seinfeld J.H. (1989) Sensitivity analysis of a chemical mechanism for

aqueous-phase atmospheric chemistry. *J. Geophys. Res.* **94**, 1105-1126.

Paulson S. E., Flagan R. C. and Seinfeld J. H. (1992a) Atmosperic photooxidation of isoprene part I: The hydroxyl radical and ground state atomic oxygen reaction. *Int. J. Chem. Kinet.* **24**, 79-101.

Paulson S. E., Flagan R. C. and Seinfeld J. H. (1992b) Atmospheric photooxidation of isoprene part II: The ozone-isoprene reaction. *Int. J. Chem. Kinet.* **24**, 103-152.

Penn R. E., Block E. and Revelle L. K. (1978) Methanesulfenic acid. *J. Am. Chem. Soc.* **100**, 3622-3623.

Petersson G. (1988) High ambient concentration of monoterpenes in a Scandinavian pine forest. *Atmospheric Environment* **22**, 2617-2619.

Peters L. K., Berkowitz C. M., Carmicheal G. R., Easter R. C., Fairweather G., Ghan S. J., Hales J. M., Ruby Leung L., Pennel W. R., Potra F., Saylor R. D. and Tsang T. T. (1995) The current state and future direction of Eulerian models in simulating the tropospheric chemistry and transport of trace species: A review. *Atmospheric Environment* **29**, 189-222.

Pham M., Müller J. -F., Brasseur G. P., Granier C. and Mégie. (1995) A three-dimensional study of the tropospheric sulfur cycle. *J. Geophys. Res.* **100**, 26,061-26,092.

Piccot S. D., Watson J. J. and Jones J. W. (1992) A global inventory of volatile organic compound emissions from anthropogenic sources. *J. Geophys. Res.* **97**, 9897-9912.

Pilinis C. and Seinfeld J. H. (1987) Continued development of a general equilibrium model for inorganic multicomponent atmospheric aerosols. *Atmospheric Environment* **21**, 2453-2466.

Pilinis C. and Seinfeld J. H. (1988) Development and evaluation of an Eulerian photochemical gas-aerosol model. *Atmospheric Environment* **22**, 1985-2001.

Potukuchi S. and Wexler A. S. (1995) Indentifying solid-aqueous phase transitions in atmospheric aerosols-I. Nuetral-acidity solutions. *Atmospheric Environment* **29**, 1663-1676.

Potukuchi S. and Wexler A. S. (1995) Indentifying solid-aqueous phase transitions in atmospheric aerosols-II. Acidic solutions. *Atmospheric Environment* **29**, 3357-3364.

Potukuchi S. and Wexler A. S. (1997) Predicting vapor pressures using neural networks. *Atmospheric Environment* **31**, 741-753.

Pruppacher H. R. and Klett J. D. (1978) *Microphysics of clouds and precipitation.* Reidel, Hingham, Massachusetts.

Pszenny A. A. P., Harvey G. R., Brown C. J., Lang R. F., Keene W. C., Galloway J. N. and Merrill J. T. (1990) Measurements of dimethyl sulfide oxidation products in the summertime North Atlantic marine boundary layer. *Global Biogeochem. Cycles* **4**, 367-379.

Rasmussen R. A. (1972) What do the hydrocarbons from trees contributeto air pollution? *J. Air Pollut. Control Assoc.* **22**, 537-543.

Riba M. L., Tathy J. P., Tsiropoulos N., Monsarrat B. and Torres L. (1987) Diurnal variation in the concentration of α-pinene and β-pinene in the Landes Forest (France). *Atmospheric Environment* **21**, 191-193.

Roberts J. M., Fehsenfeld F. C., Albritton D. L. and Sievers R. E. (1983) Measurements of monoterpene hydrocarbons at Niwot Ridge, Colorado. *J. Geophys. Res.* **88**, 10,667-10,678.

Roberts J. M., Hahn J. M., Fehsenfeld F. C., Warnock J. M., Albritton D. L. and Sievers R. E. (1985) Monoterpene hydrocarbons in the night-time troposphere. *Envir. Sci. Technol.* **19**, 364-369.

Robinson R. A. and Stokes R. H. (1959) *Electrolyte SOlutions.* 2nd ed., Butterworth, London.

Rood M. J., Shaw M. A., Larson T. V. and Covert D. S. (1989) Ubiquitous nature of ambient metastable aerosol. *Nature* **337**, 537-539.

Saltzman E. S., Savoie D. L., Zika R. G. and Prospero J. M. (1983) Methane sulfonic acid in the marine atmosphere. *J. Geophys. Res.* **88**, 10,897-10,902.

Saltzman E. S. and Cooper D. J. (1988) Shipboard measurements of atmospheric dimethylsulfide and hydrogen sulfide in the Caribbean and Gulf of Mexico. *J. Atmos. Chem.* **7**, 191-209.

Saxena P., Hudischewskyj A. B., Seigneur C. and Seinfeld J. H. (1986) A comparative study of equilibrium approaches to the chemical characterization of secondary aersols. *Atmospheric Environment* **20**, 1471-1483.

Saxena P., Hildemann L. M., McMurry P. H. and Seinfeld J. H. (1995) Organics alter hygroscopic behavior of atmospheric particles. *J. Geophys. Res.* **100**, 18,755-18,770.

Scheinder S. H. (1989) The greenhouse effect: Science and policy. *Science* **243**, 771-781.

Schlesinger M E., Jiang X. and charlson R. J. (1992) Implication of anthropogenic atmospheric sulphate for the sensivity of the climate system *Proceedings of the Conference on Global Climate Change: Its Mitigation through Improved Production and Use of Energy,*

Los Alamos, NM, 21-24 October, 1991. Eds. J.C. Allred and A.S. Nichols, American Inst. Physics.

Schwartz S.E. and Freiberg J.E. (1981) Mass-transport limitation to the rate of reaction of gases in liquid droplets: application to oxidation of SO_2 in aqueous solutions. *Atmospheric Environment* **15**, 1129-1144.

Schwartz S.E. (1986) Mass-transport considerations pertinent to aqueous-phase reactions of gases in liquid-water clouds. In *Chemistry of Multiphase Atmospheric Systems* (edited by Jaeschke W.), pp. 415-471. Springer, Heidelberg

Schwartz S. E. (1988a)Are global cloud albedo and climate controlled by marine phytoplankton. *Nature* **336**, 441-445.

Schwartz S.E. (1988b) Mass-transport limitation to the rate of in-cloud oxidation of SO_2: re-examination in the light of new data. *Atmospheric Environment* **22**, 2491-2499.

Schwartz S. E. (1996) The whitehouse effect-shortwave radiative forcing of climate by anthropogenic aerosols: An overview. *J. Atmos. Sci.* **27**, 359-382.

Schwarzenbach R. P., Gschwend P. M. and Imboden D. M. (1993) *Environmental Organic Chemistry.* John Wiley and Sons, Inc., New York.

Seidell A. and Linke W. F. (1965) *Solubilities of Inorganic and Metal-organic Compounds.* American Chemical Society, Washington, D.C.

Seigneur C. and Saxena P. (1984) A study of atmospheric acid formation in different environments. *Atmospheric Environment* **18**, 2109-2124.

Seinfeld J. H. (1986) *Atmospheric Chemistry and Physics of Air Pollution.* John Wiley, New York.

Shaw M. A., Pandis S. N., Flagan R. C. and Seinfeld J. H. (1991) Aerosol formation in photochemical reactions of biogenic hydrocarbons in the presence of NO_x. Abstracts of the 10th Annual Meeting of the American Association for Aerosol Research, Traverse City, MI.

Shaw M. A. and Rood M. J. (1990) Measurement of the crystallization humidities of ambient aerosol particles. *Atmospheric Environment* **24A**, 1837-1841.

Shepson P. B., Edney E. O., Kleindienst T. E., Pittman J. H., Namie G. R. and Cupitt L. T. (1985) The production of organic nitrates from hydroxyl and nitrate radical reactions with propylene. *Envir. Sci. Technol.* **19**, 849.

Shi B. and Seinfeld J.H. (1991) On mass-transport limitation to the rate of reaction of gases

in liquid droplets. *Atmospheric Environment* **22**, 2491-2499.

Shine K. P., Derwent R. G., Wuebbles D. J. and Morcette J. -J. (1990) Radiative forcing of climate. In *Climate Change: The IPCC Scientific Assessment,* Cambridge University Press.

Sievering H., Ennis G. and Gorman E. (1990) Size distribution and statistical analysis of nitrate, excess sulfate, and chloride deficit in the marine boundary layer during GCE/CASE/ WATOX. *Global Biogeochem. Cycles* **4**, 395-405.

Simonaitis R., Olyszyna K. J. and Meagher J. F. (1991) Production of hydrogen peroxide and organic peroxides in the gas phase reactions of ozone with natural alkenes. *Geophys. Res. Lett.* **18**, 9-12.

Simonaitis R., Meagher J. F. and Bailey E. M. (1997) Evaluation of the condensed carbon bond (CB-IV) mechanism against smog chamber data at low voc and NOx concentrations. *Atmospheric Environment* **31**, 27-43.

Slinn W. G. N. (1991) Hints of another gremlin in the greenhouse: Anthropogenic sulfur. *Atmospheric Environment* **25A**, 2473-2489.

Spann J. F. and Richardson C. B. (1985) Measurement of the water cycle in mixed ammonium acid sulfate particles. *Atmospheric Environment* **19**, 819-825.

Spiro P. A., Jacobs D. J., and Logan J. A. (1992) Global inventory of sulfur emissions with $1^\circ \times 1^\circ$ resolution. *J. Geophys. Res.* **97**, 6023-6036.

Staffelbach T. A. and Kok G. L. (1993) Henry's law constants for aqueous solutions of hydrogen peroxide and hydroxymethyl hydroperoxide. *J. Geophys. Res.* **98**, 12,713-12,717.

Stokes, R. H., and R. A. Robinson (1966) Interactions in aqueous nonelectrolyte solutions. *J. Phys. Chem.* **70**, 2126-2131.

Stockwell W. R. (1986) A homogeneous gas-phase mechanism for use in a regional acid depositional model. *Atmospheric Environment* **20**, 1615-1632.

Stockwell W. R. (1995) On the HO_2 + HO_2 reaction: Its implication in atmospheric chemistry models. *J. Geophys. Res.* **100**, 1695-11,698.

Stockwell W. R., Middleton P., Chang J. S. and Tang X. (1990) The second generation regional acid deposition model chemical mechanism for regional air quality modeling. *J. Geophys. Res.* **95**, 16,343-16,367.

Streitwieser A. and Heathcock C. H. (1976) *Introduction to Organic Chemistry.* MacMillan, New York.

Stull R. B. (1988) *An Introduction to Boundary Layer Meteorology.* Kluwer, Boston.

Suhre K. and Rosset R. (1994) DMS oxidation and turbulent transport in the marine boundary layer: A numerical study. *J. Atmos. Chem.* **18**,379-395.

Suto M., Manzanares E. R. and Lee L. C. (1985). Detection of sulfuric acid aerosols by ultraviolet scattering. *Envir. Sci. Technol.* **19**, 815-820.

Tang I. N. and Lee J. H. (1987) Accommodation coefficients of ozone and SO_2: implications on SO_2 oxidation in cloud water. In *The Chemistry of Acid Rain, ACS Symposium Series 349,* American Chemical Society, Washington, D.C., pp 109-117.

Tang I. N., Wong W. T. and Munkelwitz H. R. (1981) The relative importance of atmospheric and nitrates in visibility reduction. *Atmospheric Environment* **15**, 2463-2471.

Tang I. N. and Munkelwitz H. R.(1984) An investigation of solute nucleation in levitated solution droplets. *J. Colloid Interface Sci.* **98**, 430-438.

Tang I. N., Munkelwitz H. R. and Wang N. (1986) Water activity with single suspended droplets: The NaCl-H_2O and KCl-H_2O systems. *J. Colloid Interface Sci.* **114**, 409-415.

Tang I. N. and Munkelwitz H. R. (1993) Composition and temperature dependence of the deliquescence properties of hygroscopic aerosols. *Atmospheric Environment* **27A**, 467-473.

Tang I. N. and Munkelwitz H. R. (1994a) Aerosol phase transformation and growth in the atmosphere. *J. Appl. Meteor.* **33**, 791-796.

Tang I. N. and Munkelwitz H. R. (1994b) Water activities, densities, and refractive indices of aqueous sulfates and sodium nitrate droplets of atmospheric importance. *J. Geophys. Res.* **99**, 18,801-18,808.

Tang I. N. (1997) Thermodynamic and optical properties of mixed-salt aerosols of atmospheric importance. *J. Geophys. Res.* **102**, 1883-1893.

Wexler, A. S. and J. H. Seinfeld, 1990: The distribution of ammonium salts among a size and composition dispersed aerosol. *Atmos. Environ., 24A,* 1231-1246.

Thompson A. M. and Zafiriou O. C. (1983) Air-sea fluxes of transient atmospheric species. *J. Geophys. Res.* **88**, 6696-6708.

Tuazon E.C. and Atkinson R. (1989) A product study of the gas-phase reaction of methyl vinyl ketone with the OH radical in the presence of NO_x. *Int. J. Chem. Kinet.* **21**, 1141-1152.

Tuazon E. C. and Atkinson R. (1990a) A product study of the gas-phase reaction of methacrolein with the OH radical in the presence of NO_x. *Int. J. Chem. Kinet.* **22**, 591-602.

Tuazon E. and Atkinson R. (1990b) A product study of the gas-phase reaction of isoprene with the OH radical in the presence of NO_x. *Int. J. Chem. Kinet.* **22**, 1221-1236.

Turnipseed A. A. and Ravishankara A. R. (1993) The atmospheric oxidation of dimethyl sulfide: Elementary steps in a complex mechanism, In *Dimethylsulfide: Oceans, Atmosphere and Climate* (edited by Restelli G. and Angletti G.), pp. 185-195. Kluwer, Dordrecht.

Tyndall G. S. and Ravishankara A. R. (1989a) Kinetics and mechanisms of the reactions of CH_3S with O_2 and NO_2 at 298. *J. Phys. Chem.* **93**, 2426-2435.

Tyndall G. S. and Ravishankara A. R. (1989b) Kinetics of the reaction of CH_3S with O_3 at 298 K. *J. Phys. Chem.* **93**, 4707-4710.

Vairavamurthy A., Andreae M. O. and Iverson R. L. (1985) Biosynthesis of dimethylsulfide and dimethylpropiothetin by Hymenomonas carterae in relation to to sulfur source and salinity variations. *Limnol. Oceanogr.* **30**, 59-70.

Wallington T. J., Atkinson R., Tuazon E. C. and Aschmann S. M. (1986a) The reaction of OH radical with dimethyl sulfide. *Int. J. Chem. Kinet.* **18**, 837-846.

Wallington T. J., Atkinson R., Winer A. M. and Pitts J. N. Jr. (1986b) Absolute rate constants for the gas-phase reactions of the NO_3 radical with CH_3SCH_3, NO_2, CO, and a series of alkanes at 298± K. *J. Phys. Chem.* **90**, 4640-4644.

Went F. W. (1960a) Organic matter in the atmosphere, and its possible relation to petroleum formation. *Proc. Natl. Acad. Sci. U.S.A.* **46**, 212-221.

Went F. W. (1960b) Blue hazes in the atmosphere. *Nature* **187**, 641-643.

Westberg H. H. and Rasmussen R. A. (1972) Atmospheric photochemical reactivity of monoterpene hydrocarbons. *Chemosphere* **4**, 163-168.

Wexler A. S. and Seinfeld J. H. (1991) Second-generation inorganic aerosol model. *Atmospheric Environment* **25 A**, 2731-2748.

Wexler A. S. and Seinfeld J. H. (1992) Analysis of aerosol ammonium nitrate: departures from equilibrium during SCAQS. *Atmospheric Environment* **26A**, 579-591.

Wexler A. S. and Seinfeld J. H. (1994) Modelling urban and regional aerosols-I. Model develpoment. *Atmospheric Environment* **28**, 531-546.

Whitby, K. T. (1978) The physical characteristics of sulfur aerosols. *Atmospheric Environment* **12**, 135-159.

Whitten G. Z., Hogo H. and Killus J. P. (1980) The carbon-bond mechanism: A condensed kinetic mechanism for photochemical smog. *Envir. Sci. Technol.* **18**, 280-287.

Wine P. H., Kreutter N. M., Gump C. A. and Ravishankara A. R. (1984) Kinetics of OH reactions with the atmospheric sulfur compounds H_2S, CH_3SH, CH_3SCH_3, and CH_3SSCH_3. *J. Phys. Chem.* **85**, 2660-2665.

Wolff G. T. (1984) On the nature of nitrate in coarse continental aerosols. *Atmospheric Environment* **18**, 977-981.

Worsnop D. R., Zahniser M. S., Kolb C. E., Gardner J. A., Watson L. R., Doren J. M. V., Jayne J. T. and Davidovits P. (1989) Temperature dependence of mass accommodation of SO_2 and H_2O_2 on aqueous surfaces. *J. Phys. Chem.* **93**, 1159-1172.

Wylie D. J. and de Mora S. J. (1996) Atmospheric dimethylsulfide and sulfur in aerosol and rainwater at a coastal site in New Zealand. *J. Geophys. Res.* **101**, 21,041-21,049.

Yin F., Grosjean D. and Seinfeld J. H. (1990a) Photooxidation of dimethyl sulfide and dimethyl disulfide. I: Mechanism development. *J. Atmos. Chem.* **11**, 309-364.

Yin F., Grosjean D. Flagan R. C. and Seinfeld J. H. Photooxidation of DMS and DMDS I, mechanism evaluation. *J. Atmos. Chem.* **11**, 365-399.

Yokouchi Y., Okaniwa M., Ambe Y. and Fuwa K. (1983) Seasonal variation of monoterpenes in the atmosphere of a pine forest. *Atmospheric Environment* **17**, 743-750.

Yokouchi Y. and Ambe Y. (1985) Aerosols formed from the chemical reaction of monoterpenes and ozone. *Atmospheric Environment* **19**, 1271-1276.

Yvon S. A., Saltzman E. S. and Cooper D. J. (1996) Atmospheric sulfur cycling in the tropical Pacific marine boundary layer(12°S, 135°W): A comparison of field data and model results 1. Dimethylsulfide. *J. Geophys. Res.* **101**, 6899-6909.

Yvon S. A. and Saltzman E. S. (1996) Atmospheric sulfur cycling in the tropical Pacific marine boundary layer(12°S, 135°W): A comparison of field data and model results 2. Sulfur dioxide. *J. Geophys. Res.* **101**, 6911-6918.

Zaytzev I. D. and Aseyev G. G. (1992) *Properties of Aqueous Solutions of Electrolytes,* translated by Lazarev M. A. and Sorochenko V. R., CRC Press, Boca Raton.

Zdanovskii A. B. (1948) New methods of calculating solubilities of electrolytes in multicomponent systems. *Z. Fiz. Khim* **22**, 1475- 1485.

Zhang S.-H., Shaw M., Seinfeld J. H. and Flagan R. C. (1992) Photochemical aerosol formation from α-pinene and β-pinene. *J. Geophys. Res.* **97**, 20,717-20,729.

Zimmerman P. R., Chatfield R. B., Fishman J., Crutzen P. J. and Hanst P. L. (1978) Estimates on the production of CO and H_2 from the oxidation of hydrocarbon emissions

from vegetation. *Geophys. Res. Lett.* **5**, 679-682.

Zimmerman J. and Poppe D. (1996) A supplement for the RADM2 chemical mechanism: The photooxidation of isoprene. *Atmospheric Environment* **30**, 1255-1269.

Appendix A

Empirical Data

The binary solution molality of the k^{th} electrolyte at the same water activity as the multicomponent solution, $m_k^o(a_w)$, is calculated in terms of the solute weight percent, $wt_k\%$, as

$$m_k^o(a_w) = \frac{1000 \times wt_k\%}{(100 - wt_k\%)M_k} \tag{A.1}$$

where the following polynomial function of a_w is used to fit the $wt_k\%$ vs a_w data

$$wt_k\% = \sum_{i=1}^{6} a_i \times a_w^{i-1} \tag{A.2}$$

The coefficients $a_1, \ldots, a_6$ are listed in Table (A.1) along with the lowest water activity to the point at which the fit is valid.

Table A.1: List of coefficients used in Equation (A.2).

Species	a_1	a_2	a_3	a_4	a_5	a_6	a_w
$(NH_4)_2SO_4$	55.7746	340.600	-1246.28	1609.07	-758.625	0.0	0.33
$(NH_4)_3H(SO_4)_2$	54.8479	324.668	-1095.82	1340.44	-622.268	0.0	0.35
NH_4HSO_4	99.9463	-4.44746	-211.964	162.271	136.701	-180.971	0.09
NH_4NO_3	29.0600	683.665	-2690.93	4669.83	-3880.30	1188.37	0.25
NH_4Cl	207.255	-578.282	708.227	-337.359	0.0	0.0	0.47
NaCl	69.7436	12.9500	-328.584	515.543	-269.459	0.0	0.44
$NaNO_3$	102.909	-38.7459	-173.813	352.626	-244.899	0.0	0.10
Na_2SO_4	-45.2046	831.382	-958.888	-2142.77	4562.16	-2248.38	0.50
$NaHSO_4$	95.8828	-44.3537	-34.4257	40.6049	-58.1498	0.0	0.02
H_2SO_4	77.0059	-169.642	559.358	-1232.53	1313.98	-547.514	0.02
HNO_3	89.3258	-211.049	695.363	-1512.98	1580.25	-641.018	0.03
HCl	41.9972	-55.1763	59.4494	-45.2738	0.0	0.0	0.03

Table A.2: Deliquescence points of pure salts at 298.15 K and their temperature dependency parameters in Equation (6.16).

Salt	%DRH @ 298.15 K	θ_s	A	B	C	Ref.[a]
$(NH_4)_2SO_4$	80	762.6	0.1149	-4.489×10^{-4}	1.385×10^{-6}	TM
$(NH_4)_3H(SO_4)_2$	69	—	—	—	—	
NH_4HSO_4	40	—	—	—	—	
NH_4NO_3	62	1962.1	4.2980	-3.623×10^{-2}	7.853×10^{-5}	TM
NH_4Cl	77	239.0	1.0	0.0	0.0	WS
NaCl	75	226.3	0.1805	-5.310×10^{-4}	9.965×10^{-7}	TM
$NaNO_3$	74	1597.0	0.1868	-1.677×10^{-3}	5.714×10^{-6}	TM
Na_2SO_4	84	-1176.8	0.3754	-1.763×10^{-3}	2.424×10^{-6}	TM
$NaHSO_4$	52	—	—	—	—	PS

[a] TM, Tang and Munkelwitz (1993); WS, Wexler and Seinfeld (1991); PS, Pilinis and Seinfeld (1987).

Table A.3: Polynomial coefficients for binary activity coefficients fitted for ionic strengths up to 100 mol kg^{-1}.

Ion Pair	b_1	b_2	b_3	b_4	b_5	Ref*
$NH_4^+ \cdot NO_3^-$	-2.48853	2.91219	-6.21873	9.55365	-5.53277	KM
$NH_4^+ \cdot Cl^-$	-2.28099	5.59336	-8.31218	10.6277	-5.21597	KM
$Na^+ \cdot Cl^-$	-2.23080	7.44165	-6.83748	6.78788	-1.94559	KM
$Na^+ \cdot NO_3^-$	-2.38934	4.00721	-7.74416	10.6300	-5.95990	KM
$H^+ \cdot NO_3^-$	-2.09150	9.30160	-18.8676	22.8304	-12.2958	CB
$H^+ \cdot Cl^-$	-3.15365	15.7096	-8.57785	1.28312	5.64853	WX
$NH_4^+ \cdot OH^-$	-1.63618	1.30818	10.5695	-26.6700	24.6655	PC
$Na^+ \cdot OH^-$	-2.27696	8.59497	-5.74177	3.47904	0.84303	KM

* KM, fit of data generated using the model of Kusik and Meissner (1978); WX, Meissner and Kusik model parameter taken from Wexler and Seinfeld (1991). CB, fit of data generated using the extended Pitzer and Simonson model given in Clegg and Brimblecombe (1990). PC, NH_4OH is assumed to be present in aqueous $(NH_4)_2SO_4$, $\gamma_{NH_4^+}$ is calculated using the method given in Clegg and Brimblecombe (1995), and γ_{OH^-} is estimated from Pitzer's expression, but including only the $NH_4^+ - OH^-$ ionic interaction.

Table A.4: Diffusivities and mass accommodation coefficients.

	Species	D_L[a] ($cm^2\ s^{-1}$)	α_m (-)	Source for α_m
1.	HNO_3	2.30×10^{-5}	1×10^{-2}	Assumed
2.	HNO_2	2.68×10^{-5}	1×10^{-2}	Assumed
3.	SO_2	2.11×10^{-5}	5×10^{-2}	Gardner *et al.*, 1987
4.	H_2SO_4	1.69×10^{-5}	1×10^{-2}	Assumed
5.	HCl	2.47×10^{-5}	1×10^{-2}	Assumed
6.	HCOOH	1.97×10^{-5}	1×10^{-2}	Assumed
7.	CH_3COOH	1.46×10^{-5}	1×10^{-2}	Assumed
8.	CO_2	2.13×10^{-5}	1×10^{-2}	Assumed
9.	MSA	1.37×10^{-5}	1×10^{-2}	Assumed
10.	NH_3	3.53×10^{-5}	1×10^{-2}	Assumed
11.	HO_2	3.32×10^{-5}	2×10^{-1}	Mozurkewich *et al.*, 1987
12.	H_2O_2	3.05×10^{-5}	2×10^{-1}	Worsnop *et al.*, 1989
13.	HCHO	2.21×10^{-5}	1×10^{-2}	Assumed
14.	NO_2	2.87×10^{-5}	6.3×10^{-4}	Lee and Tang, 1988
15.	NO_3	2.42×10^{-5}	1×10^{-2}	Assumed
16.	O_3	2.89×10^{-5}	5.3×10^{-4}	Tang and Lee, 1988
17.	OH	4.59×10^{-5}	8×10^{-2}	Hanson *et al.*, 1992
18.	CH_3O_2	1.90×10^{-5}	1×10^{-2}	Assumed
19.	CH_3OH	2.03×10^{-5}	1×10^{-2}	Assumed
20.	CH_3OOH	1.84×10^{-5}	1×10^{-2}	Assumed
21.	DMS	1.32×10^{-5}	1×10^{-2}	Assumed
22.	DMSO	1.26×10^{-5}	1×10^{-2}	Assumed
23.	$DMSO_2$	1.20×10^{-5}	1×10^{-2}	Assumed
24.	N_2O_5	—	1×10^{-2}	Assumed

[a] Aqueous-phase diffusivity is estimated by (Schwarzenbach *et al.*, 1993)
$D_{L,i} = 13.26 \times 10^{-5} / (\mu^{1.4} (\bar{V}_i)^{0.589})$
where μ is the solution viscosity at temperature of interest (cPoise); and $\bar{V}_i$ is the molar volume of species i ($cm^3\ mol^{-1}$), obtained from Table A.5. Gas-phase diffusivity is assumed equal to 0.1 $cm^2\ s^{-1}$ for all species.

Table A.5: Diffusion volumes of organic molecules (Fuller *et al.*, 1966).

Element	Volume Contribution $cm^3\ mol^{-1}$
C	16.5
H	2.0
O	5.5
N	5.7
Cl	19.5
S	17.0
Rings	-20.2

Vita

Rahul A. Zaveri was born on October 1, 1969 in Bombay, India. In July 1987, he began his undergraduate studies in Chemical Engineering at the University of Bombay, Department of Chemical Technology. He graduated in July 1991 and joined the Department of Chemical Engineering at the University of Kentucky in August 1991 from which he earned the Master of Science degree in 1993. In August of 1993, he entered the Doctoral program in the Department of Chemical Engineering at Virginia Polytechnic Institute and State University, and graduated in June 1997. He then joined the Atmospheric Sciences Technical Group at Battelle Pacific Northwest National Laboratory for his post doctoral training.